Catalytic Nanomaterials for Amplified Biosensing

Colleen N. Loynachan

Imperial College London
Department of Materials

Submitted in accordance with the requirements for the degree of
Doctor of Philosophy

October 2018

Declaration of Originality

I declare that the original scientific content in this thesis is my own, unless otherwise stated or referenced within. Experimental work or data analysis done in collaboration with, or with the assistance of others is appropriately acknowledged within the text and relevant figure captions. The work presented in this thesis was performed at Imperial College London and Massachusetts Institute of Technology.

Copyright Declaration

The copyright of this thesis rests with the author and is made available under a Creative Commons Attribution Non-Commercial No Derivatives license. Researchers are free to copy, distribute or transmit the thesis on the condition that they attribute it, that they do not use it for commercial purposes and that they do not alter, transform or build upon it. For any reuse or redistribution, researchers must make clear to others the license terms of this work.

Acknowledgements

I am grateful to my advisor, Professor Molly Stevens, who has been a supportive mentor over the last four years, and whose standards for excellence and ability to manage and lead such a large, dynamic, and interdisciplinary group continue to inspire me. Thank you for providing generous resources, opportunities, and freedom for me to grow into an independent scientist.

The postdoctoral researchers I have worked with have been the most patient and supportive teachers. I would especially like to thank Dr. Michael Thomas for his thoughtful mentorship and guidance in all aspects of my experimental work. I have learned a great deal about nanoparticle synthesis, sensing, and experimental design from him and it was an adventure learning the joys and pains of lateral flow assays together. Dr. Yiyang Lin taught me peptide synthesis and has always been graciously willing to answer any questions at all hours. Dr. Adrian Najer taught me about gel filtration chromatography, fluorescence correlation spectroscopy, and has been a very positive motivator on the *in vivo* sensing project. Dr. Eleanor Gray prepared the modified nanobody used in this thesis and helped run the clinical HIV samples, Dr. Daniel Richards optimized the site-selective modification of the nanobody, Dr. Jennifer Brookes performed simulations of the nanobody, and Benjamin Miller performed characterization of the nanobody binding constants. Dr. Eunjung Kim helped with scanning electron microscopy imaging, Dr. Qu Chen helped with high resolution transmission electron microscopy, Dr. Ulrike Kauscher performed cryogenic electron microscopy, and Dr. Shweta Agarwal helped with scanning transmission electron microscopy and energy-dispersive X-ray spectroscopy analysis. Masters' student Marie Kim helped with synthesis of nanomaterials for the lateral flow work. I would also like to acknowledge Sandra Hemmington, David Hall, and Josh Denton at Mologic Ltd. for sharing industrial know-how and support in lateral flow development.

I want to thank the many other members of the Stevens Group for their help in the lab and for fruitful discussions, including Dr. Adam Gormley, Dr. Bakul Gupta, Dr. Stuart Higgins, Dr. Chris Spicer, Dr. Chris Wood, Dr. Shaodong Zhang, Dr. Marta Broto, Dr. Yunlei Xianyu, Dr. Adam Creamer, Dr. James Armstrong, Dr. Stacey Skaalure, Dr. Anika Nagelkerke, Dr. Maggie Holme, Dr. Carolyn Ibsen, Dr. Christine Wang, Dr. Jane Hsu, Dr. Ye Wang, Nayoung Kim, Lucia Massi, Valeria Nele, Marco Sorbona, Michael Potter, Jelle Penders, Brian Chen, and Alexis Belessiotis-Richards. It has been a pleasure to share the lab with such talented researchers. Thank you also to Sabrina Skeete, Dr. Ben Pierce, and Dr. Akemi Nogiwa Valdez for supporting the group in so many ways.

I have been fortunate enough to engage in productive collaborations with researchers from outside the Stevens Group. I am grateful for the support of Dr. Vijay Chudasama (University College London), Professor Rachel McKendry (University College London), Professor Irene Yarovsky (Royal Melbourne Institute of Technology), and Professor Sangeeta Bhatia (Massachusetts Institute of Technology) for fostering these external collaborations. I am thankful to the EPSRC i-Sense mobility fellowship for funding a fruitful collaboration with MIT. My work with Ava Soleimany and Dr. Jaideep Dudani at MIT has been a source of great intellectual enjoyment and personal growth.

I am grateful to the Marshall Aid Commemoration Commission for generous funding of my graduate studies in the UK, and I feel fortunate to be a part of the Marshall community in London. I have learned a great deal about the importance of the special relationship and will continue to promote positive US – UK relations through scientific collaboration.

I owe a great deal to the influence of my early scientific mentors at MIT, including Professor Polina Anikeeva and Professor Linn Hobbs. I could not ask for better role models and am immensely grateful that they believed in me and gave me the confidence to pursue research.

To Alex Brogan, my ideal companion, for being a constant source of happiness, love, support, and inspiration in my life. I never knew life could be so perfectly balanced and full of joy until I met you. Special thanks to our affectionate kitties Scout and Olive for never leaving my side through the writing process.

None of this work would have been possible without the love and support of my mom, dad, and sister, Emily, who have given me everything and have encouraged and supported me along every path I have chosen. Thank you for teaching me about perseverance, strong work ethics, how to be a creative thinker, and for helping me to always see the beauty and art in my scientific endeavors.

Abstract

Accurate, timely, and sensitive diagnosis is the first step in appropriately treating disease. The development of diagnostics that can be used in non-hospital and point-of-care (PoC) settings is key for democratizing access to disease diagnosis and treatment when it is most effective. The application of PoC diagnostics in early disease detection is often limited due to insufficient sensitivity for the short time frames and limited resources available in these settings. To overcome these challenges, this thesis presents the synthesis, characterization, and application of catalytic nanomaterials for signal amplification and enhanced sensitivity in PoC diagnostic platforms. The nanomaterials developed here span a broad size regime from 1.5 nm clusters of atoms to 300 nm diameter particles and have been demonstrated for use in both *in vitro* and *in vivo* biosensing platforms. The platinum and gold nanomaterials exhibited robust and efficient peroxidase-like activity in their ability to oxidize chromogenic substrates in the presence of hydrogen peroxide to generate additional colored signals that could be used for amplification of disease detection, even after exposure to harsh conditions such as elevated temperatures.

The larger catalytic nanomaterials were employed as extraordinarily stable and highly amplifying labels in a simple paper-based lateral flow assay (LFA). The nanocatalyst-labeled LFA surpassed the sensitivities of both commercial and published reports to date for paper-based detection of p24, one of the earliest and most conserved biomarkers of HIV. The smaller catalytic nanoclusters were efficiently renally cleared and were deployed in a modular nanosensor platform to monitor disease-associated protease activity *in vivo.* Catalytic activity of cleared gold nanoclusters in collected urine provided a simple, sensitive, and rapid colorimetric urinary readout of disease state. The clinical utility of both platforms presented here was investigated through detection of acute phase HIV in clinical human plasma samples using the nanocatalyst-labeled LFA, and successful non-invasive detection of tumors in a mouse model of colorectal cancer using the protease-nanosensors with colorimetric urinary readout. This thesis demonstrates the broad applicability and versatility of catalytic nanoparticle amplification for use in disease detection. A pipeline for further development of both sensing platforms for detection of other biomolecules at the PoC is presented.

Publications & Conference Presentations

The work presented in Chapter 1 has been published, in part, in the book chapter:

K. L. Herpoldt, **C. N. Loynachan**, and M. M. Stevens, “Nanomaterials for Biological Sensing.” *Reference Module in Materials Science and Materials Engineering,* 2017.

The work presented in Chapter 2 has been published:

C. N. Loynachan, M. R. Thomas, E. R. Gray, D. A. Richards, J. Kim, B. S. Miller, J. C. Brookes, S. Agarwal, V. Chudasama, R. A. McKendry, and M. M. Stevens. “Platinum Nanocatalyst Amplification: Redefining the Gold Standard for Lateral Flow Immunoassays with Ultrabroad Dynamic Range.” *ACS Nano.* 2018, *12*, 279–288.

The work presented in Chapter 3 is in preparation for submission:

C. N. Loynachan, A. P. Soleimany, J. S. Dudani, Y. Lin, Q. Chen, A. Najer, S. N. Bhatia, M. M. Stevens. “Renal clearable catalytic gold nanoclusters for *in vivo* disease monitoring” (*in preparation*).

P. Charchar, A. J. Christofferson, **C. N. Loynachan**, Y. Xianyu, A. Belessiotis, M. M. Stevens, I. Yarovsky, “A Mechanistic Study of Hydrogen Peroxide Disproportionation on Glutathione-capped Gold Nanoclusters” (*in preparation*).

The thesis work was selected for oral presentations at the following international conferences:

RSC 5th International Conference on Multifunctional, Hybrid and Nanomaterials (Spring 2017); Materials Research Society (Spring 2018 and Fall 2018), and an invited talk at the American Chemical Society National Meeting (Fall 2018).

Scope of the Thesis

Chapter 1 introduces the key background and literature that motivated the work presented in this thesis. It serves as a general introduction to disease diagnosis and presents background on molecular recognition, and the fundamental design principles of immunoassays and activity-based sensors. Additionally, this chapter explores the role of nanomaterials in biosensing systems, and introduces some unique properties of nanomaterials, including enzyme-mimetic catalytic activity, particularly peroxidase-mimicking activities, which is further exploited in the following results chapters. While Chapter 1 serves as a general introduction, because the thesis covers a broad range of topics, each subsequent chapter begins with a more specific review of relevant literature specific to the theme of the chapter and includes context for the results.

Chapter 2 examines the use of catalytic nanoparticles as labels in paper-based lateral flow assays (LFA). The chapter begins with background on early detection of HIV and introduces relevant biomarkers. The principles of lateral flow assay development are outlined and the key factors that affect test sensitivity are discussed. Fundamental theory related to shape and size-controlled synthesis of nanoparticles is presented. A series of catalytic nanomaterials are synthesized and characterized, and the optimized nanoparticle label, consisting of a gold core with porous platinum shell, is taken forward for the development of the LFA. Each component of the LFA is optimized, including nanoparticle size and porosity, recognition elements, and test architecture. The exceptional thermal stability of this system is highlighted through accelerated aging studies. The optimized nanocatalyst amplified LFA is used for sensitive detection of acute phase HIV in clinical plasma samples.

Chapter 3 investigates the use of renally clearable gold nanoclusters as probes for *in vivo* detection of disease-associated proteases. The chapter begins with background on activity-based sensors for protease detection, introduction to protein and peptide-templated nanocluster synthesis techniques, and discussion of *in vivo* clearance mechanisms of nanoparticles. Nanocluster synthesis methods were optimized in terms of size and peroxidase-like activity. A novel synthesis method to produce renal-clearable catalytic nanoclusters incorporating protease-cleavable peptides was developed and particles were subsequently assembled into protease-responsive nanosensors. The nanosensors were deployed for *in vitro* detection of MMP9 and thrombin, proteases in involved in cancer and blood clotting cascades, respectively. Finally, the nanosensor platform was used to successfully detect tumors *in vivo* in a mouse model of colorectal cancer with a simple colorimetric urinary readout.

Finally, **Chapter 4** summarizes the major findings of the thesis and discusses possible scope for future work incorporating catalytic nanoparticles into both *in vitro* and *in vivo* biosensing platforms. Emphasis is placed on how the modular and versatile platforms presented in Chapters 2 and 3 can be expanded for detection of other diseases and translated for use in relevant clinical settings.

Contents

1. Introduction 20

1.1 Disease Diagnosis 20
1.1.1 Diagnosis at the point-of-care 23
1.2 Biomarkers 24
1.3 Biomarker detection 25
1.3.1 Antibodies and antibody fragments 25
1.3.2 Antibody-antigen interactions 27
1.3.3 Principles of immunoassays 28
1.3.4 Activity-based probes 31
1.4 Nanoparticles in biosensing 33
1.4.1 Noble metal nanoparticles 33
1.5 Nanomaterials with enzyme-like activities 34
1.5.1 Mechanism of hydrogen peroxide disproportionation on metal nanoparticles 35

2. Development of nanocatalyst amplified lateral flow assay 39

2.1 Introduction 39
2.1.1 Aims 39
2.1.2 Background 40
2.1.2.1 HIV Diagnostic Landscape & Early detection 40
2.1.2.2 Lateral flow assay (LFA) 44
2.1.2.2.1. Nanoparticle label 47
2.1.2.2.2. Recognition molecules 47
2.1.2.2.3. Flow speed (reaction time) 49
2.1.2.2.4. Balancing nonspecific binding (NSB) 49
2.1.2.3 Signal amplification techniques for colorimetric lateral flow assays 50
2.1.2.4 Metal nanocatalysts 51
2.1.2.5 Growth of metal nanoparticles 52
2.1.2.5.1. Homogeneous nucleation 52
2.1.2.5.2. Heterogenous nucleation 52
2.1.2.5.3. Growth modes 53
2.1.3 Overview of PtNC amplified LFA design 55
2.2 Materials & Methods 58
2.2.1 Synthesis of gold nanoparticle seeds 58
2.2.2 Synthesis of porous platinum core-shell nanoparticles (PtNCs) 58

2.2.3 Characterization of nanoparticles 59
2.2.4 Preparation of PtNC-antibody conjugates 59
2.2.5 Evaluation of peroxidase-like activity 60
2.2.6 Production of cysteine presenting nanobody *via* site directed mutagenesis of an existing nanobody 61
2.2.7 Site-selective modification of nanobody 61
2.2.8 Characterization of antibody components 61
2.2.9 Preparation of PtNC-amplified lateral flow assay 62
2.2.10 Preparation of aged samples for accelerated stability testing 63
2.2.11 Structural model of nanobody 63
2.2.12 Image analysis of lateral flow test strips 64
2.3 Results & Discussion 65
2.3.1 Nanocatalyst composition 65
2.3.2 Synthesis and characterization of platinum nanocatalysts 70
2.3.3 Effect of PtNC size and porosity on catalytic activity 78
2.3.4 Physiological stability 84
2.3.5 Lateral flow test optimization and architecture to support catalytic amplification 86
2.3.6 Antibody modification and conjugation of affinity reagents 91
2.3.7 Effect of catalytic nanoparticle label size in lateral flow 97
2.3.8 Stability of nanobody and nanocatalyst against accelerated ageing 100
2.3.9 Performance of nanocatalyst LFA in serum and clinical samples 103
2.3.10 Challenges for clinical translation 107
2.4 Conclusions and future work 110
2.4.1 Conclusions 110
2.4.2 Detection of other analytes 111
2.4.3 Expanding library of catalytic labels 113

3. Catalytic nanoclusters for *in vivo* disease monitoring 116

3.1 Introduction 116
3.1.1 Aims 116
3.1.2 Background 116
3.1.2.1 Protein and peptide templated nanoclusters 118
3.1.2.2 Catalytic activity of noble metal nanoparticles 120
3.1.2.3 Renal clearance of nanoparticles 120
3.1.2.4 Hepatic clearance of nanoparticles 122
3.1.2.5 Tumor targeting ability of engineered nanoparticles 123

3.1.3 Overview of protease nanosensor platform 124
3.2 Materials & Methods 127
3.2.1 Materials 127
3.2.2 Solid phase peptide synthesis 127
3.2.3 Nanocluster synthesis & purification 127
3.2.3.1 Protein-templated nanoclusters 127
3.2.3.2 Peptide-template nanoclusters 128
3.2.4 Characterization of Nanoparticles 129
3.2.5 Evaluation of Peroxidase-like Activity 129
3.2.6 Steady-state kinetic assays 130
3.2.7 AuNC complex assembly and purification 130
3.2.8 Gel filtration chromatography assays 131
3.2.9 Fluorescence correlation spectroscopy (FCS) 132
3.2.10 *In vivo* renal clearance studies 135
3.2.11 Urine catalytic activity assays 135
3.2.12 Inductively coupled plasma-mass spectrometry (ICP-MS) 136
3.2.13 Cell culture and secreted protease assay 136
3.2.14 Pharmacokinetic studies 136
3.2.15 Colorectal cancer xenograft studies 137
3.2.16 Statistical analyses 137
3.3 Results & Discussion 138
3.3.1 Optimization of synthesis of protein and peptide templated nanoclusters 138
3.3.2 Preliminary *in vivo* renal clearance 143
3.3.3 Design of gold nanocluster functionalized protease nanosensors 147
3.3.4 Synthesis and characterization of peptide-functionalized AuNCs 147
3.3.5 Catalytic activity of peptide-templated AuNCs 153
3.3.6 AuNCs are cleared *via* the kidney and retain their catalytic activity in urine 160
3.3.7 Formation and characterization of nanosensor complexes 163
3.3.8 Engineered AuNC nanosensor complexes are sensitive to protease activity 165
3.3.9 Kinetics of *in vitro* recombinant protease cleavage 170
3.3.10 Biocompatibility of AuNC nanosensors 173
3.3.11 AuNC nanosensors enable colorimetric urinary detection of disease 175
3.4 Conclusions and future work 180
3.4.1 Conclusions 180
3.4.2 Mechanism of AuNC catalytic activity 180
3.4.3 Expanding the library of biological templates for nanocluster synthesis 182

4. Conclusions and Future Work 185

4.1 Conclusions 185

4.1.1 *In vitro* sensing 185

4.1.2 *In vivo* sensing 187

4.2 Future scope of catalytic nanomaterials for amplified biosensing 189

4.2.1 Rational design of enzyme-mimetic nanomaterials 189

4.3 Perspective 190

5. References 191

List of Figures

Figure 1.1 Structure of conventional immunoglobulin G (IgG) antibody 26
Figure 1.2 Schematic of sandwich immunoassay. 29
Figure 1.3 Schematic illustrating the disparate time scales in a lateral flow assay. 31
Figure 1.4 Schematic of *in vivo* protease nanosensor platform. 33
Figure 1.5 TEM images of three typical peroxidase nanozymes 35
Figure 1.6 Schematic showing disproportionation of hydrogen peroxide. 36

Figure 2.1 Biomarkers present in blood days post HIV infection 42
Figure 2.2 Typical configuration of a lateral flow assay test strip 45
Figure 2.3 Comparison of two different nucleation processes 53
Figure 2.4 Scheme showing amplified LFA 56
Figure 2.5 Image processing procedure for analysis of LFA strips 64
Figure 2.6 TEM images of catalytic nanoparticles 66
Figure 2.7 Strucutre of TMB and oxidized TMB 67
Figure 2.8 TEM images of Pd-Ir nanocubes and PtNCs. 69
Figure 2.9 Scheme showing synthesis of Au-Pt core shell structure (PtNC). 71
Figure 2.10 Effect of PVP on PtNC synthesis. 72
Figure 2.11 TEM images of PtNCs synthesized with varying AuNP seed concentrations 74
Figure 2.12 EDS mapping of PtNCs of varying sizes 75
Figure 2.13 TEM images of PtNCs formed by varying [Au]: [Pt] 76
Figure 2.14 DLS and catalytic activity of PtNCs 77
Figure 2.15 Catalytic activity normalized to surface area 79
Figure 2.16 TEM of nanoscale roughness of PtNCs 80
Figure 2.17 STEM and EDS investigation of porosity 81
Figure 2.18 Investigation of PtNC porosity through AuNP core size variation.. 83
Figure 2.19 PtNC activity in physiological environments 85
Figure 2.20 Catalytic development strategies for LFA 88
Figure 2.21 PtNC biotin LFA 89
Figure 2.22 SEM images of biotinylated PtNCs bound on the streptavidin test line 90
Figure 2.23 Comparison of membrane blocking strategies for LFA. 91
Figure 2.24 Scheme for site-selective chemical modification of nanobody 93
Figure 2.25 Optimization of PtNC antibody modification 96
Figure 2.26 LFA of antibody physisporption and running buffer optimization 97
Figure 2.27 Effect of PtNC diameter on LFA test line intensity 99

Figure 2.28 Reproducibility of PtNC synthesis 100
Figure 2.29 Thermal stability of nanobody. 101
Figure 2.30 Accelerated aging study of PtNC LFA. 102
Figure 2.31 Time to result versus sample size 103
Figure 2.32 PtNC LFA limit of detection in serum 105
Figure 2.33 Clinical HIV seroconversion panel 107
Figure 2.34 Effect of EDTA anticoagulants on LFA stability 109
Figure 2.35 Dynamic ranges of 4th generation LFA, ELISA, and PtNC LFA. 111
Figure 2.36 Process flow for the rapid prototyping of PtNC LFA 111
Figure 2.37 Pd-Ir versus HRP labeled LFA. 114

Figure 3.1 Schematic of the structure of Au-thiolate nanoclusters 119
Figure 3.2 Design of *in vivo* protease nanosensor platform 125
Figure 3.3 Experimental gel filtration chromatography set-up 132
Figure 3.4 Examples of FCS autocorrelation curves. 135
Figure 3.5 Characterization of protein-templated nanocluster synthesis 140
Figure 3.6 TEM of Lyz-AuNCs 141
Figure 3.7 TEM images of glutathione-protected AuNCs. 142
Figure 3.8 Catalytic activity of nanoclusters synthesized with varying core metals 143
Figure 3.9 Catalytic activity of GSH-AuNCs in synthetic urine. 144
Figure 3.10 Preliminary *in vivo* renal clearance study. 145
Figure 3.11 Schematic showing one-pot synthesis of AuNCs 148
Figure 3.12 LC-MS chromatograms of protease-cleavable peptide substrates 150
Figure 3.13 UV-vis and fluorescent spectra of AuNCs 151
Figure 3.14 TEM images of AuNCs synthesized with different peptide sequences. 152
Figure 3.15 DLS of AuNCs synthesized with different peptide sequences 153
Figure 3.16 Optimization of catalytic activity assay for GSH-AuNCs. 155
Figure 3.17 Characterization and limit of detection of peptide functionalized AuNCs. 157
Figure 3.18 Optimization of activity and biotin loading on AuNCs. 159
Figure 3.19 *in vivo* renal clearance of AuNCs by catalytic activity and ICP-MS 162
Figure 3.20 DLS for AuNCs and AuNC-Neutravidin complexes. 164
Figure 3.21 TEM of purified AuNC-$P1_{20}$-NAv complexes 165
Figure 3.22 Protease cleavage assays based on gel filtration chromatography. 167
Figure 3.23 Gel filtration chromatography controls and effect of linker length. 169
Figure 3.24 Effect of protease substrate loading on AuNC cleavage efficiency. 170
Figure 3.25 FCS experiments to monitor *in vitro* protease cleavage kinetics 173
Figure 3.26 Biocompatibility of AuNC-NAv complex. 175

Figure 3.27 Pharmacokinetics and organ accumulation of avidin carrier protein..... 176
Figure 3.28 Tumor detection *in vivo* with AuNC-functionalized protease nanosensors 177
Figure 3.29 Controls for *in vivo* tumor experiment. 178
Figure 3.30 Molecular dynamics simulation frames of GSH-AuNCs. 181
Figure 3.31 Biological templates for AuNC synthesis 183

List of Tables

Table 2.1 Criteria for ideal point-of-care tests outlined by the World Health Organization ... 43
Table 2.2 Selected noble metals and their physicochemical properties[108] ... 54
Table 2.3 Comparison of kinetic parameters of catalysts ... 78
Table 2.4 Affinity constants for components used in PtNC-labeled LFA ... 94
Table 2.5 Biomarkers requiring sensitive detection in point-of-care settings ... 112

Table 3.1 Proteins and peptides selected as templates for nanocluster synthesis ... 139
Table 3.2 Library of protease-cleavable thiol-terminated peptide sequences ... 148
Table 3.3 Comparison of the kinetic parameters of various catalysts ... 154
Table 3.4 Quantification of cleavage products from *in vitro* protease cleavage assay ... 170

List of Abbreviations

ART	Antiretroviral treatment
AuNC	Gold nanocluster
BSA	Bovine serum albumin
CN/DAB	4-Chloro-1-naphthol/3,3´-Diaminobenzidine, tetrahydrochloride
D_h	Hydrodynamic diameter
DLS	Dynamic light scattering
EDS	Energy-disperse X-ray spectroscopy
ELISA	Enzyme-linked immunosorbent assay
FBS	Fetal bovine serum
FCS	Fluorescence correlation spectroscopy
GFC	Gel filtration chromatography
GFM	Glomerular filtration membrane
GSH	Glutathione (γ-Glu–Cys–Gly)
HIV/ AIDS	Human Immunodeficiency Virus/ Acquired Immunodeficiency Syndrome
HRP	Horseradish peroxidase
ICD	Immune complex disruption
ICP-MS	Inductively coupled plasma-mass spectrometry
ID	Injected dose
LC-MS	Liquid chromatography-mass spectrometry
LFA	Lateral flow assay
LoD	Limit of detection
Lyz	Lysozyme
MMP	Matrix metalloproteinase
NAAT	Nucleic acid amplification test
NAv	Neutravidin
NCD	Noncommunicable disease
NSB	Nonspecific binding
p.i.	Post injection
PD	Pyridazinedione
PoC	Point-of-Care
PtNC	Platinum nanocatalyst
PVP	Polyvinylpyrrolidone
RES	Reticuloendothelial system
SEM	Scanning electron microscopy

STEM	Scanning transmission electron microscopy
TEM	Transmission electron microscopy
THR	Thrombin
TMB	3,3',5,5'-Tetramethylbenzidine
WHO	World Health Organization

Chapter 1

Introduction

1. Introduction

1.1 Disease Diagnosis

A single drop of blood, a urine sample, or a nasal swab holds a wealth of information about the health status of a patient. These biological samples can contain antibodies that have been raised to fight infection, antigens secreted by pathogens, and biomarkers related to disease state. Sensitive and specific detection of relevant biological markers in a complex physiological matrix is key to the development of diagnostic tests. In diagnosis of both infectious and noncommunicable diseases, early detection is critical so that appropriate treatment can be administered when it has the highest rate of effectiveness.

The emergence and re-emergence of infectious diseases, such as Human Immunodeficiency Virus (HIV), malaria, and influenza, is one of the greatest threats to human health. New disease strains are continuously emerging, and resulting outbreaks can spread rapidly, causing enormous losses to health and livelihood. The best strategy to control outbreaks is to identify the source of infection and stop it spreading at an early stage or prevent it altogether. However, due to poor diagnostic tools, many infections remain undiagnosed and untreated, or are diagnosed at a late stage when treatment is less effective. This results in the ongoing transmission of serious infections, such as HIV, and the delay in identifying emerging threats like pandemic influenza, leading to major human and economic consequences for millions of people. Therefore, early diagnosis and vigilant surveillance is critical in the treatment and prevention of infectious diseases. Despite advances in the development of diagnostics, therapeutics and vaccines, it has become increasingly more complex to contain these outbreaks due to the ease of world travel, migration, and global trade.

Since the beginning of the HIV epidemic in the early 1980s, more than 70 million people have been infected and about 35 million people have died of HIV-related illnesses.[1] Highly active antiretroviral treatments (ART) have had a significant impact on reducing HIV-related mortality in recent years. HIV diagnostic testing is a key component of efforts to combat the HIV epidemic as knowledge of HIV status allows individuals to prevent transmission of HIV and to access life-prolonging ART. However, without access to sensitive diagnostic tests this linkage to care is not possible, particularly in resource-limited settings. Sub-Saharan Africa carries a disproportionate burden of HIV, accounting for more than 70 % of the global burden of infection, and within this region young women are particularly vulnerable.[2] A key to reducing this burden in underserved communities is to widen access to sensitive diagnostics and ART. Stigma and discrimination around the virus have prevented many from testing to know if they

are infected. To reduce the HIV burden, comprehensive and innovative HIV testing programs, which include self-testing, would improve knowledge of HIV status and widen access to treatment. Essential to this is the development of diagnostic tests that are globally accessible.

The H1N1 swine flu pandemic in 2009, the Ebola epidemic in West Africa in 2014 – 2016, the outbreak of Middle East Respiratory Syndrome coronavirus in the Republic of Korea in 2015, the 2016 outbreak of Zika virus, and the ongoing 2018 Kivu Democratic Republic of the Congo (DRC) Ebola virus outbreak are only a few of many recent examples of emerging infectious diseases in the modern world, which have each caused enormous global societal and economic impact. The Ebola epidemic in 2014 prompted the World Health Organization (WHO) to launch two urgent initiatives to stimulate the development of rapid, sensitive, safe and simple Ebola diagnostic tests.[3] Without an effective vaccine in 2014, and an experimental vaccine to date, the only Ebola control measure available to stop transmission is the rapid identification of infected patients for isolation and care. The standard diagnostic molecular assays used in laboratories supporting the Ebola response require laborious procedures performed by trained staff which are costly and time intensive. These requirements are difficult to meet in resource-constrained and remote settings, thus severely limiting testing capacity. For example, the containment of the Ebola outbreak in eastern Democratic Republic of the Congo, and distribution of experimental vaccines has been complicated by the instability of the outbreak occurring in an active war zone.[4] In response to the WHO's call for Ebola diagnostics, there have been significant developments in Ebola diagnostics over the last four years. Whereas health workers fighting the Ebola epidemic in West Africa in 2014 had to wait up to a week for results from diagnostic tests, this year a genetic test, GeneXpert, was deployed in DRC, delivering results within several hours. The value of rapid diagnoses in DRC has already been acknowledged, as it has allowed those infected to be isolated promptly.[5] GeneXpert technology is a cartridge-based fully automated nucleic acid amplification test (NAAT) that purifies, concentrates, amplifies and identifies target nucleic acid sequences in under 2 h. While the GeneXpert has made strides toward delivering sensitive nucleic acid testing at the PoC, it still requires instrumentation that is not yet globally accessible as it requires a stable and uninterrupted electrical power supply and linkage to a computer for data analysis.[6] In the current DRC outbreak, other Ebola diagnostics for detection of Ebola proteins using a lateral flow testing platform are being screened as alternatives to GeneXpert.[5]

The guidelines for the WHO's ideal point-of-care (PoC) test include that it should be suited for use in peripheral health clinics with no laboratory infrastructure in place. Testing procedures should involve fewer than three steps, produce results in less than 30 min, and have no biosafety requirements beyond wearing basic personal protective equipment.[3] Paper-based

lateral flow tests meet many of the PoC testing criteria, where colored lines on a test strip indicate the presence or absence of disease markers.

The 2014 Ebola epidemic and re-emergence of the virus this year has exposed the fundamental role of diagnostics in both disease control and case management, which is not only true for Ebola but also for other viral infections. The devastating outbreak has revealed weaknesses in our global capacity to rapidly respond to epidemics with effective diagnostics.[7] In order to prevent and monitor future outbreaks, there is a desperate need for the development of early detection systems for infectious agents that are simple, provide a rapid result and are agile so that they can be readily reimagined for detection of any target.

Effective diagnostics have a fundamental role in disease control and case management for both infectious and noncommunicable diseases (NCDs). While the importance of early detection of infectious diseases was discussed above, detection of noncommunicable diseases is also of great importance. NCDs include cardiovascular disease, cancer, chronic respiratory diseases and diabetes and are the leading cause of death worldwide.[8,9] The Lancet Report on the Global Burden of Diseases highlights the importance of early detection and screening for NCDs, which has been shown to improve the outcomes of treatment interventions when provided early to patients.[9] Since 80 % of all NCD deaths occur in low- and middle-income countries, it is important to develop diagnostics that are globally accessible.

Biosensors are analytical devices incorporating a biological sensing element toward an analyte of interest. The most common format of a biosensor is a biological compound immobilized on the surface of a transducer. The function of the transducer is to translate the interaction of the analyte with the biological element into an electrochemical, magnetic, or optical signal, which can be more easily measured and quantified. For example, optical transducers undergo a change in their optical properties in response to an analyte, such as a change in absorption, reflectance, or emission, which can then be qualitatively or quantitatively measured for the output reading.[10]

The sensitive and specific detection of proteins, nucleic acids, and small molecules is of great importance in both the study of their fundamental functions and the development of biosensor technologies and molecular diagnostics. Nanomaterials are ideally suited for use in biosensing applications due to their unique properties and useful behaviors not present in their bulk form: for example, T2 magnetic resonance and superparamagnetic properties of ferrite nanoparticles,[11] intense color and localized surface plasmon resonance of metallic

nanoparticles,[12] and bright, tunable fluorescence of semiconductor nanoparticles.[13] These properties, along with their large surface area to volume ratio for optimal functionalization with biomolecules, make nanomaterials excellent biosensor signal transducers. Although there has been tremendous progress in the field of nanoparticle biosensor development, there are still many hurdles to overcome. The main challenges include reproducible synthesis of nanoparticles that are stable in physiological environments and improving the sensitivity and specificity of biosensors. Overcoming these challenges requires robust surface functionalization techniques for detection of analytes in complex biological fluids and optimization of the transduction event for enhanced sensitivity. These challenges must be addressed for commercialization and the widespread use of advanced nanoparticle biosensors in healthcare, environmental evaluation, food analysis, and other diagnostic applications.

This thesis explores the development of nanoparticle-enabled diagnostic tests for both infectious and noncommunicable diseases.

1.1.1 Diagnosis at the point-of-care

Diagnostic platforms can be separated broadly into two categories: laboratory-based or point-of-care (PoC). Detection of disease outside of hospital settings at the PoC presents many challenges, as resources and access to temperature-controlled environments are greatly limited and instrumentation requiring trained personnel is generally unavailable. PoC devices are required to be inexpensive, easy-to-use by non-specialists, and portable devices that provide a rapid result. The development of PoC devices for both infectious and noncommunicable diseases is critical for democratizing access to sensitive diagnostic tests. In the context of this thesis, the terms “sensitivity” and “specificity” are used to describe the performance of an assay or diagnostic test. Here sensitivity is defined as the limit of detection (LoD) of the assay, which is the lowest quantity of a substance that can be distinguished from the absence of that substance (blank value) and is calculated to be three standard deviations above the mean of the blanks. A reduction in the limit of detection of an assay results in an improvement in the sensitivity of the test. The LoD can be determined by running a calibration experiment of known standards and measuring the background signal (blanks).[14] Here the term specificity is used to describe the ability of a method to detect one element in the presence of other elements.

1.2 Biomarkers

Biomarkers are measurable indicators of the presence of a disease state or the overall health status of a patient. Biomarkers may include, but are not limited to, proteins and nucleic acids and may be measured in any biological fluid or tissue sample. The ability to detect certain biomarkers in biological fluids is challenging because biomarkers are frequently found in low concentrations in the circulation, are difficult to resolve in complex matrices, and can be degraded rapidly *in vivo* and *ex vivo*.

Antibodies are proteins produced by the immune system to neutralize infections and can be used as biomarkers to monitor disease after seroconversion, which is the time period over which antibodies toward an infection develop and become detectable. Antigens are molecules that can stimulate an immune response (*e.g.* antibody production) in a host organism and can include peptides and proteins and parts of or substances produced by viruses or bacteria. Since antigens can elicit production of antibodies in a host, their detection in biosensing platforms is typically through capture by antibodies that have been produced specifically toward the antigen of interest. Immunoassays are tests that measure the presence of an analyte, including antibodies and antigens, in biological samples. In an immunoassay, one of the binding partners of the antibody-antigen pair, or a secondary antibody, is labeled with a detection moiety. The detection moiety is typically an enzyme, which can produce a colorimetric, fluorogenic or chemiluminescent product, that can be used to indicate the presence of the analyte in the biological sample. One advantage of an antigen test over an antibody test is that antigens are present in the sample right away, whereas it can take time for the immune system to develop antibodies after infection or exposure to the antigen.[15]

Detection of enzymes or enzyme activity can also be an indicator of disease. Proteases, or proteolytic enzymes are enzymes that catalyze the breakdown of proteins by hydrolysis of peptide bonds. Proteases play fundamental roles in both normal physiological and disease processes. Dysregulated protease activity is implicated in pathological processes, including cancer, cardiovascular diseases, inflammation, and neurodegenerative diseases.[16] Proteases act on specific peptide substrates, hydrolyzing peptide bonds to generate two or more distinct protein or peptide fragments. Protease activity can be monitored by analyzing the formation of fragments from the enzyme substrate using mass spectrometry. For real-time monitoring of protease activity in cells and *in vivo*, peptide substrates can be designed to include fluorescent or near-infrared tags, including fluorophores or quantum dots,[17] that alter fluorescence properties upon cleavage events (through quenching or fluorescence resonance energy transfer mechanisms). These enzyme-activity sensing probes have been deployed for imaging

of protease activity in live cells,[18] for *in vivo* tumor detection and blood clots (thrombin activation),[19] and fluorescence-guided tumor resection.[20]

While not explored in this thesis, detection of genetic materials can allow for early and sensitive diagnosis of disease. Watson-Crick base pairing between single strands of complementary DNA is one of the strongest and most specific forms of molecular recognition and can be exploited in biosensing applications for detection of genetic material. Since the amount of genetic material (*e.g.* viral RNA) in physiological fluids is typically very small, nucleic acid testing includes an amplification step, called nucleic acid amplification testing (NAAT). In the case of HIV, viral RNA is the earliest detectable biomarker in the blood after infection. Monitoring viral load can be useful for staging disease progression, obtaining drug resistance profiles, and is also needed to determine the effectiveness of subsequent treatment.[15] Viral load is determined using quantitative HIV-1 RNA nucleic acid testing. The most commonly used viral load assays are based on quantitative reverse transcription polymerase chain reaction (RT-qPCR) amplification. RT-qPCR detects amplified target at each amplification cycle using a fluorescently-labeled probe specific for the virus. However, PCR requires thermocycling to mediate DNA melting, followed by primer annealing and extension, making it challenging to adapt to PoC use. The development of isothermal DNA amplification techniques have enabled translation of some of these nucleic acid testing technologies to the clinic.[21]

1.3 Biomarker detection

1.3.1 Antibodies and antibody fragments

Antibodies are deployed by the immune system to detect and capture foreign molecules (antigens) in the body, and upon antibody-antigen recognition, a signaling cascade is triggered that leads to the destruction of the antigen. The specificity and high affinity of antibodies toward their target *in vivo* can be exploited in *in vitro* biosensing systems. It is important to understand the structure and binding ability of antibodies and antibody fragments to optimize their use in biosensing applications. An antibody, also called immunoglobulin (Ig), can be divided into two regions: the antigen-binding fragment (Fab) and the constant fragment (Fc). Antibodies (*ca*. 160 kDa) consist of four polypeptide chains, two identical heavy (H) chain and two light (L) chains, which are joined together by covalent disulfide bridges (Figure 1.1). Each chain consists of a variable (V) and a constant (C) region. The antibody non-covalently binds to a specific region on the antigen called an epitope through hydrogen bonding, hydrophobic, and electrostatic interactions. Conventional antibodies can be monoclonal or polyclonal, where

monoclonal antibodies bind one epitope per antigen and polyclonal antibodies can recognize multiple epitopes on one antigen and are inhomogeneous in terms of specificity and affinity toward their target antigen.[22,23] The variable regions of heavy and light chains localize to the Fab domains and provide the structural basis for antigen and epitope-selectivity.

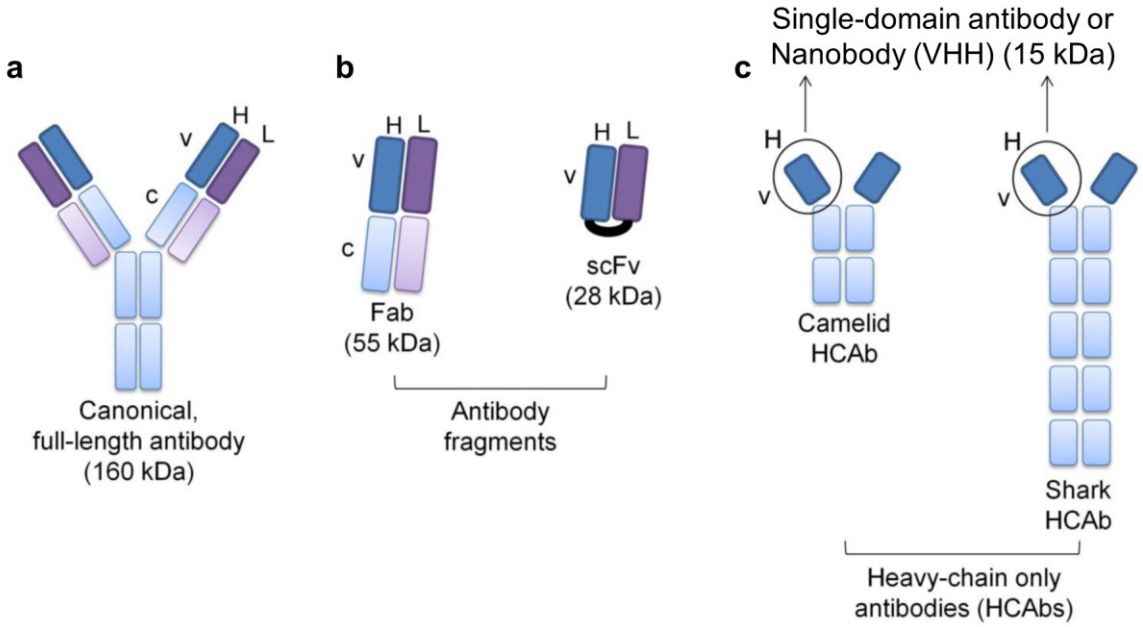


Figure 1.1 (a) Structure of conventional immunoglobulin G (IgG) antibody (v – variable, c – constant, H – heavy chain, L – light chain), which is the most abundant antibody in serum. (b) Fragments of conventional antibodies: fragment antigen-binding (Fab) and single-chain variable fragment (scFv). (c) Single-domain antibodies derived from the heavy-chain only antibodies that occur naturally in camelids (left) and sharks (right). Figure adapted from Doshi *et al*.[24] with permission.

Advances in recombinant antibody technology have led to the production of fully functional antibody fragments at scale using vectors in bacterial systems.[25] Antibody fragments have desirable characteristics for use in sensing systems including low molecular weight, increased flexibility, and high physiochemical stability, resulting in small and agile diagnostic probes.

Single-domain antibodies, also called nanobodies, are the smallest available intact antigen binding fragments (*ca*. 15 kDa). Nanobodies can be derived from the heavy-chain only antibodies that occur naturally in camelids and sharks. These small binding fragments have found use in a variety of diagnostic and therapeutic applications due to their scalable production using standard microbial expression systems, which also allows for the addition of functional modifications. Nanobodies are extremely robust and have demonstrated high resistance to chemical denaturation and thermal degradation, including reversible refolding after thermal cycling.[26–28] Additionally, nanobodies can be produced with functional handles

that allow for site-selective modifications with precise control over the position of the modifications, to ensure accessibility of the paratope (antigen-binding region) for maximum capturing capacity of the antigen.[29,30] Their small size allows them to recognize epitopes that are inaccessible to conventional antibodies, which contributes to their high affinity toward their target (K_D in low nanomolar and picomolar range) making them ideally suited for ultrasensitive assays.[23,29]

1.3.2 Antibody-antigen interactions

Immunoassays involve a binding reaction between an analyte and antibody, or any molecule and its cognate ligand. The strength of the binding interaction between an antibody and its target antigen is a key parameter in immunoassay design. The noncovalent and reversible reactions between antibodies and antigens can be described as chemical equilibria, where kinetics (association and dissociation rate constants) determine how the rate of the antibody-antigen interaction relates to the local concentration. For a biomolecular reaction between an antigen and antibody, the reversible reaction can be described by **Equation 1.1**:

$$[Ag] + [Ab] \underset{k_d}{\overset{k_a}{\rightleftharpoons}} [Ag - Ab] \qquad (\mathbf{1.1})$$

Here, [Ag] is the concentration of antigen, [Ab] is the concentration of antibody, [Ag – Ab] is the concentration of the antigen-antibody immunocomplex, k_a is the association rate constant for complex formation (also known as k_{on}), and k_d is the dissociation rate constant (also known as k_{off}). The ideal antibody for an immunoassay would have a high rate of association (k_{on}) and low rate of dissociation (k_{off}), so that it binds with high affinity to its antigen and does not dissociate during wash steps. It is important to note that this model is an over-simplification of the chemical interactions occurring within the assay, which include hydrogen bonding, electrostatic interactions, hydrophobic, van der Waals forces, conformational changes, and nonspecific binding between reactants.

The ratio of the two rate constants gives the equilibrium constant between the antibody and its antigen: K_{eq} (where the equilibrium dissociation constant $K_D = 1/ K_{eq}$) (**Equation 1.2**):

$$K_{eq} = \frac{k_a}{k_d} = \frac{[Ag-Ab]}{[Ag][Ab]}; K_D = \frac{k_d}{k_a} = \frac{[Ag][Ab]}{[Ag-Ab]} \qquad (\mathbf{1.2})$$

K_{eq} represents the ratio of bound to unbound analyte and antibody and is also known as the affinity constant. K_D is the key measure of an antibody's ability to function well in an immunoassay and is used to evaluate the strengths of biomolecular interactions, where lower K_D values represent higher affinity and better performance in the immunoassay. Most conventional antibodies have K_D values in the low micromolar to nanomolar range, with exceptional antibodies displaying low nanomolar to picomolar range affinities.[15] The affinity constants of antibodies can be measured using techniques such as isothermal titration calorimetry or surface plasmon resonance.

The above equations provide a useful framework for understanding the reactions between an antibody and antigen in equilibrium, which is the case for most immunoassays (*e.g.* ELISA, outlined below). For the case of lateral flow assays (LFA), where the test never reaches chemical equilibrium, antibodies with high affinity are required. In LFA, the affinity needs to be driven primarily by a fast on-rate (k_{on}), since the potential time for binding at the test line is on the order of several seconds. The use of biotin-streptavidin ($K_D \approx 10^{-15}$ M) interactions at the test line has been shown to drive sensitivity and facilitate efficient nanoparticle capture at the test line (§2.1.2.2.2).[31–33]

1.3.3 Principles of immunoassays

An immunoassay is a biochemical test used to detect the presence of a target analyte. The affinity reagents used to detect the analyte, typically antibodies, determine the sensitivity and specificity of the assay. The sandwich immunoassay is a standard assay format, in which the analyte is captured between two antibodies (Figure 1.2). An important and challenging aspect of immunoassay design is screening and selecting an antibody pair that recognizes two non-overlapping epitopes on an antigen and exhibit high affinity binding toward the target. In the sandwich configuration, a capture antibody immobilized on a solid phase captures the analyte from the sample. A detection antibody, which binds a different epitope to the capture antibody, is used as the basis for the signal generation system. Enzymes or other tags (*e.g.* radioisotope or fluorophore) can be linked directly to the detection antibody or introduced through a secondary antibody that recognizes the primary antibody. When enzymes are used for detection, the assay is called an enzyme-linked immunosorbent assay (ELISA). The enzyme can also be linked to a protein such as streptavidin if the detection antibody is labeled with biotin. The most commonly used enzyme in immunoassays is horseradish peroxidase (HRP) or streptavidin linked HRP (for biotinylated detection antibodies). After an incubation period to allow the antibodies to bind with the analyte, unbound labeled antibody is washed away and the concentration of analyte in a sample can be determined by measuring the signal generated

from the detection label against a calibration curve. For HRP-labeled detection systems, the sample is mixed with H_2O_2 and a peroxidase substrate to generate a measurable product.

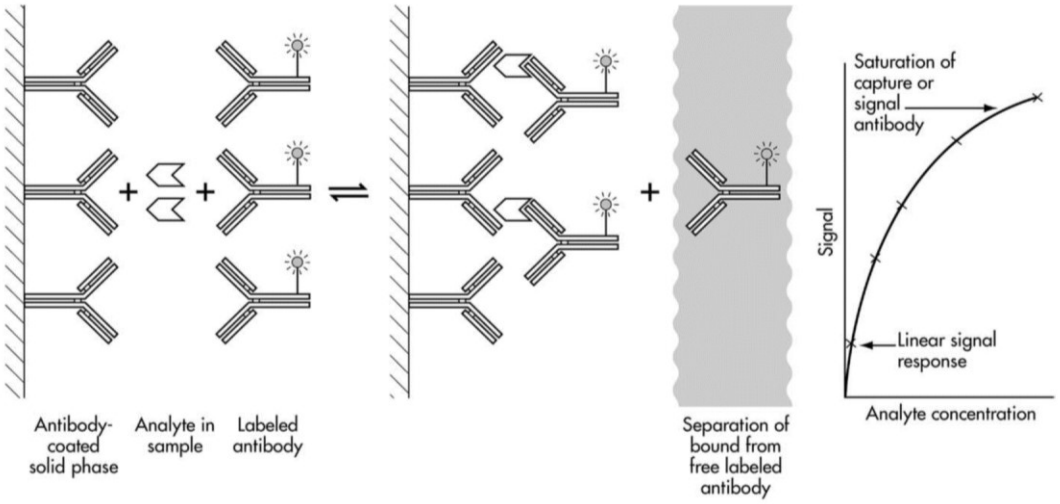


Figure 1.2 Schematic of sandwich immunoassay. An antibody immobilized onto the solid phase (*e.g.* 96-well plate or nitrocellulose membrane) captures the test analyte from the sample, and a different antibody that is specific for a different epitope of the analyte is used for detection. The detection antibody is labeled with a radioisotope, enzyme, fluorophore or other detection element. After incubation to allow the antibodies to bind with the analyte, the unbound labeled antibody is washed away. The signal generated from the detection antibody is measured against a calibration curve to determine the concentration of analyte present in the sample. Figure adapted from Wild *et al.*[15]

Tetramethylbenzidine (TMB) is the most popular chromogenic substrate for HRP detection in ELISA and yields a blue color when oxidized, typically because of oxygen radicals produced by the hydrolysis of hydrogen peroxide by HRP. Fluorescent or chemiluminescent peroxidase substrates can also be used to increase sensitivity but require more complex instrumentation for the readout. In ELISA, sensitivity is largely determined by the affinity of the antibody-antigen interaction and the sensitivity of the detection label and substrate system used. The advantage of enzyme labeled assays is the amplification from enzyme activity. For example, a single molecule of HRP can convert *ca*. 1000 molecules of substrate per second, increasing sensitivity of the assay.[34] ELISA has limitations due to instability of the enzyme and antibody components and variability in enzyme activity with temperature and pH. Inorganic “enzyme-mimetic” nanomaterials are emerging as sensitive labels for immunoassays in place of biological enzymes to improve stability and limit of detection of the assay (§1.5).[35]

It is important to note that in the sandwich immunoassay configuration, false negative results are possible in situations where there are very high concentrations of the analyte in the sample, called the Hook effect. In this scenario, excessively high concentrations of analyte simultaneously saturate both the capture and detection antibodies thus preventing the

formation of detectable complexes and decreasing observed signal. The limit of detection or analytical sensitivity of immunoassays is typically defined as the concentration corresponding to 3 standard deviations above the mean of the measured zero concentration calibration blanks.[15]

Lateral flow assays (LFA) are simple paper-based devices for detection of a target analyte in a liquid sample, typically through an immunoassay configuration (discussed in depth in Chapter 2). LFA test strips have a test line for capture of the target analyte. Like ELISA, LFA can adopt a sandwich configuration at the test line, where the capture antibody is immobilized on a nitrocellulose membrane rather than a 96-well plate. Instead of an enzyme-labeled detection antibody, LFA employs a colored nanoparticle, typically a 40 nm gold nanoparticle that is functionalized with the detection antibody. When the sample is added to the test strip, the analyte gets captured by an antibody at the test line and labeled with the nanoparticle-antibody conjugate, producing a colored signal at the test line.

The dynamic processes that make LFA fast and sensitive occur over a large range of time and length scales. Figure 1.3 illustrates the disparate length and timescales present within an LFA and the various components that contribute to test sensitivity, some of which are optimized in Chapter 2. Weigl and coworkers[32] have developed a mechanistic model to simulate phenomena across these length and time scales, with the aim of identifying critical parameters to improve LFA performance. Modelling LFA parameters is complex and included: mass transport of reactants through the porous nitrocellulose membrane, diffusivity of nanoparticle-antibody conjugates, density of ligands on nanoparticles, concentration of nanoparticle-antibody conjugates, effective k_{on} and k_{off} rates for the liquid-phase reaction of antigen with nanoparticle-antibody conjugates, and the capture of antigen-nanoparticle conjugates at the test line. In the model, affinity constants, sample volume, flow rate, and nanoparticle concentration were all found to impact test sensitivity and are further discussed in Chapter 2 in terms of optimizing LFA test development.

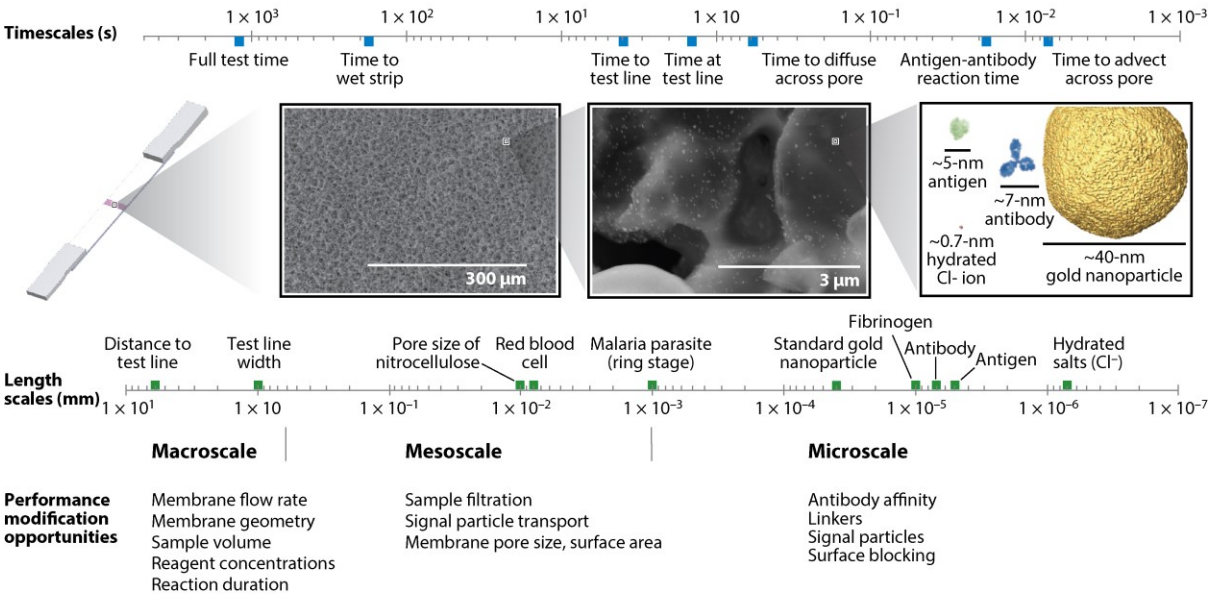


Figure 1.3 Schematic illustrating the disparate time scales (top) and length scales (bottom) involved in a lateral flow assay. Scanning electron microscope (SEM) images (center) highlight the difference in length scale between nanoparticle labels (bright spots, *ca*. 40 nm) in LFA and nitrocellulose pore sizes (*ca*. 10 µm). Figure adapted from Gasperino *et al*.[32] with permission.

1.3.4 Activity-based probes

While the gold standard for cancer diagnosis is a biopsy, cancer-specific circulating biomarkers released from tumor cells have emerged as an alternative way to screen for cancer in people without symptoms. Blood biomarkers have limitations, particularly in early cancer detection where circulating biomarkers such as prostate specific antigen (PSA) and ovarian cancer growth-related cancer antigen 125 (CA-125) lack both sensitivity and specificity.[36] These biomarkers are frequently shed by healthy cells in physiological conditions, shed from tumors at low rates, significantly diluted in blood, and circulate only for short periods. If tumor-specific biomarkers could be improved to enhance sensitivity and specificity, they could act as markers for early cancer detection, which often improves patient outcomes. For example, diagnosis when cancer is localized to the organ of origin correlates with significantly greater long-term survival as compared with when the cancer has metastasized.

Gambhir and coworkers[37] demonstrated in a mathematical model that shedding rates of current clinical blood biomarkers from tumors, like CA-125, are likely 4 orders of magnitude too low to enable detection of a developing tumor within the first decade of tumor growth. By the time a patient becomes symptomatic and presents at the clinic, their cancer has likely advanced beyond curability. There is a need for tumor-specific circulating biomarkers to enable screening and early detection of cancer when it is most treatable.

Activity-based probes are a class of diagnostic agents that are administered in a pro-diagnostic form and produce a strong diagnostic signal after enzymatic activation.[38] The activity-based probes rely on disease-associated enzymes, typically proteases, to cleave substrates and generate a detectable signal. Since each enzyme can cleave many substrates in a time, protease detection is inherently amplified.

Bhatia and coworkers[39–43] pioneered the development of a class of activity-based probes called synthetic biomarkers. Discussed in depth in Chapter 3, these synthetic biomarkers are activity-based probes designed to sense disease-associated protease activity *in vivo*. In brief, synthetic biomarkers are made of nanoparticles conjugated with tumor-targeting peptide ligands and peptides cleavable by specific proteases overexpressed in the tumor microenvironment (*e.g.* matrix metalloproteinase 9, MMP9). Following administration *in vivo*, the synthetic biomarkers accumulate at the disease site, peptides are cleaved by local proteases, the cleavage fragments are cleared into urine (through size-dependent filtration), and the urine is analyzed by multiple analytical platforms to detect the signal from cleaved probes (Figure 1.4). The signal in urine can be correlated to the catalytic activity of disease-associated proteases, and in some cases can be used as an alternative to innate blood biomarkers.[43] Using the nanosensor platform, the synthetic biomarkers outperformed the ovarian cancer blood biomarker, by detecting tumor volumes that were 2.4-fold lower.[43] The sensitivity of the synthetic biomarker system benefits from amplification in signal due to both enzyme activity *in vivo* and renal concentration of detection probes. The synthetic biomarker system is promising for enabling earlier cancer detection and is being further developed for clinical testing by the company Glympse Bio. To translate the synthetic biomarker sensing system to a clinical or PoC compatible setting, further optimization of the nanomaterials and readout platforms is required, which serves as the motivation for Chapter 3.

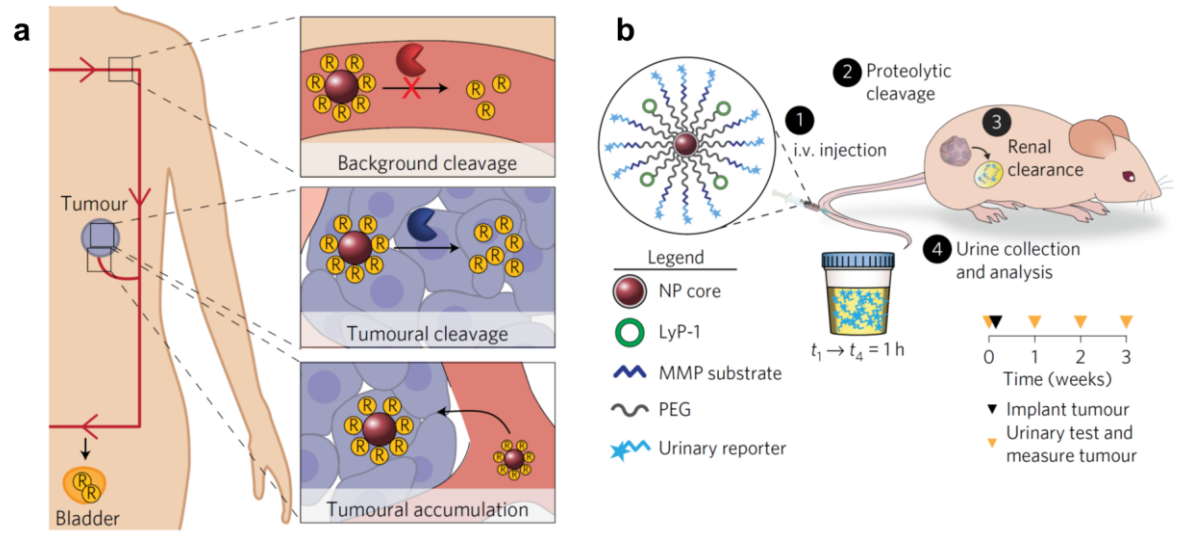


Figure 1.4 (a) Schematic of *in vivo* protease nanosensor platform. Encircled 'R's represent urine reporters, which are tethered to a nanoparticle core, and accumulate in the bladder after release by disease-associated proteases (*e.g.* MMP9 in tumor environment). (b) Schematic showing urine testing in a mouse flank tumor model. i.v., intravenous, t, time at given testing step (1 – 4). Protease nanosensors are labeled with protease-cleavable peptide substrates linking the renal-clearable urinary reporters to the core nanoparticle, and tumor targeting ligands (*e.g.* Lyp-1 tumor-penetrating peptide to direct nanosensor to site of disease). Figures adapted from Kwon *et al*.[43] with permission.

1.4 Nanoparticles in biosensing

Biology and nanotechnology both inhabit the same length scale, with some biomolecules being on the order of 1 – 200 nm, which makes nanomaterials in this range ideally suited for use in biosensing applications. Nanoparticles have unique physiochemical properties and can be produced in a diverse range of well-controlled sizes, shapes, and can be capped with a variety of different ligands that enable stability in physiological environments. Based on the composition of the nanomaterial, a variety of functionalization chemistries (*e.g.* electrostatic, covalent, and physical adsorption) are available for modifying the surface with biomolecules, such as proteins, peptides, and nucleic acids that can be used for sensing.

1.4.1 Noble metal nanoparticles

Plasmonic nanoparticles exhibit unique optical properties due to localized surface plasmon resonance (LSPR). Gold nanoparticles (AuNPs) have received particular interest in the biosensing field because of their stability, and ease of synthesis and modification.[44] LSPR is the collective oscillation of electrons in the conduction band of AuNPs in resonance with a specific wavelength of incident light. This results in a strong absorbance band in the visible region that is highly sensitive to interactions with external agents (*e.g.* biomolecules). For

example, an analyte binding to the surface of an AuNP will lead to a LSPR peak shift, producing an optical signal that can be used for sensing.[45,46] The LSPR of monodisperse AuNPs (*ca*. 15 nm) typically gives rise to a solution with a strong red color. This optical response is highly dependent on AuNP size, shape, aggregation state, and dielectric constant of the medium. When AuNPs are aggregated, interparticle plasmon coupling leads to a red-shift in the absorbance peak, producing a pronounced perceived color shift from red (sharp peak around 520 nm) to blue (broad peak in 600 – 750 nm regime). The ability to link the aggregation state of the plasmonic particles to the presence or absence of a target molecule has led to the creation of a variety of assays based on colorimetric shifts. Notably, Mirkin *et al*.[47] developed oligonucleotide-functionalized gold nanoparticles, where particle aggregation was initiated when the AuNPs interacted with a complementary strand of DNA, which generated a shift in LSPR resulting in a color change.

1.5 Nanomaterials with enzyme-like activities

Both inorganic catalysts and biological enzymes facilitate chemical reactions by lowering the activation energy, thus increasing the rate of reaction, allowing it to proceed at reduced temperatures and pressures. Biological enzymes are used in a variety of immunoassay configurations for amplification to enable sensitive analyte detection. However, enzymes suffer from instability in harsh environments such as varying pH and increasing temperature, and are susceptible to denaturation by proteases, hindering their application at the PoC. This has motivated the development of artificial enzymes and nanomaterials with enzyme-like characteristics to replace their biological counterparts as labels in immunoassays. Over the last decade, a variety of nanomaterials have been explored to mimic the function and sometimes structure of biological enzymes. This class of materials is sometimes referred to as “nanozymes” or nanoparticles possessing enzyme-like characteristics, including peroxidase, oxidase, glucose oxidase, and catalase-like activities.[35]

Of interest for immunoassay development is a class of nanomaterials with intrinsic peroxidase-like activity. Peroxidases are a class of metalloenzymes, containing an iron heme group, used to reduce hydrogen peroxide to water through a redox cycle. Peroxidases use hydrogen peroxide to oxidize both inorganic and organic compounds, such as TMB.[48,49] Under specific reaction conditions, iron oxide,[34] carbon,[50] gold,[51] platinum,[52] palladium,[53] and iridium[54] nanoparticles have all demonstrated peroxidase-like activity through the oxidation of substrates in the presence of hydrogen peroxide.

Yan and coworkers[34] first reported the intrinsic peroxidase-like activity of ferromagnetic iron oxide nanoparticles, where Fe_3O_4 magnetic nanoparticles were used as labels to replace HRP in a simple solution-phase immunoassay. The ferromagnetic nanozymes showed high stability across a broad range of pH and temperature conditions and recyclability of the nanozyme label. Since this first "nanozyme" report over a decade ago, many new enzyme-mimetic nanoparticle formulations have been developed, spanning a broad range of morphologies, sizes, compositions and surface chemistries (Figure 1.5).

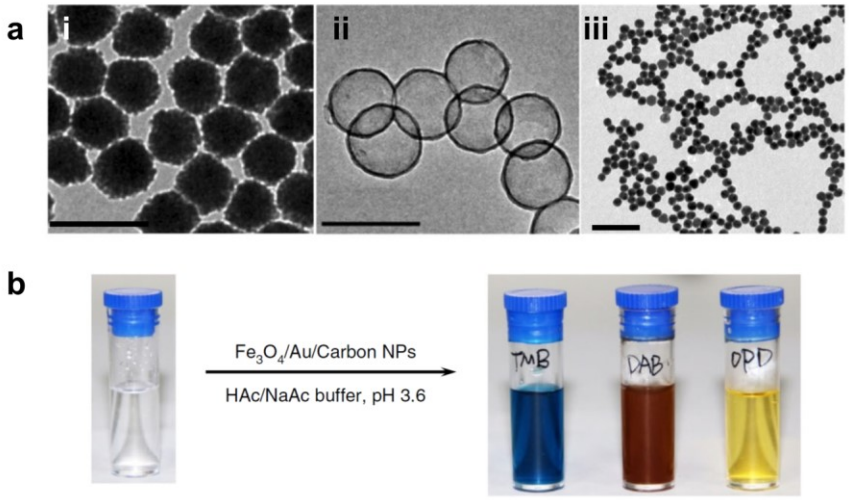


Figure 1.5 (a) Transmission electron microscope (TEM) images of three typical peroxidase nanozymes: (i) Fe_3O_4, (ii) carbon, and (iii) AuNPs. Scale bars represent 200 nm, 200 nm and 100 nm, respectively. (b) Fe_3O_4, carbon and AuNPs show peroxidase-like activity and catalyze the oxidation of peroxidase substrates (TMB, diaminobenzidine (DAB) and o-phenylenediamine (OPD)) in the presence of H_2O_2 to produce colorimetric reactions. Figure adapted from Jiang *et al*.[50] with permission.

Since the catalytic activity of the nanomaterials is highly dependent on these physiochemical properties, Yan and coworkers[50] recently reported a standardized protocol to define nanozyme catalytic activity that will allow for comparison between different nanozyme formulations. The protocol involves calculating the catalytic efficiency of nanozymes by evaluating the Michaelis-Menten kinetics of peroxidase-mimicking nanomaterial catalyzed oxidation of chromogenic substrates to determine their catalytic constants (§2.2.5 and §3.2.6). This thesis investigates the design of peroxidase-mimicking nanoparticles to catalyze the disproportionation of hydrogen peroxide, particularly platinum and gold nanomaterials.

1.5.1 Mechanism of hydrogen peroxide disproportionation on metal nanoparticles

Hydrogen peroxide is unstable on platinum and gold surfaces, typically decomposing into either hydroxyl radicals or a water molecule and an atomic oxygen.[55,56] The disproportionation

of H_2O_2 on both platinum[57] and gold[58] nanoparticles has been shown to be strongly dependent on pH. Liu *et al*.[57] and He *et al*.[58] used electron spin resonance (ESR) spectroscopy to characterize the formation of free radicals on platinum and gold nanoparticles, respectively. ESR results suggest that platinum and gold nanoparticles possess peroxidase-like activity of decomposing hydrogen peroxide into hydroxyl radicals under acidic conditions, and catalase-like activity of producing H_2O and O_2 under neutral and alkaline conditions (Figure 1.6). Xia *et al.*[53] also showed that hydrogen peroxide was decomposed to hydroxyl radicals on palladium and iridium surfaces in acidic conditions using a terephthalic acid (TA) probe which could easily react with hydroxyl radicals to form a highly fluorescent 2-hydroxyterephthalic acid.

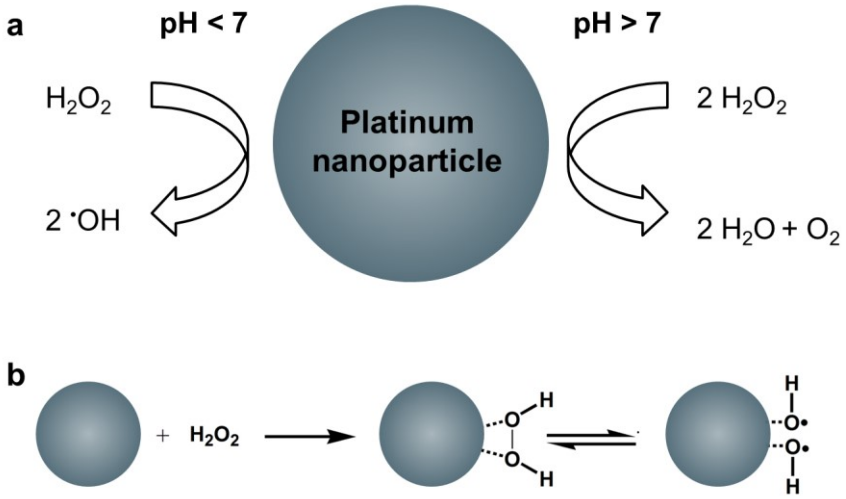


Figure 1.6 (a) Schematic showing the interaction of hydrogen peroxide with a platinum (or gold) nanoparticle surface in acidic (left) or alkaline (right) conditions. (b) Proposed mechanism of decomposition of hydrogen peroxide on noble metal nanoparticle surface in low pH condition.

In the proposed mechanism of H_2O_2 decomposition at low pH (pH < 7), first H_2O_2 is adsorbed on the platinum or gold surface, and the O–O bond is weakened and subsequently broken into two hydroxyl radicals through homolytic cleavage. The hydroxyl radicals may be stabilized on the surface of the particles to facilitate oxidation of the substrate, such as TMB. Catalytic activity, or propensity of the metal nanoparticles to catalyze the decomposition of hydrogen peroxide, is also expected to be dependent on the atomic arrangement of the particle surface, which will influence the adsorption energies of the reactants.

Enzyme-mimetic nanoparticles with high catalytic activity (> k_{cat} for HRP: 10^4 s^{-1}) represent a highly stable alternative to their biological counterparts and are ideally suited for use as labels to amplify signal in point-of-care immunoassays. The following chapters explore the synthesis of platinum and gold nanomaterials and their use in two different sensing platforms: a paper-

based lateral flow assay and an activity-based probe for *in vivo* sensing. In both cases, the peroxidase-like activity of the nanomaterials is exploited for colorimetric detection of disease state.

Chapter 2

Development of Nanocatalyst Amplified Lateral Flow Assay

2. Development of nanocatalyst amplified lateral flow assay

This chapter includes work published in Loynachan *et al.*[59]

2.1 Introduction

2.1.1 Aims

This chapter examines the use of catalytic nanoparticles as labels in paper-based lateral flow assays (LFAs), with the aim of bridging the sensitivity regimes of state-of-the-art biosensing techniques and point-of-care (PoC) compatible diagnostic tests. The goal here is to develop a paper-based test for use in global health applications that is as sensitive as the best conventional diagnostics, while retaining all the cost, simplicity and usability advantages of LFA. First the synthesis and characterization of catalytic nanoparticles is discussed, followed by their application in a paper-based diagnostic platform for early detection of HIV.

Lateral flow tests are one of the most widely used PoC diagnostics, however, their application in early disease diagnostics is often limited due to insufficient sensitivity for the requisite sample sizes and the short timeframes of PoC testing. To address this, a serum-stable, nanoparticle catalyst-labeled LFA was developed. The nanocatalyst amplified LFA had a sensitivity surpassing that of both current commercial and published sensitivities for paper-based detection of p24, one of the earliest and most conserved biomarkers of HIV. This chapter outlines the synthesis and characterization of porous platinum core-shell nanocatalysts (PtNCs), which show high catalytic activity when exposed to complex human blood serum samples. The application of antibody functionalized PtNCs with strategically and orthogonally modified nanobodies with high affinity and specificity toward p24 was explored, and the key larger nanoparticle size regimes needed for efficient amplification and performance in LFA was established. Harnessing the catalytic amplification of PtNCs enabled naked-eye detection of p24 spiked into sera in the low femtomolar range (*ca.* 0.8 $pg \cdot mL^{-1}$), and the detection of acute phase HIV in clinical human plasma samples in under 20 minutes. The LFA developed in this chapter is simple, rapid, and capable of significantly reducing the HIV acute phase detection window. This diagnostic may be readily adapted for detection of other biomolecules; as an ultrasensitive screening tool for infectious and noncommunicable diseases and can be capitalized upon in PoC settings for early disease detection.

2.1.2 Background

The emergence of infectious diseases is one of the greatest threats to human health. The recent outbreaks of Zika and Ebola viruses, and the ongoing HIV pandemic continue to highlight the need for diagnostic tools that are affordable, sensitive, simple, and able to rapidly detect pathogens under challenging circumstances. These demands have led to the uptake of paper-based LFAs as the most prominent rapid PoC diagnostic tests. Although meeting many of these criteria, their sensitivity generally falls short of other bench-top protein and nucleic acid detection methods.[60] The continuing hurdle of developing PoC diagnostics is that compromises must be made between sensitivity, simplicity, speed, and cost. A great challenge is the development of diagnostics for use in resource-limited settings that require exceptional performance in all these categories but also resilience towards a lack of cold-chain support.

Sensitive diagnostic platforms often include signal or target amplification mechanisms, such as polymerase-chain reaction (PCR) and isothermal nucleic acid amplification for detection of nucleic acids or enzyme-catalyzed signal amplification and immuno-PCR for detection of protein targets.[61,62] However, these techniques are relatively resource demanding, requiring technical expertise to run and interpret (*e.g*. purification steps), and utilize equipment that is often incompatible with use in resource-limited settings where unreliable power supplies and maintenance challenges restrict their use.[63,64] Due to their high catalytic efficiency and extraordinary stability in harsh environments, such as high temperature and extreme pH, mixed noble-metal catalytic nanoparticles have emerged as promising materials for signal amplification in colorimetric immunoassays.[34,52,53,65–67] This chapter shows that incorporating inorganic nanoparticle catalysts in lateral-flow testing formats, through an investigation of their size and porosity, provides a pathway to significantly improve the sensitivity of simple to read, absorbance-based LFAs. This has resulted in a simple and cost-effective paper based diagnostic test with a level of performance far in advance of current standards for LFA. Here, peroxidase-mimicking porous platinum core-shell nanocatalysts (PtNCs) are integrated into a lateral flow assay for sensitive detection of p24, the viral capsid protein of HIV.

2.1.2.1 HIV Diagnostic Landscape & Early detection

Human immunodeficiency virus (HIV) is a lentivirus spread through certain body fluids that attacks the body's immune system, specifically CD4 T cells. When the CD4 cells become depleted, the body can no longer effectively fight infection or disease, which leads to the development of acquired immunodeficiency syndrome (AIDS) when the immune system is severely damaged by HIV. The virus itself is semi-spherical with a diameter of *ca*. 120 nm and

is composed of two copies of viral RNA that are enclosed by a conical capsid composed of 2000 copies of the viral protein p24 (Figure 2.1). While no effective cure for HIV currently exists, early detection of the virus is important, as effective antiretroviral treatments (ART) can reduce viral load. According to the World Health Organization (WHO) there were 36.9 million people living with HIV in 2017, and 25 % of the people living with HIV were unaware of their infection.[68] Two to four weeks after infection is the acute stage, where there is a large amount of virus in an infected individual's blood (viremia) making it the most contagious period.[69] In this acute stage, viremia increases exponentially and then declines to a steady-state level as immune response controls HIV replication. However, people with acute infection are often unaware of their infection because they might not present any symptoms during this period. A sensitive diagnostic test is required to properly identify and treat HIV.

There are several biomarkers that can be used to diagnose HIV that are present at different concentrations across varying time periods post infection (Figure 2.1). The markers of HIV in blood evolve with the stage of infection. The sequence of biomarkers to identify infection in order of appearance in blood are; viral RNA, viral capsid protein p24 antigen, and anti-HIV antibodies.[70] The presence of p24 in the blood encompasses a window period during high viremia before antibodies to HIV can be detected. When antibodies become detectable in a process called seroconversion, p24 is often no longer detectable in blood samples most likely due to antigen-antibody complexing in the blood. HIV RNA is detectable in blood 7 – 10 days after infection and can be detected using polymerase chain reaction (PCR) or other nucleic acid amplification technologies (NAAT). However, NAAT is generally limited to high resource settings as it requires sophisticated and expensive equipment, rigorous laboratory conditions, and highly trained staff.

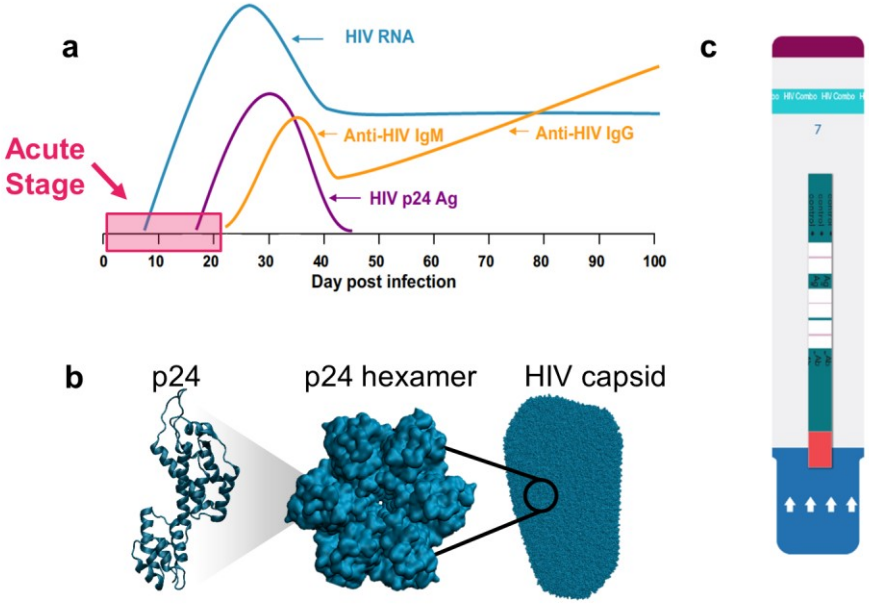


Figure 2.1 (a) Biomarkers present in blood days post HIV infection, with acute stage HIV infection highlighted in red. Figure adapted from Fiebeg *et al.* with permission.[70] (b) Structure of p24 protein, hexamer of native full-length HIV-1 capsid protein (PDB: 4XFX), and structure of the entire HIV-1 capsid (PDB: 3J3Q) visualized using VMD software. The protein p24 self assembles to form the HIV viral capsid which protects the viral RNA. (c) Photograph of the Alere HIV Combo test, which is the most sensitive PoC test for HIV to date, detecting both p24 antigen and HIV-1/2 antibodies.

Laboratory diagnosis of HIV infection is primarily based on serology, either detection of HIV-1/2 antibodies or simultaneous detection of antibodies and HIV-1 p24 antigen to increase diagnostic sensitivity.[68] These markers can either be detected by ELISA or using a rapid diagnostic test such as LFA. The antigen p24 is detectable *ca*. 5 days after HIV RNA and can be detected by “fourth-generation” lateral flow assays which can detect both antibody and antigen levels combined on a single strip. HIV antibodies are detectable about 1 week after p24. However, this timeframe is variable between individuals, and could take several months for antibodies to reach detectable levels.[69]

The WHO outlined requirements for a successful PoC diagnostic, which include being affordable, sensitive, specific, user-friendly, rapid, robust, equipment-free and deliverable to end users (Table 2.1). Lateral flow testing is standard in PoC diagnostics because it is rapid, easy to use, portable and low cost. When the result can be read visually through a colorimetric signal or label (such as AuNP or colored latex particle, or carbon NP), the test can be performed without any specialized equipment to read the result. Additionally, this simple platform enables its use in remote areas without the need for highly qualified personnel. Sensitivity of LFA generally lags behind other bench top approaches, mainly because of the time necessary to read the result (sec-min for LFA, hours for bench top).

Table 2.1 Criteria for ideal point-of-care tests outlined by the World Health Organization[71]

ASSURED characteristic	Target specification
Affordable	< $500 per machine, < $10 per test
Sensitive	Sensitive with few false-negatives. Sensitivity defined as
Specific	Specific with few false-positives
User-friendly	Simple to perform tests with minimal training
Rapid and robust	< 30 minutes for diagnosis, shelf life > 1 year at room temperature
Equipment-free	Compact, battery powered, on-site data analysis, no cold chain transport or storage
Deliverable to end users	Portable, hand-held

Acute HIV infection poses a unique challenge in diagnosis as it encompasses a period from initial infection to complete seroconversion (the period over which patient antibodies against proteins of HIV develop). During this window period, there is a lack of detectable circulating biomarkers, with antibodies appearing *ca.* 28 days after infection.[69,72] HIV p24 is the earliest protein biomarker post infection, and a test capable of detecting p24 earlier would be transformative in key target settings, such as the diagnosis of infants whose mothers are known to be HIV positive, where antibody tests are unreliable, and also to ensure early intervention with antiretroviral therapies where they have the potential to be most beneficial.[73–76] However, clinically relevant ranges of p24 during acute infection (0.1 – 1000 pg·mL^{-1} with levels above 10 pg·mL^{-1} only briefly reached during acute stage)[77] are far below the detectable limit of the leading field-ready colorimetric LFA tests (*ca.* 10 – 15 pg·mL^{-1}),[78–80] which are limited by the absorbance of the colored label and the affinities of the antibody recognition components.[81] The leading gold standard commercial assays for HIV are the Alere HIV Combo and Alere Determine HIV-1/2 Ag/Ab combo, but recent data show that the HIV-1 antigen detection component for these fourth generation lateral flow assays lacks sensitivity, and these tests failed to detect acute stage infections in field trials.[69]

Several methods have been developed to improve p24 detection in LFA. Nabatiyan *et al.*[82] reported the design of a LFA using fluorescent microparticle labels, which achieved high sensitivity (sub pg·mL^{-1}), but required acid-shock and neutralization treatment for immune complex disruption (ICD) and a fluorescent microscope to analyze the result, limiting its use in resource-limited settings. Parpia *et al*.[83] presented the use of carbon nanoparticles as labels in LFA for colorimetric detection of acute pediatric infection. The test achieved 50 pg·mL^{-1}

sensitivity and detection of HIV-positive infant plasma samples, but required heat shock treatment for ICD, making it multi-step and less user-friendly. While achieving promising sensitivity for p24, these tests have not yet been successfully translated to the clinic or field and there is still room to improve on early detection of HIV through development of a more sensitive colorimetric readout for p24.

2.1.2.2 Lateral flow assay (LFA)

Lateral flow assays are a well-established technology that is particularly relevant for PoC or field-use applications. The tests utilize porous membranes, biological recognition elements, and usually a visible signal-generating system to produce a low cost, simple, and rapid diagnostic result. Lateral flow tests were first developed commercially in the mid-1980s as a simple urine-based pregnancy test for home use. Most pregnancy tests provide a visual readout of human chorionic gonadotropin (hCG), a hormone produced by the placenta after implantation.[84] While the lateral flow testing platform has been established for several decades, recent advances in materials science and nanotechnology have led to significant improvements in test sensitivity. The low cost, field utility, and performance of lateral flow tests have led to their uptake for detection of a variety of infectious and noncommunicable diseases that have been deployed in home and hospital settings, and for rapid detection of disease in previously unserved settings.

The format of LFA is like the sandwich ELISA (§1.3.3), however, a colored particle is usually used in place of an enzyme as the detection label. Figure 2.2 shows the typical configuration of a lateral flow assay.

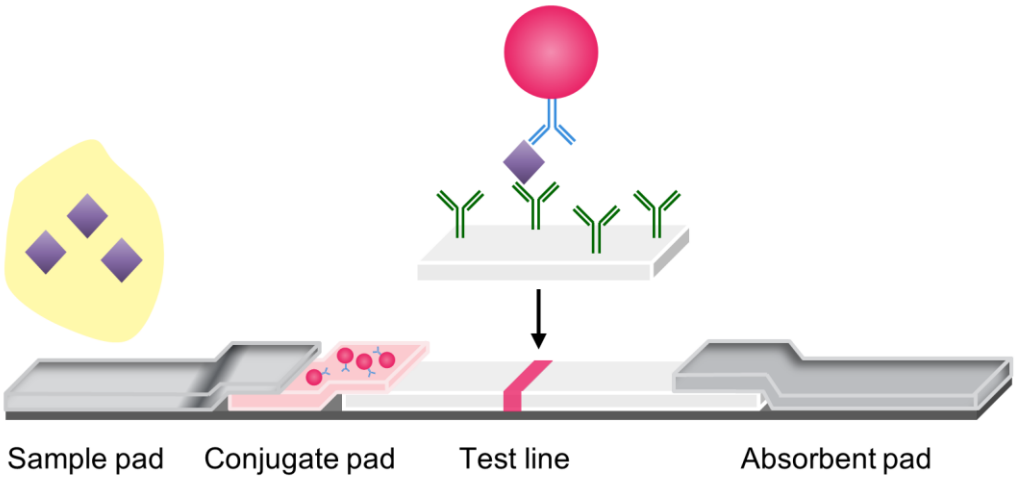


Figure 2.2 Typical configuration of a lateral flow assay test strip employing colored nanoparticle labels (red) for detection of target analyte (purple) through antibody-antigen sandwich at the test line.

A typical lateral flow test strip is composed of several overlapping membranes, including a sample pad, a conjugate pad, a nitrocellulose membrane, and an absorption or wicking pad (Figure 2.2). Biological recognition elements are spotted onto the nitrocellulose membrane (test line) to capture the analyte of interest. The clinical sample containing the analyte of interest is applied to the sample pad and drawn through the strip through capillary action. The sample first migrates through the glass fiber conjugate pad, where a nanoparticle conjugate has been immobilized (dried down in a sucrose buffer). The particles are typically colloidal gold, colored latex, or fluorescent or paramagnetic monodisperse nanoparticles. The particles have been conjugated to a specific biological recognition element (antibody, antigen, aptamer, nucleic acid sequence depending on the assay format). The sample solution remobilizes the dried conjugate, and the analyte in the sample interacts with the conjugate as both migrate *via* capillary flow into the next section of the strip, which is the nitrocellulose membrane. The membrane has been modified with a line of antibodies, antigens, or other affinity reagents that are specific to the target present in the sample. These lines of spotted proteins serve to capture the target analyte and the nanoparticle-conjugate as they migrate over the test line. Excess reagents move past the capture lines and are entrapped in the wicking or absorbent pad. Most LFAs also include a control line downstream of the test line to validate the activity of the assay reagents and fluid flow through the membrane. The result can be read by eye or by a specialized reader (for absorbance, fluorescence, or chemiluminescence depending on the particle type used for the label) as the presence or absence of lines on the strips.[60,84]

Although lateral flow tests offer advantages in terms of ease of use, low cost, rapid time to result and equipment-free operation, they tend to suffer in sensitivity. Whereas a typical ELISA

can achieve picogram per milliliter sensitivity, the limit of detection of a typical colloidal gold-labeled LFA is generally limited to nanogram per milliliter regimes, dependent on the sensitivity of the label and affinity reagents. A major challenge in LFA development is extending their performance into applications that require higher accuracy and sensitivity while maintaining their advantages as a PoC diagnostic tool.

Developing a lateral flow test is complex because of the large number of components brought together to produce a functional test strip. Changing one material or reagent typically affects the performance of others. Therefore, designing a paper-based immunoassay requires an understanding of the various components and how they interact with each other, the test strip, and clinical samples. For example, proteins bind to nitrocellulose through a combination of electrostatic and hydrophobic forces, which is advantageous for spotting a test line of antibodies on the membrane.[85] However, this can introduce challenges because the membrane also has the potential to bind other proteins nonspecifically. To overcome this challenge, surfactants, such as Tween-20, and blocking agents, such as bovine serum albumin (BSA) or skimmed milk, are added to the test system to minimize nonspecific binding (NSB).

Several strategies have been employed to increase the sensitivity of colorimetric LFAs. These include modifying the nanoparticle label or altering the physical properties of the device (flow movement, speed, etc.) by modifying its design or architecture. Most LFA detection is done visually, either by naked-eye for simplicity or by using optical readers. In principle, any colored particle can be used for the label, however latex particles and gold nanoparticles are most commonly used. The ‘gold standard’ for LFA uses colloidal gold nanoparticle (AuNP) labels due to their high extinction coefficient, so the result can easily be read by eye with a clear red line indicating a positive result. However, there is growing use of fluorescent, chemiluminescent, and magnetic field measurement systems to increase sensitivity.[86]

The development of lateral flow technologies has been accompanied by the design of smart phone applications which can be used to detect the test lines of LFAs and translate the signal into a user-friendly result.[87] The use of smart-phone connected diagnostics could aid in geographically tracking and monitoring infectious disease, controlling outbreaks, allocating resources appropriately, and connecting patients to treatment and care.

The following sections outline the key design parameters that affect lateral flow assay sensitivity.

2.1.2.2.1. Nanoparticle label

A variety of signal generation elements have been employed in LFA, including colloidal gold,[60] colored latex particles,[85] carbon black nanoparticles,[83] fluorescent particles (including quantum dots),[82] and paramagnetic[88] particles. While fluorescent particles can generally provide lower limits of detection than optical labels, the readout requires fluorescence readers which add cost and complexity to the system. Gold nanoparticles have also been exploited for thermal contrast amplification, where laser excitation of AuNPs provides a thermal signature with *ca*. 8 – 32 fold amplification in signal compared to its visual signature.[89–91]

Within the range of colorimetric labels available, colloidal gold, typically in the 20 – 80 nm size regime is most often used, with 40 nm AuNPs being the most common label due to their physiochemical properties.[60] AuNPs offer intense color signals due to localized surface plasmon resonance (LSPR), and 40 nm AuNPs have an absorption cross-section 5 orders larger than organic dyes.[46,92] Functionalization of colloidal gold with biomolecules is also easy and scalable by means of thiol-gold chemistry and a range of van der Waals and electrostatic interactions leading to physical adsorption.[93]

There have been varied reports on the impact of nanoparticle size on test line signal. The number of nanoparticles captured at the test line will depend on the transport and binding of particles, which are both affected by particle size. Binding ability will be influenced by the number of antibodies that can be loaded per nanoparticle, which scales with surface area.[94] Zhan *et al.*[89] found that 100 nm AuNPs provided higher visual contrast in LFA than 30 nm AuNPs, and claimed that further increases in nanoparticle size would decrease capture as larger particles have slower diffusion rates, however this was not experimentally validated. The possibility for nonspecific interactions also increases as particle size increases, where an increase in surface area for antibody physisorption may result in multivalent NSB. Therefore, the benefits of using nanoparticles > 100 nm as labels in LFA requires further investigation and optimization for each target. Smaller particles have also found advantages in certain assay configurations. 20 – 40 nm gold nanoparticles have been shown to achieve higher packing density of particles at the test line compared to larger labels that exhibit steric hindrance (> 100 nm).[15,94]

2.1.2.2.2. Recognition molecules

For direct antigen detection immunoassays (§1.3.3), antibodies are the core recognition elements. Antibodies can be monoclonal or polyclonal or produced through antibody

engineering methods, such as phage display, *e.g*. to screen for high affinity single-domain antibodies (nanobodies). The focus in this chapter is on direct antigen detection using antibodies and nanobodies, however additional recognition molecules, such as aptamers[95] and nucleic acids,[96] can also be employed for detection of other biomarkers.

The kinetic constants of affinity reagents are a key consideration in LFA development. The binding affinity is defined by the equilibrium dissociation constant K_D (§1.3.2), where lower K_D values correspond to higher affinity between antibody and antigen. Good antibodies will have nanomolar or sub-nanomolar K_D. For LFA, affinity needs to be primarily driven by a fast association rate constant (k_{on}) because of the very short potential time for reagent binding at the test line, which is limited to several seconds.[15]

Orientation of the antibodies or affinity reagents on the surface of the nanoparticle and on the test line can also impact sensitivity. In particular, oriented attachment of antibodies on nanoparticle surfaces has shown to improve conjugation efficiency and antigen binding capability compared to uncontrolled conjugation methods, such as carbodiimide and maleimide bioconjugation chemistries.[97,98] Oriented attachment can be achieved through covalent conjugation chemistries and site-selective modification strategies. Binding of proteins to gold or other metal nanoparticles is typically achieved through passive physical adsorption, which results in random orientation of antibodies, but is easily scalable.[93] Particles with additional reactive groups on the surface offer potential for covalent conjugation of antibodies using site-selective chemistries. With site-specific chemistries it is possible to introduce reactive handles, such as biotin, onto antibodies in a way that does not inhibit antigen binding.[99]

The use of biotin-streptavidin interaction at the test line for capture of nanoparticle conjugates on the solid phase has been demonstrated to improve assay sensitivity over standard antibody sandwich systems.[100] Biotin-streptavidin interaction has a K_D approximately 5 orders of magnitude lower than the best performing monoclonal antibodies, which enables high affinity binding at the test line. Streptavidin can be immobilized on the solid phase to facilitate capture of biotinylated nanoparticle-antibody conjugates. In this scenario, the nanoparticle is conjugated with the detection antibody, the nanoparticle-antibody conjugate captures antigen in solution and is sandwiched to a biotinylated capture antibody. The sandwich forms in the aqueous phase as the complex runs up the membrane. The biotinylated nanoparticle conjugate is immobilized at the test line through high affinity biotin-streptavidin interactions. In this format, the antibody capture occurs in solution where reaction kinetics are favored, as opposed to on the solid phase if the capture antibody is directly immobilized on the test line.

2.1.2.2.3. Flow speed (reaction time)

The amount of signal generated at the test line is related to the flow of reactants through the membrane. Nitrocellulose membrane selection, based on pore size, is key to controlling the flow rate of reactants. Capillary flow rate determines the length of time that reactants have to form immunocomplexes before reaching the test line.[85] Therefore a membrane with faster flow rate (larger pores) will result in lower sensitivity compared to a membrane with smaller pores and slower flow rate. Flow rate can also be controlled by introducing flow delays onto the membrane. Wax can be used as an inexpensive architectural tool to control the flow rate of the sample due to its hydrophobicity. Rivas *et al.*[101] reported the use of hydrophobic wax pillars printed onto the nitrocellulose membrane to produce flow delays, which have been shown to improve limits of detection by increasing the reaction time and residence time of reactants at the test line to allow for effective formation of the immunocomplex. Polymers such as polyvinyl alcohol (PVA) or polyvinylpyrrolidone (PVP) and sucrose can also be introduced into reaction buffers to increase viscosity and thus reduce flow rate. While decreasing flow rate can improve sensitivity, it also increases the time to result so must be balanced in terms of meeting the test specifications.

2.1.2.2.4. Balancing nonspecific binding (NSB)

Optimization of LFA design is predominately based on maximizing positive test line signal and minimizing nonspecific signal due to NSB of reagents to the membrane or to each other. Nonspecific signal may arise from interactions between assay components with the membrane, assay components and test line reagents, protein-protein interactions, or may be specific to the conformational changes of an antibody induced when bound to the nanoparticle surface. It is important to find the source of NSB and triage blocking agents to minimize the effects so that it does not limit assay sensitivity. Proteins such as bovine serum albumin (BSA) or β-casein (1 – 3 wt%) and surfactants at low concentration such as Tween-20 (0.01 - 0.2 wt%) can be incorporated into reaction buffers to minimize nonspecific protein-protein interactions. BSA and β-casein can act as nonspecific proteins to compete for binding sites. Tween-20, PVA and PVP can be used to reduce protein binding to the membrane. Surfactants can interfere with hydrophobic interactions, while polymers can interfere with protein binding with the aim of reducing nonspecific interactions. Other blocking agents such as skimmed milk or gelatin can also be used to reduce NSB.

2.1.2.3 Signal amplification techniques for colorimetric lateral flow assays

Several signal amplification techniques have been employed to enhance the sensitivity of colorimetric lateral flow assays, enabled predominately by advances in materials science and nanotechnology.[102] Focusing on AuNPs as the comparator system, which are typically used as labels in commercial LFA, most of the reported signal amplification techniques can be categorized into two areas: the first relies on enhancing AuNP signal by increasing the size of the label, and the second technique is based on the generation of secondary colored signals through enzymatic or catalytic processes.

A common signal enhancement strategy is to tune particle size. One method for increasing particle size for gold nanoparticle labels bound at the test line is to perform a silver enhancement step. In this method, AuNPs act as catalysts to reduce Ag^+ ions to metallic Ag in the presence of a reducing agent. The Ag is reduced on the AuNP surface, enlarging particle size and increasing the extinction coefficient. Yang *et al.*[103] showed that this silver enhancement strategy could achieve 100-fold improvement in the limit of detection. This enhancement technique can also be applied to gold enhancement, but both suffer from homogenous nucleation or nucleation in other reagents bound at the test line (*e.g.* proteins), which can increase background signal.

Biological enzymes have also been used to amplify test line signal. Parolo *et al.*[104] presented an LFA based on the use of AuNPs as both labels and carriers of enzymatic labels. AuNPs were modified with both antibodies toward the target (human IgG as model analyte) and horseradish peroxidase (HRP) molecules. After running the LFA, the strip was treated with a peroxidase substrate, and 10-fold signal amplification was achieved through the generation of insoluble colored products deposited at the test line. While this platform offers enhancements in sensitivity, one drawback is the inherent instability of the enzyme probes which are susceptible to protease digestion in biological samples and denaturation in PoC environments.

Catalytic nanomaterials with intrinsic peroxidase-like activity have emerged as promising labels for signal enhancement in biosensing applications. Iron oxide,[34] platinum,[67] palladium,[53] and iridium[54] nanoparticles have demonstrated artificial peroxidase activity by catalyzing the oxidation of peroxidase substrates, such as tetramethylbenzidine (TMB) in the presence of hydrogen peroxide. These peroxidase mimics offer advantages over biological enzymes due to improved thermal and chemical stability and improved catalytic efficiency resulting from high surface area.

Recently, Gao *et al.*[67] reported the development of platinum-decorated gold nanoparticles for use as dual-functional labels in LFA. Conventional 40 nm AuNPs were coated with an ultrathin Pt shell. Due to the thin conformal Pt coating, the Au@Pt NPs retained the plasmonic activity of the underlying AuNP seed with the added functionality of catalytic activity enabled by the Pt coating. The Au@Pt NPs were employed as labels for detection of prostate specific antigen (PSA) and could be used in a low sensitivity mode for detection of high concentrations of PSA using only the plasmonic properties of the AuNP. For detection of low concentrations of PSA, the catalytic activity of the Pt shell could be used to catalyze the oxidation of TMB, resulting in significant signal amplification at the test line.

While several lateral flow systems described above have reported the use of catalytic nanoparticle labels, the optimal size regime for catalytic labels in this context has yet to be investigated and forms the basis of discussion in this chapter.

2.1.2.4 Metal nanocatalysts

Heterogeneous catalysis involves making and breaking bonds between a catalytic surface and both the reactants and products, and is widely used in the chemical, pharmaceutical, and automobile industries to convert raw materials into valuable fuels and chemicals.[105] Transition metal nanoparticles are attractive catalysts due to their high surface area to volume ratio and high surface energy. Catalytic efficiency can be highly dependent on size, shape, and composition of the nanoparticle due to the variation in spatial arrangement of surface atoms, where atomic arrangements can offer specificity toward various reactions based on favorable adsorption energies of reactants, intermediates and products. An example of heterogeneous catalysis is the use of platinum nanoparticles in catalytic converters to catalyze the oxidation of carbon monoxide to less harmful carbon dioxide. Platinum catalysts are also employed in petroleum cracking, fuel cell, and electrode materials.[105] El-Sayed and coworkers[106,107] demonstrated that controlling the shape of platinum nanoparticles could be used to tune their catalytic activity. They found that the average rate constant of catalytic reactions increased exponentially as the percentage of surface atoms at corners and edges increased in Pt nanoparticles of varying shapes for electron-transfer reactions. It has been shown that the activity and selectivity of a nanocatalyst can be greatly enhanced by use of nanoparticles presenting crystal facets that are intrinsically more active for a specific reaction.[106]

2.1.2.5 Growth of metal nanoparticles

2.1.2.5.1. Homogeneous nucleation

In a typical synthesis of metal nanoparticles, a metal precursor is either decomposed or reduced to generate zero-valent atoms.[108] In a reduction synthesis, the metal precursor, which is in a higher oxidation state than the atomic species, is reduced to atoms in the presence of a reducing agent, *e.g.* ascorbic acid. When the concentration of atoms reaches a point of supersaturation, the atoms start to aggregate into small clusters (nuclei) through homogenous nucleation. These nuclei then grow, rapidly depleting the concentration of metal atoms in solution. Nucleation events stop when the concentration of atoms drops below the supersaturation level. Existing nuclei continue to grow into larger nanocrystals through atomic addition and agglomeration of other seeds until an equilibrium state is reached between the atoms on the surface of the nanocrystal and the atoms in solution. While homogenous nucleation can proceed in a one-pot synthesis, the size ranges accessible are limited. The particles formed through homogenous nucleation can be used as seed templates for heterogenous nucleation. Seed-mediated nanoparticle synthesis is a powerful method to achieve fine control of nanocrystal size, shape, composition and structure.[109]

2.1.2.5.2. Heterogenous nucleation

In seed-mediated growth of nanoparticles, preformed colloidal seeds act as templates for atom deposition. The seeds are incorporated into a growth solution composed of metal precursors at a concentration below supersaturation, and capping agents to initiate the growth of a secondary layer of metal on the seeds.[109] This process can be repeated in a layer-by-layer fashion to significantly increase particle size while maintaining fine control over growth due to the well-defined number of nucleation points. Modelling the process of heterogeneous nucleation requires additional surface energy contributions: the substrate–medium surface energy (γ_{bm}) and the nucleus–substrate (seed) surface energy ($\gamma_{\alpha b}$). The free energy barrier is lower for heterogeneous nucleation, which makes seed-mediated growth more favorable than homogenous nucleation (Figure 2.3). While heterogeneous nucleation is energetically more favorable, both homogenous and heterogenous nucleation can occur concomitantly if the precursor concentration exceeds the threshold for homogeneous nucleation (supersaturation), which results in diverse and uncontrolled particle sizes. To promote only heterogenous nucleation on seeds, reduction kinetics must be controlled. For example, a syringe pump can be used to control the injection rate of the precursor into the suspension of

seeds to manipulate the reaction kinetics. Lower temperature and weak reducing agents can also be used to slow reduction rate.

Because of the defined number of nucleation sites, seeded synthesis methods can produce a broad range of well-defined sizes and shapes that are inaccessible in a one-pot approach, where homogeneous nucleation and seed-mediated growth occur simultaneously.[109] Important experimental parameters for seeded synthesis include the type and concentration of the seed, precursor, reductant, stabilizing agent, temperature and injection rate. A key advantage of seed-mediated synthesis is that particle size can be controlled by fine tuning the concentration of precursor solution relative to the seed concentration.

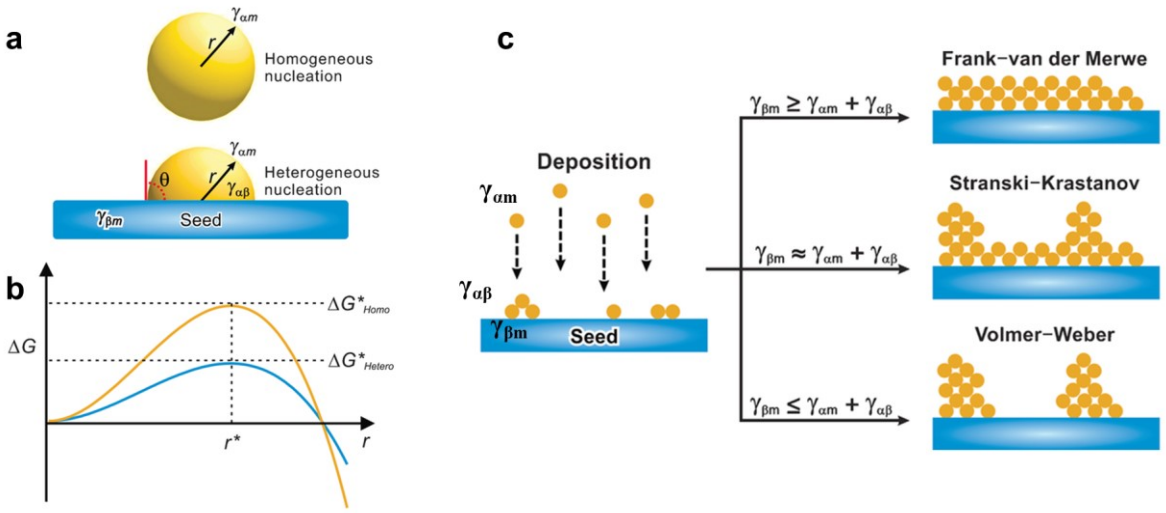


Figure 2.3 (a) Comparison of two different nucleation processes: homogeneous in solution and heterogenous, initiated on the surface of a seed. (b) Plot showing the change in Gibbs free energy as a function of size for homogenous nucleation (yellow) and heterogeneous nucleation (blue). (c) The three possible growth modes for the deposition of metal atoms on the surface of a nanoparticle seed, where deposition is dictated by surface energies: $\gamma_{\alpha m}$ is the interface between the deposited layer and solution, $\gamma_{\beta m}$ is for the substrate and solution, and $\gamma_{\alpha\beta}$ is for the deposited layer and the substrate (seed). Figure adapted from Xia *et al.* with permission.[109]

2.1.2.5.3. Growth modes

The deposition mode of a substrate on a core material is largely determined by the surface energies of the three interfaces: $\gamma_{\alpha m}$ for the deposited layer and the solution, $\gamma_{\beta m}$ for the substrate (seed) and the solution, and $\gamma_{\alpha\beta}$ for the deposited layer and the substrate (Figure 2.3). Frank-van der Merwe or layer-by-layer growth mode occurs when the lattice mismatch between the core and the shell is small (< 5 %). If the mismatch between the core and the

shell is relatively large, growth tends to follow Volmer-Weber or island growth mode (Figure 2.3), which minimizes interfaces during growth.

Of interest in this chapter is the deposition of platinum on gold seeds. Most noble metals, including Au, Ag, Pt and Pd, crystallize in a face-centered cubic (fcc) lattice. When the lattice difference is less than 5 % between deposited layer and seed, epitaxial crystal growth is favored, which means that the underlying seed structure is adopted in the shell.

Table 2.2 Selected noble metals and their physicochemical properties[109]

Metal	Crystal lattice	Lattice constant [Å]	Bond energy [kJ·mol^{-1}]	Cohesive energy [kJ·mol^{-1}]	Surface energy [J·m^{-2}] [a]
Pt	fcc	3.92	306.7	564	2.30, 2.73, 2.82
Au	fcc	4.08	226.2	368	1.28, 1.63, 1.70
Pd	fcc	3.89	> 136	367	1.92, 2.33, 2.23
Ir	fcc	3.84	361	670	2.97, 3.72, 3.61

[a] Facet order for fcc: {111}, {100}, {110}

The percent of lattice mismatch between gold and platinum is relatively small, only 3.9 %, suggesting a layer-by-layer growth model would be favored. However, Pt also has a high cohesive energy (Table 2.1, 564 kJ·mol^{-1}), which has been shown to hinder the layer-by-layer growth mode. As a result, Pt tends to first generate small nuclei which form islands on the surface of the seed, resulting in dendritic morphology. Guo *et al.*[110] observed this effect when depositing Pt on Au seeds, where the resulting product had a porous dendritic morphology, which exhibited high activity towards oxygen reduction reaction. Gao *et al*.[52] discovered that these “urchin-like” *ca*. 35 nm Au core – Pt shell nanoparticles are also efficient at catalyzing the disproportionation of hydrogen peroxide, and subsequently used them as peroxidase-mimicking labels for a solution-based immunoassay for detection of prostate-specific antigen (PSA), a biomarker for prostate cancer. Lim *et al*.[111] observed dendritic growth of Pt on Pd seeds, which was attributed to an autocatalytic process where Pt nuclei form on the Pd seed and can serve as catalytic sites for further reduction of the Pt precursor resulting in a branched and porous morphology. While a dendritic Pt morphology is common in seeded synthesis, it is also possible to produce conformal layer-by-layer coatings of Pt on Au seeds by carefully controlling reaction parameters. Xia and coworkers[67] demonstrated that the thickness of Pt shells grown on Au seeds can be controlled with atomic precision by adjusting the amount of Pt precursor introduced to the synthesis. The key to maintaining layer-by-layer growth mode was to ensure a slow Pt deposition relative to surface diffusion to allow for atoms to spread across the entire surface of Au leading to a conformal Pt coating. They also showed that when

the Pt precursor injection rate was increased, Pt dendrites were formed instead of smooth and conformal shells.

2.1.3 Overview of PtNC amplified LFA design

A lateral flow assay can be used to quickly establish whether a target analyte is present in a complex sample (blood, plasma, sera, *etc.*) using a simple colorimetric readout. The core process in a LFA begins when a detection label (typically an intensely colored nanoparticle) is hydrated by the sample, drawn along the paper membrane by capillary action and bound, *via* a target analyte, to a region of the strip called the test line. To achieve this, both the nanoparticles and the test line must be decorated with affinity ligands (typically antibodies) capable of binding discrete regions of the target analyte. To achieve a high level of sensitivity in a LFA format, the components must exhibit fast binding reaction kinetics towards the solid-phase to ensure that the particle labels can bind to the test line within the short time window during which the sample is flowing past. The use of a high affinity binding system like biotin-streptavidin ($K_D \approx 10^{-15}$ M) for the test line binding capture step is essential for moving towards the goal where all target antigens are labeled with a nanoparticle at the test line.[112] The advantage of this architecture means that the antibody binding complex forms in solution such that the biotin-streptavidin interaction is the rapid binding event which immobilizes the complex at the test line. This circumvents the often poor performance of conventional antibody capture, as the biotin-streptavidin binding affinity is over four orders of magnitude higher than a conventional antibody-antigen interaction.[31]

The platinum nanocatalyst (PtNC) amplified LFA takes advantage of the simple, low cost LFA platform, but incorporates a strong amplification mechanism through the catalytic activity of the nanoparticle itself to increase the signal intensity through local deposition of chromogens at the test line. The schematic in Figure 2.4 highlights the essential components and configuration of the PtNC amplified LFA. During the assay, a plasma (or serum) sample is introduced into a vessel containing both lyophilized antibody-modified PtNCs and orthogonally biotinylated camelid antibody fragments (nanobody-biotin) capable of binding to discrete epitope regions of the HIV-1 p24 capsid protein. Next, a lateral flow strip, composed of a nitrocellulose reaction membrane and an absorbent pad, is used to draw the solution up the strip towards a streptavidin bearing test line by capillary action. When present, p24 in the sample can then be sandwiched between the antibody-PtNC conjugate and a biotinylated antibody fragment, forming a biotinylated complex that is captured at the streptavidin coated test line. At high target concentrations (0.2 – 10 ng·mL^{-1} p24) a clear black line is visible with the naked eye due to the intrinsic absorbance of the particles bound at the test line, indicating

a positive test result. Lower concentrations of the target are visualized by taking advantage of the catalytic amplification of the PtNCs that act to disproportionate H_2O_2, enabling the oxidation of a chromogenic substrate.[55,57,113,114] After running the plasma sample through, followed by a chase buffer, the test line is exposed to a mixture of hydrogen peroxide and a chromogenic substrate. Any PtNC captured on the test line will oxidize the substrate, generating an insoluble colored product. This amplification step increases the window of sensitivity and lowers the detection limit by two orders of magnitude. Because of the unambiguous colored product deposited at the test line, the assay result can be easily read by eye or captured by a mobile phone camera for analysis, with the potential for semi-quantitative result readout with a pre- and post-amplification signal regime.

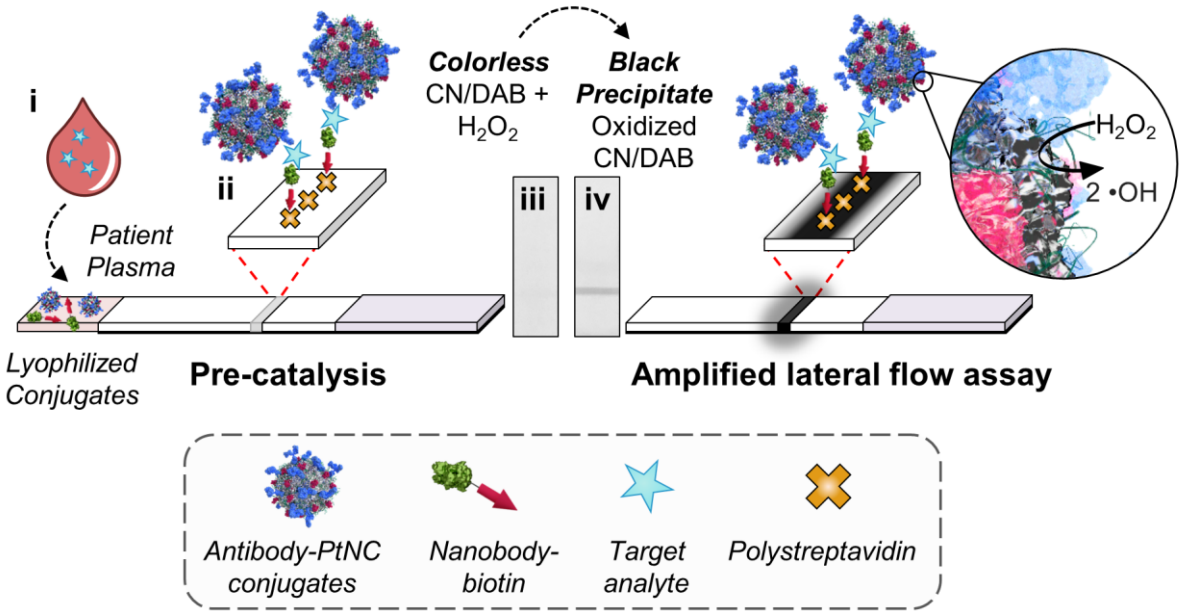


Figure 2.4 Scheme showing amplified LFA, where (i) functionalized Pt nanocatalysts (PtNC) and biotinylated nanobody fragments are mixed with a plasma or serum sample. (ii) In the presence of a target, PtNCs become biotinylated through complexation with the target, and rapid high affinity biotin-streptavidin binding enables a [target] dependent deposition of PtNC at the test line (iii). (iv) PtNCs bound at the test line catalyze the oxidation of CN/DAB (4-Chloro-1-naphthol/3,3´-Diaminobenzidine, tetrahydrochloride) substrate in the presence of hydrogen peroxide producing an insoluble black product which is clearly visible with the naked eye.

Through the design and optimization of a nanocatalyst amplification platform, high affinity and orthogonally designed binding components, and lateral flow architecture, a high level of sensitivity and broad dynamic range previously unattainable in LFA formats is achieved. The catalytic amplification process developed herein allows the test, in spiked serum, to surpass the published sensitivity of the leading commercial rapid tests for p24 (Alere Determine HIV-1/2 Ag/Ab Combo and Alere HIV Combo, for example) by a factor of up to 20. This platform

enabled detection of low femtomolar concentrations of p24 in spiked serum (*ca.* 32.5 fM), and naked-eye detection of acute stage HIV in clinical plasma samples in under 20 minutes.

2.2 Materials & Methods

An Eppendorf Thermomixer Comfort heating block was used for temperature and agitation-controlled experiments.

2.2.1 Synthesis of gold nanoparticle seeds

Gold nanoparticle seeds with a diameter of *ca*. 15 nm were synthesized by sodium citrate reduction of $HAuCl_4$. In a typical synthesis, 10 mL gold (III) chloride trihydrate aqueous solution (20 mM, Sigma) was added to 180 mL purified water under reflux at 100 ºC. The temperature was then reduced to 70 ºC, and reaction initiated by fast injection of 10 mL trisodium citrate dihydrate (68 mM, BDH Chemicals) with vigorous stirring and refluxed for 5 min. Resulting *ca*. 15 nm gold nanoparticle (AuNP) seeds were cooled to room temperature and subsequently stored at 4 ºC. Seed concentration in molarity (moles of nanoparticles per liter) was determined by TEM size analysis and initial gold concentration used in synthesis. In brief, the mass of gold used in the synthesis was converted into a volume using the density of Au (19.32 $g \cdot cm^3$). Next the average volume of a single nanoparticle was calculated based on the average size from TEM image analysis. The number of particles formed during synthesis was calculated using the total volume of gold divided by the volume of an average gold particle. Using the total number of particles synthesized in a known volume, the molar concentration of particles could be calculated using Avogadro's number and the total solution volume in which the particles were synthesized. Molar concentrations of nanoparticles are used in further discussions, in particular to understand antibody loading densities in terms of number of antibodies per particle using the molar ratios. The gold seeds used in this chapter were prepared by Dr. Michael R. Thomas.

2.2.2 Synthesis of porous platinum core-shell nanoparticles (PtNCs)

120 nm PtNCs were synthesized *via* reduction of chloroplatinic acid hydrate on gold seeds adapted from Gao *et al.*[52] In a typical synthesis, 31 µL (10 nM) 15 nm Au seeds were mixed with 969 µL purified water (*MilliQ*), followed by addition of 20 µL 20 wt% poly(vinylpyrrolidone) (PVP MW 10 kDa, Sigma). The solution was vortexed briefly and incubated for 5 min for polymer to coat and stabilize particles. 40 µL of L-ascorbic acid (100 $mg \cdot mL^{-1}$, Sigma) was then added to the mixture followed by 40 µL chloroplatinic acid hydrate (100 mM, Sigma), mixed, and immediately incubated at 65 ºC for 30 min until the color of the solution changed from red to brown/black indicating successful deposition of platinum. PtNCs were then cooled

to room temperature in a water bath, and excess reagents were removed through four sequential washing cycles at 1250 relative centrifugal force (rcf) for 12 min with resuspension into purified water. PtNC size in the range of 50 – 120 nm was controlled by changing the volume of AuNP seed solution while keeping the amount of PVP, ascorbic acid, and H_2PtCl_6 constant. PtNCs larger than 120 nm (mean number distribution by DLS) were synthesized *via* a step-wise layer-by-layer (LBL) platinum reduction and deposition approach. 120 nm PtNCs were used as seeds for subsequent deposition of platinum layers iterating on the above synthesis to achieve colloidally stable PtNCs up to *ca*. 280 nm. The particle concentrations for PtNCs were estimated based on the starting gold seed concentration and assuming that all platinum is reduced onto gold seeds (heterogenous nucleation) with no free nucleation in solution (homogeneous nucleation). With this assumption, the final PtNC concentration was estimated to be equal to the gold seed concentration used in synthesis.

2.2.3 Characterization of nanoparticles

Dynamic light scattering (DLS, Zeta Sizer Nanoseries, Malvern Instruments Ltd.) was used to characterize the hydrodynamic diameter of nanoparticles. Absorption measurements were recorded on a SpectraMax M5 multimode microplate reader (Molecular Devices Ltd.). For electron microscopy characterization, samples were drop-casted onto carbon-coated copper grids (Electron Microscopy Sciences), and TEM imaging was performed using a JEOL 2100Plus or JEOL 2100F operating at 200 kV. High angle annular dark field (HAADF) images were acquired in scanning transmission electron microscopy (STEM) mode using a camera length of 10-12 cm (HAADF5) on JEOL 2100F. The microscope was equipped with Gatan Orius SC 1000 (2×4k) high-angle annular dark field detector, Gatan annular dark field detector/bright field detector. Small camera length ensured that diffraction contrast was excluded from the imaging and contrast was related to the atomic number (Z) or density of the particles. Corresponding elemental compositional mapping PtNCs was determined by energy-disperse X-ray spectroscopy (EDS) in STEM mode. Scanning electron microscopy (SEM) imaging was performed on a Leo Gemini 1525 FEG SEM equipped with a secondary electron in-lens detector operating at 5 kV. STEM imaging and EDS mapping was performed with Dr. Shweta Agarwal and SEM was performed with Dr. Eunjung Kim.

2.2.4 Preparation of PtNC-antibody conjugates

In a typical conjugation, 200 µL 120 nm PtNC (300 pM) were mixed with 20 µL HEPES buffer (pH 6, 0.1 M) followed by addition of 2 µL of a 23 µM solution of monoclonal anti-HIV-1/2, purified (Capricorn Products, HIV-018-48303). The mixture was incubated for 3.5 h under

shaking (800 rpm) at 20 ºC for antibody physisorption. Modified particles were subsequently blocked by addition of 200 µL blocking solution: 2 wt% β-casein from bovine milk (Sigma) in PBS for 1.5 h under shaking (800 rpm) at 20 ºC. Excess reagents were removed through 3 wash steps in *assay running buffer* (0.2 wt% β-casein, 0.2 wt% Tween20 [Sigma] in 50 mM phosphate buffer pH 7.2). Particles were ultimately resuspended in *particle storage buffer* (10 wt% sucrose [Sigma], 1 wt% bovine serum albumin [BSA, Sigma], 1 wt% PVP 10 kDa, 0.1 wt% β-casein, 0.1 wt% Tween20 in 50 mM phosphate buffer pH 7.2). Horseradish peroxidase was also modified with anti-HIV-1/2 antibody following Lightning-Link Horseradish Peroxidase kit (Innova Biosciences) with no deviation from the manufacturer's protocol.

2.2.5 Evaluation of peroxidase-like activity

All assays were carried out at room temperature in a 96-well plate (Corning UK). For stability and activity of PtNCs in complex environments, 10 µL PtNCs or antibody modified PtNCs (300 pM) were mixed with 90 µL of either: deionized water; 2 wt% β-casein in PBS; fetal bovine serum (FBS, Sigma); or human plasma pool (Lee Biosciences) for up to 24 h at room temperature. PtNCs were further diluted in purified water to 5 pM for catalytic activity test. For activity test, 10 µL PtNCs (5 pM) diluted in purified water were added to a microwell plate followed by addition of 200 µL 1-Step Ultra TMB ELSA Substrate Solution (Thermo Scientific). The absorbance of the reaction solution at 652 nm was monitored up to 25 min after addition of substrate.

Steady-state kinetic assays were carried out at room temperature in a 96-well plate with 220 µL solution with estimated path length (l) of 0.5 cm. 25 mM NaOAc/HOAc solution (pH 4.0) was used as the reaction buffer. For kinetic assays varying 3,3′,5,5′-Tetramethylbenzidine (TMB), PtNCs (0.1 pM, 20 µL) were mixed with TMB (10 µM to 1 mM, 100 µL) and H_2O_2 (5 M, 100 µL).

For kinetic assays varying H_2O_2, PtNCs (0.1 pM, 20 µL) were mixed with H_2O_2 (0 to 10 M, 100 µL) and TMB (1 mM, 100 µL). After addition of substrates (TMB and H_2O_2) in the buffer system containing PtNCs, the absorbance of the reaction solution at 652 nm of each sample was immediately measured as a function of time with intervals of 20 s using a spectrophotometer for 10 min. These "absorbance *vs* time" plots were then used to obtain the slope at the initial point ($Slope_{Initial}$) of each reaction (over first 150 s). The initial reaction velocity (v) was calculated by $Slope_{Initial}/ (\varepsilon_{TMB\text{-}652\ nm} \times l)$, where $\varepsilon_{TMB\text{-}652\ nm}$ is the molar extinction coefficient of TMB at 652 nm, which is $3.9 \times 10^4\ M^{-1}\cdot cm^{-1}$. The plots of reaction velocity, v, against TMB and H_2O_2 concentrations were fitted using nonlinear regression of the Michaelis-Menten

equation. The kinetic parameters were calculated based on the Michaelis-Menten equation (**Equation 2.1**):

$$v = \frac{V_{max}[S]}{K_m + [S]} \quad (\mathbf{2.1})$$

where V_{max} represents the maximal reaction velocity, [S] is the concentration of substrate, and K_m is the Michaelis-Menten constant. Vmax was obtained from fitting to the model using GraphPad Prism software, and the catalytic constant (k_{cat}) was calculated using the equation: $k_{cat} = V_{max}/[E]$, where [E] is the PtNC concentration.

2.2.6 Production of cysteine presenting nanobody *via* site directed mutagenesis of an existing nanobody

The C-terminus of a validated nanobody against p24, 59H10, characterized in Gray *et al*.[115], comprises an alanine spacer, myc and His_6 tags. To insert a Cys residue in this region to generate ...HHHHHHCZ the following primers were used with the QuikChange Site-Directed Mutagenesis kit (Agilent) following the manufacturer's instructions, verified by sequencing, and the resultant cysteine presenting nanobody purified as described previously.[115]
F – GCCGCACATCATCATCATCATTGCTAATGAGAATTCACTGG and
R – CCAGTGAATTCTCATTAGCAATGATGATGATGATGATGTGCGGC
Mutations were verified by sequencing. The nanobody was produced by Dr. Eleanor Gray.

2.2.7 Site-selective modification of nanobody

Site-selective modification of the cysteine presenting nanobody was achieved through reaction of the reduced nanobody with bromopyridazinedione-PEG_8-biotin. Synthesis and characterization of pyridazinedione-biotin, and subsequent site-selective modification of the cysteine mutated nanobody (shown by LCMS, SDS-PAGE), is described in the Supplementary Methods of Loynachan *et al.*[59] where production and characterization of the modified nanobody was performed by Dr. Daniel R. Richards.

2.2.8 Characterization of antibody components

Affinity constants for antibody components were measured on the FortéBio Octet RED96 benchtop interferometer (Pall ForteBio LLC, as previously described in Gray *et al.* and Miller *et al*.).[115,116] Biolayer interferometry (BLI) is a label free optical analytical technique for

measuring biomolecular interactions that analyzes the interference pattern of white light reflected from two surfaces – a layer of immobilized protein (*e.g.* analyte) on a biosensor tip and an internal reference layer.[117] Molecules binding to the biosensor tip cause a shift in the interference pattern (in nm) that can be monitored in real time. As outlined in Gray *et al.*,[115] first p24 was immobilized on amine-reactive probes, and the binding kinetics of either nanobody or monoclonal antibody (Capricorn 1/2) to the immobilized p24 was analyzed. Analyte binding proceeded for at least 60 min. Normalization was carried out using an *in situ* probe functionalized with p24 and dipped in sample solution without added antibody, to account for nonspecific reactions occurring on the surface. At high concentrations of antibody, the signal appeared to plateau and reach equilibrium within the time frame of the experiment. However, at low antibody concentrations, the signal did not reach equilibrium within this time frame. Therefore, the equilibrium signal was determined by fitting the raw data for each concentration to the exponential equation: $y = A[1 - \exp(-k_{obs}t)]$, where y is the binding in nm, A represents the equilibrium signal, k_{obs} is the observed rate constant, and t is time. The equilibrium signal (A) as a function of the concentration was then fitted to a Langmuir isotherm $y = B[c/(K_D + c)]$, where K_D represents the binding affinity of the protein to p24, B is the saturation signal when all the available sites are occupied, and c is antibody concentration, assuming a 1:1 binding model. The kinetic on-rate constant, k_{on}, and off-rate constant, k_{off}, presented were defined by the equation $k_{obs} = k_{off} + k_{on} \times c$ and were determined as the slope (k_{on}) and intercept (k_{off}) of the linear regression performed on k_{obs} as a function of the concentration. Affinity constants were measured and analyzed by Mr. Benjamin Miller.

2.2.9 Preparation of PtNC-amplified lateral flow immunoassay

The lateral flow strips with polystreptavidin test line were manufactured by Mologic Ltd (UK). The strips were 33 mm long and 5 mm wide. The distance between the test line and the bottom of the strip was 7 mm. Clinical utility of assay was tested on human plasma from HIV Seroconversion Panel Donor No. 75062 (ZeptoMetrix Corporation, product code: HIV9079). Donor source plasma was collected from a U.S. licensed blood collection facility. Donor was un-treated and asymptomatic throughout the collection period. 50 µL of each panel member was run on PtNC LFA (outlined below).

All PtNC lateral flow assays for p24 detection were performed by submerging a polystreptavidin strip into a 96-well plate containing the following solution in each well: 10 µL of nanobody-biotin (200 nM), 50 µL p24 spiked into: FBS; plasma; or infected patient clinical plasma sample; and 15 µL PtNC antibody conjugate (300 pM). When the solution had fully

wicked up the strip (*ca.* 10 min), the strip was moved into another well filled with 100 µL *assay running buffer* for 3 min to wash through any residual serum (which may contain peroxidases that can also perform catalysis). Next, the strip was immersed in another well for 5 min filled with 330 µL (enough solution to cover test line on strip in well) freshly prepared *PtNC development solution* containing a modified Pierce CN/DAB (4-Chloro-1-naphthol/3,3´-Diaminobenzidine, tetrahydrochloride) Substrate Kit (Thermo Scientific) adjusted with hydrogen peroxide solution 30 % (w/w) (Sigma) to a final added peroxide concentration of 4 M. Finally, the strip was moved into a well containing 330 µL purified water for 1 min to stop the reaction. Strips were imaged with an iPhone 6 mobile phone camera for all experiments, except the clinical samples, which were imaged using a camera (Canon PowerShot G15) approved for use in contained environment for handling infectious samples. Images of strips were acquired 5 min after removal from the water.

2.2.10 Preparation of aged samples for accelerated stability testing

An accelerated aging test was carried out to simulate real-time shelf-life aging. All aging experiments were performed in a non-binding 96-well plate (Corning, UK). In each well, 15 µL of either PtNC-antibody conjugate (300 pM) or HRP-antibody conjugate (50 nM) in *particle storage buffer* was added, followed by 10 µL nanobody-biotin (200 nM) and 50 µL particle storage buffer. Plates were immediately frozen at -80 ºC for 30 min and freeze dried overnight. When removed from freeze dryer, plates were stored in a sealed plastic bag filled with silica bead desiccant at either room temperature or 44 ºC for accelerated aging study. Aging at 44 ºC for *ca*. 42 days is functionally equivalent to room temperature (23 ºC) aging for 6 months. Aging conditions were selected following guidelines of ASTM F1980 Standard Guide for Accelerated Ageing of Sterile Medical Device Packages and Westpak Accelerated Aging Time Calculator.[118,119] Accelerated aging techniques are based on the assumption that the chemical reaction involved in the deterioration of materials follow the Arrhenius reaction rate function, which states that a 10 °C increase in temperature will cause the reaction rate to double.
To examine long-term stability of reagents, 50 µL spiked serum or plasma was added to freeze dried reagents. After dissolution of reagents in sample, the strip was inserted into the well following the above protocol for wash and development (§2.2.9).

2.2.11 Structural model of nanobody

The structural model was predicted using the i-tasser webserver, http://zhanglab.ccmb.med.umich.edu/I-TASSER/, for the sequence provided.[120] The nanobody simulation was developed by Dr. Jennifer Brookes.

2.2.12 Image analysis of lateral flow test strips

Images of lateral flow strips were acquired using an Apple iPhone 6 and analyzed with ImageJ software.[121] ImageJ Gel Analyzer plug-in was used to plot intensity profiles of LFA strips and analyze test line intensities.

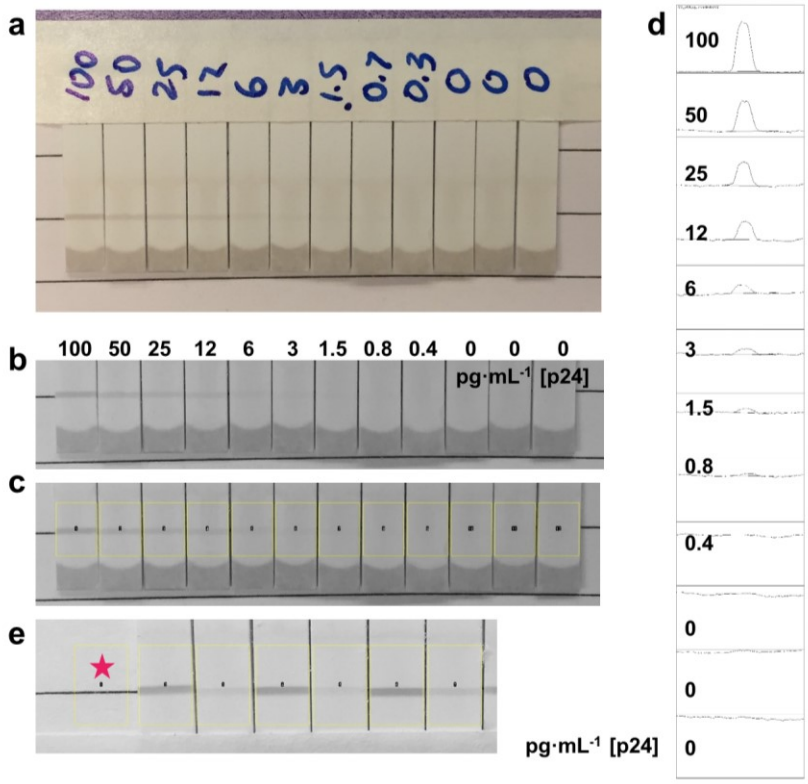


Figure 2.5 Image processing procedure for analysis of LFA strips. First, an image of the test strips was acquired using an iPhone 6 camera. Images were taken with test strips laid on the same area of a standard lab bench. One image from each independent experiment (n ≥ 3) was analyzed (a). Next, the image was imported into ImageJ software, and (b) converted to a 16-bit grayscale image. Next, using the Gel Analyzer function, rectangular regions surrounding the test line were selected (c). A rectangular region with a defined aspect ratio of 3:2 was used, with the width of the region spanning the test line on an individual strip, and the height being 1.5 times the width of the test line. The selected rectangular regions were analyzed using the Gel Analyzer function in ImageJ. In brief, the profile plots of the test lines were generated (d), peaks of interest were defined, and then the peak areas were measured using the Wand Tool. Peak areas corresponding to "test line signal intensity" were compared between test strips within a single image. For six week accelerated aging experiment, test line intensities were normalized to a standard line (e) (highlighted by the star), which was present in all images, to account for variation in lighting between time points.

2.3 Results & Discussion

2.3.1 Nanocatalyst composition

A variety of nanomaterials were investigated for potential use as catalytic labels in LFA: including iron oxide, manganese ferrite, palladium, iridium, platinum, and gold. Iron oxide, manganese ferrite, palladium and iridium nanoparticles were synthesized by collaborators Dr. Dokyoon Kim and Prof. Taeghwan Hyeon at Seoul National University, while platinum and gold nanoparticles were produced in-house. The elemental composition of nanomaterials was selected primarily on existing literature, where iron oxide nanoparticles,[34] Pd-Ir core-shell nanostructures,[53] and platinum nanoparticles[52] were reported to exhibit intrinsic peroxidase-like activity and high catalytic efficiency in biological environments. Pd-Ir nanostructures were of interest because of the recent work by Xia and coworkers[53] which showed that thin coatings of Ir on Pd cubes had significantly higher catalytic activity than Pd cubes alone and had the highest reported catalytic activity of peroxidase-mimics to date. In their study, density functional theory (DFT) modelling was used to calculate theoretical adsorption energies for key reaction species, which were found to be consistently more exothermic on Ir coated Pd compared to Pd surfaces alone, indicating that the Ir coating increased reactivity. It was proposed that the mismatch between Ir and Pd lattice constants can induce expansive strain which may also increase surface reactivity. Therefore Pd-Ir nanocubes with high catalytic activity were reasonable candidates for use as labels in LFA. While these nanomaterials have been used as peroxidase mimics in solution-based biosensing assays, this chapter investigates their use in a lateral flow assay configuration. Transmission electron microscopy (TEM) images in Figure 2.6 show the sizes and shapes of catalytic nanomaterials that were screened for use in LFA.

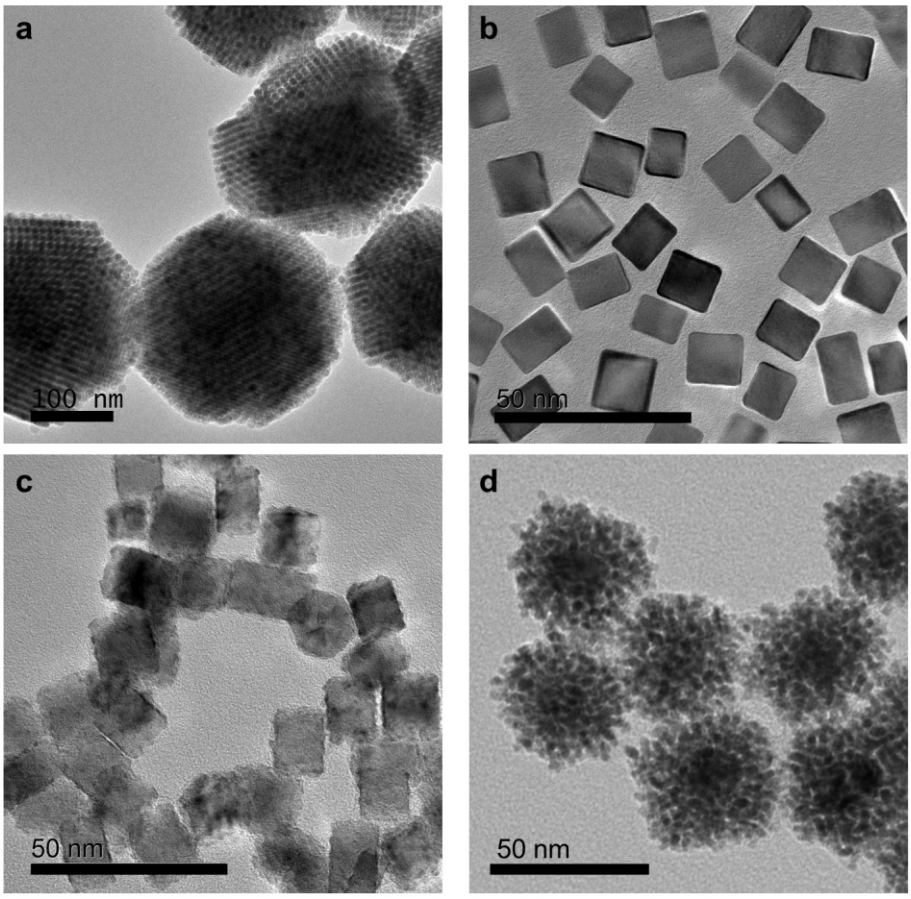


Figure 2.6 TEM images of catalytic nanoparticles (a) iron oxide clusters *ca*. 250 nm, (b) *ca*. 20 nm palladium nanocubes, (c) palladium nanocubes coated in a *ca*. 2 – 5 nm iridium shell, and (d) *ca*. 50 nm platinum coated gold core-shell nanoparticles with dendritic morphology.

To assess which composition to take forward for the development of the sensing system, the catalytic activity and size distribution of particle batches was investigated. The catalytic activity was measured using a peroxidase substrate commonly used to detect horseradish peroxidase (HRP) activity in enzyme-linked immunosorbent assay (ELISA) formats, 3,3',5,5'-tetramethylbenzidine (TMB). TMB is a chromogen that yields a blue color when oxidized to TMB diimine, typically because of oxygen radicals produced by the hydrolysis of H_2O_2 by HRP (Figure 2.7). TMB chromogen has maximal absorbances at 370 nm and 652 nm. To varying degrees, all the nanoparticle compositions screened exhibited the ability to disproportionate hydrogen peroxide and oxidize TMB in a concentration-dependent manner. While all compositions that were screened exhibited peroxidase-like activity in agreement with literature,[34,52,53] only the Pt coated Au nanoparticles could be synthesized with precise size control and in a reproducible and scalable manner.

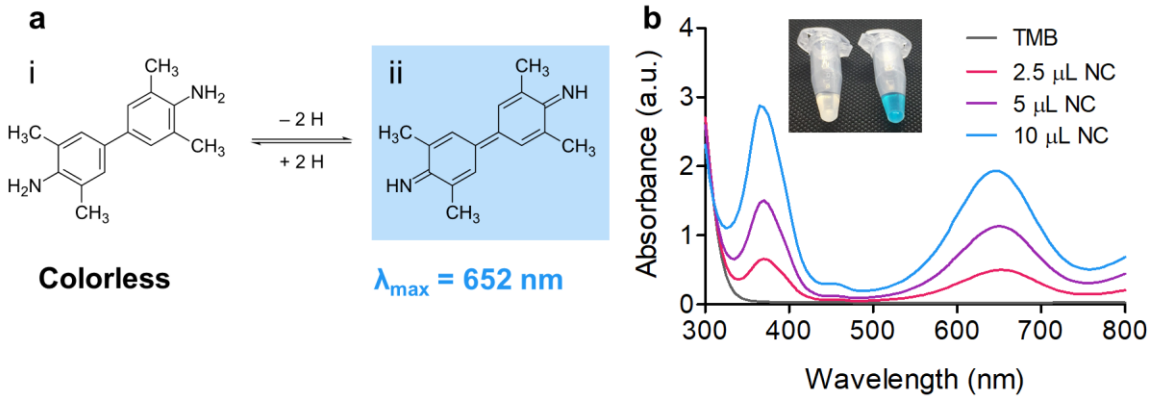


Figure 2.7 (a) Strucutre of 3,3',5,5'-tetramethybenzidine (TMB) (i), and oxidized TMB (TMB diimine) (ii). (b) Representative UV/vis spectra showing increase in absorbance correlated to oxidation of TMB in presence of varying concentrations of nanocatalysts (NC). An increase in absorbance at both 370 nm and 652 nm was observed for increasing concentration of NC with fixed concentration of TMB and H_2O_2 substrates.

As discussed in the seed-mediated synthesis section (§2.1.2.5), heterogenous nucleation allows for size control by varying the ratio of seed concentration to precursor concentration. While the Pd-Ir nanocubes were produced following the seed-mediated synthesis outlined by Xia and coworkers,[53,122] the resulting products exhibited high variability in shape and size. TEM images (Figure 2.8 a – d) show attempts at synthesizing Pd-Ir nanocubes of *ca*. (a) 10 nm, (d) 20 nm, (c) 35 nm, and (d) 50 nm in edge length. First, the synthesis of Pd cubes of varying sizes proved challenging as a variety of non-uniform shapes were produced. The variability is two-fold: in the synthesis of the Pd seed and in the deposition of iridium on Pd seeds. First, synthesis of well-defined Pd cubes is reported,[122] however small impurities and variations in reaction conditions can significantly affect the reduction kinetics, which can in turn affect the final shape. Here the synthesis by Xia and coworkers[122] was followed, where Pd cubes were synthesized with Na_2PdCl_4 precursor, L-ascorbic acid as the reducing agent, bromine ions as the capping agent to selectively promote growth of {100} facets, and PVP as a stabilizer for reaction at elevated temperatures (80 °C). While a population of cubic seeds was observed, a variety of other shapes including rods was also produced. In the discussion in the work of Xia and coworkers,[122] minor variations in injection rate of precursors and local reagent concentrations can lead to non-cubic shapes such as pentagonal rods, such as shown in Figure 2.8c. Maintaining cubic shape in production of larger Pd seeds was also challenging. Xia and coworkers[122] proposed that seeds tend to take a multiple-twinned structure to minimize the total surface energy of the system when reduction kinetics are fast, which is evident in the icosahedral shaped seeds observed in Figure 2.8d. Minor impurities or variations in concentrations of the capping agent would also affect the growth rates of the various facets and ultimately lead to different morphologies. Br^- ions should preferentially

chemisorb onto the {100} facets of Pd nanocrystals and thus favor the formation of Pd nanocrystals enclosed by {100} facets, adopting a bar or cube shape. With extremely precise control over all experimental conditions, Pd cube synthesis is possible, however, in practice it proved difficult to reproduce. Second, forcing iridium to adopt a layer-by-layer growth mechanism on Pd core was challenging due to its high cohesive energy relative to other noble metals (Table 2.2). Like Pt (§2.1.2.5.3), the high cohesive energy of Ir favors self-nucleation over a conformal coating. This is also observed in TEM images, where clear 1 – 5 nm irregularly shaped Ir particles can be observed surrounding the Pd seed instead of the desired uniform coating. To achieve a conformal coating, high temperatures (> 200 °C) are required to ensure fast surface diffusion of Ir atoms to promote the layer-by-layer growth mode on Pd surface.[123] For large Pd seeds, non-uniform island growth and irregular morphology dominates as surface diffusion of Ir atoms is not higher than the rate of atom deposition. Taken together, the polydisperse Pd-Ir nanocube synthesis route was not optimal for taking forward for further assay development. While the Pd-Ir cube synthesis could be optimized to produce atomically precise nanoparticles, ideally a synthesis method more amenable to minor variations and that could be scalable in-house was preferred.

Control of particle size is particularly critical for immunoassay development, as variability in particle synthesis will affect subsequent antibody modification steps and overall assay performance. Synthesis of platinum coated gold nanoparticles is well reported at mild reaction conditions (65 °C). Using established protocols with minor adjustments, excellent size control could be achieved by fixing the concentration of platinum precursor solution while varying the gold seed concentration.[52,110] The platinum coated gold nanoparticles served as a well-defined starting material for optimizing the use of catalytic nanoparticles in lateral flow and were thus chosen as the labels for the remainder of this chapter. Due to their catalytic activity, the platinum coated gold nanoparticles are further called platinum nanocatalysts (PtNCs).

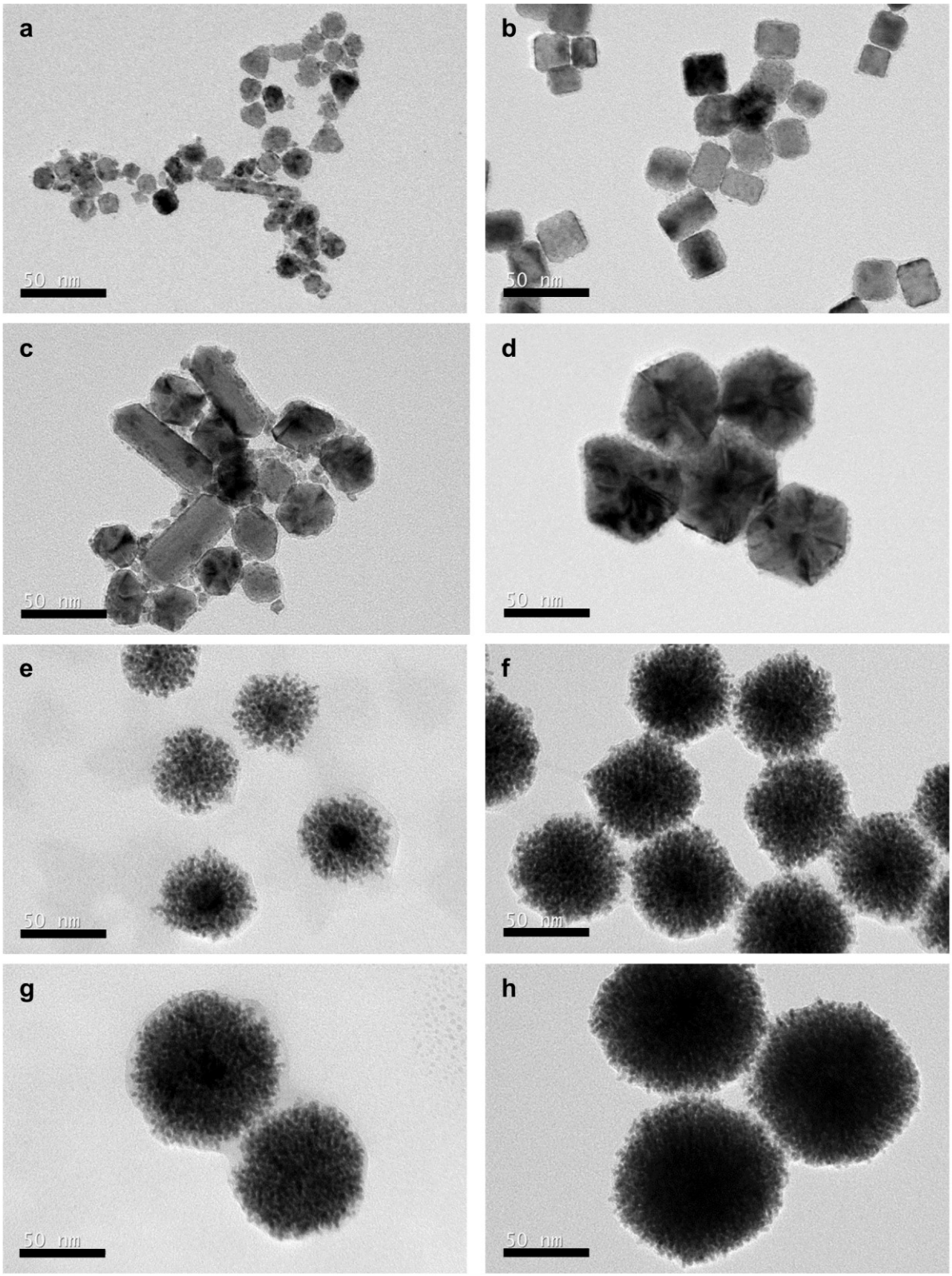


Figure 2.8 TEM images of (a – d) iridium coated palladium seeds (Pd-Ir) of varying sizes, and (e – f) platinum coated gold seeds of varying sizes. Scale bars, 50 nm.

It is important to note, that while this chapter focuses on the use of PtNCs in lateral flow assays, the irregularly shaped Pd-Ir nanoparticles (Figure 2.8d) were also optimized as labels

for detection of p24 in the same format. However, characterization of the Pd-Ir system was much more challenging due to morphological variations and aggregation compared to the monodisperse PtNC system, therefore only the latter is reported.

2.3.2 Synthesis and characterization of platinum nanocatalysts

To produce PtNCs with high catalytic activity and effective antibody modification, their synthesis required careful optimization. First gold seeds (*ca*. 15 nm) were produced through standard sodium citrate reduction of chloroauric acid following a method first introduced by Turkevich *et al.*[124] and refined by Frens.[125] The gold seeds were used as templates for heterogeneous nucleation of platinum by introducing polyvinyl pyrrolidone (PVP) as a polymeric stabilizing agent, L-ascorbic acid (in excess) as a reducing agent and fast injection of chloroplatinic acid (H_2PtCl_6) into a glass vial containing the gold seeds, and heating to 65 °C for 30 min (Figure 2.9a). The deposition of Pt could be readily achieved at relatively low temperatures (60 – 85 °C) and the reaction solution turned from red to black indicating successful deposition of Pt on Au seeds. Additionally, reagents could be injected into the reaction mixture using a pipette without the need for a syringe pump to control the rate of injection. The resulting PtNCs had a porous dendritic-like morphology stemming from the non-conformal growth mechanism of Pt on Au. The PtNCs exhibited a broad absorption spectrum, compared to the AuNP seeds, which exhibited a sharp surface plasmon resonance peak at 520 nm. Xia and coworkers[67] showed that ultrathin Pt-skins could be grown *via* a layer-by-layer mechanism on AuNP seeds to maintain the surface plasmon resonance peak even after Pt deposition by controlling the injection rate of precursors.[67] However, it was hypothesized that a porous morphology may be advantageous for enhancing catalytic activity by providing internal surface area for catalytic reactions, therefore conformal growth was not pursued.

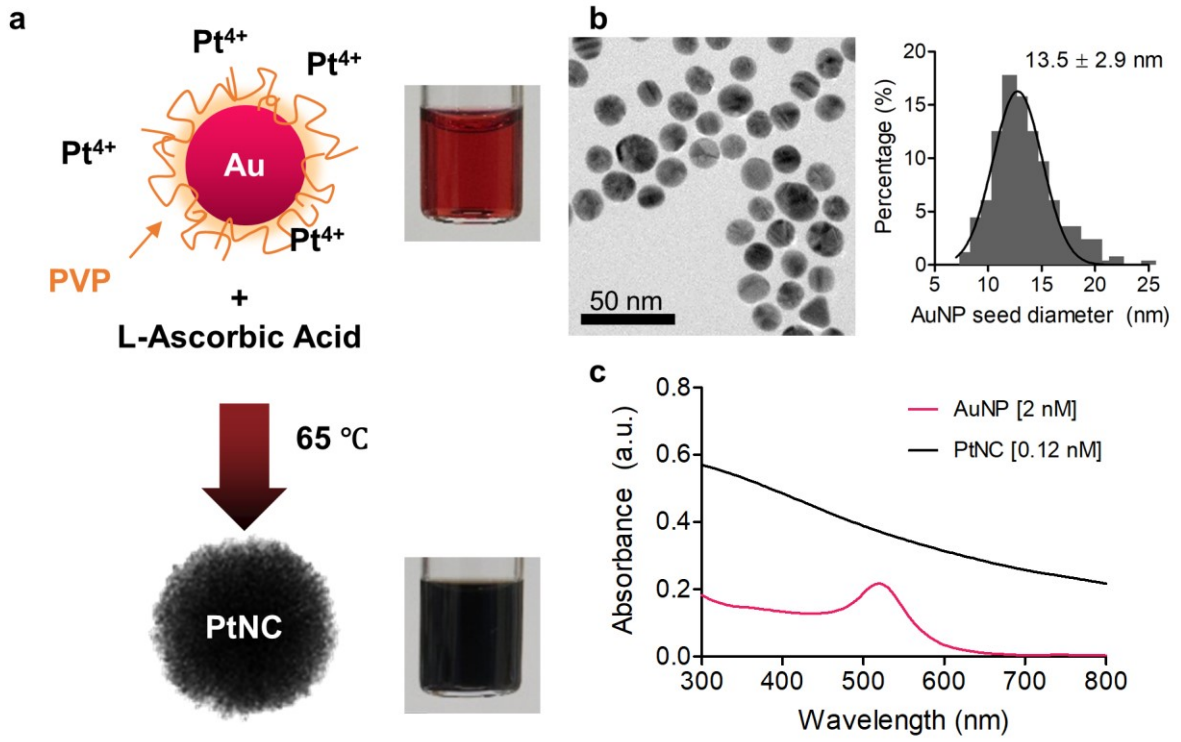


Figure 2.9 (a) Scheme showing synthesis of Au-Pt core shell structure (PtNC), where *ca*. 15 nm gold nanoparticles are used as seeds for subsequent platinum overgrowth in the presence of polyvinylpyrrolidone (PVP) as a stabilizer, and L-ascorbic acid as a reducing agent. (b) Representative TEM image of gold nanoparticle seeds. Scale bar, 50 nm. Histogram showing results of size analysis from TEM images (n ≥ 200 particles) where mean AuNP seed diameter is 13.5 ± 2.9 nm. (c) UV/Vis spectra of 15 nm gold nanoparticle seeds (2 nM, red) and *ca*. 90 nm PtNC (0.12 nM, black).

A similar aqueous-phase approach to synthesis of monodisperse platinum coated gold nanoparticles with "urchin-like" morphology was reported by Guo *et al.*[110] However, in their report, the synthesis was carried out at 100 °C, with the addition of ascorbic acid and H_2PtCl_6 without additional stabilizing agent. While at the appropriate temperature, this method produced stable colloids through accelerated reduction kinetics, the particle size range investigated was limited to 6 – 35 nm. Without the addition of a stabilizing agent, such as PVP, larger particle sizes were inaccessible using this synthesis route. Gao *et al.*[52] also reported synthesis of Pt coated gold nanoparticles using 55 nm AuNP seeds and produced Pt capped AuNPs of up to 70 nm in diameter, without stabilizing agents. In this case, the reducing agent was added in a dropwise fashion to control the reduction rate to prevent aggregation. The final concentration of H_2PtCl_6 in synthesis was low, presumably to also prevent aggregation.

In this chapter, the effect of a polymeric capping agent, polyvinylpyrrolidone (PVP) was investigated as a stabilizing agent during synthesis to widen the size range of nanoparticles accessible while maintaining a facile one-step synthesis. PVP of varying molecular weights

has been extensively used in the solution-phase synthesis of many types of colloidal particles where it is typically used as a steric stabilizer or capping agent to protect the product from undesired agglomeration.[126] Here, at the early stages of production, the particles were capped with PVP to ensure colloidal stability (Figure 2.10a – b) and to reduce the extent of fouling that occurs upon exposure to complex media during LFA. Under the experimental conditions for this synthesis, stable PtNCs could not be formed in the absence of PVP, where extensive aggregation and precipitation occurred, indicating that PVP is critical for stabilization during the reaction. The color change of the reaction solution from light red to black indicated the successful deposition of platinum on gold nanoparticle seeds.

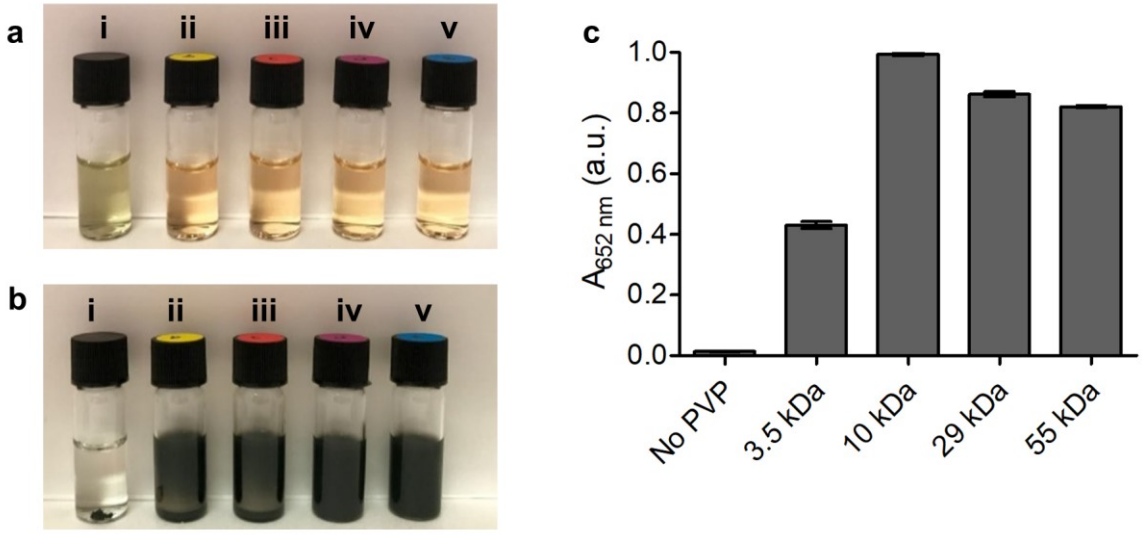


Figure 2.10 Images of PtNC reaction components containing varying molecular weights of PVP: (i) no PVP, (ii) 3.5 kDa, (iii) 10 kDa, (iv) 29 kDa, (v) and 55 kDa; before (a) and after heat treatment (b) for 30 min at 65 °C. (c) Influence of PVP molecular weight on PtNC catalytic activity, measured by the absorbance at 652 nm corresponding to the oxidation of TMB by H_2O_2 (n = 3). In the absence of PVP, significant aggregation occurred.

The molecular weight of PVP used during the particle synthesis played an important role in dictating the catalytic activity of the PtNCs as highlighted by their ability to oxidize TMB with 10 kDa PVP-capped particles performing optimally (Figure 2.10c). The role of PVP could be two-fold here. PVP acts to stabilize the particles to allow for growth of a monodisperse population and may also function as a mild reducing agent, which may aid in controlling the reduction rate of the synthesis.[114] Because of the high stability of the particles with PVP capping, they could be produced at scale, which is essential for commercial applications. For example, the concentration of H_2PtCl_6 in synthesis was 20 times higher than that used in the report by Gao *et al.,* where PVP was not used.[52] This enables the synthesis of larger and higher concentration particles with ease of handling while retaining monodispersity.

Ye *et al.*[114] reported that PVP also increases the peroxidase-like activity of platinum nanocubes. Pt cubes are typically synthesized in the presence of capping agents to promote the presentation of Pt{100} facets for nanocube formation. It was found that introducing 55 kDa PVP as a stabilizer into the nanocube synthesis could significantly increase peroxidase-like activity, compared to synthesis in the absence of PVP. This could be due to the packing of PVP on the Pt surface. For example, if PVP loosely packs on the Pt surface, the surface is exposed and more accessible to the substrate TMB, resulting in enhanced catalytic efficiency. The increased packing density of lower molecular weight PVP (3.5 kDa) could be an explanation for the decreased activity observed for these PtNCs (Figure 2.10c). As packing density of the PVP would be expected to increase with lower molecular weight polymer, the accessibility of TMB to the Pt surface is expected to decrease, leading to a decrease in catalytic efficiency. Ye *et al*. also found that Pt spheres synthesized with 55 kDa PVP without a capping agent specific to promote nanocube growth exhibited similar catalytic efficiency to the cubes, implying that Pt{111} surface is as active as Pt{100} (presented preferentially on cubes) toward the disproportionation of hydrogen peroxide. This is important to note as the spherical PtNCs produced in this chapter are likely to adopt primarily {111} facets to minimize total surface energy, where for an fcc metal (*e.g.* platinum) the surface energies increase in the order $\gamma\{111\} < \gamma\{110\} < \gamma\{100\}$.[109] In the presence of PVP, stable dispersions that were resistant to washing and long term-storage were obtained.

It has been well established that the activity of catalytic nanoparticles has a strong correlation with spatial arrangement and coordination number of atoms located in the outer-most layer, which is largely determined by faceting.[109] Future work will examine the effect of incorporating other capping ligands and stabilizing agents into PtNC synthesis, to examine the effect of shape and atomic arrangement on peroxidase-like activity. Additionally, use of other common reducing agents, including L-ascorbic acid (used here), citric acid, sodium borohydride, or PVP as a mild reducing agent could affect the final structure and thus catalytic properties which is of interest for further investigations.

High resolution TEM images (Figure 2.11) highlighted the porous dendritic morphology of the Pt shell in PtNCs. As described above, this morphology may be due in part to the high cohesive energy of platinum which favors non-conformal deposition on the AuNP seed. Xia and coworkers[67] found that when H_2PtCl_6 was injected quickly into synthesis, like the strategy adopted in this chapter, the fast reduction kinetics resulted in a nucleation burst and subsequent formation of small Pt clusters which agglomerate on the AuNP surface resulting in a “cluster-type” shell. Alternatively, when the H_2PtCl_6 and ascorbic acid were added slowly in parallel to the gold dispersion *via* a double-jet syringe pump approach, the concentration of

reactants in the system at any moment was maintained below the threshold for burst nucleation.[67] In the latter case, the platinum atoms can be slowly deposited on the gold surface forming a continuous shell. Adopting the fast injection approach of Pt precursors, PtNCs could be produced with porous platinum shells. Selected area electron diffraction patterns taken from a single PtNC reveal diffraction spots consistent with polycrystalline platinum with an fcc lattice and highlight the range of surface facets exposed that could participate in catalytic reactions (Figure 2.11d).

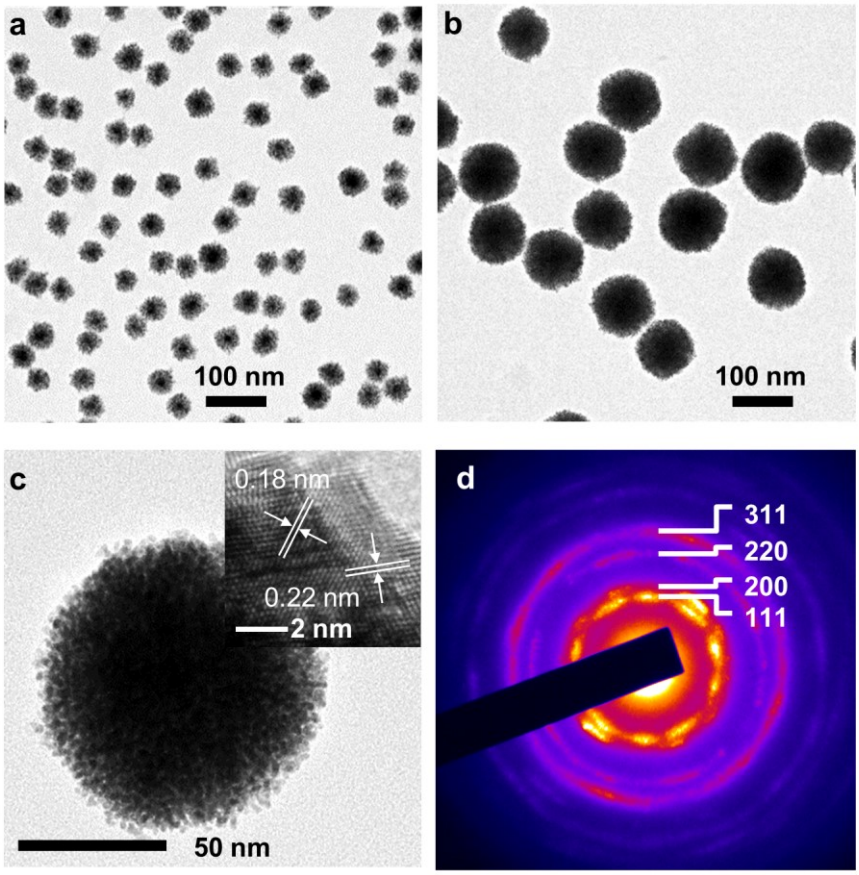


Figure 2.11 Transmission electron micrographs of PtNCs synthesized with varying AuNP seed concentrations to control size: (a) 5 nM seeds and (b) 0.3 nM seeds. (c) High-resolution TEM image of an individual PtNC formed from 0.3 nM seed concentration. Inset shows the lattice fringes corresponding to platinum {111} and {200}. (d) Selected area electron diffraction (SAED) patterns taken from a single PtNC (120 nm) with diffraction spots consistent with polycrystalline platinum with an fcc lattice.

Energy-dispersive X-ray spectroscopy (EDS) mapping revealed Au at the particle core when the Pt shell was thin (*ca*. 50 nm PtNC) (Figure 2.12). However, Au was not detected for larger 100 and 200 nm PtNCs where the Pt shell was thicker.[59] For the 50 nm PtNCs, Au was clearly present in the interior while Pt was distributed across the entire particle, indicating a core-shell structure. The origin of the porosity in the platinum shell is of great interest. The work by Roy

et al.[127] and Xia and coworkers[67] suggested that the porosity stems from platinum islands first forming through homogeneous nucleation under the rapid growth conditions and due to the high cohesive energy of Pt, followed by agglomeration on the gold surface. This growth mechanism resulted in a rough topology, which may have promoted the filamentous and porous structures observed in the PtNCs.

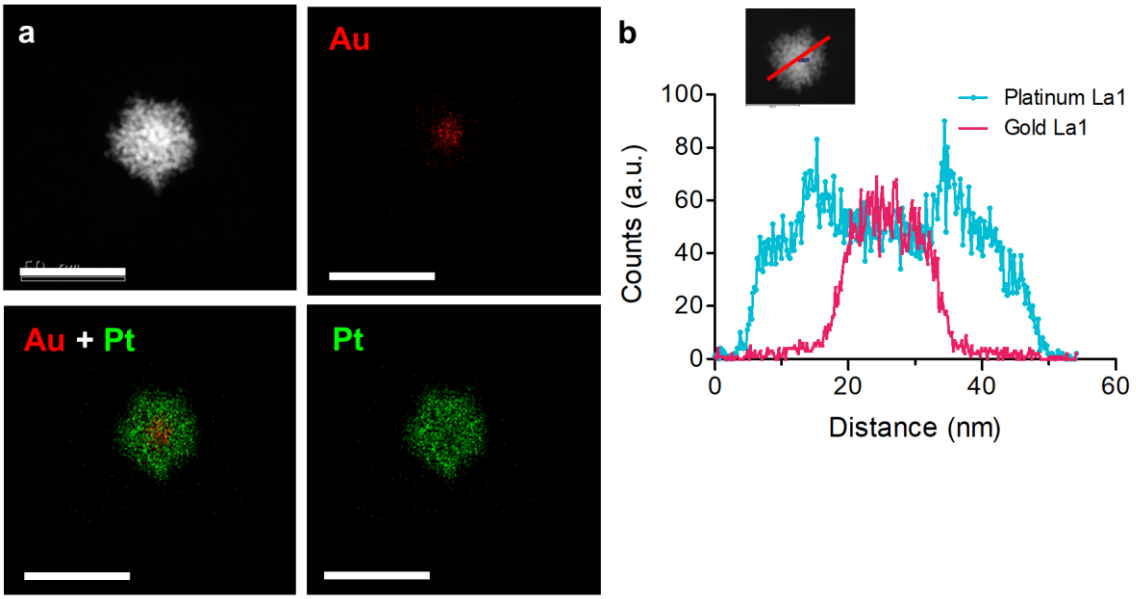


Figure 2.12 (a) Energy Dispersive X-ray (EDS) mapping of the elemental distribution of Au (red) and Pt (green) for 50 nm PtNCs (scale bar, 50 nm). (b) EDS line scan profile recorded along the central axis of an individual 50 nm PtNC further confirming core-shell structure. STEM imaging and EDS mapping was performed with Dr. Shweta Agarwal.

Nanoparticle size optimization is a significant consideration when developing catalytic nanomaterials for LFA, since the surface area, catalytic efficiency, diffusivity and propensity for multivalent nonspecific binding must all be carefully tuned by tailoring particle shape and size. TEM images (Figure 2.13) show the precise control over PtNC size and monodispersity possible using the seeded synthesis. Using a seed-mediated synthesis with *ca*. 15 nm AuNP seeds, monodisperse PtNCs could be produced ranging in size from 40 – 120 nm, by fixing the platinum concentration and varying the concentration of the AuNP seeds. Larger PtNCs could be produced by depositing a second or third layer of Pt using as-synthesized 120 nm PtNCs as seeds for the overgrowth of subsequent Pt layers. With this method, monodisperse PtNCs were produced over the size range of 40 – 280 nm diameter (Figure 2.13).

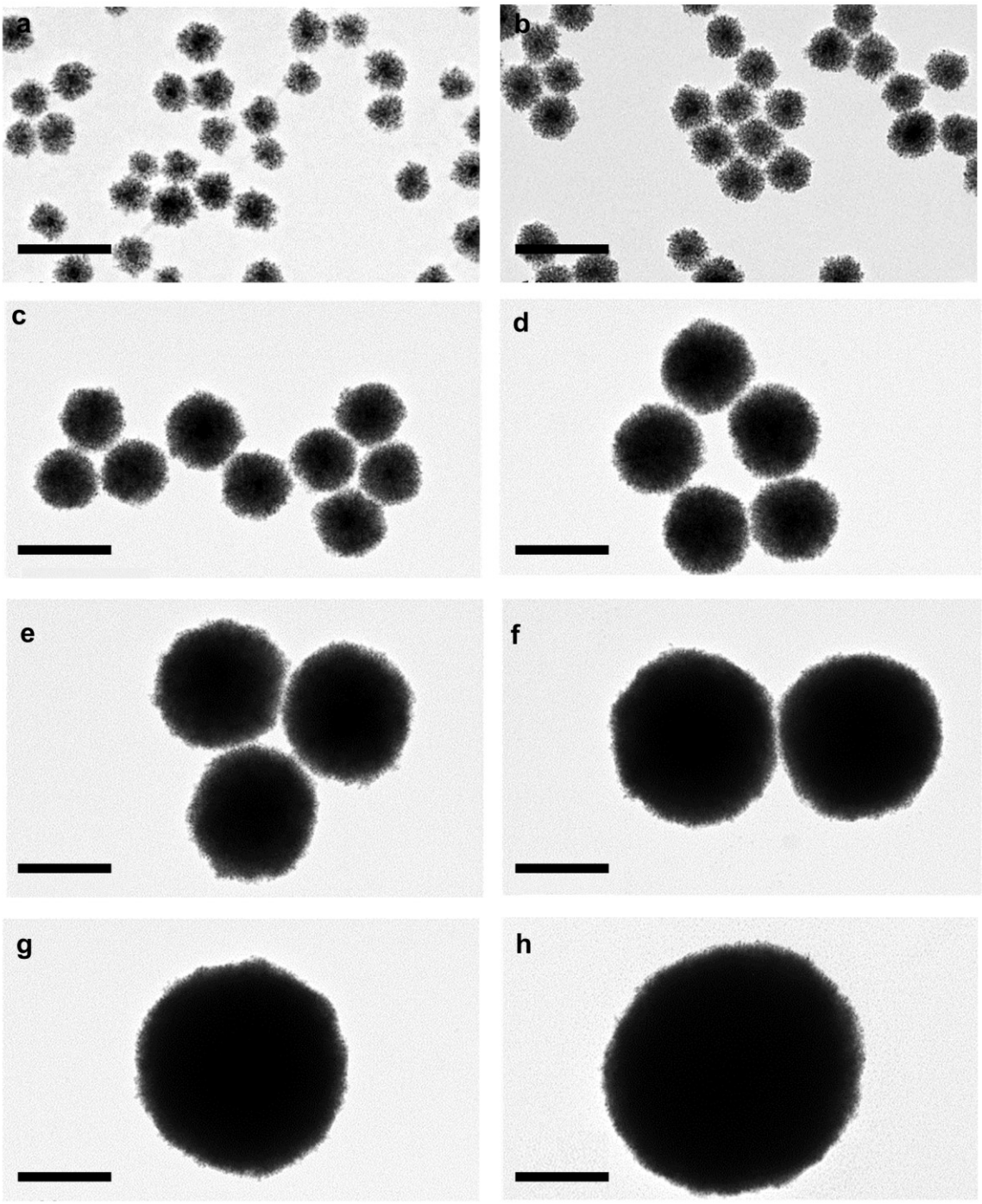


Figure 2.13 TEM images of PtNCs formed by varying [Au]: [Pt]. Batches were synthesized in presence of different gold nanoparticle seed concentrations: (a) 5 nM, (b) 2.5 nM, (c) 0.6 nM, (d) 0.3 nM, (e) 150 pM of 120 nm PtNCs as seeds, (f) 75 pM of 120 nm PtNCs as seeds, (g) 40 pM of 120 nm PtNCs as seeds, (h) 20 pM of 120 nm PtNCs as seeds. Scale bars a-h, 100 nm.

Dynamic light scattering (DLS) was used to measure the hydrodynamic diameter and polydispersity of PtNC batches. Thanks to the well-defined concentration of nucleation points (seeds) for overgrowth with platinum, the polydispersity index (PDI) as measured by DLS was maintained at a low level (0.01<PDI<0.1) for all PtNC sizes produced, ensuring reproducibility

in their synthesis (Figure 2.14a). The fine size control of this seeded synthesis allowed for control over subsequent antibody modification and investigation of size dependent catalytic properties and performance in LFA. Larger particles exhibited higher catalytic activity toward disproportionation of hydrogen peroxide and oxidation of TMB substrate, as measured by the absorbance at 652 nm (Figure 2.14b).

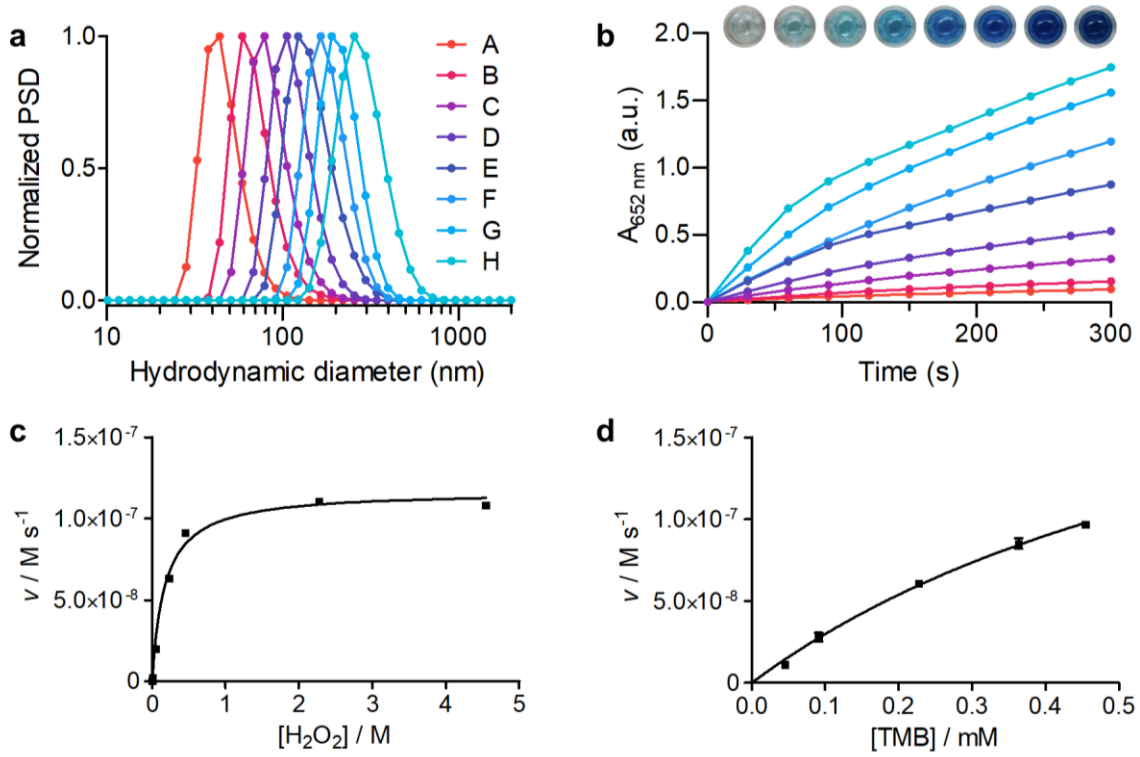


Figure 2.14 (a) Number particle size distribution (PSD) of the hydrodynamic diameter of PtNCs formed by varying [Au]:[Pt] measured by dynamic light scattering. Batches were synthesized in presence of different gold nanoparticle seed concentrations: A – 5 nM, B – 1.2 nM, C – 0.6 nM, D – 0.3 nM, E – 0.15 nM, F – 0.08 nM, G – 75 pM of 120 nm PtNCs as seeds, H – 40 pM of 120 nm PtNCs as seeds. (b) Kinetic measurement of oxidation of TMB in presence of a fixed concentration of PtNCs of varying diameter (following color scheme in part (a)). Inset, photo of the blue-colored product (oxidized TMB) generated through the reaction catalyzed by PtNCs. (c – d) Steady-state kinetic assays of 120 nm PtNCs as catalysts for the oxidation of TMB by H_2O_2. The initial reaction velocity (v) was measured in 25 mM sodium acetate buffer pH 4.0 with 9.1 x 10^{-15} M PtNCs at room temperature over 150 seconds. Error bars indicate standard deviation of three independent measurements. (c) Plot of v against H_2O_2 concentration, in which TMB concentration was fixed at 0.45 mM. (d) Plot of v against TMB concentration, in which H_2O_2 was fixed at 2.3 M.

The catalytic efficiency was further investigated through steady-state kinetics assays using 120 nm PtNCs as a model size, and the data was fit to the Michaelis-Menten model (**Equation 2.1**) to obtain kinetic parameters (Table 2.3). The k_{cat} of PtNCs (10^7 s^{-1}) is four orders of magnitude higher than HRP (10^3 s^{-1}), perhaps due to the presentation of multiple reaction sites on the surface of the PtNCs compared to the single reaction site for HRP. The apparent K_m

value of the PtNCs with H_2O_2 as the substrate was significantly higher than that for HRP, consistent with the observation that a higher concentration of H_2O_2 was required to observe maximal activity for the PtNCs. PtNCs required three orders of magnitude higher peroxide levels than their biological counterpart. Thus, in the following assays in both solution and on paper, peroxide concentrations of 2 – 4 M were used in activity measurements. The $k_{cat\text{-}specific}$ considers the catalytic efficiency normalized to surface area, where surface area here was calculated using the particle diameter from TEM assuming a non-porous shell. The PtNCs show $k_{cat\text{-}specific}$ within the same order of magnitude as Pd-Ir nanocubes, which have been reported to have the highest catalytic activity of peroxidase-mimics to date.[53]

Table 2.3 Comparison of kinetic parameters of catalysts toward the oxidation of TMB by H_2O_2

Catalyst	[*E*] / M	Substrate	K_m / M	V_{max} / M s^{-1}	k_{cat} / s^{-1}	$k_{cat\text{-}specific}$ / s^{-1} nm^{-1}
PtNC (120 nm)	9.1×10^{-15}	TMB	8.1×10^{-4}	2.7×10^{-7}	3.0×10^{7}	661.3
PtNC (120 nm)	9.1×10^{-15}	H_2O_2	1.7×10^{-1}	1.2×10^{-7}	1.3×10^{7}	287.5
Pd-Ir (19.2 nm)[53]	3.4×10^{-14}	TMB	1.3×10^{-4}	6.5×10^{-8}	1.9×10^{6}	859.0
Pd-Ir (19.2 nm)[53]	3.4×10^{-14}	H_2O_2	3.4×10^{-1}	5.1×10^{-8}	1.5×10^{6}	678.2
HRP[34]	2.5×10^{-11}	TMB	4.3×10^{-4}	1.0×10^{-7}	4.0×10^{3}	-
HRP[34]	2.5×10^{-11}	H_2O_2	3.7×10^{-3}	8.7×10^{-8}	3.5×10^{3}	-

[E] represents the catalyst concentration, K_m is the Michaelis-Menten constant, V_{max} is the maximal reaction velocity, k_{cat} is the catalytic constant the equals V_{max} /[E]. $k_{cat\text{-}specific}$ represents the specific catalytic efficiency that is derived by normalizing k_{cat} against the surface area of an individual catalyst.

2.3.3 Effect of PtNC size and porosity on catalytic activity

The size dependent catalytic activity of PtNCs was further assessed in solution. For particles with a non-porous shell, catalytic activity was expected to scale with surface area and for a fixed particle concentration, larger particles were anticipated to exhibit higher catalytic activity in proportion to their relative surface area (Figure 2.15). While this trend of increasing activity with increasing PtNC diameter held true, when the activity was normalized by surface area, the activity deviated significantly from what was expected if activity was solely proportional to surface area. The increased activity for PtNCs in the 100 – 150 nm size regime above the expected surface area scaling indicates the availability of internal surface area due to the porous nature of the Pt shells (Figure 2.16). The increase in catalytic activity with porosity

appears to plateau for particles > 150 nm, which were produced *via* a layer-by-layer approach using 120 nm PtNCs as seeds for subsequent Pt deposition. The decreased porosity could be due to the secondary platinum layers forming more conformal coatings on Pt rather than Au due to differences in cohesive energies and more favored deposition of Pt on preformed Pt shell because of lattice matching. Because of this effect, the layer-by-layer synthesis was expected to produce a denser platinum shell, which is less accessible to H_2O_2. Therefore, the larger PtNCs produced through layer-by-layer synthesis did not benefit from increased catalytic activity due to internal porous surface area. Instead they exhibited activity that scaled more closely with surface area, as would be expected for a non-porous shell. Brunauer-Emmett-Teller (BET) theory is used to study the adsorption of gas molecules on solid surfaces and can be used as an analysis technique for the measurement of specific surface area of materials.[128] Ideally BET analysis, which is commonly used to measure the specific surface area of catalysts in the field of heterogenous catalysis, would be useful to compare porosity of various PtNC formulations. However, material scale is a limitation of this technique, where the expense of platinum reagents limits the production of gram scale batches required for analysis. While BET analysis has not yet been widely adopted by the field interested in designing enzyme-mimetic nanoparticles, particularly peroxidase mimics, this could be an important technique for establishing specific surface area and pore size analysis parameters on which to compare catalytic efficiencies between “nanozyme” formulations in this emerging field.

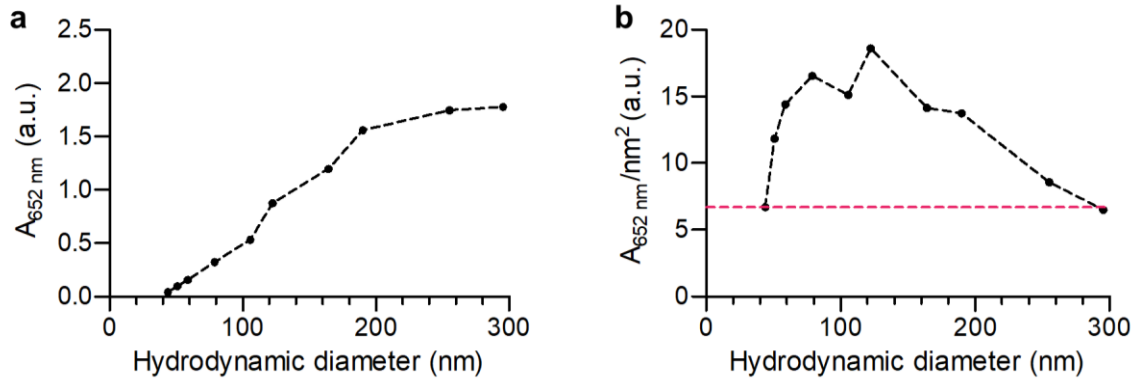


Figure 2.15 (a) Catalytic activity measured by the absorbance at 652 nm corresponding to the oxidation of TMB by H_2O_2 for PtNCs of fixed concentration and varying hydrodynamic diameter (*ca*. 40 – 280 nm). (b) Activity from (a) normalized to surface area. Red dotted line indicates theoretical value if activity scaled solely with surface area.

TEM was also used to compare differences in porosity between varying sizes of PtNCs (Figure 2.16). Nanoscale roughness appeared unchanged for varying sizes, but the density of Pt dendrites increased when the layer-by-layer synthesis was used to produce PtNCs (Figure 2.16d – e). This was consistent with the observation that activity of the larger particles scaled with surface area, correlating to lower porosity.

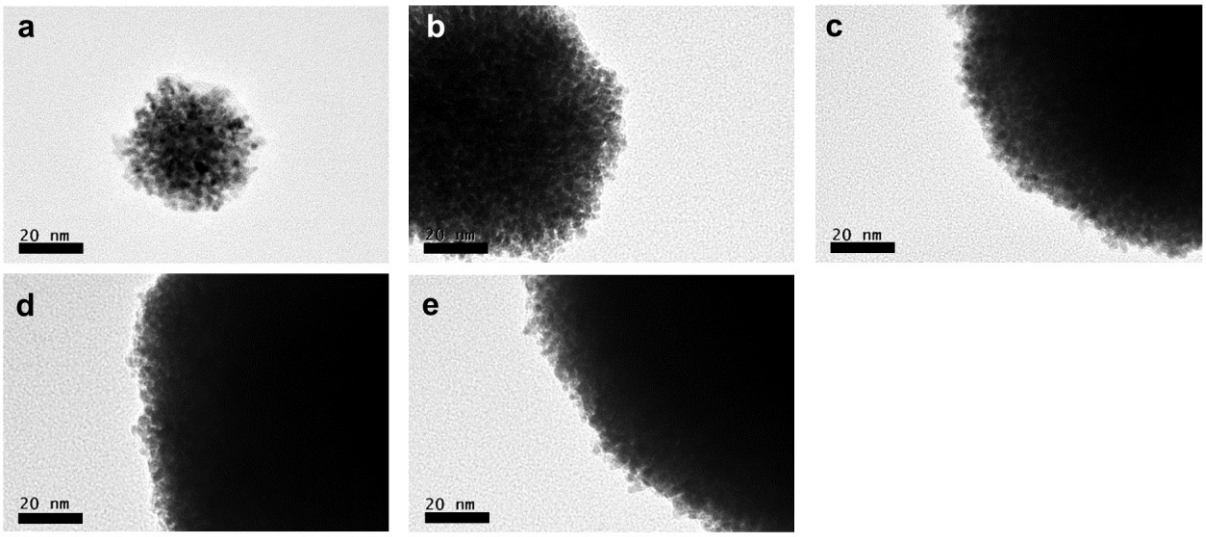


Figure 2.16 TEM of nanoscale roughness of PtNCs produced using seeded synthesis for particles of average diameter measured by DLS (number distribution): (a) 50 nm, (b) 120 nm, (c) 180 nm, (d) 215 nm, (e) 280 nm. Scale bars a-e, 20 nm.

High-angle annular dark-field STEM (HAADF-STEM) images of PtNCs of representative sizes (50 nm, 100 nm, and 200 nm) with corresponding energy dispersive X-ray point spectra (EDS) confirmed presence of platinum shells across all sizes (Figure 2.17). The intensity line profiles provided additional evidence for the increased density of Pt when the layer-by-layer synthesis approach was used to produce PtNCs ≥ 150 nm. The contrast in HAADF-STEM is sensitive to the atomic (Z) number contrast and therefore dark contrast regions in particles highlight the porosity within the Pt shell. The dark contrast regions were significantly reduced in the 200 nm PtNCs, indicating a reduction in porosity (Figure 2.17c). This reduction in porosity could also be observed in the intensity line profiles across HAADF images, where higher density platinum (lower porosity) was observed at the periphery of 200 nm PtNCs produced through a layer-by-layer synthesis approach (Figure 2.17f).

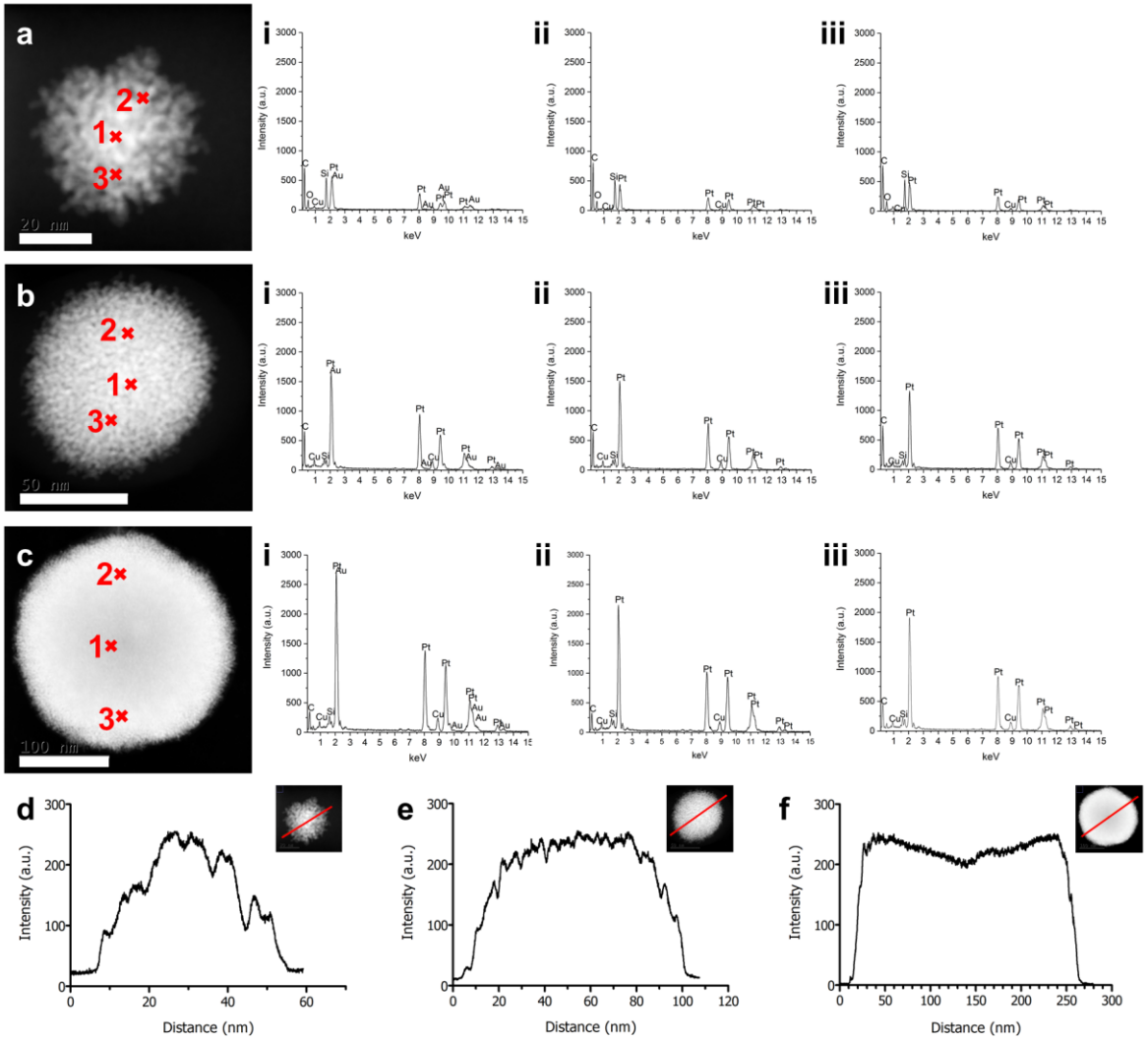


Figure 2.17 High-angle annular dark-field STEM (HAADF-STEM) images of (a) 50 nm (scale bar, 20 nm), (b) 100 nm (scale bar, 50 nm), and (c) 200 nm (scale bar, 100 nm) PtNCs with corresponding Energy Dispersive X-ray point spectra (EDS) (i – iii). Au is observed in the core for all sizes, while Pt is confined to the shell, confirming the core-shell structure. Intensity line profiles across HAADF images for (d) 50 nm, (e) 100 nm, and (f) 200 nm PtNCs. STEM imaging and EDS mapping was performed with Dr. Shweta Agarwal.

To examine the effect of internal porosity of the Pt shell on catalytic activity, a series of experiments were designed to modulate the Pt shell thickness and monitor changes in activity. It was hypothesized that the internal porosity of the shell contributed to the overall activity of PtNCs. To investigate this further, PtNCs were produced with varying AuNP seed diameters with equivalent external diameters. It was expected that if internal porosity was contributing to overall activity that particles with equivalent external diameters but smaller AuNP cores would exhibit higher activity due to the contribution from the larger porous Pt shell. Indeed, it was observed that there was a significant contribution to the PtNC catalytic activity arising from the internal catalytic surface area of the particles, which was assessed by varying the diameter of the gold core (Figure 2.18). For particles with either 90 nm or 120 nm external diameters, the

PtNCs synthesized with 15 nm cores exhibited higher activity, due to the increase in porous shell volume compared to PtNCs of equivalent external diameter with 40 nm core (Figure 2.18b). This additional surface area is accessible through nanometer-scale pores (*ca.* 1 – 2 nm by TEM image analysis) within the platinum shell. This rendered the pores inaccessible to larger molecules (*e.g.* antibodies and serum proteins), but accessible to smaller molecules such as H_2O_2. This indicated that they would be well suited for use in catalytic amplification in protein-rich serum environments. There was a two-fold increase in activity due to the use of a 15 nm core compared to a 40 nm core (Figure 2.18b). H_2O_2 can likely access a fraction of the additional surface area afforded by the larger volume of porous Pt shell, however further investigation of internal porosity should be performed using tomography or focused-ion beam milling to interrogate the internal structure. Overall, the porous structure of the Pt shell is advantageous because it provides greater active surface area for catalytic reactions. This will be of interest to probe further with BET analysis and advanced electron microscopy techniques.

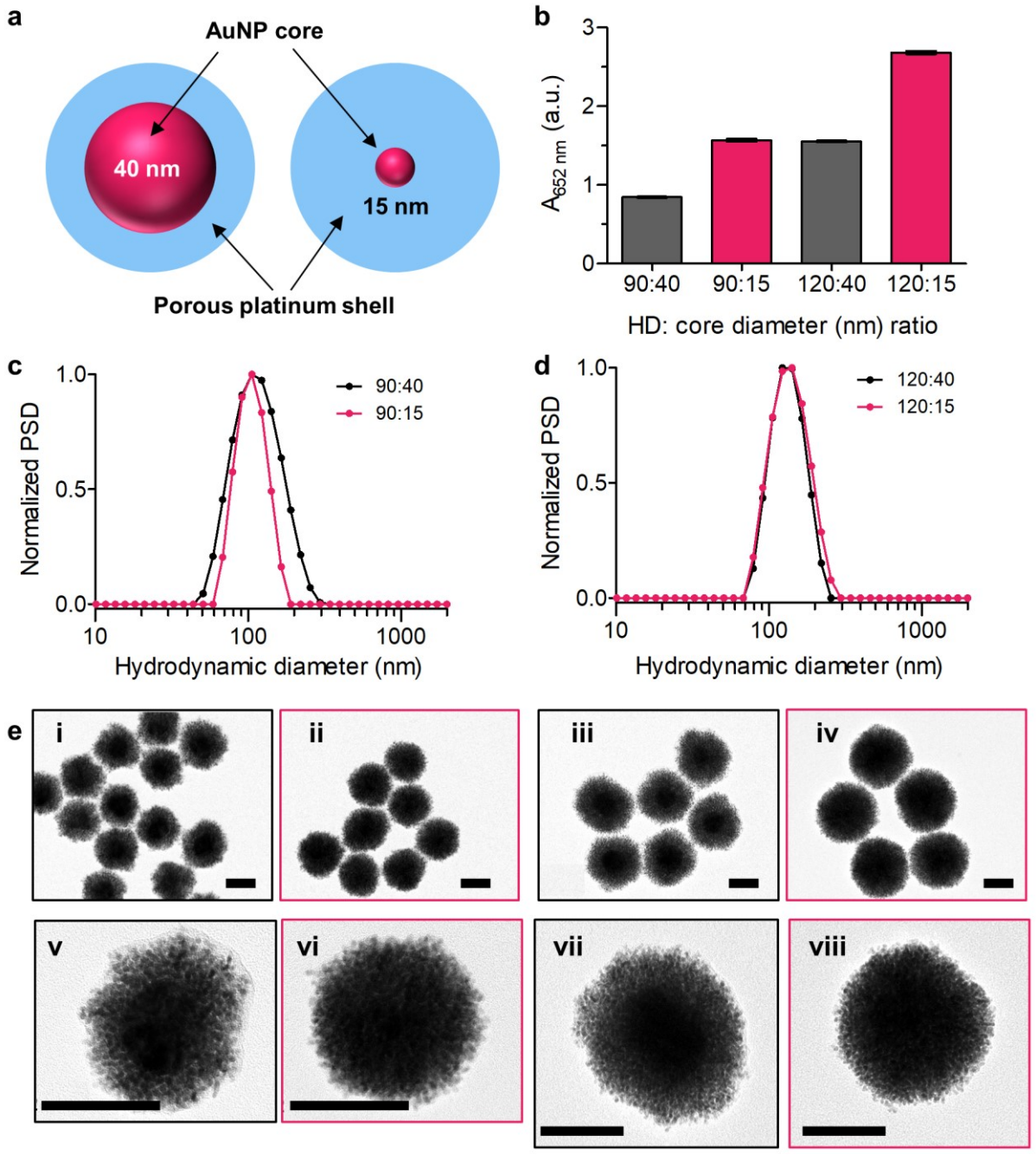


Figure 2.18 (a) Schematic illustration of PtNCs synthesized using two different AuNP core sizes: 40 nm and 15 nm. The thickness of the porous shell (blue) can be effectively modulated by maintaining the external hydrodynamic diameter of the particle but varying the core size (red). (b) Catalytic activity measured by the absorbance at 652 nm corresponding to the oxidation of TMB by H_2O_2 for 90 nm and 120 nm PtNCs synthesized using 40 nm (black) or 15 nm (red) AuNP core sizes. Error bars represent standard deviation from three independent experiments. DLS measurements showing normalized particle size distribution (intensity) for (c) 90 nm or (d) 120 nm external diameter (hydrodynamic) with either 15 nm (red) or 40 nm (black) AuNP core diameter. (e) TEM images of PtNCs with varying hydrodynamic diameter to core diameter ratio: (i, v) 90:40, (ii, vi) 90:15, (iii, vii) 120:40, and (iv, viii) 120:15 (nm). Scale bar is 50 nm.

2.3.4 Physiological stability

A key performance requirement for the use of the PtNCs in biosensing systems is that they must retain their catalytic activity following exposure to complex environments, such as patient serum, which contains *ca*. 7 wt% protein. To investigate this, PtNCs were modified with antibodies through physisorption, blocked in 1 wt% β-casein protein solution, washed to remove unbound antibodies, and then incubated with either fetal bovine serum (FBS) or human plasma pool for 30 min (maximum time frame of exposure in diagnostic test scenario) or 12 h. A catalytic activity assay was then run on the samples to measure the percent activity retained compared to bare PtNCs which had incubated in water for the same time (Figure 2.19). Unsurprisingly, the PtNCs lost a significant amount of activity after antibody modification (*ca*. 75 %). Since the catalytic activity is related to the surface area available for catalytic reactions, any proteins binding to the PtNC surface will result in a reduction in activity. Though once modified with antibodies, no further loss in activity was observed for PtNC-Ab conjugates exposed to serological environments. The difference in incubation time in serological environments, either 30 mins or 24 h, was also not significant. From this study, it appeared that most of the activity was lost in the antibody modification stage, and that once the surface was saturated with proteins, no further losses in activity were observed in subsequent serological incubations. While a significant portion of activity was lost during the antibody modification step, encouragingly the remaining *ca*. 25 % of PtNC activity was stable and could be retained and exploited for further catalytic amplification even in serological environments.

The retention of activity in serological environments may be due in part to the internal surface area of the porous Pt shell, which provided a significant increase in catalytically active internal surface area. Due to a pore size smaller than the size of proteins, these catalytic sites were inaccessible to protein fouling. Therefore, even after the external surface becomes passivated by proteins, hydrogen peroxide is still able to access the internal surface area through the nanopores without inhibition. After incubation of the PtNCs with proteins, the catalytic centers on the PtNC outer surface become blocked and passivated through protein physisorption, leaving predominately the internal porous surface area available for catalytic reactions. The higher magnification TEM images of the nanoscale roughness (Figure 2.16) indicated that the pore sizes were in the range of *ca*. 1 – 2 nm, which is too small for the larger serum proteins to penetrate (R_h *ca*. 3 – 5 nm). While protein physisorption to the outer surface of PtNCs reduces activity (Figure 2.19), the porous shell still retains a significant amount of internal activity toward peroxide disproportionation and would be an interesting direction for future study. Ideally, a polymer capping strategy could be implemented during synthesis that would

result in PtNCs that retain full activity even after incubation in protein-rich environments. This could be an avenue for further investigation.

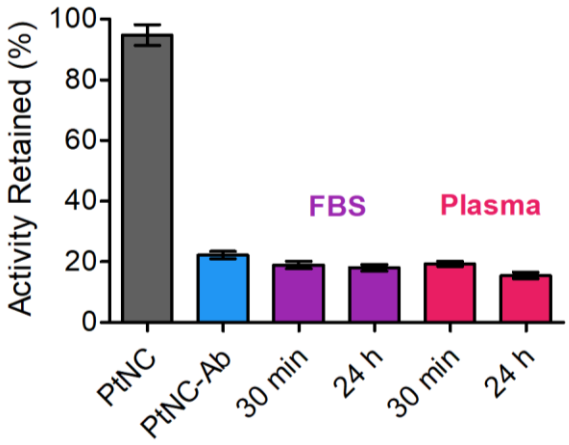


Figure 2.19 Catalytic activity of PtNCs (bare), antibody modified PtNCs (PtNC-Ab) and PtNC-Ab incubated in serological environments up to 24 h (n = 6).

2.3.5 Lateral flow test optimization and architecture to support catalytic amplification

This section describes the optimization process to build a sensitive lateral flow assay. The test was designed with the requirements that it must retain simplicity for use in PoC settings, achieve high sensitivity for protein detection (low femtomolar regime), and return a colorimetric result that can be read by eye within 15 min of sample collection.

There are many components that require optimization in the design of a high sensitivity LFA. The LFA optimization process includes; selecting the appropriate biomarker, antibody pair, nanoparticle detection label, conjugation conditions, nitrocellulose membrane, running buffer, sample volume, and overall conditions that favor positive signal and reduce nonspecific interactions. While many of these parameters were considered during assay development, a few of the key optimization steps are outlined in this section. A dipstick format was used for optimization, where the reagents were added to a 96 well plate, mixed with the sample and run up the test strip (without sample pad or conjugate pad). For optimization, visual scoring (based on analysis of test line intensity) was used to triage parameters and down-select efficiently to the most promising parameters, which simultaneously aimed to increase positive signal while minimizing background nonspecific signal.

In LFA test development, it was critical to begin triaging parameters in the lateral flow format and in the final sample matrix (serum or plasma). While typically antibody pairs and detection labels are screened by ELISA, the requirements for LFA performance are often very different and not always compatible. ELISA has long incubation times where reactants can reach equilibrium, compared to LFA where binding to the test line must occur within seconds. Because of the short contact times, antibody affinities and mobilities of the detection label have a large impact on test result. It is important to optimize reaction parameters in the target sample matrix, in this case serum or plasma. Sample matrices are complex and optimization specific to the matrix is required to minimize sample variation by employing relevant blocking agents and detergents.

For initial optimization of LFA, three key components were prepared: nitrocellulose membrane with capture reagents, nanoparticle-antibody conjugates, and appropriate buffers. The capture affinity ligand was striped onto the nitrocellulose membrane by industrial collaborator Mologic Ltd. While a variety of affinity ligands can be used as capture agents, here a polymeric formulation of streptavidin was selected to create a generic test strip, which can be optimized for capture of a variety of biotinylated components. Appropriate antibody or other affinity components must be conjugated to the nanoparticle for use as detection labels in the assay.

A running buffer that allows for the flow of the nanoparticle conjugates through the nitrocellulose membrane must be carefully selected. The running buffer was optimized empirically by triaging a variety of reagents. Commonly used running buffers include varying proportions of blocking proteins (BSA, β-casein), polymers (PVA, PVP), surfactants (Tween-20, BRIJ-35) and sugars (sucrose, trehalose) that can aid in sample flow through and wetting of the membrane. Additionally, the pH and buffer composition must be optimized to reduce NSB between specific antibody pairs while maintaining stability of the nanoparticle conjugates. The running buffer reported in this chapter was composed of 0.2 wt% β-casein and 0.1 wt% Tween-20 in pH 7.2 50 mM phosphate buffer (§2.2.4). Casein, which is a third the size of BSA was selected over BSA due to its ability to more efficiently cap the PtNCs to prevent nonspecific adsorption to surfaces after antibody modification.

In moving toward accessing the PtNC catalytic amplification in a paper-based platform, it was necessary to optimize peroxidase substrates for catalytic development in a lateral flow format. The peroxidase substrate TMB is useful for assessing the catalytic activity of PtNCs in solution. However, since both TMB and oxidized TMB are soluble, it is not suitable for use in LFA formats. Where catalytic nanoparticles have been used in LFA to date, there are several substrates that have been tested.[65,66] They typically involve selecting membrane staining, precipitating colorimetric substrates for HRP, notably diaminobenzidine (DAB) and chloronaphthol (CN) formulations. Several commercial peroxidase substrates have been optimized for detection of HRP in western blot, immunohistochemistry, immunoblotting and tissue staining applications, which require the oxidized product to be insoluble so that the chromogen sticks on the membrane for detection. Most of these pre-formulated solutions contain *ca*. 1 mM H_2O_2, which is the optimal reaction condition for HRP. Since the PtNCs perform optimally at much higher peroxide concentrations, the substrate had to be adapted for use with the PtNCs by spiking the pre-formulated substrates with H_2O_2 to a final concentration of 4 M, which in some cases can elevate nonspecific background staining. Three substrates were investigated for use with PtNCs in LFA: (a) CN/DAB, (b) DAB, and (c) a membrane-optimized precipitating TMB formulation (Figure 2.20). First, biotinylated PtNCs (120 nm diameter) were run up a lateral flow test strip bearing a streptavidin test line. Next, the strip was immersed in the peroxidase substrate spiked with 4 M H_2O_2 (development solution) for 5 min. CN/DAB displayed a dark black precipitate at the test line, DAB had a brown product, and TMB provided a dark blue product. The TMB substrate (Figure 2.20c) was poorly resolved and appeared to be partially soluble, not adequately staining the test line and instead wicking up the membrane. The combination of DAB and CN (CN/DAB) (Figure 2.20a) seemed to have a synergistic effect that resulted in greater sensitivity than DAB alone and was selected as the optimal substrate for further development of the PtNC LFA.

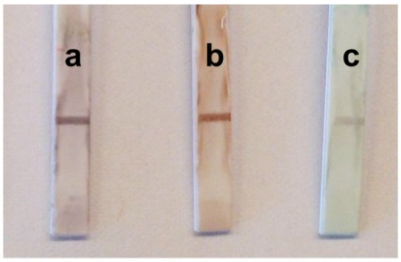


Figure 2.20 Representative image of LFA strips where biotinylated PtNCs are bound at the streptavidin test line. The nitrocellulose membranes were treated with peroxidase substrates for 5 min (a) CN/DAB (black) (b) DAB (brown), and (c) TMB (blue).

CN/DAB has a partially soluble substrate and insoluble product. While the black precipitate is easy to detect by eye, the partially soluble substrate presents a challenge as it does not flow through the nitrocellulose membrane by capillary action. Therefore, the strip must be immersed in the development solution fully above the test line so that the test line can be in direct contact with the substrate. A substrate that is fully soluble and has an insoluble product would be more desirable and would exhibit higher reaction kinetics and improved sensitivity. While the existing commercial substrates have been optimized for membrane blotting and HRP detection, there is significant room to develop better chromogenic substrates specifically optimized for inorganic catalysts in LFA applications. An optimized chromogenic substrate specific to lateral flow will be key in exploiting the sensitivity of the PtNC amplification system.

The LoD of PtNCs as labels in LFA was assessed by preparing biotinylated PtNC conjugates (PtNC-biotin) and running varying concentrations of PtNC-biotin (120 nm selected as representative size) up LFA strips bearing a streptavidin test line followed by CN/DAB development (Figure 2.21). PtNC-biotin conjugates were prepared by physisorption of BSA onto the surface of PtNCs, and subsequently labelling the BSA with biotin through lysine modification. Considering the avidin-biotin complex is the strongest known non-covalent interaction ($K_D \approx 10^{-15}$ M) between a protein and ligand,[112] this served as an efficient platform to determine the absolute limit of detection (LoD), assuming all particles are efficiently captured at the test line. When antibody-antigen or other affinity ligands are introduced into the system, the LoD can be adversely affected by a variety of other factors including nonspecific and weaker biomolecular interactions (*e.g.* higher dissociation constant, lower K_{on}) which will hinder test sensitivity. In this format, 10 µL of PtNC-biotin (varying concentrations) was mixed with 30 µL running buffer and run up the strip followed by CN/DAB catalytic amplification (5 min development). The lowest detectable signal was produced by 25 fM PtNC-biotin concentration for a 10 µL particle volume.

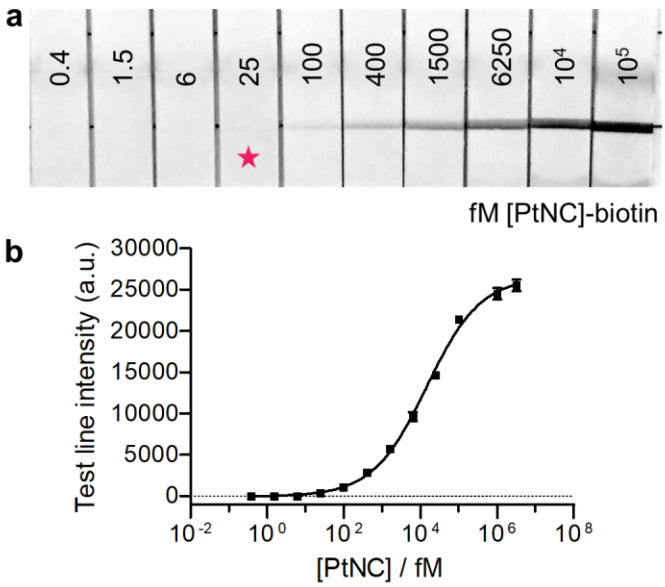


Figure 2.21 (a) Image of LFA test strips with varying concentrations of PtNC-biotin bound at the test line after CN/DAB catalytic development. (b) Plot of test line intensity (from image analysis) against PtNC-biotin concentration. Dotted line represents background signal.

The test strips containing high concentrations of PtNC-biotin bound at the test line were analyzed using scanning electron microscopy (SEM) to visualize the structure of the LFA membrane and the local distribution of PtNCs within the test line region. The strips were diagonally cut at the test line, mounted on a SEM stub, and coated with a thin layer of chromium (10 nm) for imaging. The PtNCs were clearly present in the test line region as evidenced by the bright particles (*ca*. 120 nm) against the dark matrix (Figure 2.22). In secondary electron mode, the atomic number sensitivity creates contrast in the image where higher atomic number inorganic nanoparticles appear bright against the dark low atomic number matrix, in this case bright PtNCs against the dark nitrocellulose membrane.

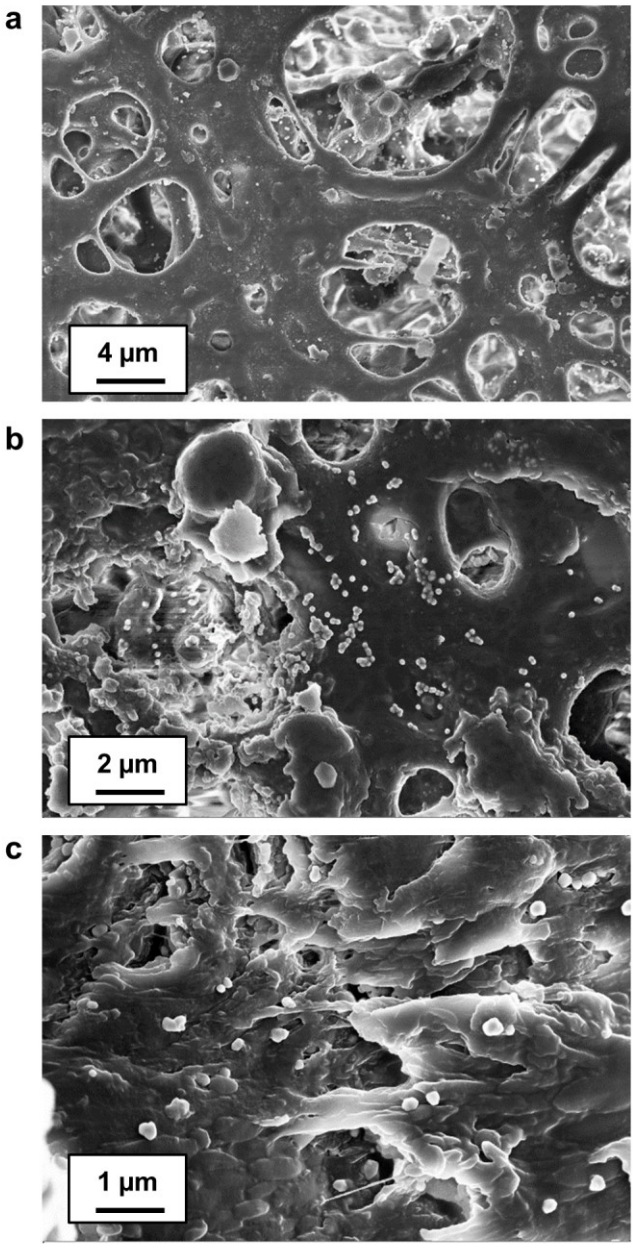


Figure 2.22 (a – c) Scanning electron microscopy (SEM) images of biotinylated PtNCs bound on the streptavidin coated membrane. SEM imaging was performed with Dr. Eunjung Kim.

Capillary flow rate is a critical performance parameter in LFA and thus requires optimization through membrane selection. The formation of immunocomplexes at the test line depends on the finite period of time that the components are sufficiently close at the molecular level to bind, which is dictated by the capillary flow rate. The flow rate of nitrocellulose membranes is a function of pore size (typically several to tens of microns) and is reported as capillary rise (s/40 mm), referring to the time required for water to vertically traverse 40 mm.[84] Membranes with two different porosities were tested: Satorius UniSart CN-95 (65 – 115 s/40 mm) and CN-140 (95 – 155 s/40 mm). The CN-140 flow rate is slower than the CN-95 because it has a smaller pore size. Generally, a slower flow rate would result in higher sensitivity (and longer

time to result) because of the increased length of time that the components of the reactive pair are close enough to bind. However, if the system exhibits any nonspecific binding (NSB), then this NSB signal will be elevated in the slower running membrane. Figure 2.23 shows a plot of test line signal intensity for the same sample when run up membranes presenting different pore sizes. It is common in manufacturing LFA devices to pre-block the nitrocellulose membrane with blocking buffers that can include sugars, polymers, proteins and surfactants. Blocking the membrane can help prevent NSB and produces a chemically uniform surface. Nitrocellulose membranes bind proteins through a combination of electrostatic and hydrophobic forces through interaction of nitrate esters with peptide bonds within the protein. While this is useful for loading the test line with affinity reagents, it could cause unwanted and nonspecific protein adsorption if not adequately blocked. Common membrane blocking agents are BSA, gelatin, casein, PVA, and PVP. PVP (1 wt%) and sucrose (1 wt%) were tested here. After the polystreptavidin was spotted on the test line and dried, the CN-95 membranes were blocked either by immersing the strips into a combined PVP/sucrose mixture or by separately immersing the strips first into a PVP solution followed by a sucrose solution in a two-step procedure. While the slower running CN-140 membrane exhibits higher test line signal than unblocked CN-95, the two-step PVP/sucrose blocking procedure resulted in comparable test line signal while maintaining its faster flow rate (and thus shorter time to result). The CN-95 membranes produced a result within 12 min, whereas slower running CN-140 required 18 min. Two-step blocked CN-95 membranes were taken forward for assay development due to their balance of fast flow rate and low NSB.

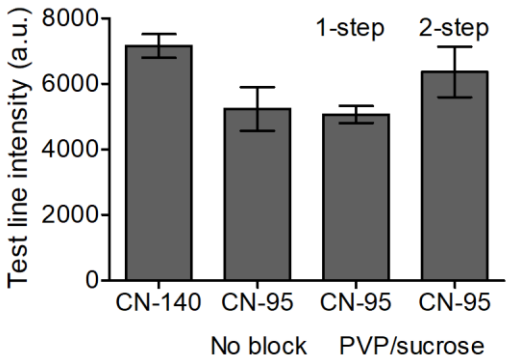


Figure 2.23 Test line intensity for lateral flow test strips prepared with different blocking formulations and membrane porosity. For a fixed sample volume of 50 µL, CN-140 membrane required 18 min for test result, while CN-95 membranes required 12 min.

2.3.6 Antibody modification and conjugation of affinity reagents

In development of the sandwich-style lateral flow assay, two affinity components that could simultaneously bind to the target analyte, p24, with high sensitivity and specificity were

required. In this chapter, an antibody fragment (nanobody) and conventional antibody were previously screened by Gray *et al*.[115] and selected as a high affinity binding pair for p24 detection. For the assay design, one affinity component must be biotinylated to act as an anchor to the streptavidin test line, and the other affinity component must be physically adsorbed onto the PtNC for capture of the target. Here the conventional antibody was selected for adsorption onto the PtNC, and the nanobody was site-selectively biotinylated.

Figure 2.24 outlines the site-selective modification strategy used to prepare robust antibody fragments with oriented biotin presentation in the assay. Thermally robust and high-affinity nanobody components were integrated into the nanocatalyst-labeled LFA. Nanobodies are single domain antibody fragments that contain a complete antigen binding site but are one tenth the size of a conventional antibody (§1.3.1). In addition to their small size and stable conformation, they can be efficiently mass produced in bacteria with site-selective mutations that enable biorthogonal chemistry.[23,98] A p24-binding nanobody validated against a broad spectrum of HIV subtypes was selected as a binding pair for use in the LFA. Because of the ease and control over nanobody modification and purification, the p24 nanobody was selectively biotinylated to facilitate PtNC-analyte complex binding to the streptavidin test line (Figure 2.24).[115]

An anti-p24 nanobody containing a solvent-accessible terminal cysteine residue was expressed to enable site-selective biotinylation. The position of the cysteine residue, at the end of a flexible 6-mer HIS-tag linker, was chosen to maximize the distance between the subsequent modification and the paratope of the nanobody (structural model in Figure 2.24), thus minimizing disruption.[115] Site-selective biotinylation of the cysteine residue was achieved through reaction with a biotin-functionalized pyridazinedione (PD), the first example of nanobody modification using PD chemistry.[59] Analysis of the nanobody post-modification using mass spectrometry confirmed addition of only a single molecule of biotin, evidencing no undesirable off-target conjugation. Pyridazinediones have a proven track record in antibody modification, and hold many advantages over other cysteine-selective reagents such as maleimides and haloacetamides, which have been shown to react with lysine residues and often display poor long-term stability.[129–132] Through this approach, the nanobody was engineered to present biotin away from the p24 binding region, enabling oriented presentation in the assay.

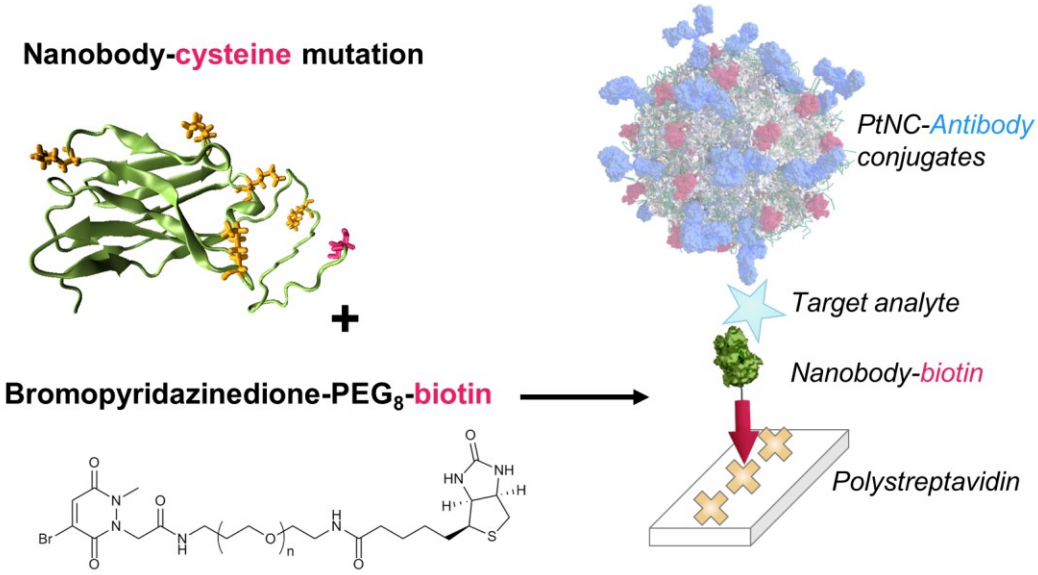


Figure 2.24 Scheme for site-selective chemical modification of a nanobody with an exposed cysteine mutation (red), where lysine residues are highlighted in orange on the structural model (left). Site-selective biotinylation of the cysteine residue (red) on the nanobody was achieved through reaction with bromopyridazinedione-PEG_8-biotin. Cartoon (right) of oriented elements at the streptavidin test line, where the star represents p24 and the PtNC is labeled with a monoclonal anitbody (blue) that binds a different region of p24 than the biotinylated nanobody. Nanobody simulation was developed by Dr. Jennifer Brookes, and nanobody site-selective modification was performed by Dr. Daniel Richards.

The binding kinetics of the modified and unmodified nanobodies with p24 were assessed. The site-selective modification had no significant impact on the equilibrium dissociation constant (K_D), confirming that the modification does not interfere with the antigen binding region (Table 2.4). The values of K_D extracted from the Langmuir fit were compared with the values of K_D obtained by dividing k_{off}/k_{on} (extracted from linear fit of k_{obs}), as this tests how well the data fit the Langmuir model (§2.2.8). The difference between these values may be explained by the potential deviation from the Langmuir adsorption model, which assumes a 1:1 biomolecular interaction. Bivalent molecules, such as antibodies, can potentially interact with two antigen molecules when the antigen, *e.g.* p24, is immobilized on the surface. These avidity effects can create non-ideal binding profiles and result in an artificially high affinity measurement.[117]

Table 2.4 Affinity constants for components used in PtNC-labeled LFA.[⊥]

Antibody-p24 Complex	k_{off} (s^{-1})	k_{on} ($M^{-1}s^{-1}$)	K_D (M) (k_{off}/ k_{on})	K_D (M) Langmuir Adsorption model
Nanobody (59H10)	4.3 (3.3-5.2) $\times10^{-4}$	1.6 (1.5-1.8) $\times10^{5}$	2.7×10^{-9}	2.0 (1.3-2.6) $\times10^{-9}$
Nanobody-biotin	4.0 (2.7-5.3) $\times10^{-4}$	1.6 (1.3-1.9) $\times10^{5}$	2.5×10^{-9}	3.0 (2.6-3.5) $\times10^{-9}$
Capricorn 1/2	2.4 (1.6-3.3) $\times10^{-4}$	4.3 (3.6-5.0) $\times10^{4}$	5.6×10^{-9}	2.1 (1.9-2.3) $\times10^{-9}$

[⊥]Each biophysical parameter is shown with the corresponding 95 % confidence interval indicated in brackets. The k_{on} and k_{off} were determined from the observed reaction rate, k_{obs}. The K_D was determined either by calculation of k_{off}/k_{on} or from fits of the experimental data using the Langmuir Adsorption isotherm (1:1 binding model). Affinity constants were measured by Mr. Benjamin Miller.

The site-selectively biotinylated nanobody circumvents the nonspecific modification of the nanobody paratope, which is rich with lysine residues (highlighted in orange in the nanobody model in Figure 2.24), where standard carbodiimide crosslinker modification strategies will risk interfering with the binding site and thus knock out activity. The site-selective biotinylation of the cysteine presenting nanobody preserves epitope recognition and ensures efficient use of the p24 available in the sample. While incorporating a nanobody pair into the LFA platform would be of interest, a p24 binding nanobody pair was not available, so monoclonal antibodies were screened as binding partners to the nanobody-biotin. The monoclonal antibody (mAb), anti-HIV-1/2 (Capricorn products), which is a p24 binding pair with the nanobody-biotin, was selected to physically adsorb onto the nanocatalysts.[115] It was important to select a monoclonal antibody over a polyclonal antibody, so that all antibodies were structurally identical and recognize a single epitope on the antigen for reproducible assay production. A challenge with polyclonal antibodies is that they can potentially recognize multiple epitopes on an antigen which could overlap and interfere with the binding epitope of the nanobody.

Optimization was required to conjugate the monoclonal antibody onto the PtNC surface. Physical adsorption was selected for modifying PtNCs with antibodies over chemical crosslinking, as the latter involves modification of the surface of the protein, which may disrupt binding performance. Physical adsorption is also a scalable and efficient way to produce PtNC-antibody conjugates, where mixing the PtNCs with antibodies in the correct stoichiometry and at an appropriate pH yields PtNCs with efficiently conjugated antibodies. Physical adsorption of proteins to noble metal nanoparticle surfaces is commonly used in biosensing applications, and is a well-established technique to prepare nanoparticle conjugates in both industry and academia.[133,134] The mechanism of physical adsorption is based on electrostatic, hydrophobic and van der Waals interactions between the protein and

nanoparticle surface, where pH can alter the association dynamics and effect conjugation efficiency. Therefore, a pH titration and antibody loading sweep was performed to optimize the conjugation conditions (Figure 2.25). Physical adsorption is optimized slightly above the isoelectric point (pI) of the antibody, where the protein exhibits net electrical neutrality. A slight positive charge on the antibody would promote physisorption to the negatively charged particle through electrostatic interactions but can also induce aggregation through crosslinking of the particles, so pH must be carefully balanced. In the absence of available information on the pI for the anti-HIV mAb tested here, the optimal conjugation conditions were determined empirically. For anti-HIV mAb, pH 6 was optimal for conjugation resulting in the highest test line signal intensity in the range of pH 5 – 8 (Figure 2.25a). The time for physisorption was also investigated (Figure 2.26a). This process happens quickly, where within 30 min to 3 h antibodies have physisorbed onto the PtNCs. Longer incubation times (24 h) did not significantly improve test line signal, so 3 h was set as the incubation time for conjugation. After antibody physisorption, β-casein was added to the PtNC-Ab conjugates. β-casein is a blocking agent used to mask any remaining sites of potential particle-particle or particle-protein interactions, preventing aggregation and NSB during the assay.

Once optimal pH and timeframe for physisorption was determined, the optimal antibody loading density was investigated. An excess of antibody to nanoparticle surface area was typically used to ensure dense surface binding and nanoparticle stability post conjugation. After PtNC incubation with varying concentrations of antibodies at pH 6 for 3 h, the particles were centrifuged and the concentration of antibody in the supernatant (unbound fraction) was measured using a Thermo Scientific Micro-BCA (bicinchoninic acid) Protein Assay Kit. Interestingly, it was observed that when particles were incubated in a large excess of antibodies (4 times excess to maximal surface coverage), the loading efficiency was decreased. PtNCs loaded with a sweep of antibody concentrations were tested in LFA to determine which formulation produced the highest test line signal and highest signal to noise ratio (lowest background signal) (Figure 2.25b – c). The best performing PtNC-Ab formulation was found to have a surface concentration of antibodies representing a monolayer (*ca*. 430 mAb per 120 nm diameter PtNC). Antibody coverage densities were calculated using the cross-sectional area of the antibody assuming a *ca*. 10 nm diameter protein, and surface area of PtNC sphere (using Z-average diameter from DLS). This monolayer antibody coverage was achieved by incubating particles with a 2-fold excess of antibodies with respect to PtNC surface area. When incubating PtNCs with a > 2-fold excess of antibodies with respect to surface area, the antibody coverage density decreased, perhaps due to crowding and sub-optimal packing densities due to steric hindrance.[135] The test line signal was quantified using the ratio of the intensity of the test line (for 50 pg·mL^{-1} p24 spiked FBS) to the intensity of the

test line for the blank sample (background). Test line signal intensity from the blank control sample indicates nonspecific binding. Test line to background ratio was highest when PtNCs had a monolayer of antibody coverage. Particles conjugated in less than an excess of antibodies resulted in PtNC aggregation during the conjugation, which led to elevated nonspecific binding in the blank sample and decreased test line to background ratio. A small shift to larger particle diameter was observed in DLS for bare PtNCs and PtNCs modified with a monolayer of antibodies. Encouragingly, the antibody physisorption process at the optimized conditions did not cause aggregation of the particles.

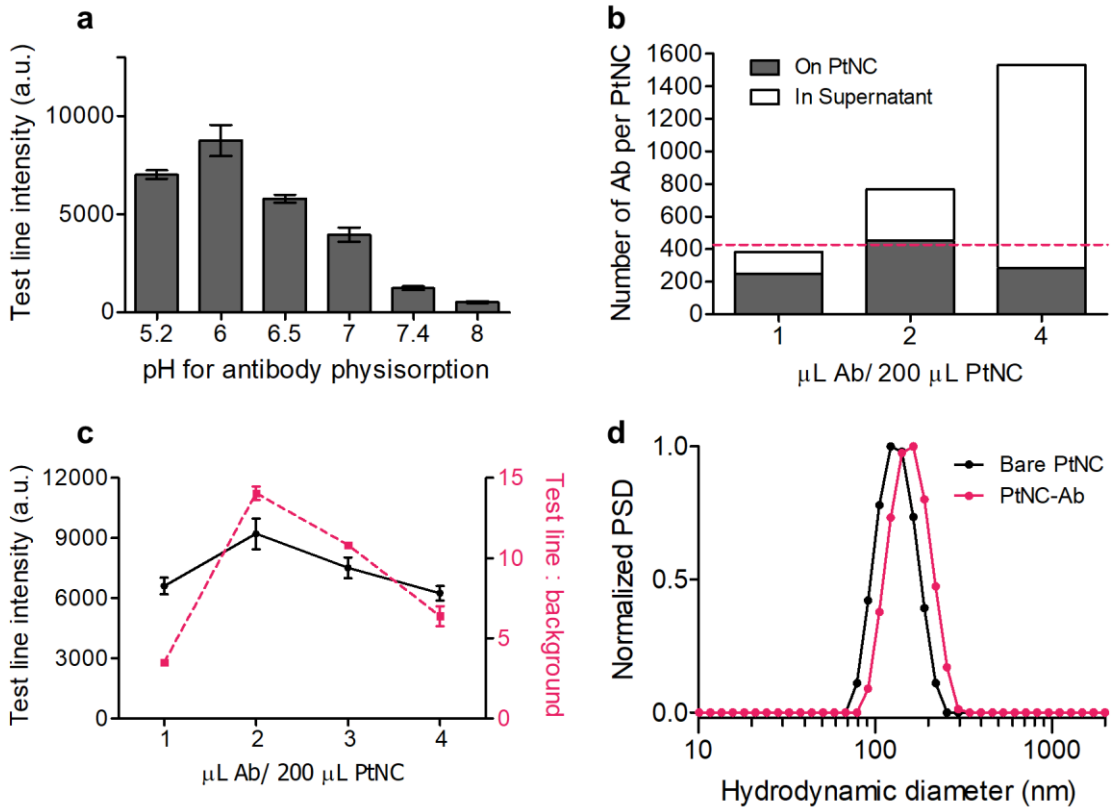


Figure 2.25 (a) Plot of test line intensity against pH of antibody physisorption, showing the pH dependency of antibody conjugation, with pH 6 (pH adjusted using 10 mM HEPES buffer) being optimal. (b) The number of antibodies conjugated to PtNCs (120 nm diameter) after incubation of a fixed particle concentration in presence of varying antibody concentrations for 3 h. When PtNCs were incubated in a 2-fold excess of antibodies with respect to surface area, a monolayer was formed (2 µL Ab/200 µL PtNC condition). Red dotted line indicates the theoretical maximum number of antibodies to fully coat PtNCs. (c) Plot of test line intensity and "test line to background ratio" against varying antibody coverage on PtNCs. (d) DLS measurements of normalized particle size distribution (intensity) for bare PtNCs (black) and antibody modified PtNCs (red). All data are averaged from ≥ 3 independent measurements where error bars represent the standard deviation from the mean.

To investigate the stability of the physisorbed antibodies on the PtNCs, the test line signal intensity was monitored for particle batches prepared and stored in running buffer over time (freshly prepared, 48 h, 168 h). The running buffer consisted of 0.2 wt% β-casein and 0.1 wt%

Tween-20 in phosphate buffer pH 7.2. The test line signal intensity decreased over the course of a week while stored at 4 °C in running buffer. The presence of the surfactant in the running buffer may lead to desorption or dissociation of the physically adsorbed antibody from the PtNC surface over time, leading to a decrease in positive signal intensity. Because of stability issues (desorption of antibody over time in presence of surfactants), PtNC-Ab conjugates were always prepared fresh (< 24 h storage in running buffer) for LFA experiments. While the desorption of antibodies in solution over time was not ideal, the nanoparticle conjugates were freeze-dried in the final format of the LFA. Therefore, long-term storage in solution was not a concern (Figure 2.26b).

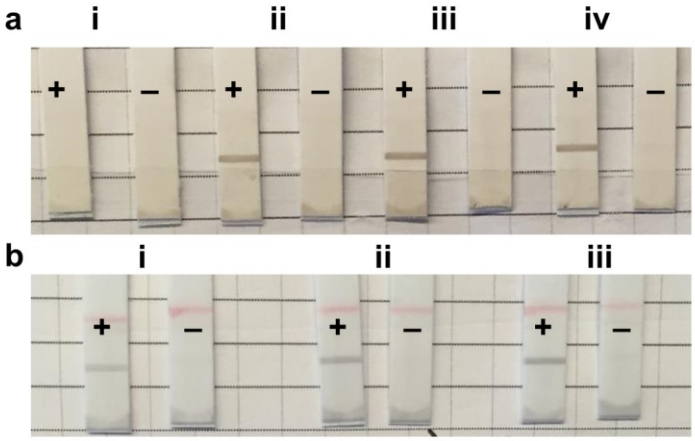


Figure 2.26 (a) Representative images of lateral flow test strips comparing physisorption time frames for PtNCs with excess monoclonal anitbody for (i) 0 h (no antibody), (ii) 30 min, (iii) 3 h, and (iv) 24 h incubation times. (b) Stability of PtNC-Ab conjugates incubated in running buffer for (i) 168 h, (ii) 48 h, and (iii) 0 h (freshly prepared). A positive (+) 100 $pg \cdot mL^{-1}$ p24 spiked serum sample is shown next to a negative (-) control blank serum sample.

In the test strips in Figure 2.26, some background signal can be observed in the negative (-) control samples (non-spiked, blank serum). Understanding the origin of this nonspecific signal is important in reducing any background binding and false positives. The nonspecific signal here could be caused by nonspecific binding between nanoparticle conjugates and nanobody or nanoparticle conjugates and streptavidin test line. The addition of β-casein as a blocking agent in the running buffer served to reduce the nonspecific interactions.

2.3.7 Effect of catalytic nanoparticle label size in lateral flow

PtNCs provide an ideal platform for assessing the role of catalytic particle size on sensitivity in LFA because they can be produced with exceptional control over size and subsequently modified with a monolayer of antibodies following the above physisorption protocol. The nanometer scale roughness and morphology of the particles produced during this seeded

synthesis appeared unchanged with increasing size (Figure 2.16), except for PtNCs > 150 nm produced by the layer-by-layer synthesis that exhibit a more densely packed Pt shell and reduced porosity (§2.3.3). The size of the nanocatalyst had a distinct effect on the test line signal intensity obtained for PtNC sizes up to *ca.* 280 nm when employed in the LFA (Figure 2.27). Larger particles with increased surface area for catalytic reactions would be expected to generate a higher signal in LFA format, and indeed, up to a diameter of 150 nm, this was observed experimentally. PtNC sizes ranging in diameter from 50 to 280 nm were synthesized and modified with an optimal surface density of antibody (monolayer coating, Figure 2.25). Keeping the PtNC concentrations constant (150 pM), the different sized PtNCs were used as catalytic labels in the LFA format for serum samples spiked with 100 $pg \cdot mL^{-1}$ p24 and the biotinylated nanobody. The resulting variation in signal intensity as a function of particle size is shown in Figure 2.27. Larger particles provided increased signal intensity, reflecting the increased surface area available for catalytic reactions. However, this effect was most prominent approaching a threshold in the region of 120 – 150 nm, above which a reduced performance was observed. This reduced signal intensity for larger particles was potentially due to a reduction in diffusivity and a concomitant decrease in internal porosity (and therefore catalytic activity), resulting from the layer-by-layer synthesis (§2.3.3). A similar reduced signal intensity has also been observed for large gold nanoparticles. Li *et al.*[94] reported the effect of the size of gold nanoparticles in the range of 20 – 180 nm on test line signal intensity. They observed that AuNP labels in the 100 nm size regime exhibited the highest signal intensity. Larger 180 nm AuNPs created steric hindrance at the test line and were less able to bind antigen already laid down at the test line, reducing the signal intensity. A combination of steric effects, diffusivity of the particle label, and reduced internal porosity of the larger PtNCs may contribute to their reduced performance in LFA. An optimal performance regime was exhibited by PtNCs in the 120 to 150 nm diameter range, so due to their facile one-step synthesis, low nonspecific binding, and minimizing the need to use excessive platinum, 120 nm PtNCs were used for further experiments (Figure 2.27iv).

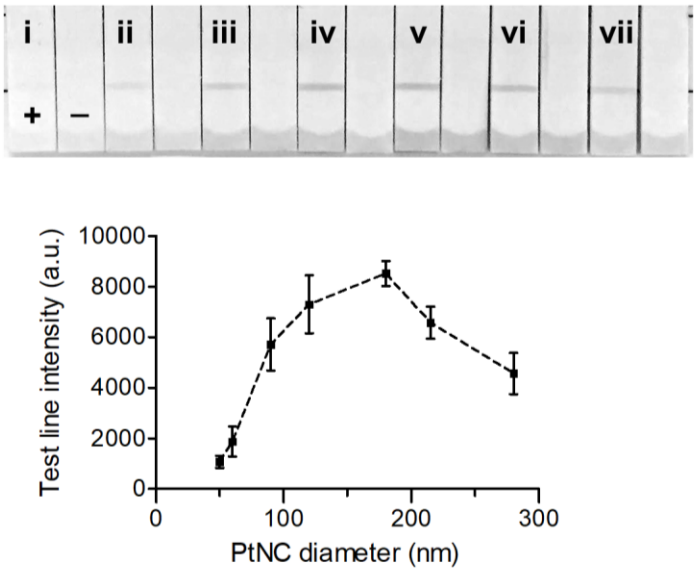


Figure 2.27 Test line intensity for antibody modified PtNCs (150 pM) varying in size from *ca*. 50 to 280 nm (mean number distribution by DLS) for detection of 100 pg·mL^{-1} p24 in FBS with 5 min development in CN/DAB and H_2O_2. All data are averaged from ≥ 3 independent measurements where error bars represent the standard deviation from the mean. Inset, representative image of lateral flow test strips incorporating PtNC labels of increasing size (50 – 280 nm, left to right), where test line intensity is a measure of the intensity of the blank (-) sample subtracted from the positive sample (+).

The reproducibility of PtNC synthesis and modification was investigated, as a requirement for scaling up reagents for diagnostic development. Figure 2.28 shows the test line intensity produced by five independently synthesized and antibody modified batches of 120 nm PtNCs for detection of 50 pg·mL^{-1} p24 spiked sera. The coefficient of variation between five independently synthesized and antibody modified batches was 2.4 %, indicating that PtNC amplified LFA is reproducible through the synthesis, antibody conjugation, and assay running steps. This suggests that the nanocatalyst platform holds great promise for reliable clinical sample detection. Additionally, the hydrodynamic diameter of the five independently synthesized batches of PtNCs was measured by DLS. The diameters corresponding to each batch overlapped, showing consistency in PtNC production, and importantly no peak associated with aggregates was observed, which would increase nonspecific binding in LFA and hinder test sensitivity.

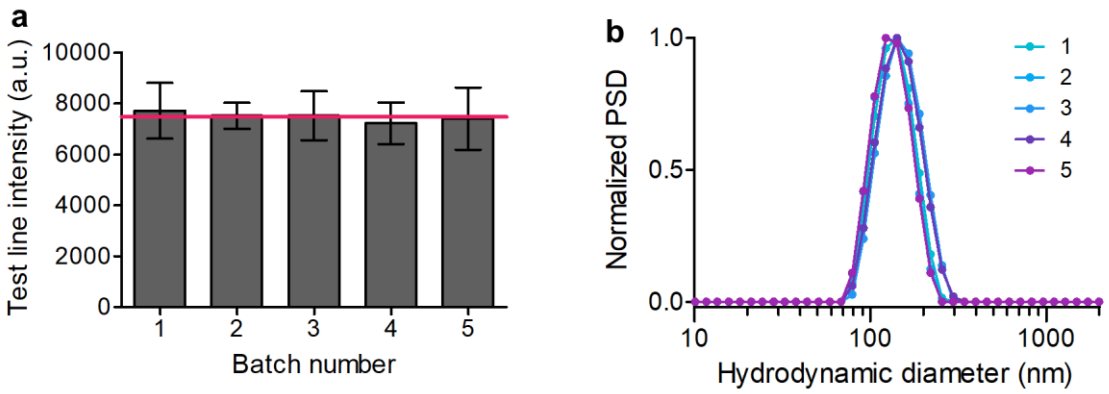


Figure 2.28 (a) Test line intensity for five independently synthesized batches of PtNCs (120 nm) for detection of 50 pg·mL^{-1} p24 in FBS with 5 min development in CN/DAB and H_2O_2. Red line indicates average test line intensity for triplicate measurements across all batches. Coefficient of variation (n = 5) was 2.4 %. (b) Normalized particle size distribution (intensity PSD) for five independently synthesized batches of PtNCs using the same starting seed concentration where the distributions overlap closely.

2.3.8 Stability of nanobody and nanocatalyst against accelerated ageing

Conventional antibodies can be readily physisorbed onto metallic nanoparticles and show significant thermal stability when lyophilized. This process is standard in most LFA manufacturing processes, where typically 40 nm gold colloids functionalized *via* physisorption of antibodies are employed as the detection labels.[85] The amplified LFA also exhibits excellent long-term stability of the bio-recognition components, where a combination of a conventional antibody and a biotinylated nanobody are used in tandem. Temperature dependent circular dichroism (CD) spectra show that the nanobody employed in the LFA is thermally stable up to 82 ºC and refolds reversibly upon cooling from 95 to 25 ºC (Figure 2.29a). The binding ability of the nanobody and a comparator monoclonal antibody at elevated temperatures was examined by ELISA. The nanobody retained at least 50 % binding activity, even after incubation at 90 °C, indicating its ability to re-fold. The conventional antibody loses most of its binding ability above 60 °C (Figure 2.29b). The nanobody exhibited significantly greater thermal stability than conventional immunoglobulins and there is great potential in pairing two nanobody components in LFA to further improve the thermal stability for use in the most adverse conditions.[27–29,136,137]

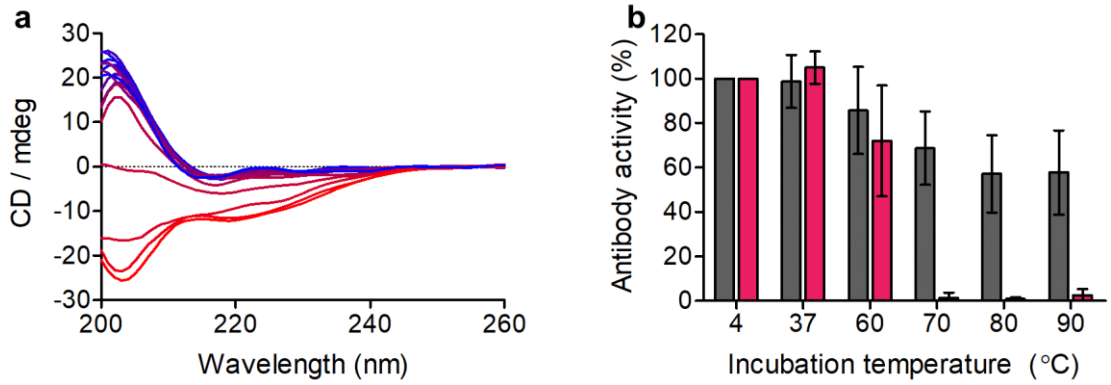


Figure 2.29 (a) Temperature dependent circular dichroism spectra showing thermal denaturation of nanobody between 25 °C (blue) to 95 °C (red). (b) Activity of p24 binding nanobody (gray) and a comparator monoclonal antibody (red) as assessed by its ability to re-bind to p24 by indirect ELISA after 2 h incubation at varying temperatures (4 – 90 °C). Error bars represent standard deviation from three independent experiments. ELISA was performed by Dr. Eleanor Gray and CD was performed with Dr. Alex Brogan.

Stability is a key aspect of PoC devices where the performance of both the detection labels and the antibody components must be independent of the storage conditions the test might be exposed to. Many assays require controlled temperature storage conditions, which imposes cost on the supply chain and may prevent use in high temperature regions, thus limiting the test's use in the developing world. Enzymes and antibody reagents are typically the most susceptible components to long-term storage, although with appropriate drying conditions and matrices, long-term dried storage is possible.[138] One of the advantages of using an inorganic catalyst over biological enzyme for detection is thermal stability (Figure 2.30a). PtNCs showed no significant loss in activity when thermally treated for 3 h at 60 °C, whereas horseradish peroxidase (HRP) lost *ca*. 70 % activity indicating denaturation at elevated temperatures.

Accelerated aging studies, shown in Figure 2.30b, were carried out on lyophilized reagents – comparing the stability of peroxidase-mimicking PtNC labels to their biological counterpart HRP, the most common enzyme used for catalytic amplification in immunoassays. For aging studies, nanobody-biotin and either antibody conjugated HRP or PtNC were lyophilized in optimized drying buffer mixtures containing sucrose, BSA, PVP and Tween-20. Sucrose or trehalose was a key addition to the drying buffers as it aided in stability and re-solubilization of the particles and affinity reagents. The PtNC-Ab conjugates and nanobody-biotin were frozen at -80 °C in the presence of 10 wt% sucrose (in drying buffer), which acted as a cryoprotectant, and subsequently lyophilized in a 96-well plate. The sugar molecules form a layer around the particles that helps to stabilize the protein from denaturation and prevents particle aggregation.[139] The resulting freeze-dried PtNC-Ab conjugate and nanobody-biotin

mixes had a cake-like structure. The sucrose also acted as a viscosity enhancer, to slow flow rate and increase reagent dwell time at the test line, which resulted in improved sensitivity.

After freeze-drying and aging at 44 °C or room temperature over a period of 6 weeks, p24 spiked plasma was added to the dried samples, flowed up the strip, and the test line intensity was quantified after catalytic amplification. PtNC-amplified LFA showed no notable change in test line intensity over 6 weeks aging at room temperature, and only minimal change in test line intensity when incubated at 44 °C for 6 weeks (6-month room temperature aging equivalent). An initial *ca.* 25 % decrease in signal intensity was observed after three days of incubation at 44 °C, after which no additional signal was lost over a 42-day period. In contrast, anti-HIV-1/2 antibody-functionalized HRP labels were found to lose 90 % of signal intensity after two weeks of room temperature dry storage when run in LFA (these samples did not withstand elevated temperature aging conditions). The resilience of these components is critical in determining the system's suitability for PoC use, especially in resource-limited settings where cold-chain transport is not guaranteed. This also highlights the benefit of using robust inorganic catalytic nanoparticles in the place of conventional enzymes where the catalytic amplification obtained using the porous PtNCs was highly resilient to accelerated aging conditions.

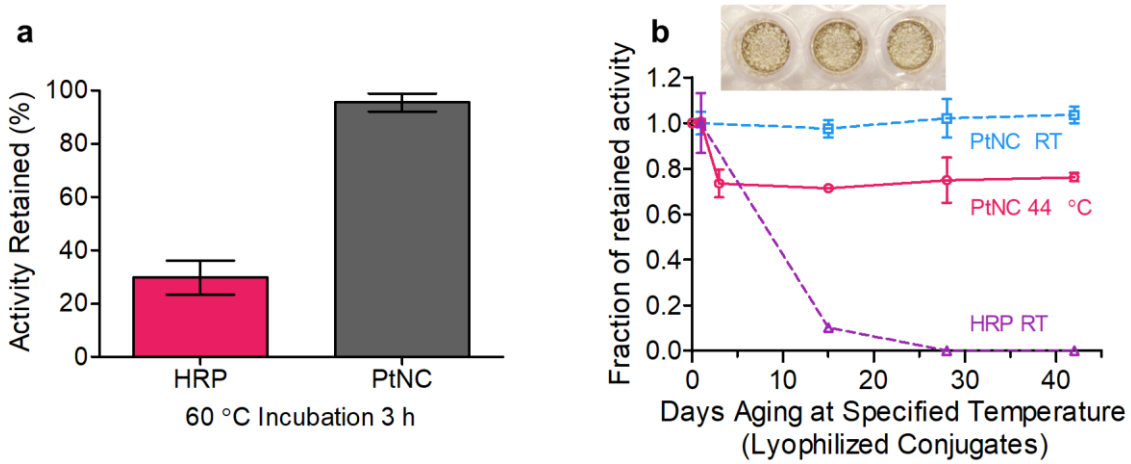


Figure 2.30 (a) Thermal stability of HRP and PtNCs. (b) Intensity of test line (for detection of 500 pg·mL^{-1} p24-spiked plasma) against days of test component aging at 44 ºC or room temperature (RT). For aging experiment, nanobody-biotin and either PtNC or HRP-antibody conjugates were lyophilized in appropriate buffers and incubated at specified temperature. At aging time points, spiked plasma was added to the vessel of freeze-dried components and flowed up the LFA test strip followed by catalytic amplification.

2.3.9 Performance of nanocatalyst LFA in serum and clinical samples

An important consideration in the design of LFA is the sample volume to be tested. A careful balance must be achieved between maximizing sensitivity while achieving a test result in the desired time frame. The sample volume scales linearly with the “time to result” and the test line intensity, where sensitivity increases with larger sample volumes that take a longer time to produce a readout (Figure 2.31). For example, a small 20 µL plasma sample produced a readout within 5 min but was 4.5-times less sensitive than a larger 120 µL plasma sample that took 30 min to run through the membrane and read the result. The target for PtNC LFA was to use a standard finger prick of blood, which represents *ca*. 50 µL plasma (once blood cells are separated through centrifugation or filtration). For a 50 µL sample, the PtNC LFA produced an amplified colorimetric result within 12 min, which is an acceptable time frame for PoC test.

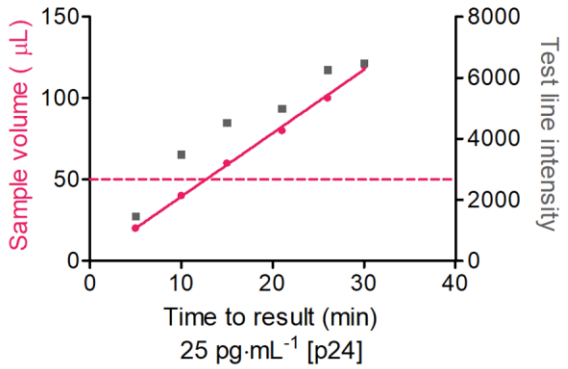


Figure 2.31 Representative data showing the reduction in time to result possible with reducing sample sizes for 25 pg·mL^{-1} p24 spiked sera volumes (red) where larger samples require longer run time but provide higher test line intensity (gray). The dashed red line indicates the volume of blood in a standard finger prick.

The sensitivity of the nanocatalyst-labeled LFA (employing 120 nm PtNC labels) before and after catalysis is highlighted with a plot of the normalized test line signal intensity against the concentration of p24 in spiked sera before and after catalytic amplification (Figure 2.32). Test line signal intensity was captured by a mobile phone camera, a readily available tool for image acquisition.[140] Unlike enzyme-labeled immunoassays which require catalysis for visualization, the PtNC labeled LFA achieved two windows of sensitivity: pre-and post-catalysis, taking advantage of both the absorbance of the particles and their peroxidase-mimicking activity. This empowered the assay with a dual range diagnostic regime, quantifiable by use of mobile phone-based detection and image analysis. The dose-response calibration curves of test line signal intensity against log[p24] were fit to the four-parameter logistic regression

(**Equation 2.2**), where H is the Hill slope, I_{max} is the intensity at infinite concentration, I_{min} is the intensity at zero concentration, and EC_{50} is the inflection point:

$$f(x) = I_{min} + \frac{(I_{max} - I_{min})}{1 + (\frac{x}{EC_{50}})^{-H}} \quad (\mathbf{2.2})$$

The fitting was used to determine the p24 concentration corresponding to half the maximum test line signal intensity (EC_{50}). For the pre-development regime, the EC_{50} corresponded to 4320 pg·mL^{-1}, and for the post-development regime the EC_{50} was 46.1 pg·mL^{-1}. The difference in pre and post-development regimes was an amplification factor of 93.6, enabling the PtNC amplified LFA to rival the sensitivities of more sophisticated bench top techniques such as ELISA. While the amplification factor at the test line in LFA format was on the order of 10^2, the effective turnover number (k_{cat}) for PtNCs was determined to be on the order of 10^7 substrate molecules per second from a steady-state kinetics analysis (§Table 2.3). The discrepancies between the turnover number measured in aqueous solution and the amplification factor in LFA can be attributed to several factors. First, the steady-state kinetics measurements were carried out in idealized buffer conditions using bare PtNCs, whereas the LFA experiments were performed in human plasma samples, where *ca*. 75 % catalytic activity is knocked out by PtNC modification with antibodies and serum protein adsorption on the particle surface. Additionally, the substrates used in solution assays versus on paper were different, where TMB was used in solution and CN/DAB on paper due to varying solubilities of the oxidized products. It is important to note that in the LFA format, PtNCs were immobilized via antigen capture at the test line on a solid phase (nitrocellulose membrane). The lower signal enhancement on the paper membrane compared to in solution could be ascribed to the compromise of catalytic activity of PtNCs when the catalytic reaction is confined to the solid phase.[141] Additionally, the accumulation of PtNCs and possible aggregation of particles at the test line could result in a reduced total area of active Pt surface.[67] Because of the opacity of the nitrocellulose membrane, the particles bound at the test line are only visible if they are located near the surface of the membrane. While the particles may be captured evenly through the depth of the membrane, any particles bound deeper than *ca*. 10 µm from the surface are invisible to the user as the color is masked by the membrane's opacity.[85] Analyzing the LFA is a surface-based measurement, whereas analyzing the activity in solution in a 96-well plate format is a bulk measurement, and thus the amplification factor and turnover numbers measured on each of these platforms are not directly comparable.

When the test line intensity was plotted against p24 concentration on a log-log scale, the assay exhibited two linear dynamic ranges. The linear dynamic range spanned over 4 orders of

magnitude from 10,000 to < 1 pg·mL^{-1} protein target (Figure 2.32b) through measurement of pre- and post- amplification. This can enable a broader potential quantitative range of the test if an image is taken before and after amplification. The limit of detection or analytical sensitivity of the PtNC LFA was defined as the concentration corresponding to 3 standard deviations above the mean of the measured zero concentration calibration blanks. PtNC-amplified LFA enabled the detection of p24 in spiked sera down to a level of 0.8 pg·mL^{-1} (*ca.* 32.5 fM) in under 20 min. This sensitivity is within the clinically relevant range for [p24] during acute stage infection when the individual is most infectious, but also when early intervention with antiretroviral therapies is most beneficial.[76]

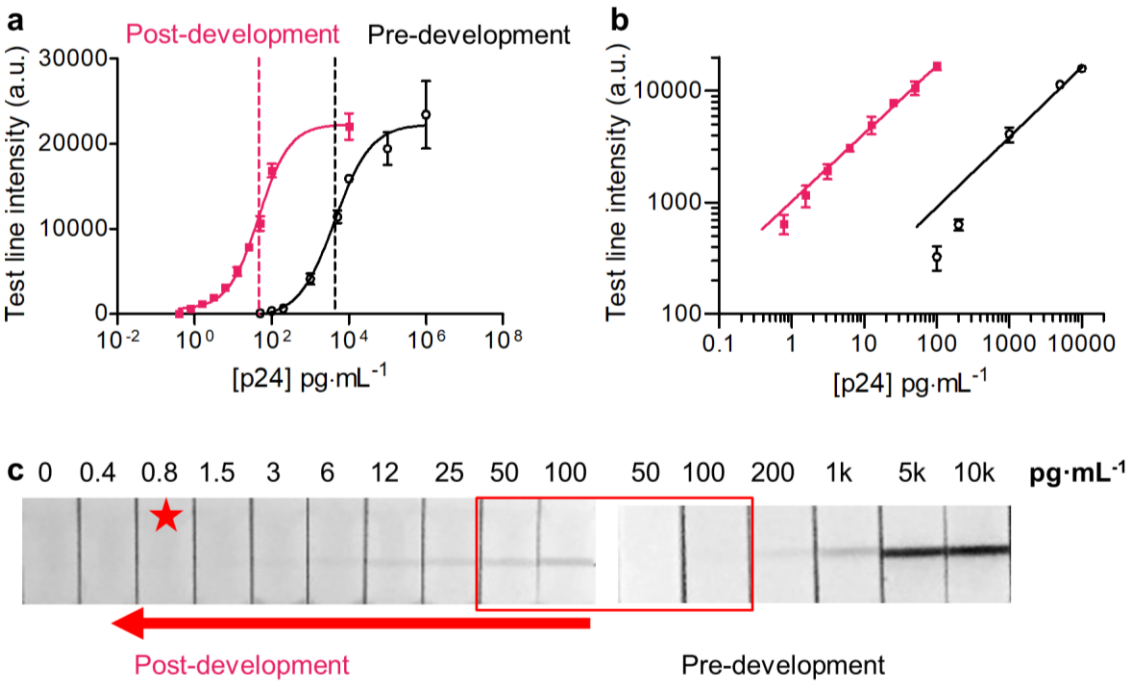


Figure 2.32 Normalized test line intensity obtained by mobile phone camera images for a dilution series of p24 spiked into sera before (black) and after amplification (red) in a mixture of CN/DAB and H_2O_2 for 5 min using 120 nm PtNC labels. Error bars represent standard deviation from three independent experiments. (b) Illustration of the broad linear dynamic range across 4 orders of magnitude from 10,000 to 1 pg·mL^{-1} achieved with the present method with nonlinear (log scale) regression least squares fit (pre-development: 0.62x + 1.7, R^2 = 0.9813; post-development: 0.61x + 3.0, R^2 = 0.9853). (c) Representative mobile phone images of test strips before and after catalytic development (red box highlights pre- and post-development for 50 and 100 pg·mL^{-1} samples), corresponding to varying concentrations of p24-spiked sera. Brightness in image has been increased for clarity of reproduction. The star represents the lowest concentrations distinguishable by image analysis where limit of detection represents three standard deviations above the mean of the blanks.

The commercial gold standard test for p24, the Alere HIV Combo test, can detect p24 down to < 25 pg·mL^{-1} in serum without any amplification using 200 nm selenium colloids as the detection label.[78] The higher sensitivity of the Alere test in the “pre-amplification regime” is

likely due to its use of proprietary affinity reagents with lower K_D values than the ones employed in the PtNC LFA. The PtNC LFA still exhibits nonspecific binding which limits the concentrations of reagents (especially PtNC concentration) that can be used in the assay, whereas the commercial test will employ antibodies that have been optimized to reduce NSB. With similar antibody components to Alere, it is expected that the PtNC amplification strategy could significantly improve on the sensitivity of the commercial test.

The performance of the PtNC LFA was evaluated with clinical human plasma samples using an HIV seroconversion panel collected by ZeptoMetrix (Panel Donor No. 75062). It is challenging to obtain blood samples representing early acute HIV infection, as most patients do not seek medical attention until weeks to months after infection. The panel of samples tested here was from a blood donor, who over the course of donating became infected with HIV. The archived samples from blood donors (usually collected twice a week during the donation period) provide a unique record of infection encompassing time points before viral exposure through to seroconversion.[70]

Longitudinal clinical samples from the same blood donor spanning a one-month blood collection period encompassing seroconversion were assessed. In a blinded experiment, PtNC amplified LFA could successfully detect positive antigen levels in infected plasma from ZeptoMetrix panel samples 7 through 14, corresponding to increasing levels of antigen in the blood during acute phase infection, followed by immune complex formation (Figure 2.33). Panel samples 13 and 14 correspond to low levels of p24: 10.8 $pg \cdot mL^{-1}$ ~ 211,000 copies/mL HIV-1 RNA and 4.6 $pg \cdot mL^{-1}$ ~ 46,300 copies/mL, respectively (verified by ZeptoMetrix HIV p24 antigen ELISA and Roche Cobas Amplicor HIV-1 Monitor). The low levels of p24 detected in these clinical samples (4.6 and 10.8 $pg \cdot mL^{-1}$) represent concentrations lower than what is currently possible to detect using the gold standard commercial LFA (Alere Combo). PtNC amplified LFA provides a platform for detection of acute HIV infection at the PoC by accessing a wider detection range for p24. A 4th generation HIV LFA test incorporates an antibody detection line to ensure the test can detect HIV infection across the seroconversion regime.[68] In future work, a similar dual antibody and antigen detection approach is envisaged for the PtNC-amplified LFA, which would still benefit from the increased dynamic range for immune response monitoring with exceptional levels of sensitivity towards p24 at the early stages of infection.

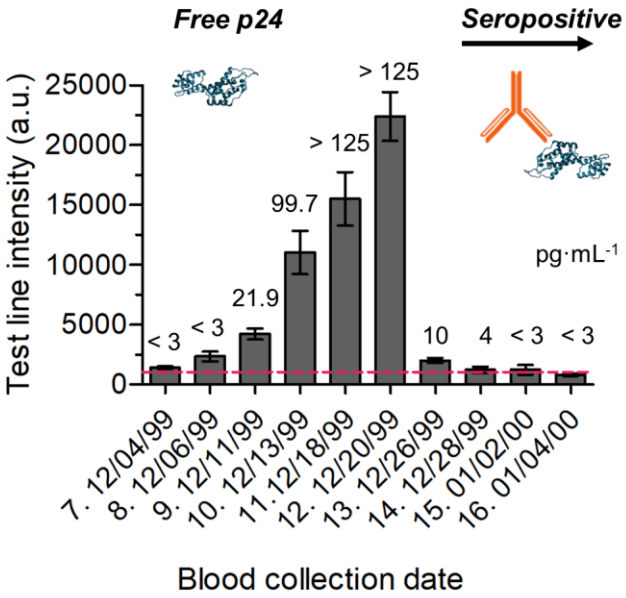


Figure 2.33 Clinical sample HIV seroconversion panel results for a single donor showing the change in test line intensity as a function of sample blood collection date covering the seroconversion period. 50 µL of each clinical sample was added to a vessel containing lyophilized test reagents and run up the LFA strip followed by catalytic amplification. Red dotted line indicates cut-off (average test line intensity of 3 non-spiked blank plasma samples plus three times standard deviation). Error bars represent standard deviation from three independent experiments. Clinical samples were run on LFA with assistance of Dr. Eleanor Gray.

2.3.10 Challenges for clinical translation

While the PtNC amplified LFA exhibits excellent sensitivity in spiked serum and plasma, and detection of p24 in a clinical sample, significant optimization is still required to translate the proof of concept test into a clinically useful diagnostic. In its current configuration, the test is in a dipstick format. The next step for diagnostic development would be to move toward a full LFA format, where a sample and conjugate pad are incorporated into the platform. Moving towards this step requires optimization of buffers and reagents for drying PtNC-Ab conjugates and affinity reagents onto glass fiber pads. Additionally, a control line will need to be incorporated as an internal quality control and to show the end user that the assay is functional, and results are valid. The control line should be a secondary antibody that is specific to the species of the monoclonal antibody conjugated to the PtNCs (*e.g.* control line could be goat anti-mouse secondary antibody, as anti-HIV mAb was produced in mouse). In this way, the PtNCs should be captured at the control line regardless of the presence of the target analyte. Additional filtration membranes may be incorporated into the device sample pad to allow for analysis of whole blood. However efficient separation of blood cells from serum and plasma is challenging and results in a loss of sample volume, so would require further optimization.

Once the full format LFA is constructed, housing and cassette designs should be considered. The cassette houses the test and provides optimal flow rate control by applying pressure at appropriate points on the strip.[85] The cassette could also serve a dual purpose to house reagents for the catalytic amplification, to move from a multi-step to a single-step platform for ease of use.

Scaling up production of reagents is another consideration in further assay development. The PtNCs can be produced at scale (~ 100 mL scale at 300 pM particle concentration, enough to run ~ 10,000 LFA tests), but affinity reagents and site-selective modification strategies are currently limited to smaller quantities due to antibody costs.

To date, the test has only been optimized for certain matrix conditions – namely fetal bovine serum, human plasma pool, and a set of clinical samples from a single source. A preliminary experiment was designed to test the assay performance on non-infected plasma collected from donors at University College London (UCL). Individual variability and anticoagulants in these samples presented a challenge that was not previously encountered in the plasma pool samples (Figure 2.33). In p24-spiked plasma from the UCL donors, significant aggregation of PtNCs and elevated NSB was observed (Figure 2.34). The hypothesis was that this could be due to variations in anticoagulants used during blood collection. For example, the plasma pool (Lee Biosciences) was stabilized with the anticoagulant citrate phosphate dextrose, and the Zeptometrix panel was stabilized with 4 wt% sodium citrate, while the UCL samples were stabilized with dipotassium ethylenediaminetetraacetic acid (K2-EDTA). While encouraging that the PtNC LFA performs in the presence of certain anticoagulants, EDTA is one of the most common anticoagulants used in hospitals and in PoC settings. The function of EDTA is to chelate calcium present in the blood specimen to arrest the coagulation process for preservation of the sample for later testing. Since EDTA is widely used, the effect of anticoagulants on the stability of PtNC LFA requires further investigation. The interaction between EDTA-stabilized plasma and PtNCs induces aggregation where the PtNC aggregates bind to the meniscus front, hindering flow, preventing specific binding and simultaneously increasing NSB. This aggregation could be due in part to variations in sample pH and salt content. The addition of other blocking agents could help suppress this aggregation. This issue also could be an artefact of the dipstick format. When developed into a full format LFA with sample and conjugate pad, this aggregation effect may be minimized. The variation in NSB between donor samples was striking, and surprising as the aggregation and elevated NSB was not present in spiked plasma pool. While the plasma pool is a reasonable test matrix, it may act to dilute any effects from individual donors that could cause variability in the test. Additionally, it is common in LFA manufacturing processes to pre-treat

the sample pad with 1 M borate pH 9.5, which can minimize variation between individual samples by controlling the pH and ionic strength of the solution that emerges from the sample pad. Differences in pH and ionic strength may change the charge densities of PtNCs and affinity reagents inducing undesired aggregation as soon as the sample contacts the test reagents resulting in NSB.

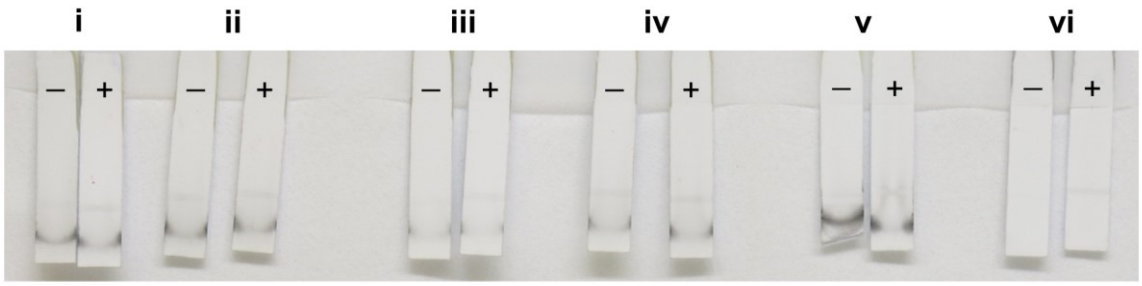


Figure 2.34 Variability in LFA results for blank (-) and 10 ng·mL^{-1} p24 spiked (+) into plasma from 5 healthy volunteers (i – v) stabilized in EDTA compared to spiked human plasma pool (Lee Biosciences) (vi) before catalytic development.

Another consideration in further development of the PtNC LFA for early HIV detection would be to incorporate an immune complex disruption step. Extra-viral p24 in seroconverted individuals is predominately immunocomplexed and would thus be unavailable for capture in a p24 immunoassay. Incorporation of a heat treatment, acid shock, or addition of detergents into the LFA format for immune complex disruption, followed by neutralization, could help increase the detectable concentration of p24 by releasing p24 from virus and anti-p24 antibodies.[142] However, this step would increase test complexity and could potentially compromise other test reagents (despite high stability of PtNC and nanobody components). Ideally the LFA would also include a test line for HIV-1/2 antibodies and free HIV-1 p24 antigen, harnessing PtNC amplification to enhance both antibody and antigen signal. This will require functionalizing the PtNCs with affinity reagents for detection of both targets to widen the usefulness of the test across the period of seroconversion.

2.4 Conclusions and future work

2.4.1 Conclusions

This chapter reports on one of the simplest and most sensitive absorbance-based LFA for protein detection to date. Its utility in a clinically significant range for p24 detection in spiked sera and plasma was demonstrated, as well as the detection of acute phase HIV infection in serial clinical samples. Unprecedented sensitivity was achieved in a simple paper-based platform by pairing porous catalytic inorganic nanoparticles and thermally robust antibody fragments with easily modifiable functional groups for oriented presentation of the solid phase recognition elements. Capitalizing on the porous nature of the catalyst, the optimal size regime for catalytic nanoparticles as amplifying labels in LFA was established. The high catalytic activity of the noble metal PtNCs towards peroxide disproportionation was balanced with the simultaneous tendency for biomolecules to adsorb and block the reactive surface by careful tailoring of PVP coatings and antibody conjugation. The pairing of nanobody and nanocatalyst components in LFA resulted in a simple, robust, and highly amplifying system. The PtNC amplified LFA is easy to use with a colorimetric output that can be read by the naked-eye or by mobile phone camera in less than 20 min.

PtNC amplified LFA accesses a broad dynamic range of p24 concentrations, which spans over four orders of magnitude (Figure 2.35). This dual sensitivity regime was enabled by the inherent coloration of the PtNC (for detection of 100 – 10,000 $pg \cdot mL^{-1}$ analyte) and their ability to catalytically generate a colored product to decorate the test line, accessing a second regime from 100 to less than 1 $pg \cdot mL^{-1}$ analyte. This is 2 orders of magnitude broader dynamic range than standard colorimetric ELISAs or 4th generation LFAs, which are limited to either post-catalysis or to the coloration of a particle label, respectively.[15]

The applications for this rapid test with broad dual dynamic range extend far beyond HIV diagnostics. This sensitive platform may be readily adapted for detection of other biomarkers across multiple stages of disease progression and monitoring of therapeutic efficacy. The versatile and modular platform incorporates highly efficient inorganic catalytic labels into existing LFA technology, enhancing its potential uptake into PoC diagnostics for the detection of any protein target.

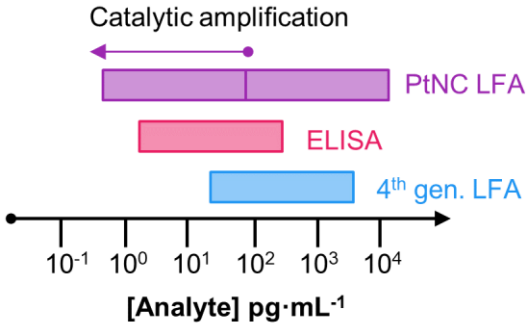


Figure 2.35 Schematic comparing the dynamic ranges of 4th generation LFA, ELISA, and PtNC LFA.

2.4.2 Detection of other analytes

While early detection of HIV was the primary focus of this chapter, the PtNC LFA platform should be adaptable for detection of any protein target by changing the affinity components in the system. The coupling of orthogonally modified nanobody and physisorbed full antibody enabled the rapid engineering of a PtNC amplified assay. Nanobody mutation, expression and orthogonal modification can be readily achieved within several days, where the preparation of the appropriate PtNC catalysts can be performed simultaneously for use on a standard, commercially available streptavidin lateral flow membrane (Figure 2.36). The rate-limiting step in the further development of PtNC LFA for detection of other analytes is the selection of high affinity antibody or nanobody pairs for the target that exhibit affinity constants necessary for fast binding kinetics in LFA (k_{on} > 10^5 $M^{-1}s^{-1}$; K_D sub-nanomolar or low nanomolar).

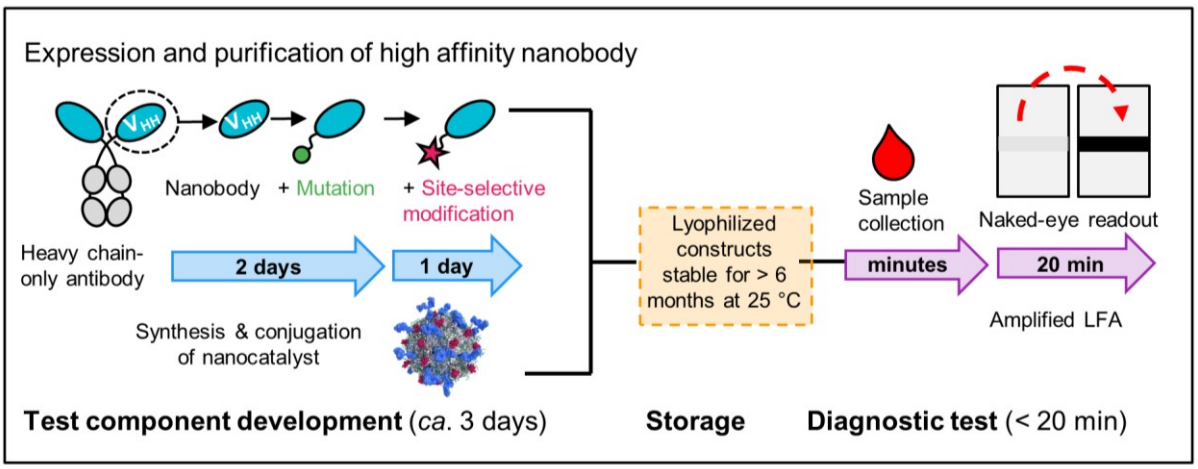


Figure 2.36 Process flow for the rapid prototyping of amplified paper-based diagnostics for protein biomarkers, incorporating orthogonally modified nanobodies and highly active nanocatalyst labels.

There are many other protein biomarkers that would benefit from early and sensitive detection by employing the nanocatalyst labeled LFA technology, highlighted in Table 2.5. There is a broad gap in the rapid diagnostic market for tests sensitive in the low femtomolar target regime that the PtNC LFA approach may be applied to. Some diseases would benefit from multiplexed detection, or detection of multiple biomarkers from a single sample on one test strip. This could be particularly useful when there are multiple serotypes or strains, for distinguishing between disease with similar symptoms, or in the case of HIV, for detecting different biomarkers present at different stages of disease (*e.g.* viral RNA, p24, HIV antibodies).

Table 2.5 Biomarkers requiring sensitive detection in point-of-care settings

Biomarker	**Ideal [Ag] detection regime**	**Current PoC "gold standard" and dynamic range**	**Specimen type**
HIV[77] – early detection and monitoring: p24 antigen	0.1 – 1000 $pg \cdot mL^{-1}$	Alere HIV Combo. Analytical sensitivity: 11 – 18 $pg \cdot mL^{-1}$ p24 in 30 min	Blood, plasma, serum
Influenza A/B: influenza A and B nucleoprotein antigens	Low $pg \cdot mL^{-1}$	BD, Alere, RT-PCR or viral culture	Nasal swab
Cardiac Troponin (Heart attack, myocardial infarction)	< 3 – 50 $pg \cdot mL^{-1}$	Roche CARDIAC Trop T Sensitive test (visual): cut-off 100 $pg \cdot mL^{-1}$	Blood, plasma
IL-6 **Inflammatory** cytokine biomarker (relevant for diabetes, pandemic influenza A H1N1)	0.1 $pg \cdot mL^{-1}$	ELISA: GE Life Sciences IL-6 Human – High-Sensitivity, Biotrak assay. 0.63 – 20 $pg \cdot mL^{-1}$ in 5 h	Blood, plasma
Early **Sepsis** (procalcitonin - PCT) inflammation, bacterial infection	< 50 $pg \cdot mL^{-1}$	PCR based pathogen detection	Blood, plasma

Most of the optimization in this chapter was done empirically, by changing parameters such as PtNC concentration, antibody loading, membrane porosity, blocking agents, *etc.*, and subsequently measuring the effect on test line intensity through inspection and analysis of test line intensity and iterating as necessary. These iterative optimization steps would have to be repeated for any new target and antibody pair. While much LFA optimization does require a trial-and-error approach as nonspecific interactions between components and heterogeneity in biological samples can be challenging to predict, advances in modelling techniques for LFA could be interesting to investigate for increasing the efficiency of the LFA development process. Recent work by Weigl and coworkers[32] presents a computational model that integrates LFA theory to predict and quantify assay performance. With the aim of developing high fidelity LFA, the model considers underlying mass transport and reaction theory in LFA devices to better predict how individual parameters may affect the outcome and assay

sensitivity. The mechanistic model takes input parameters such as kinetic constants of all reactants, fluidic parameters (dimensions and porosity of membrane, viscosity of sample), and surface energy of the LFA structural materials as well as optical properties of the signal particles and tracks the reactions and flow of all constituents through the LFA. When this model becomes publicly available it will be interesting to validate computational with experimental results for various targets and begin to use the predictive power for designing sensitive tests more efficiently.

2.4.3 Expanding library of catalytic labels

PtNCs served as an excellent platform for identifying some of the key parameters for their use in LFA. However, there exists a variety of other nanomaterials in different shapes and sizes, which could rival the sensitivity of PtNC labels and would be interesting to explore further. While 40 nm gold nanoparticles are the most commonly used nanoparticle label in LFA, other particles marketed for high-sensitivity lateral flow include: 200 nm selenium nanoparticles (Alere/Abbott), 400 nm dyed, fluorescent and paramagnetic polystyrene beads (Millipore), and 150 nm particles containing a silica core and 15 nm gold shell (nanoComposix). The gold "nanoshell" particles marketed by nanoComposix have a large extinction cross section and because of their low-density silica core, flow unimpeded through the nitrocellulose membrane. It would be interesting to explore the density dependence of different particle types on LFA, as mobility will affect reaction kinetics, *e.g.* analyte molecules and particles moving more slowly past a test line will have greater probability of binding events. Since particle mobility will be dependent on shape and size, it would be interesting to explore the use of low-density core materials (silica 2.65 $g \cdot cm^3$, polystyrene 1.04 $g \cdot cm^3$) with a variety of thin shells, including catalytically active shell materials such as platinum (high density, 21.5 $g \cdot cm^3$) or other mixed noble metals.

During LFA optimization, an interesting observation was that molecular-sized materials have a sharper binding interface at the test line than nanoparticles, potentially due to size, density, and surface presentation of binding ligands. HRP-biotin (44 kDa, *ca*. 4.5 nm) exhibited razor-sharp binding at the streptavidin test line interface, whereas the Pd-Ir-biotin (*ca*. 20 nm Pd-Ir nanocube §2.3.1) binding was more diffuse and uniform across the test line (Figure 2.37). The image analysis shows that the area under the Pd-Ir peak is larger and 3-fold broader than for HRP, however the HRP peak has a larger "height at peak maximum." A sharp interface at the test line is important in naked-eye detection as it allows the positive signal to be more easily differentiated from NSB by eye. This difference in binding could be related to differences in diffusion between HRP and Pd-Ir through the porous membrane, or potentially an issue with

the availability of the biotin. The biotin may be embedded in the PVP capping layer on the Pd-Ir rendering it inaccessible for binding. While this chapter explored many parameters, it would be interesting to investigate density dependent reaction kinetics and binding in addition to affinity component accessibility on a range of surfaces.

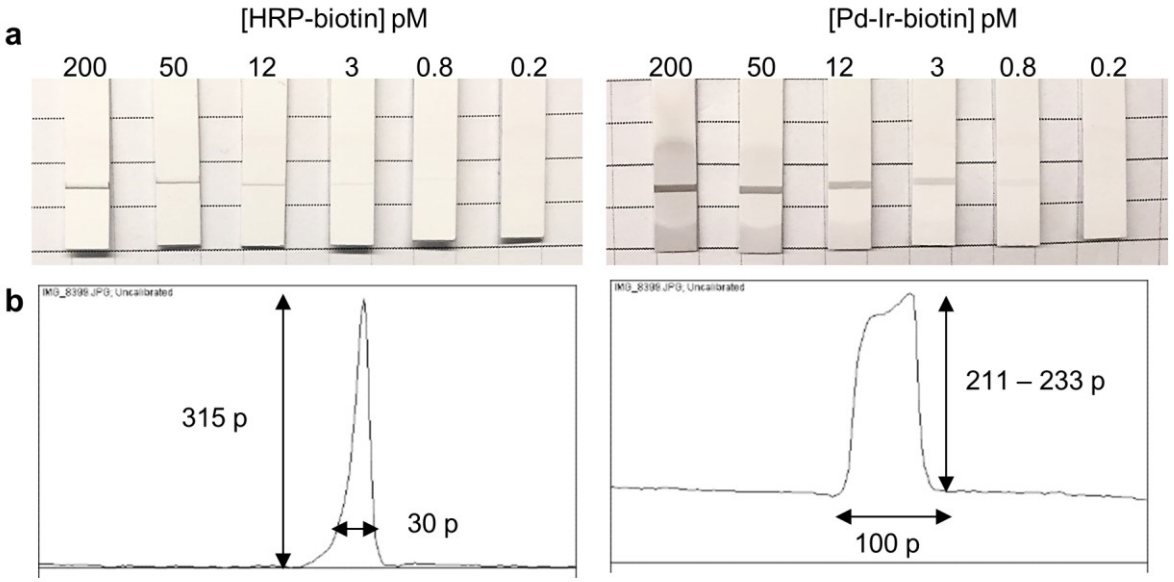


Figure 2.37 (a) Images comparing sharpness of test line interfaces for biotinylated HRP and Pd-Ir nanocube captured on streptavidin test line after catalytic development with CN/DAB. (b) Intensity profiles for test lines corresponding to 200 pM biotinylated HRP (left) or Pd-Ir (right), where taller peaks represent darker test lines and wider peaks represent wider test lines.

An additional parameter worth further investigation is the effect of AuNP core size on PtNC activity. While 15 and 40 nm core AuNPs were investigated in this chapter (Figure 2.18), 1.5 nm gold nanoclusters presented in Chapter 3 may also serve as a core material for PtNC synthesis, potentially increasing the internal porous surface area. Another area of interest for further exploration would be hollow nanostructures, *e.g.* nanocages or nanoframes which can engage both outer and inner atoms for catalytic reactions *via* hollow interiors or porous architecture.[143] Finally, an extensive investigation on the role of capping agents, reducing agents and nanoparticle shape, and porosity on peroxidase mimicking activity would enable the development of next generation catalytic labels in biosensing applications.

Chapter 3

Catalytic Nanoclusters for *In Vivo* Disease Monitoring

3. Catalytic nanoclusters for *in vivo* disease monitoring

3.1 Introduction

3.1.1 Aims

This chapter investigates the use of catalytic nanoparticles in a biosensing system for detection of protease activity *in vivo*. Several synthesis strategies are explored for the development of a renally clearable catalytic nanomaterial. Promising systems are taken forward for further development into a functional protease nanosensor for *in vitro* and *in vivo* detection of disease state.

3.1.2 Background

There is a need for simple and sensitive diagnostic tools to enable early detection of disease, particularly in low and middle-income countries, which bear a significant burden of both infectious and noncommunicable disease.[144] Mortality rates due to infectious diseases worldwide have substantially decreased, meaning that the effects of an increasing ageing population will lead cancer to become a primary cause of morbidity and mortality in coming years.[8] With this brings the challenge of how to tackle the cancer burden from a global health perspective. Surveillance, screening and new diagnostic tools that are globally accessible will be key in addressing the challenges of global oncology. Additionally, diagnostic tools that monitor for cancer recurrence after treatment would be useful for home settings as follow up to clinical care. Particularly, advances in nanotechnology offer solutions in the form of infrastructure-free detection tools, that when applied globally, irrespective of the local resources available, can enable earlier diagnosis and better treatment.

Early detection of disease requires specific and sensitive biomarkers that can inform clinical decisions and improve patient outcomes. In the case of cancer, when diagnosed early, many primary tumors can be treated effectively without invasive clinical interventions.[144] However, a challenge is the prohibitively low rates at which most biomarkers are shed from tumors, impeding early detection. Recent computational studies estimated that tumors could remain undetectable for over a decade before concentrations of blood biomarkers become sufficiently elevated to detect disease, which corresponds to a tumor size > 2.5 cm in diameter.[37] The insufficient sensitivity of blood biomarkers is primarily due to the tremendous dilution factor on release of the proteins from tumor cells into systemic circulation. To overcome the

insensitivities of static blood biomarkers, enzymatic turnover, *e.g.* proteolytic activity, can be leveraged to amplify responses to disease-specific environments.

Protease activities are implicated in a wide range of human diseases including; cancer, inflammation, and infectious diseases such as HIV and malaria. Because of their biological importance, proteases have been used as biomarkers for diagnosis and patient monitoring.[38] Protease activity is typically measured by the cleavage of functionalized peptide substrates, resulting in a detectable contrast change. The most common tools are: substrate-based probes that fluoresce upon proteolytic cleavage in the disease environment; high resolution mass spectrometry techniques to analyze the peptide fragments produced by proteolytic cleavage events; and as recently demonstrated, the use of T_1 magnetic resonance imaging to detect distance-dependent changes driven by proteolysis.[19,145–149]

Over the last five years, Sangeeta Bhatia and co-workers have developed multiplexed protease-responsive nanoparticles, which release small reporter probes into the urine in response to proteolytic cleavage in disease environments.[39,41–43,150,151] Kwong *et al.* exemplifies the protease-responsive nanomaterial platform for multiplexed detection of disease.[39] In this platform, a nanosensor composed of an iron oxide nanoparticle core (*ca*. 30 nm diameter) is functionalized with protease-cleavable peptide sequences that are tethered to mass-encoded peptide reporter fragments. Each mass-encoded peptide is associated with a protease implicated in a specific disease state, thus ten different mass-encoded peptides allow for multiplexing and subsequent detection of multiple proteases in one sample. The nanosensors are injected into the bloodstream, and the nanoparticle acts as a chaperone to guide the probe to the disease site through passive accumulation *via* leaky vasculature. After arrival in the disease microenvironment, the nanosensors are cleaved by aberrantly active proteases, releasing the mass-encoded peptide fragments into the host urine for detection by mass spectrometry. The detection of specific mass fragments in the urine can be correlated to the activity of various proteases *in vivo.* The efficacy of this platform was first demonstrated for noninvasive detection of liver fibrosis and early stage colorectal cancer without the need for invasive biopsies. Additionally, this study showed that monitoring protease activities can provide early detection of cancer compared to clinically used blood biomarkers by taking advantage of the combined effects of protease amplification and renal concentration. An advantage of this system is the amplification of disease-specific responses by leveraging enzymatic turnover. For example, a single copy of a protease can cleave hundreds of peptides per hour. The renal system's natural capacity to rapidly remove < 5.5 nm particles and filter them into urine (*e.g.* from 5 L blood to 300 mL excreted urine volume) is an additional concentration and sensitivity enhancement.[152] If measured in the blood *ex vivo*, secreted

proteases are significantly diluted in circulation, and are challenging to detect above plasma proteins and pan-protease inhibitors in plasma, which motivates the detection of proteases *in vivo* at the disease site.[39]

In the protease nanosensor platform, reporter probes can be engineered so that they can be detected in urine by a range of analytical techniques, including mass spectrometry[39] and immunoassays.[41] While these techniques offer high sensitivity for protease detection, they also require specialized imaging and analytical equipment, which may not be available in non-hospital and resource-limited settings. New diagnostic tools that can probe protease activity with a simple and sensitive readout are required for precision medicine to become globally accessible. The ability to monitor protease activities *in vivo* with a simple and sensitive readout may enable earlier detection and monitoring of disease at the point-of-care (PoC).

3.1.2.1 Protein and peptide templated nanoclusters

Development and characterization of functional metal nanoclusters are of interest for biosensing and bioimaging applications due to their facile synthesis and unique properties that differ from conventional gold nanoparticles (> 4 nm). Many of the protein-templated nanocluster synthesis methods are inspired by the pioneering work of Xie *et al.*, who first reported a one-pot synthetic route for preparation of gold nanoclusters (AuNCs) using the "biomineralization" capability of bovine serum albumin (BSA).[153] In a biomineralization approach, nucleation, growth and patterning of inorganic structures are controlled by interfacial interactions between mineral and protein surfaces. Here the proposed mechanism of formation of AuNCs is the sequestering of gold ions by thiols (cysteine residues) on the protein, which are further reduced in a basic environment (pH ~ 12) to gold atoms stabilized within the protein. Following the work on BSA templated-AuNC synthesis, there have been reports of nanoclusters templated in a variety of proteins with a broad range of sizes and biological activities including horseradish peroxidase, insulin, and lysozyme.[154–156] An advantage of using a protein template for nanoparticle growth is the abundance of surface functional groups that can be used for post-synthesis modifications.

Thiolate monolayer protected gold nanoclusters are another common class of < 5 nm diameter nanoparticle. The synthesis of these particles is based on the formation of gold-thiolate complexes which are reduced at elevated temperatures or with strong reducing agents (*e.g.* sodium borohydride) over time to form AuNCs (Figure 3.1).[157] These AuNCs are composed of tens to hundreds of atoms which are protected by the peptide used in the synthesis through sulfur-gold staple motifs.[158] The tripeptide glutathione (GSH, γ-Glu–Cys–Gly) has been used

extensively as a capping ligand and weak reducing agent for the synthesis of < 2 nm diameter noble metal nanoclusters (GSH-AuNCs).[157,159] GSH can reduce Au^{3+} to Au^{0} following:[160]

$$6\ GSH + 2\ Au^{3+} \rightarrow 2\ Au^{0} + 3\ GSSG + 6\ H^{+}$$

In this one-pot synthesis method, glutathione molecules react with gold ions to form Au (I)-GS oligomer complexes, which dissociate into < 2 nm AuNCs with mixed valence states over time.[161,162] Work by Jie Zheng and co-workers has demonstrated the efficient renal clearance properties and biocompatibility of GSH protected metal nanoclusters and subsequently has used these materials in a range of *in vivo* bioimaging applications, making significant strides toward clinical translation of AuNC-based imaging agents.[152,161,163–166] Specifically, the pharmacokinetics and renal clearance efficiencies of glutathione protected metal nanoclusters has been investigated in terms of particle size[167], particle density (comparing gold and silver cores),[168] length of zwitterionic capping ligand,[164] surface charge,[169] dose-dependent transport in the blood stream,[170] passive tumor targeting ability,[171] and biocompatibility studies in both mice and non-human primates.[170]

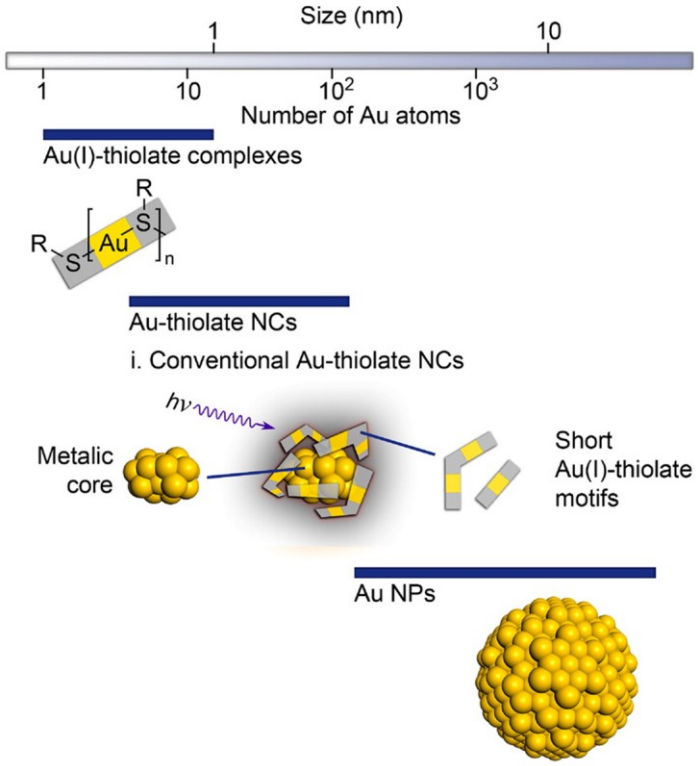


Figure 3.1 Schematic of the structure of Au-thiolate nanoclusters formed from Au(I) thiolate motifs. Figure adapted from Luo *et al*. with permission.[157]

3.1.2.2 Catalytic activity of noble metal nanoparticles

The ultra-small size of gold nanoclusters (AuNCs) (< 2 nm) induces quantum confinement effects, which result in discrete electronic and molecular-like properties, such as enhanced photoluminescence, intrinsic magnetism, and catalytic activity.[108,172] As a result of their unique properties, AuNCs have been used extensively for fluorescence and X-ray contrast bioimaging applications *in vivo*.[159,173,174] The intrinsic catalytic activity of AuNCs has also been explored for *in vitro* biosensing.[175] For example, Tao *et al.* developed a platform for rapid naked-eye detection of HER2-positive breast cancer cells using peroxidase-mimicking AuNCs encapsulated in an antibody targeted liposome.[176] The AuNC-loaded liposomes could capture breast cancer cells, which could be easily visualized with a colorimetric development step using a peroxidase substrate. The signal amplification of catalytic AuNCs provided a simple colorimetric readout of disease state, however, this property has yet to be explored for *in vivo* biosensing.

Noble metal nanoparticles and nanoclusters can function as catalysts to disproportionate H_2O_2 to generate hydroxyl radicals, which in turn can oxidize a chromogenic substrate, providing a colorimetric measure of activity, similar to the biological enzyme horseradish peroxidase (HRP).[53,59,175] Employing peroxidase-mimicking catalytic AuNCs as reporter probes in sensing applications may enable rapid and facile disease diagnosis in PoC settings, where equipment and personnel may be limited. This can be addressed by leveraging the catalytic activity of AuNCs to develop a nanoscale system that produces a direct colorimetric urinary readout of disease state. Kidney filtration is a desirable pathway for particle clearance, because glomerular filtration is highly dependent on size, charge, and shape. The filtration-size threshold for glomerular proteins is generally accepted to be *ca*. 5 nm in hydrodynamic diameter.[177–179] The hypothesis is that by producing AuNCs < 2 nm capped with a zwitterionic peptide to minimize *in vivo* protein adsorption, renal filtration could be used to concentrate AuNCs in urine and subsequently harness their intrinsic catalytic activity for a colorimetric readout.

3.1.2.3 Renal clearance of nanoparticles

To meet the requirements of the U.S. Food and Drug Administration (FDA), all injected contrast agents need to be cleared from the body in a reasonable time frame. Excretion is a biological process that eliminates unwanted materials from the body by two major routes: renal (urine) and hepatic (bile to feces). Understanding nano-bio interactions, which govern the targeting, clearance, and sequestration properties of nanoparticles in the body, is key to

effectively translate nanomaterials into clinical applications. Kidney filtration and renal clearance of nanoparticles is a desirable route of excretion, as the main function of the kidneys is to filter particles from the blood and quickly remove them from the body. Due to the fast clearance pathway *via* the kidneys, the potential toxicity of renally clearable nanoparticles is reduced. With the aim of developing a sensor that can be efficiently cleared through the kidneys, a basic understanding of the transport mechanisms of metal nanoclusters in the kidneys is critical. A recent review by Du *et al.* covers the key aspects of nanoparticle transport and interactions in the kidneys with particular focus on metal nanoclusters.[152] In particular, there are strong size, charge, composition and shape dependencies which dictate renal clearance efficiencies.

Kidney filtration is strongly size-dependent owing to the architecture of the glomerular filtration membrane (GFM).[167] For example, low molecular-mass proteins with a hydrodynamic diameter (D_h) < 6 nm can easily cross glomerular filtration barriers, while the kidney filtration threshold for metal-based nanoparticles is 5.5 nm, which was defined by the renal clearance of quantum dots of different sizes.[180] Thus the pore size of the GFM prevents the filtration of nanoparticles with D_h > 6 nm, resulting in an increased accumulation of particles in organs of the reticuloendothelial system (RES), which includes the liver and spleen. In the RES, macrophages can internalize nanoparticles and, if not degradable, retain them for a long time in the body, which can lead to unintended side effects and potential for long-term toxicity of accumulated particles. Engineered nanoparticles in the size range of 1 – 6 nm are readily cleared into the urine; however, their clearance efficiency depends greatly on size within this range. Gold nanoparticles in the 1 - 2 nm size range exhibit renal clearance efficiencies of *ca*. 50 % injected dose (ID) 24 h post injection (p.i.)., however a strong decrease in clearance efficiency was observed for nanoparticles outside of this range.[167] As expected due to the pore size of the GFM, a significant decrease in renal clearance efficiency was observed for 6 nm AuNPs (4 % ID) 24 h p.i. Surprisingly, Du *et al.* also showed a decrease in renal clearance efficiency for nanoparticles with $D_h \leq 1$ nm, which have stronger interactions with the GFM and tend to get trapped within the membrane hindering clearance over short time frames, leading particles in the 1 – 2 nm regime to be the optimal size for rapid renal clearance.[167]

Another important consideration in renal clearance of nanoparticles is charge, since the GFM behaves like a charge-selective barrier due to the presence of negatively charged heparan sulfate proteoglycan. Cationic polymers and proteins have shown faster renal clearance than neutral or anionic counterparts due to electrostatic interactions with the GFM. However for peptide-templated nanoclusters, strongly negatively charged particles (GSH-AuNCs) have been shown to clear faster than weakly negatively charged particles, which are faster than

positively charged particles.[169] The difference in charge dependent clearance between proteins and nanoparticles may be due to other effects such as shape, flexibility, ligand length and density and requires further investigation.

An example of a promising clinically translatable inorganic particle was designed by Bradbury and co-workers, who synthesized renal clearable silica nanoparticles (C dots; Cornell dots) that can be used for positron emission tomography and optical dual modality imaging.[181] C dots have been applied in cancer detection, selectively targeting disease (and metastases) while exhibiting bulk renal clearance. C dots have recently been tested in a phase 0 human clinical trial, successfully translating the use of renally excreted inorganic nanoparticles from mouse to human.[181]

3.1.2.4 Hepatic clearance of nanoparticles

The hepatic system represents the primary route of excretion for particles that do not undergo renal clearance. The liver is an important organ for the elimination of foreign substances and particles through phagocytosis. In contrast to small molecules, or nanoparticles < 5.5 nm in diameter, which can be eliminated in urine within several hours to days, nanomaterials in the *ca*. 5.5 – 100 nm size regime are often severely trapped in the RES for a long time.[178] For example, liver accumulation of non-renally clearable inorganic nanoparticles are generally in the range of 10 – 100% ID/g 4 – 48 h p.i., which is 10 – 1000 time higher than liver uptake of renally clearable nanoparticles or small molecular probes.[182] Unless the larger nanoparticles can dissociate or degrade into smaller fragments (< 5.5 nm), they will not filter through the kidneys. Because of the high surface energy of nanoparticles, once they are introduced into the bloodstream, a “protein corona” is generally formed, resulting from the adsorption of *ca*. 3000 kinds of serum proteins in the blood.[182] Serum protein adsorption results in an increase of the hydrodynamic diameter and initiation of macrophage uptake in the RES. Adsorption of opsonins on nanoparticles, known as opsonization, also initiates the rapid recognition by the receptors on the cell surface of macrophages in RES and results in internalization by macrophages, which results in the sequestration of opsonized nanoparticles by the liver and spleen. Coating nanoparticles with polyethylene glycol (PEG) is a common strategy to reduce opsonization. While PEGylation can increase blood circulation time, ultimately the majority of particles > 5.5 nm will accumulate in RES organs.

The role of macrophages is to internalize foreign objects and digest them using enzymes in the lysosomes. However, since gold nanoparticles are chemically stable, they are often retained in the body for months to years once they are internalized by macrophages since

they cannot be effectively digested by lysosomal enzymes. On the other hand, iron oxide[183] and silica nanoparticles[184] can decompose inside macrophages and are eliminated through bile excretion, but elimination is very slow compared to renal clearance of small molecular probes (weeks to months compared to hours/days for the latter). Significant progress has been made in the last decade on developing inorganic nanoparticles that are renally clearable with high renal clearance efficiencies. This has been achieved primarily by reducing nanoparticle size below the glomerular filtration threshold, and by developing protein-adsorption resistant surface chemistry. Zwitterionic ligands, namely glutathione, have emerged as excellent capping agents to minimize protein adsorption.[152,182]

3.1.2.5 Tumor targeting ability of engineered nanoparticles

In the same way that nanoparticles can be engineered to promote renal clearance, they can also be designed to target specific disease environments. For example, if a nanoparticle is intended for use in imaging or detection of tumors, it is important to consider how the nanoparticle might target the disease state as well as be cleared efficiently from the body in a reasonable time frame. However, there are many challenges with achieving high tumor targeting efficiency, as evidenced in the literature over the last decade, only 0.7 % (median) of the administered nanoparticle dose is found to be delivered to the solid tumor, which is mainly due to the competing clearance and uptake process in the complex *in vivo* environment.[185]

The main route for nanoparticle transport to a tumor environment is through the enhanced permeability and retention effect (EPR), which is passive targeting of nanoparticles caused by high-density and leaky tumor vasculature leading to accumulation of nanoparticles > 5.5 – 100 nm in the tumor site. The ability of nanoparticles to passively target and accumulate in tumor environments due to EPR relies on their ability to escape kidney filtration, delay uptake by RES, and be retained in the blood plasma for longer time scales than small molecules. The challenge of achieving both tumor targeting and renal clearance is that the design requirements are contradictory. Liu *et al.* investigated the tumor targeting ability of renal clearable GSH-AuNCs. Due to their molecular size, GSH-AuNCs achieve rapid kidney filtration, which should limit passive tumor accumulation.[171] However, Liu *et al.* found that GSH-AuNCs can also passively target tumors through the EPR effect owing to their density-dependent margination in blood vessels (Au, 19.3 $g \cdot cm^{-3}$, denser than other circulating small molecules) where high-density gold nanoparticles more quickly marginate to the blood vessel wall which slows their elimination from the blood into the urine.[168] Furthermore, any AuNCs not accumulated in the tumor environment are efficiently excreted through the kidneys.

Some strategies for active tumor targeting have been to incorporate tumor-specific antibodies, aptamers or other affinity ligands onto nanoparticles for targeting receptors on tumor cells or tumor vasculature, or by targeting tumors with tumor-penetrating peptides.[186] Tumor-penetrating peptides are a unique class of peptides that mediate active internalization and transport of nanomaterials into tumor tissues.[43]

3.1.3 Overview

This chapter presents the design of catalytic AuNC-functionalized protease nanosensors that are disassembled in response to dysregulated protease activity at the site of disease and cleared *via* the kidneys to provide a colorimetric readout in urine (Figure 3.2). A versatile and modular peptide-templated method was developed to synthesize protease-responsive AuNCs, and AuNCs were subsequently tethered to a protein carrier for delivery *in vivo*. The overall size of the AuNC-protein complex is larger than the renal filtration threshold. However, upon interaction with the target protease, the AuNC-protein complex is disassembled, liberating the AuNCs. The system was designed to employ nanocatalysts that are both small enough to be filtered through the kidneys following proteolytic cleavage, and to contain a surface capping ligand for significant retention of catalytic activity in complex physiological environments. With this method, it was demonstrated that the synthesized AuNCs were small enough to be filtered efficiently through the kidneys and retained catalytic activity in cleared urine. Figure 3.2 outlines the nanocatalyst sensing platform: (a) First catalytic AuNCs were conjugated to a protein scaffold *via* a protease-cleavable peptide linker to create a complex which was above the renal clearance size threshold. (b) The AuNC-protein complex was injected intravenously, could interrogate the complex physiological environment, and could be disassembled in response to disease-associated proteases. (c) AuNCs that were liberated from the protein scaffold by proteases are *ca*. 1.5 nm in diameter and were efficiently cleared by the kidneys. (d) A colorimetric assay was used to measure the peroxidase-like activity of collected urine as a measure of cleared AuNCs.

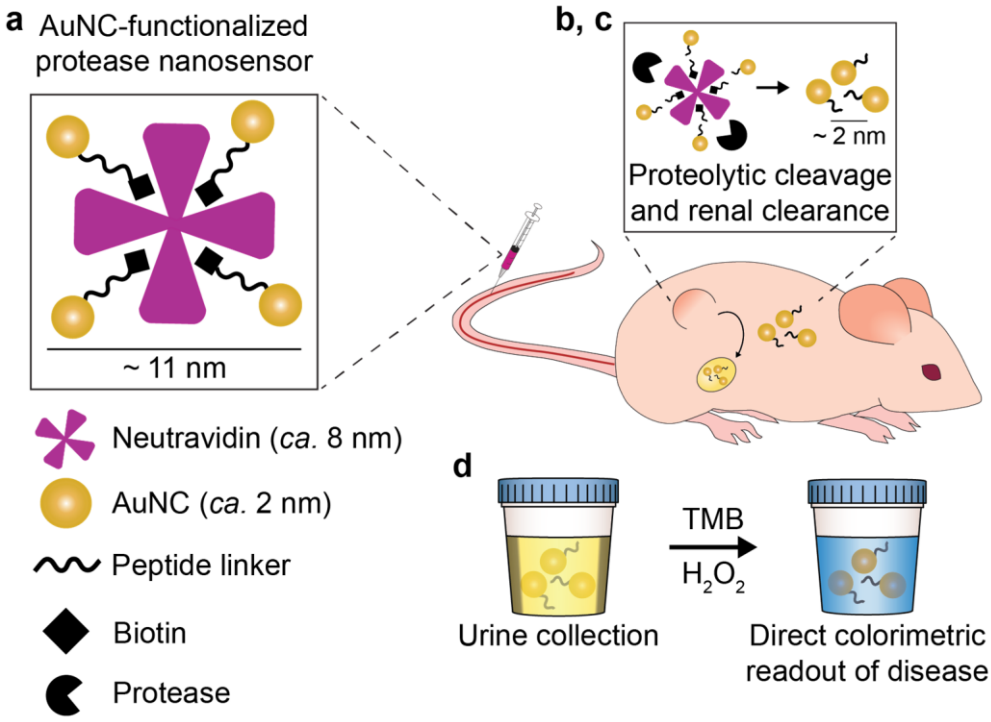


Figure 3.2 Design of nanocatalyst signal amplification sensing system. (a) Catalytic gold nanoclusters (AuNCs) were conjugated to a neutravidin protein scaffold through a biotinylated protease-cleavable peptide linker. (b) The protease-sensitive nanocluster complex was injected intravenously and designed to specifically disassemble when exposed to the activity of relevant dysregulated proteases at the site of disease. (c) After protease cleavage, liberated *ca*. 1.5 nm AuNCs were filtered into the urine. (d) Colorimetric assay to measure peroxidase-like activity was performed on collected urine to detect cleared AuNCs.

The focus here is on the detection of two model proteases that are relevant in major diseases, thrombin and MMP9. Thrombin is a serine protease that plays a key role in the formation of obstructive blood clots, or thrombosis, which is a life-threatening condition associated with diseases such as stroke and atherosclerosis.[187] MMP9 is a member of the matrix metalloproteinase (MMP) family of zinc-dependent enzymes, which is comprised of critical extracellular matrix remodeling proteases whose activity has been implicated in all stages of cancer progression.[188,189] To demonstrate the modularity of the system, a library of functionalized peptide substrates were synthesized and shown to be specifically cleaved by either thrombin or MMP9. These peptides were then used as templates for the synthesis of catalytic AuNCs, and further assembled into nanosensors. The response of the library of protease nanosensors to disease-associated proteases was assessed *in vitro* and evaluated against their utility for detection of thrombin and MMP9 activity. Then, the MMP-responsive nanosensors were applied *in vivo* to demonstrate disease detection with a rapid, colorimetric urinary readout in a mouse model of colorectal cancer. This system exhibits a dual amplification platform: leveraging both *in vivo* protease activity and inorganic catalytic activity of AuNCs to provide a PoC compatible colorimetric signal in excreted urine. The catalytic

probe system provides an amplification mechanism in the urine to significantly improve sensitivity and enables naked-eye visual readout of disease state directly in urine without the need for any additional sample processing.

3.2 Materials & Methods

3.2.1 Materials

All chemicals were purchased from Sigma-Aldrich unless otherwise stated. Milli-Q water (18.2 MΩ.cm) was used in all the experiments.

3.2.2 Solid phase peptide synthesis

Peptides were synthesized manually on Rink amide resin using standard fluorenyl methoxycarbonyl (Fmoc) chemistry. The Fmoc protecting group was removed from the resin by incubating with piperidine/DMF (20:80) for 2 x 10 min. Fmoc-protected amino acids were activated with 4 molar equivalents of the Fmoc protected amino acids, 3.95 molar equivalents of *N,N,N′,N′*-Tetramethyl-*O*-(1*H*-benzotriazol-1-yl)uronium hexafluorophosphate, and 6 molar equivalents of diisopropylethylamine in DMF. The coupling solution was added to the resin and the coupling reaction was allowed to proceed for three hours. Peptides were cleaved in trifluoroacetic acid/triisopropylsilane/H_2O (95:2.5:2.5) containing DTT for four hours. The solvent was removed in vacuum and the peptide was precipitated in cold ether. The crude products were further purified using reversed phase preparative high-performance liquid chromatography (Shimadzu) in an acetonitrile/water gradient under acidic conditions on a Phenomenex C18 Gemini NX column (5-micron pore size, a 110 Å particle size, 150 x 21.2 mm). Molecular weight of peptide library was verified using liquid chromatography-mass spectrometry (LC-MS, Agilent Technologies). Dr. Yiyang Lin assisted with peptide synthesis, purification, and analysis of LC-MS results.

3.2.3 Nanocluster synthesis & purification

3.2.3.1 Protein-templated nanoclusters

To produce lysozyme templated nanoclusters, in a typical synthesis, lysozyme (500 µL, 1 mM) was mixed with an equal volume of $HAuCl_4$ (500 µL, 6 mM) and incubated for 5 min at room temperature. Next, NaOH (50 µL, 1 M) was added to the reaction mixture to increase pH to ~ 12, and reaction was left at 37 °C gently shaking (500 rpm, Eppendorf ThermoMixer) for 12 h. To produce BSA-templated nanoclusters, in a typical experiment, $HAuCl_4$ (500 µL, 10 mM) was added to BSA solution (500 µL, 50 $mg \cdot mL^{-1}$), vortexed to mix and incubated at 37 °C. After 5 min incubation, NaOH (50 µL, 1 M) was added to the reaction mixture and the reaction was allowed to proceed shaking at 500 rpm and 37 °C for 12 h. The reaction could

be performed at small scale (1 mL) in Eppendorf tubes or at larger scale in round bottom flask by maintaining protein to metal ratio.

Nanoclusters were purified through centrifugal ultrafiltration (Amicon Ultra centrifugal filter units Ultra-15, MWCO 10 kDa, Sigma) and buffer exchanged into phosphate buffered saline (PBS, pH 7.4).

3.2.3.2 Peptide-template nanoclusters

Synthesis and purification of peptide capped AuNCs followed published procedures with modifications outlined below.[159] Briefly, freshly prepared aqueous solution of gold(III) chloride trihydrate aqueous solution ($HAuCl_4$, 20 mM, 100 µL) was mixed with 750 µL deionized water in an Eppendorf tube, followed by fast addition of L-Glutathione reduced (GSH, 20 mM) and either peptide P1 or P2 (20 mM) so that final peptide content was fixed at a total volume of 150 µL in varying ratios of P1/P2:GSH at 25 °C. The reaction mixture was heated to 70 °C under gentle stirring (500 rpm) for 24 h. The reaction mixture changed from yellow to colorless within minutes and then turned pale yellow over *ca*. 12 h, indicating first reduction of Au (III) to Au (I) by the thiol group of the peptides, followed by the reduction of Au(I) thiolate complexes to Au(0) atoms over time assisted by the favorable reduction kinetics at the elevated reaction temperature.[157,190] After 24 h synthesis, the resulting AuNC solution exhibited both orange luminescence and simultaneous peroxidase-like activity. The AuNCs could be stored at 4 °C for > 6 months with negligible changes in optical or catalytic properties. The as-prepared AuNCs were purified through centrifugal ultrafiltration (Amicon Ultra centrifugal filter units Ultra-15, MWCO 10 kDa, Sigma) and buffer exchanged into phosphate buffered saline (PBS, pH 7.2). During ultrafiltration, the AuNCs were collected in the concentrate in the filter device, while any unbound peptide was collected in the filtrate. After purification, AuNCs were resuspended in PBS (20 µM [AuNC]) and sterile filtered (Millex-GV Filter, Millipore, 0.22 µm).

The number of biotinylated ligands per AuNC was calculated by measuring biotin concentration in the filtrate from AuNC purification above, and subsequently subtracting this value from the starting concentration of biotinylated peptide used in the synthesis. Biotin concentration in the filtrate was quantified using the Pierce Biotin Quantitation kit following manufacturer's instructions (Thermo Fisher) without any modifications. The molarity of biotin in the sample was calculated using Beer Lambert's Law: $A = \varepsilon lc$, where A is the absorbance of the sample; ε is the extinction coefficient at a particular wavelength, for HABA/avidin at 500 nm it is 34000 $M^{-1}cm^{-1}$; l is the path length in cm, *ca*. 0.5 cm for 200 µL volume in a 96 well plate; and C is concentration in mol/L.

3.2.4 Characterization of Nanoparticles

Dynamic light scattering (DLS, Zeta Sizer Nanoseries, Malvern Instruments, Ltd.) was used to characterize the hydrodynamic diameter of nanoparticles. Number particle size distributions are reported for AuNC size analysis as it represents the number of particles in different size bins. The intensity distribution is dominated by large particles which scatter more intensely as the intensity is proportional to D^6, where D is the particle diameter. The intensity distributions emphasize the larger particles in the distribution, while the number distributions emphasize the smaller particles in the distribution. The number size analysis agrees well with the observed size by TEM image analysis and thus was used in the following figures. Absorption measurements were recorded on a SpectraMax M5 multimode microplate reader (Molecular Devices, Ltd.). For electron microscopy characterization, samples were drop-casted onto carbon-coated copper grids (Electron Microscopy Sciences), and TEM imaging was performed using a JEOL 2100F operating at 200 kV. For preparation of TEM samples, AuNC samples were first desalted (Zeba Spin Desalting Columns, 7K MWCO, Sigma) and 5 µL desalted sample was dropped onto the grid, allowed to incubate for 5 min, and subsequently wicked with filter paper and dried overnight before imaging. Dr. Qu Chen assisted with high resolution TEM imaging.

3.2.5 Evaluation of Peroxidase-like Activity

For stability and catalytic activity of AuNCs in physiological environments, AuNCs (20 µM, 50 µL) were incubated with PBS (50 µL), synthetic urine (Surine Negative Urine Control, Sigma), or fetal bovine serum (FBS, Gibco) for 1 h at 37 °C followed by five-fold dilution in water. For the activity assay, 50 uL of each sample was added to a 96-well plate (Corning, UK) followed by 150 uL chromogenic substrate solution: 1-Step Ultra TMB ELISA Substrate Solution (Thermo Scientific) spiked to a final concentration of 4 M hydrogen peroxide (30 % (w/w), Sigma). The absorbance of the reaction solution at 652 nm was monitored up to 25 min after addition of substrate, corresponding to oxidation of TMB by H_2O_2.

For limit of detection assays, in a 96-well plate, synthetic urine (25 µL) was mixed with AuNCs (25 µL, varying concentrations, diluted in PBS), 5 M H_2O_2 (100 µL), and 1-Step Ultra TMB ELISA Substrate Solution (100 µL). Absorbance at 652 nm was measured every 20 s for 10 min, and linear regression was used to calculate the slope (Absorbance/sec) over the first 150 sec.

3.2.6 Steady-state kinetic assays

Steady-state kinetic assays were carried out at room temperature in a 96-well plate with 220 µL solution with estimated path length (*l*) of 0.5 cm. 25 mM NaOAc/HOAc solution (pH 4.0) was used as the reaction buffer. For kinetic assays varying 3,3′,5,5′-Tetramethylbenzidine (TMB), AuNCs (20 µM, 20 µL) were mixed with TMB (10 µM to 1 mM, 100 µL) and H_2O_2 (5 M, 100 µL).

For kinetic assays varying H_2O_2, AuNCs (20 µM, 20 µL) were mixed with H_2O_2 (0 to 10 M, 100 µL) and TMB (1 mM, 100 µL). After addition of substrates (TMB and H_2O_2) in the buffer system containing AuNCs, the absorbance of the reaction solution at 652 nm of each sample was immediately measured as a function of time with intervals of 20 s using a spectrophotometer for 10 min. These "absorbance *vs* time" plots were then used to obtain the slope at the initial point ($Slope_{Initial}$) of each reaction (over first 150 s). The initial reaction velocity (*v*) was calculated by $Slope_{Initial}/(\varepsilon_{TMB\text{-}652\ nm} \times l)$, where $\varepsilon_{TMB\text{-}652\ nm}$ is the molar extinction coefficient of TMB at 652 nm, which is $3.9 \times 10^4\ M^{-1}\cdot cm^{-1}$. The plots of reaction velocity, *v,* against TMB and H_2O_2 concentrations were fitted using nonlinear regression of the Michaelis-Menten equation. The kinetic parameters were calculated based on the Michaelis-Menten equation (**Equation 3.1**):

$$v = \frac{V_{max}[S]}{K_m + [S]} \quad (\mathbf{3.1})$$

where V_{max} represents the maximal reaction velocity, [S] is the concentration of substrate, and K_m is the Michaelis-Menten constant. Vmax was obtained from fitting to the model using GraphPad Prism software, and the catalytic constant (k_{cat}) was calculated using the equation: $k_{cat} = V_{max}/[E]$, where [E] is the AuNC concentration.

3.2.7 AuNC complex assembly and purification

In a typical conjugation, 125 µL NeutrAvidin Protein (120 µM, PBS, Thermo Fisher, NAv) was mixed with 1 mL of AuNC-P1 or AuNC-P2 (20 µM) and incubated for 12 h gently shaking (500 rpm) at 37 °C. Unbound AuNCs were removed from AuNC-NAv complexes through centrifugal ultrafiltration (Amicon Ultra centrifugal filter units Ultra-15, MWCO 50 kDa, Sigma), where AuNC-NAv complexes remained in concentrate and any unbound AuNCs were collected in the filtrate. After ultrafiltration, AuNC-NAv complexes were resuspended in PBS (30 µM by [AuNC]) and sterile filtered (Millex-GV Filter, Millipore, 0.22 µm).

3.2.8 Gel filtration chromatography assays

AuNC-NAv complexes were first incubated with a recombinant enzyme: MMP9 (Active, Human, Recombinant, PF140, Merk Millipore); MMP7 (Active, Human, Recombinant, *E. coli*, 444270, Merk Millipore); MMP13 (Active, Human, Recombinant, 444287); or thrombin from human plasma (T7009, Sigma, 100 units/mL in a 0.1% (w/v) bovine serum albumin solution). Enzyme and AuNC-NAv were incubated at 37 °C gently shaking (500 rpm). Incubation times varied (1 – 12 h) and concentration of enzyme varied (50 – 100 nM), where the final peptide substrate concentration was maintained at > 1000 molar excess to enzyme concentration (see Figure captions).

Three identical glass chromatography columns were packed with Sephacryl S200 high resolution resin (column D: 1 cm, H: 18 cm, resin: GE Healthcare Life Sciences, fractionation range for globular proteins 5 – 250 kDa) to separate samples based on size (Figure 3.3). Columns were thoroughly cleaned between experiments with PBS. In a typical gel filtration chromatography (GFC) experiment, *ca*. 200 µL of 20 µM AuNC-PX, AuNC-PX-NAv, and AuNC-PX-NAv + enzyme (after incubation) were loaded onto each column in parallel. As soon as the sample was added to the resin bed, 24, 500 µL fractions were collected into individual Eppendorf tubes, while PBS was added to the column reservoir. After fractions were collected, a catalytic activity assay was performed on the samples. For the activity assay, 100 µL of each fraction was added to a 96-well plate, followed by 100 µL substrate solution (1-Step Ultra TMB ELISA Substrate Solution with 4 M H_2O_2). The absorbance of the reaction solution at 652 nm was monitored up to 25 min after addition of substrate, corresponding to oxidation of TMB by H_2O_2. The composition of the sample could be determined based on how quickly it eluted from the column as measured by activity. Larger AuNC complexes elute within the first 7 mL, and smaller bare AuNCs elute more slowly and are found in 7 – 12 mL, corroborated by DLS of column fractions. Absorbance at a fixed time point was plotted as a function of eluted volume, where clear peaks in absorbance are associated with either AuNC-NAv complexes or bare AuNCs. For AuNC-NAv complexes incubated with enzymes, the proportion of liberated AuNCs could be measured by calculating the area under the curve corresponding to 7-12 mL eluted volume (fractions corresponding to bare AuNCs).

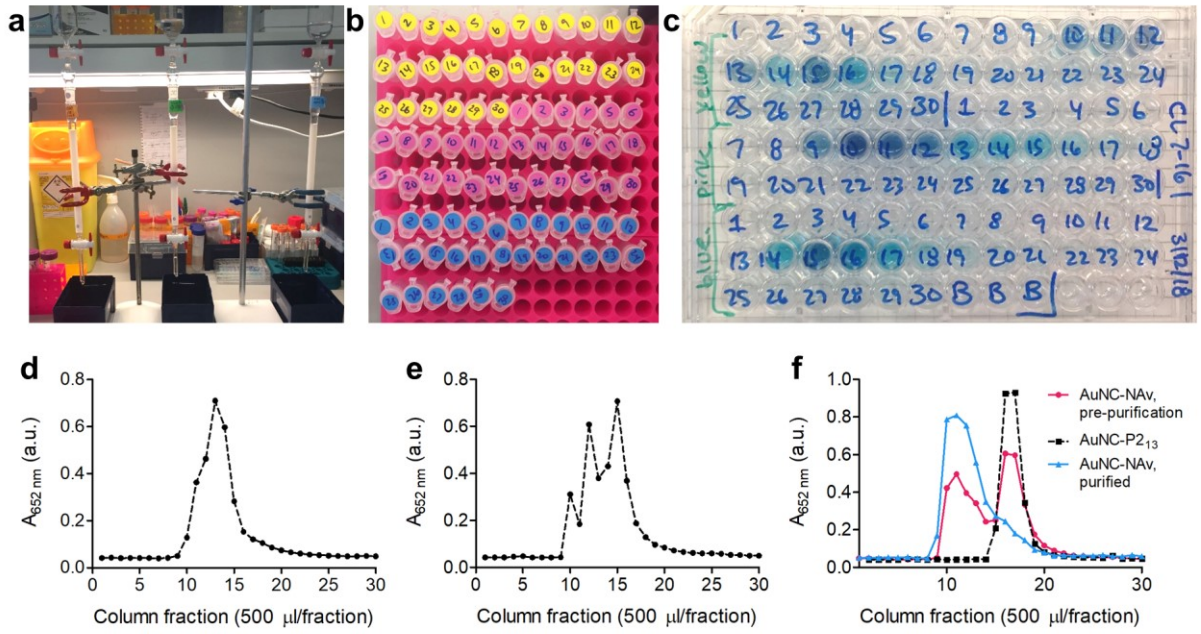


Figure 3.3 (a) Experimental gel filtration chromatography set-up for assessing *in vitro* cleavage of AuNC-neutravidin complexes. (b) 24-30 500 µL fractions are manually collected from each column. (c) Standard 96-well plate showing result of colorimetric assay, which is performed on collected fractions to assess which fractions contain AuNC-neutravidin complexes or liberated AuNCs after enzyme incubation based on elution volume (proportional to size). Each well contains 100 µL column fraction and 100 µL TMB/H_2O_2 substrate mix. (d) Colorimetric assay results of enzyme cleavage experiment using S300 resin (10 – 1500 kDa fractionation range), which is not able to effectively separate free AuNCs from AuNC-NAv complex. (e) Colorimetric assay results of enzyme cleavage experiment using S200 resin (5 – 250 kDa protein fractionation range). Clear peaks associated with different cleavage products indicate that S200 resin can effectively separate components of different sizes. (f) Optimized colorimetric assay results using S200-High resolution resin show well defined peaks associated with free AuNCs, AuNC-NAv complex, and peaks associated with both for unpurified AuNC-NAv complex (including a peak associated with unbound AuNCs).

3.2.9 Fluorescence correlation spectroscopy (FCS)

For FCS analysis, AuNC-P1 and AuNC-P2 were labeled with 50 molar excess reactive dye (Oregon Green 488 Carboxylic Acid, Succinimidyl Ester, 6-isomer, Thermo Fisher), further called AuNC-PX-OG. Unreacted dye was removed using Zeba Spin Desalting Columns 7K MWCO (Thermo Fisher). AuNC-PX-OG-NAv complexes were assembled following above protocol and purified to remove unbound AuNC-PX-OG. AuNC-PX-OG-NAv complexes were further incubated with enzymes, and kinetics of AuNC complex disassembly *via* substrate cleavage was monitored over time using FCS. Dr. Adrian Najer performed FCS experiments and FCS data analysis.

Sample preparation for measuring enzyme cleavage kinetics

For MMP9: 0.33 µL MMP9 stock (Merck PF140 lot#2872521, 0.1 mg·mL^{-1} ~ 1500 nM, 57.28 Units/h/µg P) was added per 10 µL sample stock (20 µM, AuNC), for a final enzyme concentration of 50 nM, with AuNCs in 400 molar excess to MMP9. Since AuNCs bear *ca*. 20 peptide substrates per particle, there were *ca*. 8000 molar excess peptide substrates per enzyme.

For thrombin: 0.58 µL thrombin stock (100U/ml, 32µg/ml ~ 860 nM) was added per 10 µL sample stock (20 µM, AuNC), for a final enzyme concentration of 50 nM, with AuNCs in 400 molar excess to thrombin.

All enzyme incubations were performed at 37 °C, and incubations longer than 3 h were maintained at 37 °C while shaking (300 rpm). Samples were then diluted in PBS for FCS measurements.

FCS measurements

FCS was performed on a commercial LSM 880 (Carl Zeiss, Jena, Germany) equipped with an incubation chamber. All measurements were performed at 37°C. An Ar^+ laser was used as excitation source for the 488 nm wavelength. Appropriate filter sets were used to detect the fluorescence signal (LP 505). The laser beam passed through a 40x C-Apochromat water immersion objective with a numeric aperture of 1.2 to focus the beam into the sample droplet. Measurements were performed 200 µm above the ibidi 8-well bottom plate (80826, ibidi, Germany) using a 5 µL droplet of sample for each condition. OregonGreen 488 carboxylic acid in PBS (OG488, O6149, ThermoFisher Scientific, NHS-ester was first deactivated by overnight incubation in PBS at room temperature) was used as a standard to calibrate the beam waist (D = 4.1 x 10^{-6} cm^2/s at 25 °C, and when corrected for the higher temperature used: D = 5.49 x 10^{-6} cm^2/s at 37 °C).[191] Immediately before the measurement, stocks or incubated samples were diluted 100-fold in pre-warmed PBS and 5 µL was placed into the measuring chamber. The sample was equilibrated and bleached for 5 x 5 s and 25 x 5 s intensity traces were recorded, autocorrelated and analyzed for each sample. Autocorrelation curves were created in ZEN software (Carl Zeiss, Jena, Germany) and the curves were exported for further analysis using PyCorrfit program 1.1.1.[192] For all the graphs, data for the 25 curves are given except for the autocorrelation curves, which are always the average curve for the whole measurement (125 s) (Figure 3.4). First, stocks of clusters/complexes were fit using one component fits ($G_{1comp}(\tau)$) to obtain the diffusion times for the pure components.

Second, samples incubated with enzymes were fit with two component fits ($G_{2comp}(\tau)$) with one component fixed to pure cluster diffusion (τ_1) and the other fixed to pure complex diffusion (τ_2) to yield the fraction of free clusters (F_1), which is equivalent to the fraction cleaved. A triplet fraction with a triplet time of 10 µs was included for all the curves (**Equation 3.2**).

$$G_{1comp}(\tau) = \left(1 + \frac{T}{1-T} e^{\frac{-\tau}{\tau_{trip}}}\right) * \frac{1}{N*\left(1+\frac{\tau}{\tau_D}\right)*\sqrt{1+\frac{\tau}{SP^2\tau_D}}} \quad (\mathbf{3.2.1})$$

$$G_{2comp}(\tau) = \left(1 + \frac{T}{1-T} e^{\frac{-\tau}{\tau_{trip}}}\right) * \frac{1}{N} * \left[\frac{F_1}{\left(1+\frac{\tau}{\tau_1}\right)*\sqrt{1+\frac{\tau}{SP^2\tau_1}}} + \frac{1-F_1}{\left(1+\frac{\tau}{\tau_2}\right)*\sqrt{1+\frac{\tau}{SP^2\tau_2}}}\right] \quad (\mathbf{3.2.2})$$

T is the triplet fraction with corresponding triplet time τ_{trip}, N is the effective number of diffusing species in the confocal volume ($N = n1 + n2$), τ_D is the diffusion time (τ_1, τ_2 diffusion times of corresponding fractions), F_1 fraction of component with diffusion time τ_1, and SP is the structural parameter describing the ratio of height to width of the confocal volume (fixed to 5).

The following equation relates the x-y dimension of the confocal volume (ω_{xy}^2), which was calibrated by a standard measurement of OG488 in PBS, to the diffusion coefficient (D), which was calculated for each sample using the obtained diffusion time (τ_D) (**Equation 3.3**):

$$D = \frac{\omega_{xy}^2}{4\tau_D} \quad (\mathbf{3.3})$$

Stokes-Einstein equation was used to calculate hydrodynamic radii (R_h) *via* the obtained diffusion coefficients (diffusivity, *D*). η is the viscosity of the surrounding medium (PBS in this case), $k_B$is the Boltzmann constant, and T is the absolute temperature (**Equation 3.4**):

$$D = \frac{k_B T}{6\pi\eta R_h} \quad (\mathbf{3.4})$$

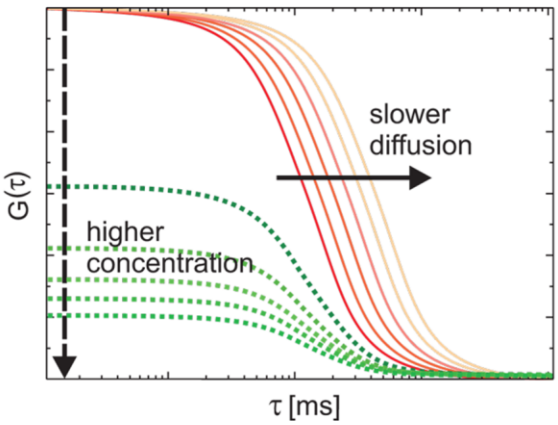


Figure 3.4 Examples of FCS autocorrelation curves. The diffusion time ($\boldsymbol{\tau_D}$) can be read from the half-maximum decay of $\boldsymbol{G(\tau)}$, which measures the average retention time of particles in the observation volume. Based on the detection volume calibration (*e.g.* using Oregon Green dye), it is converted into the diffusion coefficient. AuNCs bound to neutravidin core diffuse slower than free AuNCs. Figure adapted from PicoQuant GmbH.[191]

3.2.10 *In vivo* renal clearance studies

All animal studies were approved by the Massachusetts Institute of Technology (MIT) committee on animal care (MIT protocol 0417-025-20). GSH-templated and substrate functionalized AuNCs were diluted to 10 μM [AuNC] in sterile PBS. Wild-type female Swiss Webster mice (4-6wks, Taconic) were intravenously administered 2000 pmol AuNCs (200 μL, 10 μM) *via* the tail vein. After nanocluster injection, mice were placed in custom housing with a 96-well plate base for urine collection. After 1 h, their bladders were voided, and collected urine volume was measured. Clearance of active AuNCs was quantified *via* catalytic activity assay, and urine gold content was measured by ICP-MS. Ava Soleimany performed all animal injections and urine collection for *in vivo* experiments.

3.2.11 Urine catalytic activity assays

For all assays, 25 μL of urine was diluted into 25 μL PBS in a transparent 96-well plate and allowed to equilibrate at room temperature for 15 min 100 μL each of 5 M H_2O_2 and TMB were then added and the plate was read kinetically at 652 nm over the course of 30 min. For renal clearance studies, the concentration of active AuNCs present in the urine was quantified *via* reference to a calibration curve of known AuNC concentrations. For disease detection studies, the initial reaction velocity was quantified as the rate of change of the absorbance over the first 2 - 10 min of the reaction.

3.2.12 Inductively coupled plasma-mass spectrometry (ICP-MS)

Urine samples were digested using a matrix composed of 4 % (v/v) HCl / 4 % (v/v) HNO_3 overnight. The gold content in each sample was measured using an Agilent 7900 ICP-MS using an indium internal standard (5 ppb) and gold standard (TraceCERT, Sigma) for the calibration curve prepared in the above ICP-MS matrix.

3.2.13 Cell culture and cytotoxicity studies

Cell culture

For xenograft studies, LS174T (ATCC CL-188) cells were cultured in Eagle's Minimal Essential Medium (EMEM, ATCC) supplemented with 10 % (v/v) FBS (Gibco) and 1 % (v/v) penicillin-streptomycin (CellGro). LS174T cells were selected for tumor study as they have been shown to secrete MMP9, a gelatinase involved in the growth and invasion of solid tumors.[150] For *in vitro* cytotoxicity assays, HEK293T (ATCC CRL-3216) cells were cultured in Dulbecco's Modified Eagle Medium (DMEM, ATCC) supplemented with 10 % (v/v) FBS (Gibco) and 1 % (v/v) penicillin-streptomycin (CellGro). Cells were passaged when confluence reached 80 %. Ava Soleimany performed all cell culture experiments.

***In vitro* cytotoxicity studies**

For *in vitro* cytotoxicity studies, HEK293T cells were plated in a 96-well plate (10,000 cells per well) and allowed to adhere to the wells. 24 h post seeding, cells were incubated with varying concentrations of AuNC-neutravidin complex (diluted in PBS) for 24 h. Cell viability was evaluated using the MTS (3-(4,5-dimethylthiazol-2-yl)-5-(3-carboxymethoxyphenyl)-2-(4-sulfophenyl)-2H-tetrazolium) assay (Promega). Ava Soleimany performed all cytotoxicity experiments.

3.2.14 Pharmacokinetic studies

To analyze blood half-life of the avidin carrier, female Swiss Webster mice (4-6wks, Taconic) were injected with neutravidin-biotin labeled with the near-infrared dye VivoTag750 (VT750, PerkinElmer; 1 μM by VT750). Blood was withdrawn retro-orbitally (~70 μL) and then immediately transferred into 40 μL of PBS with 5 mM EDTA and centrifuged to pellet blood cells. Concentration of avidin carrier was measured using an Odyssey infrared scanner (Li-Cor Inc.). For biodistribution studies, nude mice bearing LS174T flank tumors were infused with labeled avidin-biotin. Mice were sacrificed 1 h post injection, and organ and tumor

accumulation were measured using an Odyssey scanner and quantified using ImageJ (NIH). Ava Soleimany performed pharmacokinetic experiments.

3.2.15 Colorectal cancer xenograft studies

Female NCr Nude mice (4-5wks, Taconic) were injected bilaterally with 3 x 10^6 LS174T cells per flank. Two weeks after inoculation (tumor *ca*. 10 mm in diameter), tumor-bearing mice and age-matched controls were injected with 15 μM MMP-sensitive AuNC nanosensors in 200 μL of PBS (concentrations determined by AuNC). After nanosensor injection, mice were placed in custom housing with a 96-well plate base for urine collection. After 1 h, their bladders were voided to collect between 100-200 μL of urine. Urine was analyzed *via* the catalytic activity and ICP-MS measurements described above. Ava Soleimany performed all animal injections and urine collection for *in vivo* experiments.

3.2.16 Statistical analyses

All statistical analyses were conducted in GraphPad 7.0 (Prism).

3.3 Results & Discussion

3.3.1 Optimization of synthesis of protein and peptide templated nanoclusters

Proteins were investigated as templates for the synthesis of nanoclusters in the renal clearance size regime. The rationale for protein selection was based primarily on size, with the requirement that the hydrodynamic diameter must be less than 5 nm to allow for efficient renal clearance. Albumin is the most abundant plasma protein in human blood, and as a natural transport protein it exhibits long circulation in the blood (*ca*. 19 days).[193] Although albumin is not renally cleared in healthy individuals (D_h *ca*. 6 nm), it was used as a model template for synthesis. Lysozyme is an antimicrobial enzyme that forms part of the innate immune system, and has also been demonstrated to be a robust scaffold for metal nanoparticle synthesis.[194]

BSA and lysozyme were selected as model proteins for the synthesis of protein-templated nanoclusters following published protocols.[153,195] Several synthesis parameters were optimized to produce nanoclusters with a defined size, high catalytic activity, stability in serum, and fluorescence to enable dual modality readouts. In a typical synthesis, chloroauric acid was added to an aqueous protein solution and pH was subsequently adjusted to *ca*. 12 initiating reduction of Au ions to Au atoms. The proposed mechanism has been compared to the biomineralization behavior of organisms in nature. In the process of biomineralization, inorganic ions are sequestered by proteins which act as scaffolds for mineralization. In the case of BSA and lysozyme, Au ions become entrapped in the protein scaffold, presumably sequestered by thiol groups (from the cysteine residues) due to strong gold-thiol interactions. When the reaction pH is adjusted to about 12, the Au ions are effectively reduced by certain amino acid residues to form AuNCs *in situ*. In this way the protein scaffold acts as both a reducing and stabilizing agent during synthesis.

There are a few key considerations for successful synthesis of nanoclusters. The presence of specific amino acid residues and the relative abundance of these amino acids in a biological molecule plays a role in the formation of AuNCs when produced in a one-pot synthesis. The protein template must contain both cysteine and tyrosine residues. Cysteine residues have a thiol group which can interact with and sequester metal ions in solution. Tyrosine residues have been shown to have reducing capability through their phenolic groups, and this reducing capability can be greatly improved by adjusting the reaction pH above the pKa of tyrosine (~ 10). Thus, the adjustment to basic pH with the addition of NaOH is key for the reduction process. The reaction temperature also plays a critical role, as AuNCs form very slowly at

lower temperatures. Table 3.1 outlines important physical parameters for various proteins and peptides used as templates for nanocluster synthesis.

Table 3.1 Proteins and peptides selected as templates for nanocluster synthesis

Protein/peptide	Molecular weight	Cysteine content (% total a.a.)	Theoretical isoelectric pt.
BSA	66 kDa	35/607 (5.8%)	5.8
Lysozyme	16 kDa	9/147 (6%)	9.3
Glutathione	0.3 kDa	1/3 (33%)	6
CD63 (Extracellular vesicle membrane protein)	25 kDa	15/238 (6.3%)	8

For BSA and lysozyme-templated nanocluster synthesis, the color of the reaction solution changed from light yellow to light brown and then deep brown, and the resulting AuNCs emitted red fluorescence under UV light (365 nm) (Figure 3.5). The ratio of protein template to gold chloride played a key role in the synthesis of AuNCs. High concentration of protein (10 – 25 $mg \cdot mL^{-1}$) was required for effective protection of AuNCs. Lower concentrations (< 5 $mg \cdot mL^{-1}$) of protein resulted in precipitation of particles due to aggregation from lack of stabilizing agent. For lysozyme-templated synthesis a ratio [Lyz]: [Au] of 1:6 was optimal for synthesis, and for BSA-AuNC the optimal ratio was [BSA]: [Au] 1:10, forming stable monodisperse fluorescent particles under these reaction conditions.

In moving towards using the protein-templated metal nanoclusters in a sensing system in physiological environments, the hypothesis was that if the protein template could retain secondary structure after metal nanocluster growth, that it could act as a stealthy probe *in vivo* with an increased blood half-life, and potentially avoid any undesirable immune response. To test this hypothesis, a common blood protein, BSA, which shares *ca.* 80% sequence homology with human serum albumin, was selected as a template for structural characterization.[196] Gold nanoclusters were grown in BSA, purified and protein secondary structure was analyzed using circular dichroism (CD) spectroscopy (Figure 3.5c). BSA secondary structure is predominately α-helical, with characteristic negative peaks at 222 nm and 208 nm and a positive peak at 192 nm (Figure 3.5c). The nanocluster synthesis induced denaturation of the protein template as evidenced by the reduction in intensity of the CD signal and shift in the structure after nanocluster growth. This structural change was not observed after thermal treatment of BSA at 80 °C for 2 h, further evidence that nanocluster growth destabilized the protein template, perhaps by disrupting disulfide bonding through Au-S interactions. The harsh synthesis conditions (sweeping from pH 2 to pH 12) could also cause protein denaturation.

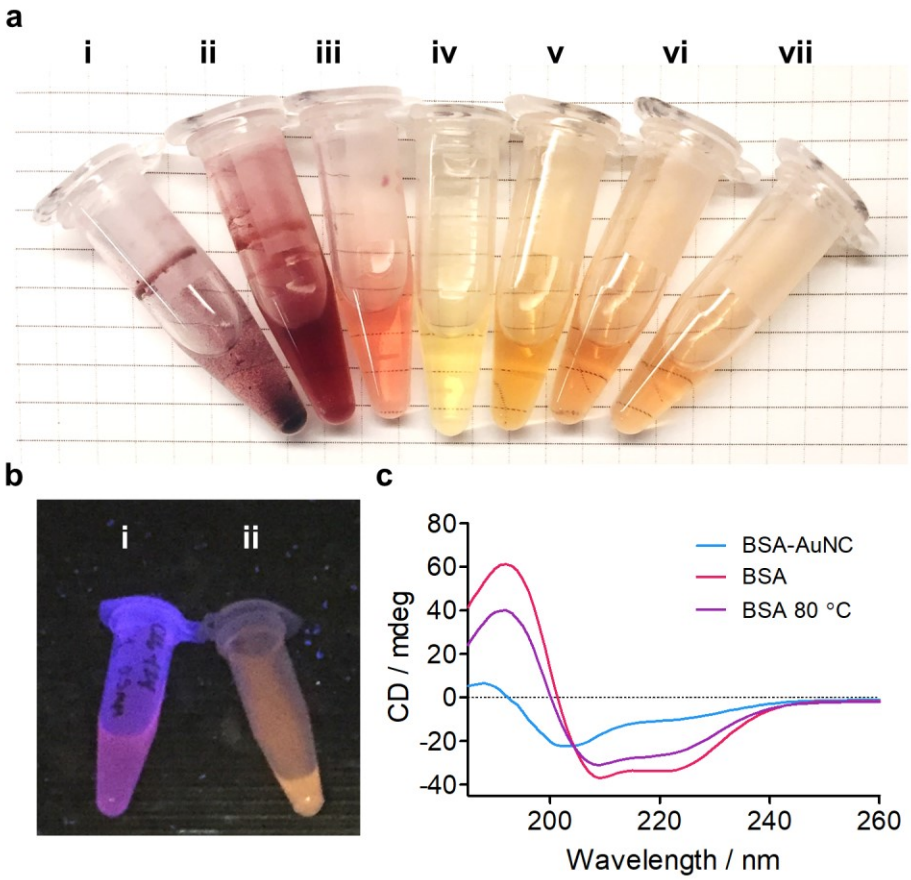


Figure 3.5 (a) Synthesis products (i – vii) 1, 5, 10, 15, 20, 30, 40 mg·mL^{-1} lysozyme (respectively) mixed with equal volume of 10 mM $HAuCl_4$, where (v-vi) form stable AuNCs. (b) (i) Lysozyme templated AuNCs (part a #v) and (ii) GSH-AuNCs under UV lamp (365 nm), exhibiting red and orange fluorescence, respectively. (c) Circular dichroism (CD) spectra showing loss of secondary structure when BSA was used as a template for synthesis of gold nanoclusters.

The size and structure of protein-templated clusters were also characterized by transmission electron microscopy (TEM). Lysozyme-templated AuNCs (Lyz-AuNC) show an average size of 3.9 ± 1.0 nm by analyzing the size of > 200 particles across > 5 images (Figure 3.6). Although few sensing systems have been reported using Lyz-AuNCs, one study indicates that Lyz-AuNCs tend to form small aggregates of *ca*. 8 nm in diameter in physiological pH,[194] which would render them too large for excretion through renal clearance pathways *in vivo*. Aggregation could be caused by structural changes induced in the protein during nanocluster synthesis. In particular, the misfolding of lysozyme has been shown to cause the formation of amyloid fibrils and larger protein aggregates which could be toxic if administered *in vivo*. It will be critical to understand how native proteins change upon the nucleation of metal nanoclusters within the protein for any future use of the protein-templated particles as *in vivo* probes.

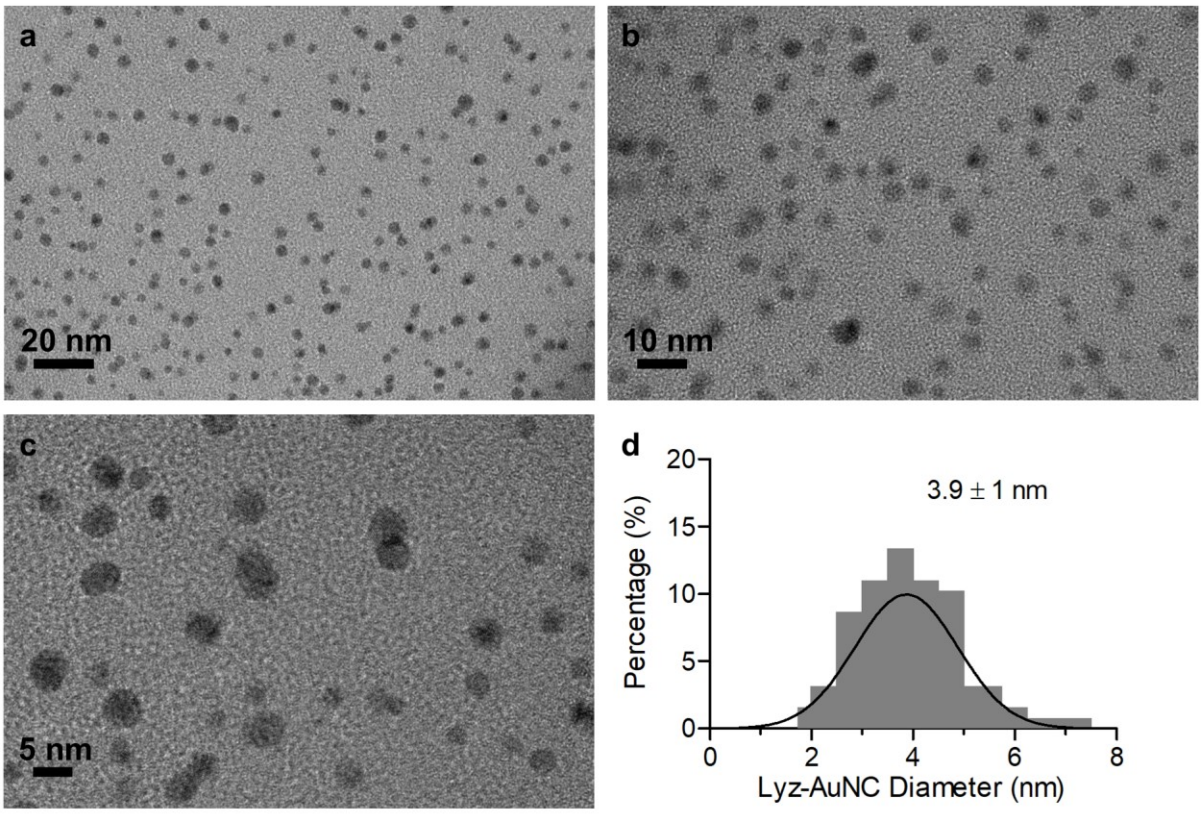


Figure 3.6 (a-c) Transmission electron microscopy (TEM) images of Lyz-AuNCs. (d) Histogram showing results of size analysis from TEM images (n ≥ 200 particles). Solid line represents Gaussian fit of size distribution.

To avoid the challenge of protein misfolding during protein-templated synthesis, the tri-peptide glutathione was investigated as a template for nanocluster synthesis. The resulting glutathione-templated nanoclusters (GSH-AuNCs) were characterized using TEM (Figure 3.7). From TEM image analysis, the average core diameter of GSH-AuNCs is 1.5 ± 0.4 nm, which corresponds to clusters composed of *ca*. 100 gold atoms.

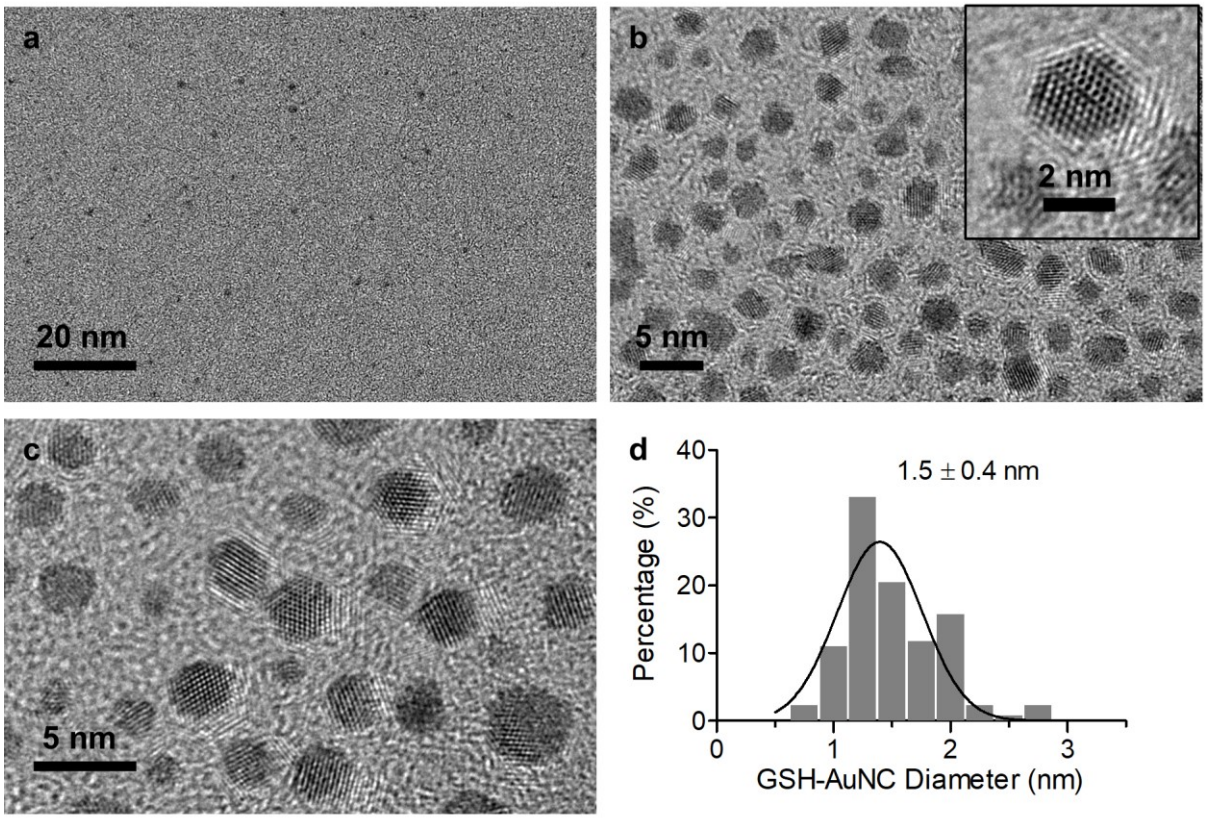


Figure 3.7 (a-c) TEM images of glutathione-protected AuNCs (GSH-AuNCs). (b) Inset shows high resolution TEM of an individual GSH-AuNC (scale = 2 nm). (d) Histogram showing results of size analysis from TEM images (n ≥ 200 particles). Legend shows mean diameter ± s.d. Solid line represents Gaussian fit of size distribution. Dr. Qu Chen assisted with TEM imaging.

The catalytic activity of protein and peptide templated nanoclusters was investigated using a simple colorimetric assay using a chromogenic peroxidase substrate. In the assay, nanoclusters were mixed with tetramethylbenzidine (TMB) and 4 M H_2O_2, and absorbance was subsequently measured at 652 nm to monitor the nanocluster-catalyzed oxidation of TMB (Figure 3.8). Both gold and platinum were investigated as nanocluster core materials. Unexpectedly, clusters composed of a gold core showed much higher activity than platinum core in the < 5 nm size regime (Figure 3.8). As platinum had been extensively investigated in Chapter 2 for use as catalytic labels in lateral flow assays, it was hypothesized that platinum would also be an efficient catalyst for disproportionation of hydrogen peroxide even at this smaller length scale. When lysozyme was used as a template for nanocluster growth, Lyz-AuNCs exhibited *ca*. 10 times higher activity than Lyz-PtNCs. Similarly, for the peptide templated synthesis, GSH-AuNCs exhibited two-fold higher activity than GSH-PtNCs, and GSH-Au-PtNC bimetallic hybrid metal clusters exhibited intermediate activity. Since AuNCs exhibited higher catalytic activity, potentially due to the higher reactivity of Au compared to Pt, this formulation was taken forward for development.

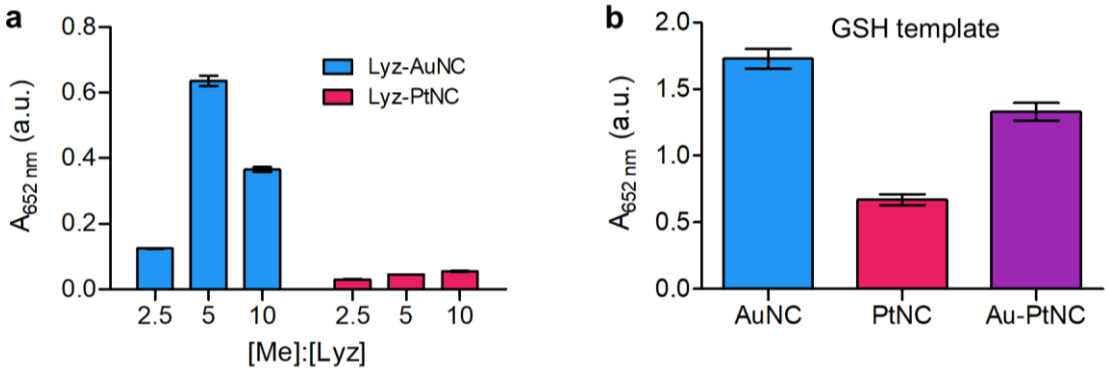


Figure 3.8 (a) Catalytic activity, measured by the absorbance at 652 nm corresponding to the oxidation of TMB by H_2O_2, of lysozyme templated nanoclusters synthesized with varying excesses of metal to protein using either gold or platinum. (b) Catalytic activity of glutathione templated nanoclusters synthesized with varying core metals: gold, platinum and gold-platinum bimetallic hybrid. AuNCs exhibited the highest activity followed by Au-Pt with intermediate activity, and PtNCs showed the lowest activity of the tested metals.

3.3.2 Preliminary *in vivo* renal clearance

In taking the AuNCs forward for development of the *in vivo* sensing system, a standard method for measuring catalytic activity of AuNCs in urine samples was developed. Samples were incubated with peroxidase substrate TMB, and catalytic activity was measured by monitoring the absorbance at 652 nm corresponding to oxidation of TMB by H_2O_2. For all catalytic activity measurements, the kinetics of development were measured so that the initial rate of reaction could be calculated. Here, the initial rate of reaction corresponds to the rate of turnover of TMB. The initial rate was calculated using linear regression analysis of the plot of absorbance versus time (Figure 3.9a). There was a significant difference between the initial rate of oxidation of TMB when GSH-AuNCs were present in urine compared to PBS spiked urine (Figure 3.9b), highlighting the peroxidase-mimicking activity of GSH-AuNCs in their ability to efficiently catalyze the oxidization of peroxidase substrates. Importantly, this assay also served to demonstrate that urine does not contain any small molecules or proteins which could also catalyze the oxidation of TMB, which would significantly elevate any background signal. The catalytic activity can be measured either through the initial rate analysis (capturing the first few minutes of kinetics) or using a fixed time-point reading of absorbance at 652 nm. The advantage of the rate analysis was that it accounts for the physiological variability in background absorbance of urine samples, which is constant unless there are catalytic particles present in the sample. The rate analysis allowed for better discrimination between blank urine and urine samples containing catalytic particles because of the significant difference in the initial rate of TMB oxidation. Additionally, samples containing a high concentration of AuNCs caused precipitation of the substrate over time resulting in variability in single time point analysis. The advantage of the initial rate analysis was that it allowed for a broader dynamic

range to be quantifiable, while for the fixed time point analysis, some of the samples could be in the linear range and some could be precipitating, increasing the variability in the readout.

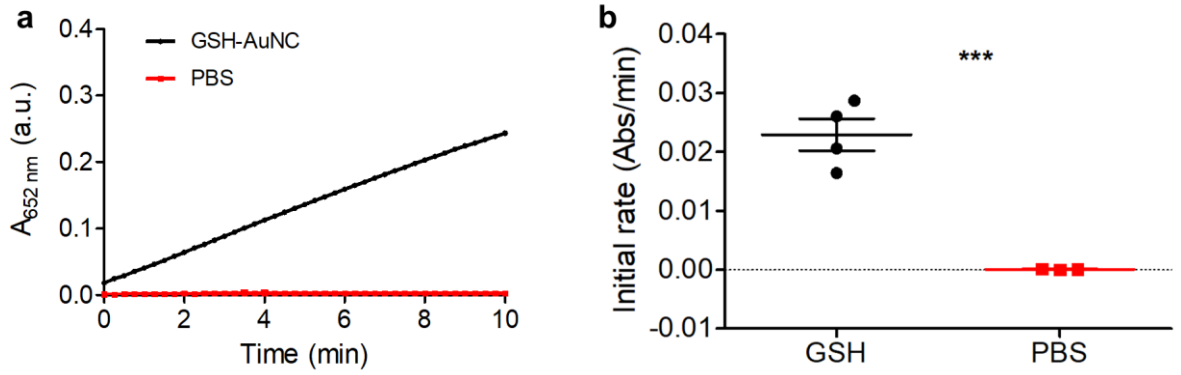


Figure 3.9 Assessment of endogenous peroxidase activity in mouse urine. (a) Kinetic measurement of catalytic activity in urine samples of mice injected with GSH-AuNCs or PBS (mean, *n* = 3 for PBS and *n* = 4 for GSH-AuNC). (b) Quantification of initial velocity of catalytic activity from (a), as measured by the rate of change of $A_{652\ nm}$ over the first 10 minutes of the reaction (mean ± s.d., *n* = 3 for PBS and *n* = 4 for GSH-AuNC, two-tailed Student's *t*-test, ****P* = 0.0009).

Once catalytic activity of AuNCs in the appropriate size regime for renal clearance was established, a preliminary *in vivo* renal clearance experiment was used to assess whether peptide-templated AuNCs renally clear, and if the cleared particles retain any activity in collected urine after *in vivo* interrogation. In this pilot study, purified AuNCs (GSH-AuNC, Lyz-AuNC, and GSH-AuNCs with post-synthesis modifications to alter surface charge) diluted into sterile PBS were injected into the tail vein of mice, urine was collected 1 h p.i., and TMB catalytic activity assay was performed on collected urine (25 µL volume) (Figure 3.10). Activity assay on collected urine samples was run alongside a dilution series of the injected dose of AuNCs in "blank urine" (urine collected from mice pre-injection with particles). Spiking "blank urine" into the dilution series served to account for any loss in activity of the AuNCs in this physiological environment. The dilution series of AuNCs provided a calibration curve which could be used to assess the percent of AuNCs in the urine samples (as measured by activity) compared to injected dose standard curve and could also be used to calculate the estimated number of AuNCs cleared (in picomoles). This assay was used to quickly assess the presence of AuNCs in urine through a simple colorimetric assay. However, the main limitation of the assay was the uncertainty of whether the activity of the injected dose in "blank urine" could be comparable to AuNCs which have been injected into the blood stream and have interrogated the renal filtration system of a mouse. The ideal measurement would be to quantify the absolute gold content in cleared urine compared to the injected dose. While the activity assay is susceptible to variability due to environmental interactions, a measure of gold content would

be more stable. Using analytical techniques to measure gold content, such as inductively coupled plasma mass spectrometry (ICP-MS), will be explored later in this chapter.

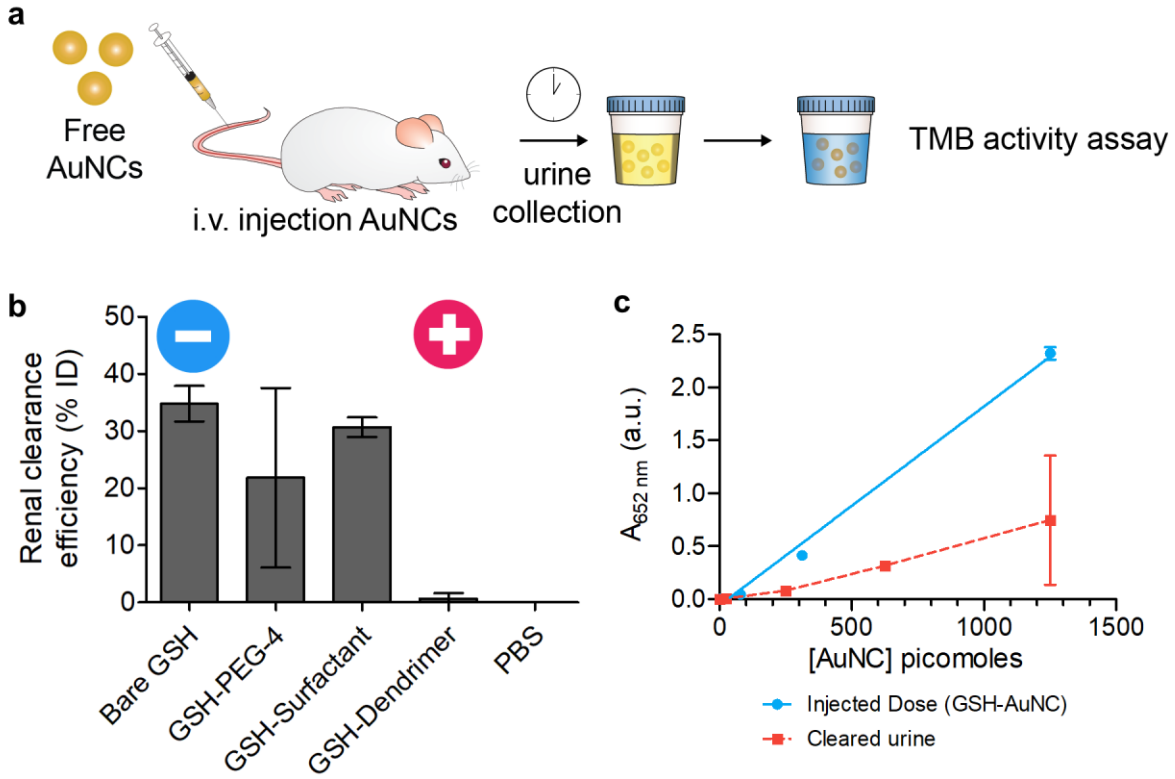


Figure 3.10 Preliminary *in vivo* renal clearance study. (a) Schematic of *in vivo* experimental set up. First, AuNCs were injected intravenously though the tail vein of a mouse. Urine was collected at 1 h p.i. and catalytic activity assay was used to assess presence of AuNCs in cleared urine against a standard curve of injected dose. (b) Renal clearance efficiency calculated from catalytic activity assay on clearance urine for AuNCs presenting varying surface charge. (c) Results of catalytic activity assay for dosing study comparing injected dose (blue) to activity measured for corresponding injected dose in clearance urine (orange) (mean ± s.d., n = 3). Ava Soleimany performed animal injections and urine collection for *in vivo* experiments.

The pilot *in vivo* renal clearance study was important to establish the feasibility of building a sensing system with nanocluster materials, understanding charge-dependent clearance, and optimizing the injected dose of AuNCs. Lyz-AuNCs did not show any activity in clearance urine. There are several reasons why lysozyme-templated clusters may not have been able to renally clear, even though TEM size analysis showed a monodisperse population < 4 nm, which should be in the renal clearance size regime (Figure 3.6). It is possible that lysozyme aggregation *in vivo* may have caused uptake by the RES organs and prevented renal clearance. The positive charge of lysozyme at neutral pH may have promoted serum protein adsorption (interactions with negatively charged proteins such as serum albumin) which would have also increased hydrodynamic diameter to > 15 nm or above the renal filtration cut-off

and would shift the route of excretion from the kidney to the liver.[180] Reports have also shown the propensity of positively charged nanoparticles to be readily taken up into cells, which could also alter clearance pathways.[197]

On the other hand, GSH-AuNCs were readily detected in urine using the catalytic activity assay with *ca*. 40% injected dose measured in the urine 1 h p.i., which suggested that the glutathione protected gold nanoclusters remained stable in physiological environments and retained catalytic activity in excreted urine. The charge-dependency of clearance was also explored by preparing a library of GSH-AuNCs that were modified with functional groups to alter surface charge, including: unmodified GSH-AuNC (negative); polyethylene glycol ($MS(PEG_4)$ *ca*. 333 g/mol, neutral/passivated); Poly(amidoamine) (PAMAM dendrimer (positively charged); and the surfactant glycolic acid ethoxylate lauryl ether (negative). The hydrodynamic diameters of all batches of modified AuNCs was measured using dynamic light scattering to ensure size remained less than 5 nm post modification and that modification did not induce aggregation in PBS.

Negatively charged unmodified GSH-AuNCs and surfactant coated GSH-AuNCs cleared to the same extent (*ca*. 40% ID 1 h p.i.), however high variability in clearance for the PEG modified GSH-AuNCs was observed. PEG coatings generally increase circulation time of nanoparticles, which may lead to uptake by RES organs and could have contributed to the variable clearance.[152] Surprisingly, positively charged PAMAM dendrimer functionalized GSH-AuNCs exhibited very low clearance (< 5 % ID 1 h p.i.). Several reports suggest higher rates of renal clearance for positively charged nanoparticles (compared to neutral or anionic counterparts) due to their favorable interactions with the negatively charged glomerular barrier, which tends to facilitate filtration of cationic macromolecules and slows the filtration of anionic macromolecules due to electrostatic interactions.[152] Interestingly both dendrimer modified GSH-AuNCs and Lyz-AuNCs showed comparatively low clearance, which indicated that perhaps their positive charge contributed to serum protein adsorption or uptake by RES and clearance through mechanisms other than kidney filtration.

For this pilot study, urine was collected at 1, 3, 8, and 24 h post injection and analyzed using the catalytic activity assay. No colorimetric signal was observed in the urine at 3 h and beyond, so 1 h was fixed as the optimal time point for urine collection post injection with AuNCs. A dosing study was also performed to evaluate whether the catalytic activity signal measured in urine correlated with the activity of the injected dose. Indeed, a dose-response effect was observed where the cleared urine signal corresponded to *ca*. 40% of the injected dose calibration curve (Figure 3.10c).

3.3.3 Design of gold nanocluster functionalized protease nanosensors

With the aim of designing a protease nanosensor that generates a colorimetric urinary readout, catalytic gold nanoclusters were first synthesized in the renal clearance size regime and linked to protease-cleavable peptide sequences. The avidin protein analogue, neutravidin, was selected as a carrier for protease-responsive gold nanocluster reporter probes. Neutravidin protein is a de-glycosylated native avidin from egg whites with a more neutral isoelectric point (pI = 6.3) than avidin (pI = 10), and less nonspecific binding properties. This protein carrier was selected for its efficient binding to biotinylated ligands, and broad use as a biocompatible nanocarrier for biopharmaceuticals.[198] Neutravidin has a hydrodynamic diameter of *ca*. 8 nm, which is greater than the renal filtration cut-off. Therefore, AuNCs bound to neutravidin should not be renally cleared. However, if AuNCs are cleaved from the neutravidin core by the relevant protease, the resulting free AuNC is small enough to be renally cleared. In this model, the AuNC-neutravidin (AuNC-NAv) complex is intravenously administered and specifically disassembled by proteases at the site of disease. Once liberated from the avidin complex through peptide substrate cleavage, free AuNCs circulate *via* the bloodstream and are efficiently filtered into the urine through the kidneys due to their size. A simple colorimetric assay to measure peroxidase activity was performed on the urine to assess the presence of AuNCs as an indicator of disease state.

3.3.4 Synthesis and characterization of peptide-functionalized AuNCs

The tripeptide glutathione (GSH, γ-Glu–Cys–Gly) has been used extensively as a capping ligand for the synthesis of < 2 nm diameter noble metal nanoclusters.[157,159] To engineer a protease-responsive system, a co-templated approach was used to synthesize gold nanoclusters, incorporating both GSH and another protease-cleavable thiol terminated peptide (Table 3.2). In this synthesis, glutathione and another thiolate ligand were added to chloroauric acid in a defined ratio, heated to 70 °C, and left to react shaking (500 rpm) for 24 h, followed by purification and buffer exchange into PBS. After addition of thiolate ligands to $HAuCl_4$, the reaction mixture changed from light yellow to colorless, which is indicative of the reduction of Au (III) to Au (I) by the thiol group of the peptides, followed by the reduction of Au(I) thiolate complexes to Au(0) atoms over time assisted by the favorable reduction kinetics at the elevated reaction temperature.[157,190] After 24 h synthesis, the successful formation of < 2 nm AuNCs was evidenced by a strong orange fluorescence exhibited under UV light (Figure 3.11). The peptides act as both a stabilizing capping ligand and reducing agent for nanoparticle formation. Gold was selected as the core metal, as it exhibited the highest catalytic activity compared to platinum and gold-platinum bimetallic hybrid

nanoclusters when synthesized with a fixed GSH:[Metal] of 1.5 as discussed earlier (Figure 3.8).

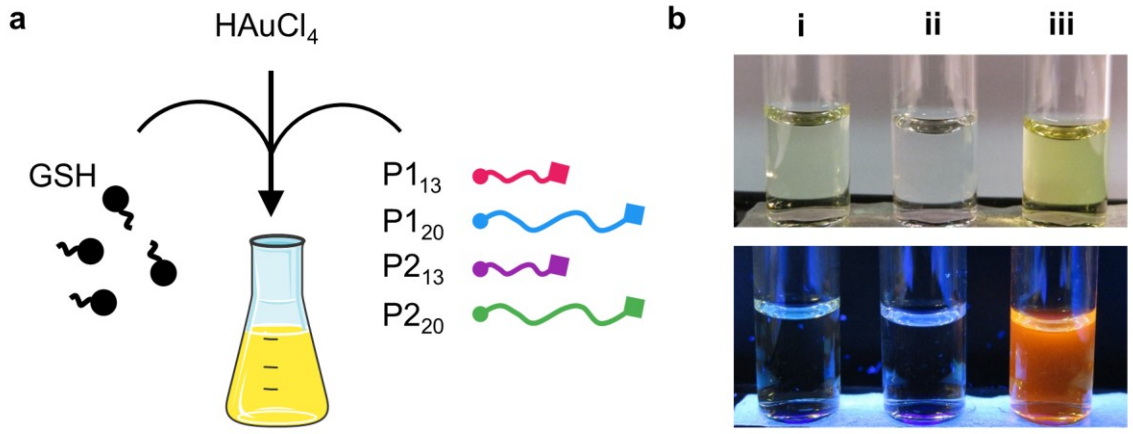


Figure 3.11 (a) Schematic showing one-pot synthesis of AuNCs, where glutathione and thiol-terminated heterobifunctional peptides ($P1_{13}$, $P1_{20}$, $P2_{13}$, $P2_{20}$) are incorporated onto the AuNC surface. (b) Photos of the reaction intermediates (below, in the presence of UV light) (i) $HAuCl_4$, (ii) $HAuCl_4$ and thiolate ligand, and (iii) reaction solution after 24 h at 70 °C.

A library of protease-cleavable peptide sequences (protease substrates) was designed to be used for the synthesis of AuNCs that are responsive to the target protease. Catalytic AuNCs were synthesized using GSH in a ratio with a thiol terminated protease-cleavable peptide sequence: $P1_{13}$, $P1_{20}$, $P2_{13}$, or $P2_{20}$, where the subscript indicates the number of amino acid residues in each sequence (Table 3.2). AuNCs synthesized with the respective peptides are subsequently labeled AuNC-$P1_{13/20}$ and AuNC-$P2_{13/20}$.

Table 3.2 Library of protease-cleavable thiol-terminated peptide sequences

Substrate ($P_{\#aa}$)	**Protease specificity**	**Sequence (↓ represents scissile bond)**	**MW (g/mol)**	**Product (g/mol)**
$P1_{13}$	Thrombin	Biotin-SGG**fPR**↓SGGSGGC	1350	846
$P1_{20}$	Thrombin	Biotin-GGGSGGGSGG**fPR**↓SGGGGGC	1750	1275
$P2_{13}$	MMP9	Biotin-GGG**PLG**↓VRGKGGC	1339	683
$P2_{20}$	MMP9	Biotin-GGGGGGGGGG**PLG**↓VRGKGGC	1739	1080
Non-cleavable	N/A	Biotin-PEG-SH	2000	N/A

The peptide substrates used as templates for AuNC synthesis were synthesized *via* solid-phase synthesis and composed of three functional domains. The core amino acid sequence was composed of the relevant enzyme recognition motif (*e.g.* fPRS for thrombin cleavage, and PLG for MMP9 cleavage). The criteria for peptide design also included a C-terminal cysteine

residue to provide a thiol group for sequestering Au ions. Finally, the N-terminus contained a labile “click” group which allowed for further site-selective modification. In this work, a biotin ligand was incorporated on the N-terminus of the peptides for efficient conjugation to an avidin carrier protein, although azide functionalization has also been demonstrated. The advantage of this synthesis route to generate both luminescent and catalytic noble metal nanoclusters is the ability to incorporate responsive and functional ligands onto the surface through simple gold-thiol interactions in a one-pot synthesis. Another design consideration was the presentation of the cleavable peptide sequences on the surface of the AuNCs. It was hypothesized that the protease might be sterically hindered from accessing the scissile bond when the peptide sequence is presented on the AuNC and simultaneously linked to the avidin core. To explore this possibility, longer peptides ($P1_{20}$, $P2_{20}$) were also synthesized by incorporating glycine spacers between the N-terminus and protease recognition motif. The number of amino acids was fixed at six residues between the C-terminal cysteine (attachment to Au surface) and protease recognition motif (amino acids bolded in Table 3.2), and the spacer arm was only varied between the biotin and scissile bond. The additional glycine residues increased the peptide length by *ca*. 500 Da or equivalent of $(PEG)_4$ spacer arm (1.5 nm). Liquid chromatography-mass spectrometry (LC-MS) was used to analyze the molecular weight of as-synthesized peptides and peptide fragments after incubation with the relevant enzyme (*in vitro* protease degradation). As designed, peptides $P1_{13}$ and $P1_{20}$ were cleaved specifically by thrombin, while peptides $P2_{13}$ and $P2_{20}$ were cleaved efficiently by MMP9 (Figure 3.12) and the molecular weight of cleaved fragments (product) is highlighted in Table 3.2. The LC-MS results show the mass of the cleavage products (in red) after enzyme incubation, which correspond well to the expected cleavage site at the scissile bond.

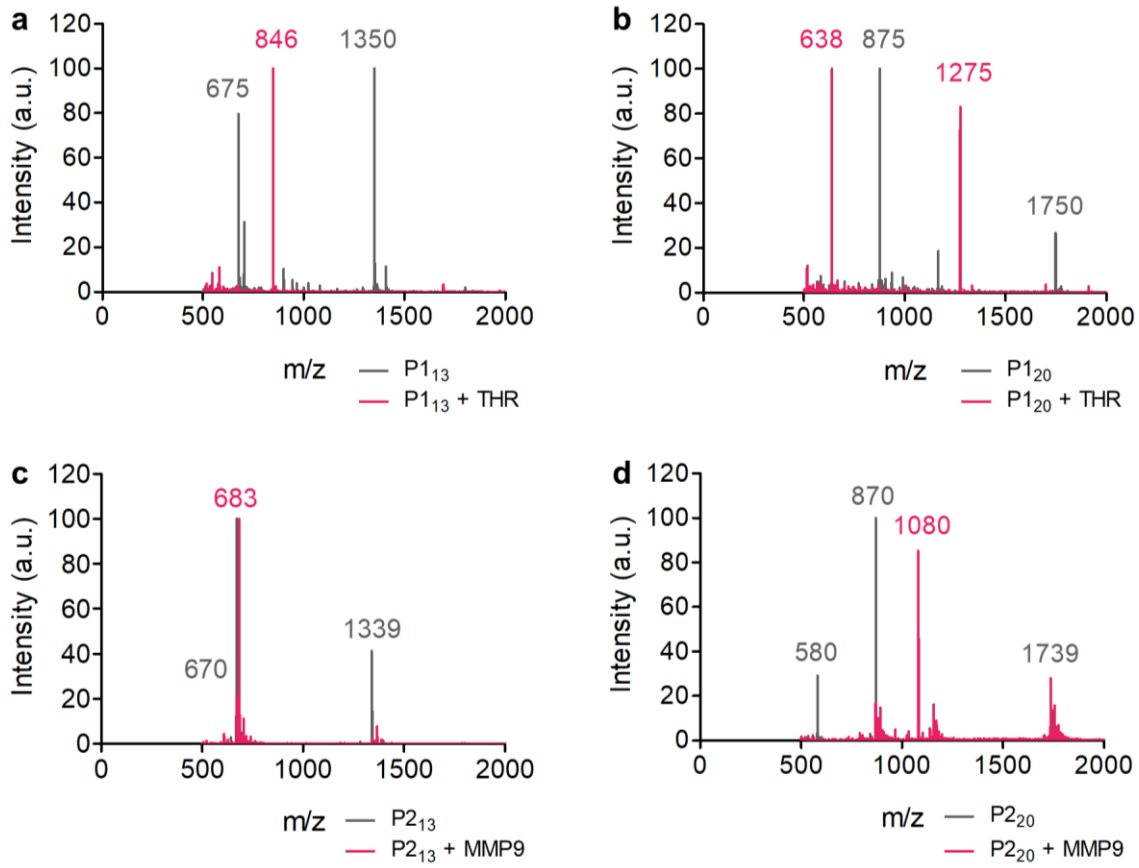


Figure 3.12 LC-MS chromatograms of (a) $P1_{13}$ and peptide fragments (red) after 12 h incubation with thrombin, (b) $P1_{20}$ and peptide fragments after 12 h incubation with thrombin, (c) $P2_{13}$ and peptide fragments after 12 h incubation with MMP9, and (d) $P2_{20}$ and peptide fragments after 12 h incubation with MMP9. Dr. Yiyang Lin assisted with analysis of LC-MS results.

TEM of the glutathione-templated AuNCs (Figure 3.7) showed that the average size (1.5 ± 0.4 nm) was below the glomerular filtration cut-off (*ca*. 5.5 nm), making them ideally suited for kidney clearance.[164,171,180,199] Additionally, the AuNCs produced here do not exhibit surface plasmon resonance, (typically at 520 nm, a characteristic absorption of large AuNPs) (Figure 3.13). Instead, the AuNCs exhibited molecular-like absorption and corresponding fluorescence properties with an emission peak at 600 nm, attributed to the discrete electronic state arising from their small size. While the fluorescence of AuNCs may be a desirable property to exploit in sensing systems,[200] the photoluminescence quantum yield is typically quite low (< 10 %, primarily in the range of 0.001 – 0.1 %), and instead this chapter looks at exploiting their unique peroxidase-mimicking activity.[172,201]

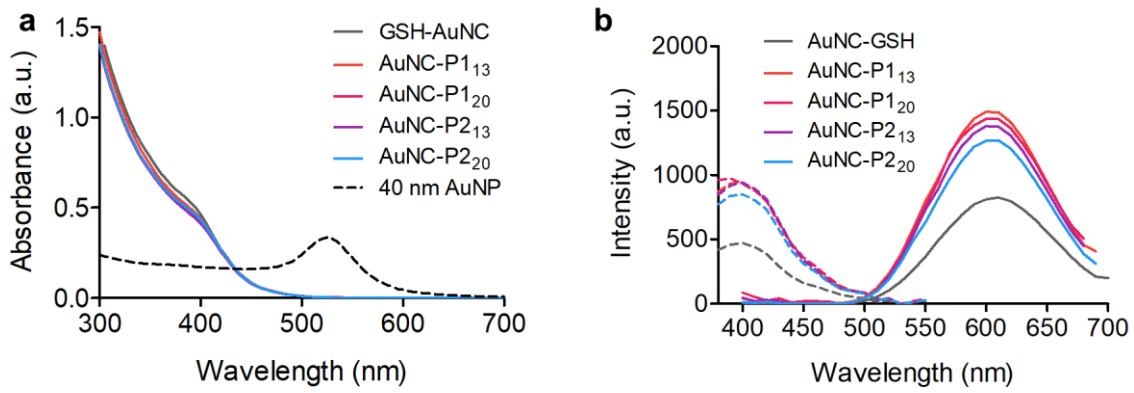


Figure 3.13 (a) UV-vis absorption spectrum of peptide templated AuNC batches compared to 40 nm AuNPs. AuNCs do not exhibit surface plasmon resonance peak at 520 nm characteristic of large (> 4 nm) gold nanoparticles. (b) Fluorescence excitation (Em: 600 nm, dotted line) and emission (Ex. 400 nm, solid line) spectrum.

The ratio of protease-cleavable peptide substrate (P1 or P2) to glutathione was varied in the AuNC synthesis to incorporate a variable number of protease-cleavable functional handles onto the AuNC surface (P1: or P2: GSH, tested at 1:2, 1:4, 1:5, 1:9). TEM and DLS were used to confirm that the co-peptide templated synthesis produced AuNCs. TEM size analysis shows a narrow size distribution for all batches with average diameter ranging from *ca*. 1.3 ± 0.4 to 1.6 ± 0.5 nm (Figure 3.14).

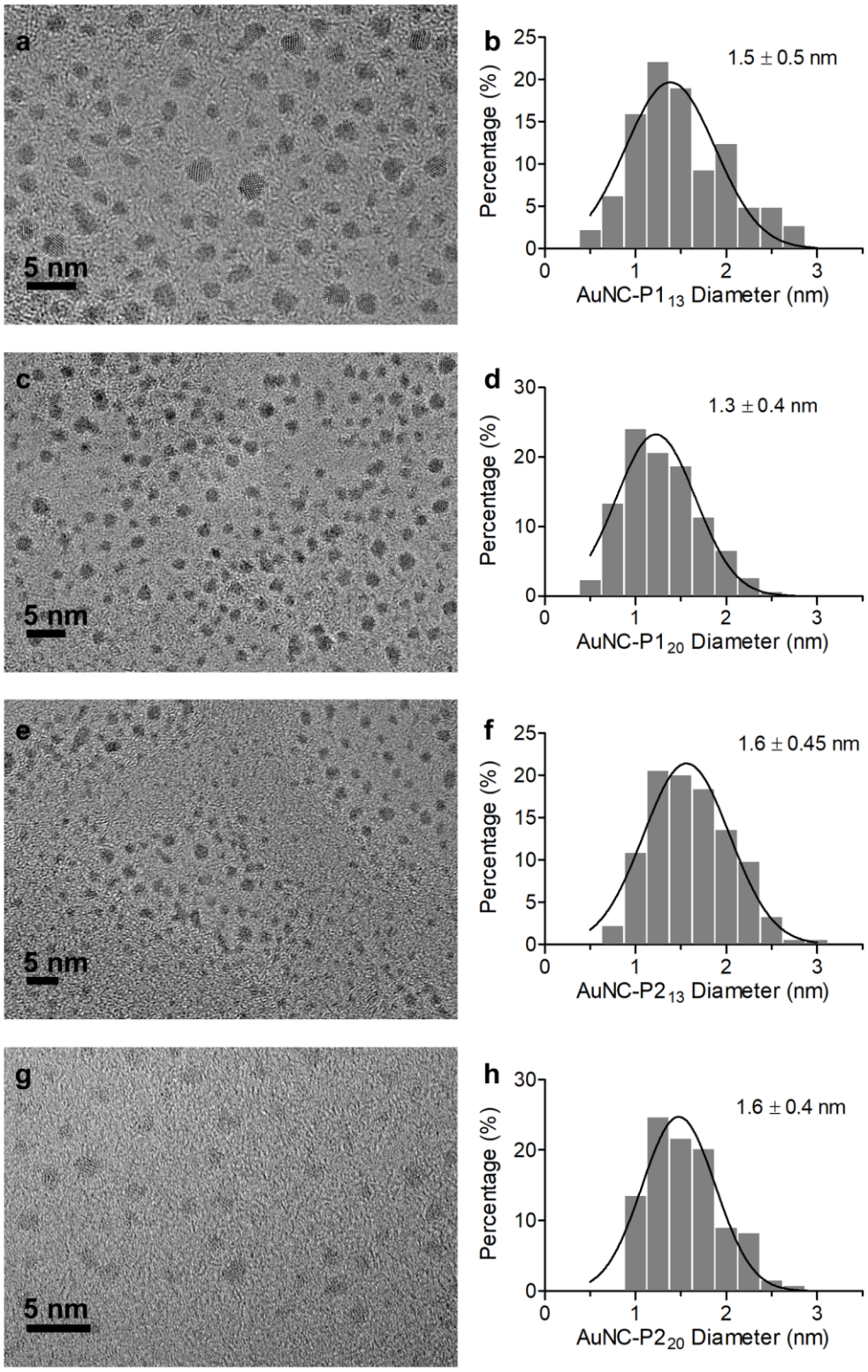


Figure 3.14 Representative TEM images of AuNCs synthesized with different peptide sequences and corresponding histogram of size analysis (a, b) AuNC-P1$_{13}$, (c, d) AuNC-P1$_{20}$, (e, f) AuNC-P2$_{13}$, (g, h) AuNC-P2$_{20}$. Scale bars, 5 nm; legends in b (n = 227), d (n = 354), f (n = 185), and h (n = 134) show mean diameter ± s.d. Dr. Qu Chen assisted with TEM imaging.

Size is a critical parameter in dictating renal clearance, it was therefore important to investigate the hydrodynamic diameter and aqueous stability of AuNCs. DLS was used to measure the

hydrodynamic diameter of all AuNC batches in PBS (Figure 3.15). While the average hydrodynamic radius is < 5 nm in all cases, when the PX: GSH increases to 1:2, the size increases. Whereas particles formed with lower PX:GSH ratio *e.g.* 1:9 have similar sizes to the particles synthesized with GSH alone. For example, for the $P1_{20}$:GSH series, the hydrodynamic diameters increased with increasing $P1_{20}$ incorporation: 1.5 nm (GSH only), 1.7 nm (1:9), 1.7 nm (1:5), 3.1 nm (1:4), and 4.9 nm (1:2) (Figure 3.15b). Independent of peptide composition, as the ratio of P1 or P2 in the synthesis increased, the overall hydrodynamic diameter of the AuNCs increased, and all ratios maintained colloidal stability.

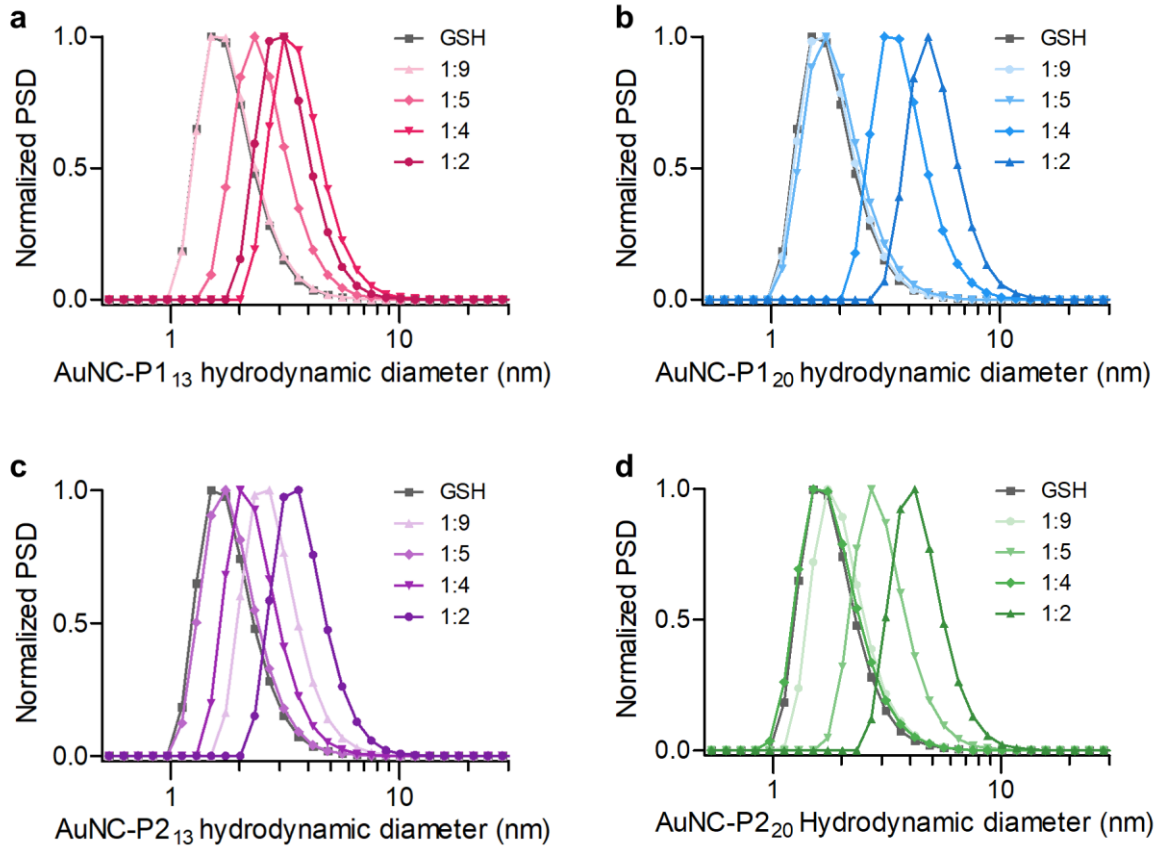


Figure 3.15 (a) Number particle size distribution (PSD) measured by dynamic light scattering (DLS) of AuNCs synthesized with different peptide sequences (a) $P1_{13}$, (b) $P1_{20}$, (c) $P2_{13}$, and (d) $P2_{20}$. Increasing intensity of colored line corresponds to increasing concentration of protease-cleavable peptide sequence in synthesis, where 1:9 corresponds to a 1:9 ratio of PX peptide: glutathione in synthesis. All particles were synthesized with a fixed total peptide concentration.

3.3.5 Catalytic activity of peptide-templated AuNCs

The peroxidase-like catalytic activity of the resulting AuNCs was measured using the oxidation of TMB by H_2O_2 as a model catalytic reaction, and absorbance at 652 nm provided a colorimetric readout of AuNC activity. The colorimetric readout was carefully optimized using

GSH-AuNCs as a model nanocluster to maximize signal intensity by varying concentration of hydrogen peroxide, pH, and concentration of sodium chloride, and measuring corresponding catalytic activity under these conditions (Figure 3.16). Colorimetric signal increased with increasing concentration of hydrogen peroxide, plateauing at *ca*. 2.5 M. As a result, PBS spiked with 2.5 M H_2O_2 was selected as the assay reaction buffer due to its neutral pH and optimal salt concentration (150 mM). While the salt concentration of urine samples may be variable (100 – 800 mM total salt content),[202] the urine samples were ultimately diluted 8-fold in the reaction buffer, minimizing variability between heterogenous samples. The increase in activity with increase in salt concentration is intriguing and will be the basis of future simulations to understand the role salt might play in stabilizing the surface ligands to allow better adsorption or docking of peroxide on the cluster surface or better accessibility to the active sites.

The catalytic efficiency of AuNCs was investigated through apparent steady-state kinetic assays, and the data was fit to the Michaelis-Menten model (**Equation 3.1**) to obtain kinetic parameters (Table 3.3). The k_{cat} of GSH-AuNCs (0.2 s^{-1}) is several orders of magnitude lower than HRP (4.0 x 10^3 s^{-1}), which is consistent with the biological enzyme having higher specificity and affinity for the substrates than its inorganic counterpart.[34]

Table 3.3 Comparison of the kinetic parameters of various catalysts toward the oxidation of TMB by H_2O_2

Catalyst	**[E] / M**	**Substrate**	**K_m / M**	**V_{max} / M s^{-1}**	**k_{cat} / s^{-1}**
AuNC c. 1.5 nm	1.8 x 10^{-6}	TMB	2.3 x 10^{-4}	3.6 x 10^{-7}	0.20
HRP[34]	2.5 x 10^{-11}	TMB	4.3 x 10^{-4}	1.0 x 10^{-7}	4.0 x 10^3

[*E*] represents the catalyst concentration, K_m is the Michaelis-Menten constant, V_{max} is the maximal reaction velocity, and k_{cat} is the catalytic constant that equals V_{max}/[*E*].

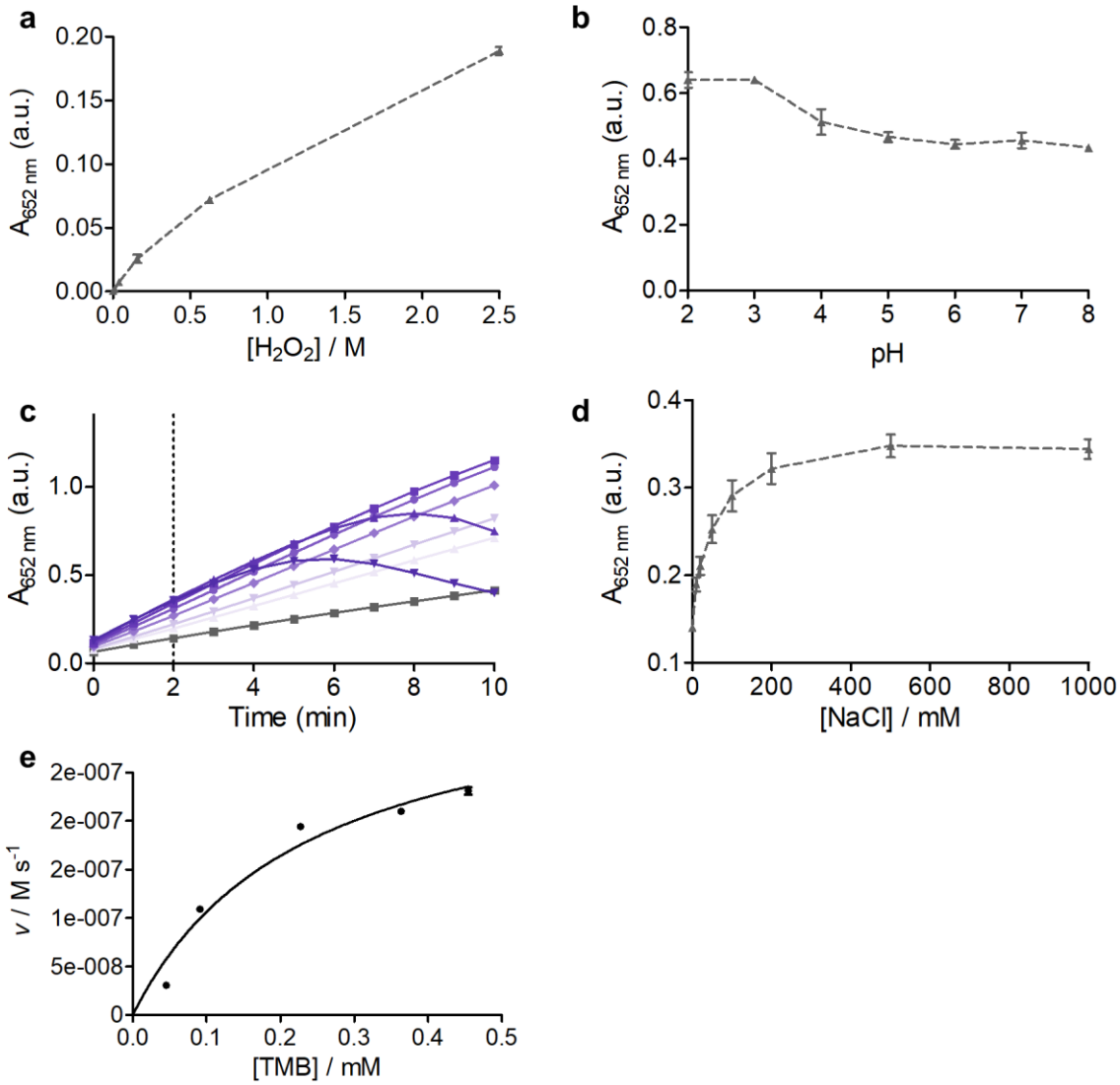


Figure 3.16 (a) Catalytic activity of GSH-AuNCs as a function of hydrogen peroxide concentration. Activity is measured by the absorbance at 652 nm corresponding to the oxidation of TMB by H_2O_2. (b) Catalytic activity of GSH-AuNCs as a function of pH, where purified GSH-AuNCs are in water and pH is adjusted with HCl and NaOH. (c) Kinetic measurement of catalytic activity with varying sodium chloride concentration (gray no salt, 0.01, 0.02, 0.05, 0.1, 0.2, 0.5, 1 M NaCl increasing color intensity), where precipitation of substrate occurred at high [NaCl]. (d) Catalytic activity with varying [NaCl] after 2 min development (dotted line in (c)). (e) Steady-state kinetic assays of GSH-AuNCs as catalysts for the oxidation of TMB by H_2O_2. The initial reaction velocity (v) was measured in 25 mM sodium acetate buffer pH 4.0 with 1.8 x 10^{-6} M AuNCs at room temperature over 150 seconds. Plot of v against TMB concentration, in which H_2O_2 was fixed at 2.3 M (mean ± s.d., n = 3).

With the optimal reaction conditions established, the catalytic activity of AuNCs synthesized with the library of protease-cleavable peptide sequences was evaluated. The glutathione templated synthesis method produced AuNCs with high reproducibility and low coefficient of variation (CoV) between the measured catalytic activities of seven independently synthesized batches of AuNCs prepared on different days with fresh dilutions of starting materials (CoV =

8.5 %). Reproducibility in synthesis and catalytic activity between batches is an important consideration in designing materials for a scalable diagnostic platform (Figure 3.17a).

AuNCs synthesized with a 1:5 ratio of P1 to GSH and a 1:4 ratio of P2 to GSH retained 50 – 100 % catalytic activity compared to AuNCs synthesized in the presence of GSH alone (Figure 3.17b). Variations in activity for co-templated AuNCs compared to only GSH-capped AuNCs could be ascribed to the bulkier protease-cleavable peptides replacing GSH in the synthesis. When the PX_{13} peptides were incorporated in the synthesis, AuNCs retained 50 – 60 % of activity compared to GSH-AuNCs, while the PX_{20} peptides retained 80 – 100% (Figure 3.17b). The higher retention of activity for PX_{20} peptides may be due in part to the glycine spacers that provide greater flexibility and could allow substrate molecules to more readily access the AuNC surface compared to PX_{13} peptides which may interact more strongly with the surface. The PX_{13} peptides may more readily block access to the AuNC surface, decreasing surface area available for interaction with substrate molecules and subsequent catalytic reactions. Independent of sequence length, P2 peptides retained more activity than P1 when incorporated into synthesis in the same ratio to GSH. The differences in catalytic activity with varying peptide sequence may be attributed to variations in peptide hydrophobicity, charge, and molecular weight affecting accessibility and affinity of substrate molecules for the catalytic surface. For example, the P2 sequence includes a charged lysine residue which may alter atomic arrangement in synthesis in such a way that stabilizes a more catalytically active AuNC structure.

There are several advantages to using inorganic AuNCs over natural peroxidases such as horseradish peroxidase (HRP). HRP (*ca*. 4.5 nm) is not readily cleared through the renal filtration pathway due to its size and tendency for proteins to be reabsorbed by the tubular epithelium, so would not be feasible to use as a reporter probe in a comparable *in vivo* diagnostic system.[203–206] Additionally, as a protein, HRP would be susceptible to nonspecific degradation by endogenous proteases *in vivo*, which would hinder activity of any cleared enzyme.[207] On the other hand, AuNCs showed extremely high stability in physiological environments (Figure 3.17c). A key performance requirement of the AuNCs is that they retain their catalytic activity following exposure to complex environments such as patient serum, which contains *ca*. 7 wt% protein. Due to their small size and zwitterionic peptide capping layer, GSH-AuNCs effectively evade nonspecific protein adsorption and exhibit robust catalytic activity even after exposure to protein-rich sera environments.[180] Similarly, AuNCs prepared *via* the co-templating method retained *ca*. 80 – 90 % of catalytic activity after 1 h incubation in undiluted fetal bovine serum (FBS) or synthetic urine compared to PBS controls. This contrasts with larger catalytic nanoparticles, such as the 120 nm platinum nanocatalysts

(PtNCs) described in §2.3.4, which only retain *ca*. 25 % activity after exposure to serum. AuNCs are on a similar size scale to serum proteins, whereas PtNCs provide a large surface area for serum protein adsorption, which leads to a significant loss of activity in physiological environments due to formation of a protein corona.

After confirming high retention of activity in physiological environments, the catalytic activity of a dilution series of each AuNC batch in synthetic urine was measured to assess the sensitivity of the reporter probes in the relevant physiological environment (Figure 3.17d). The limit of detection was *ca*. 2 picomoles in urine (where urine sample volume is fixed at 25 µL), and the activity displayed a linear response over three orders of magnitude of particle concentration.

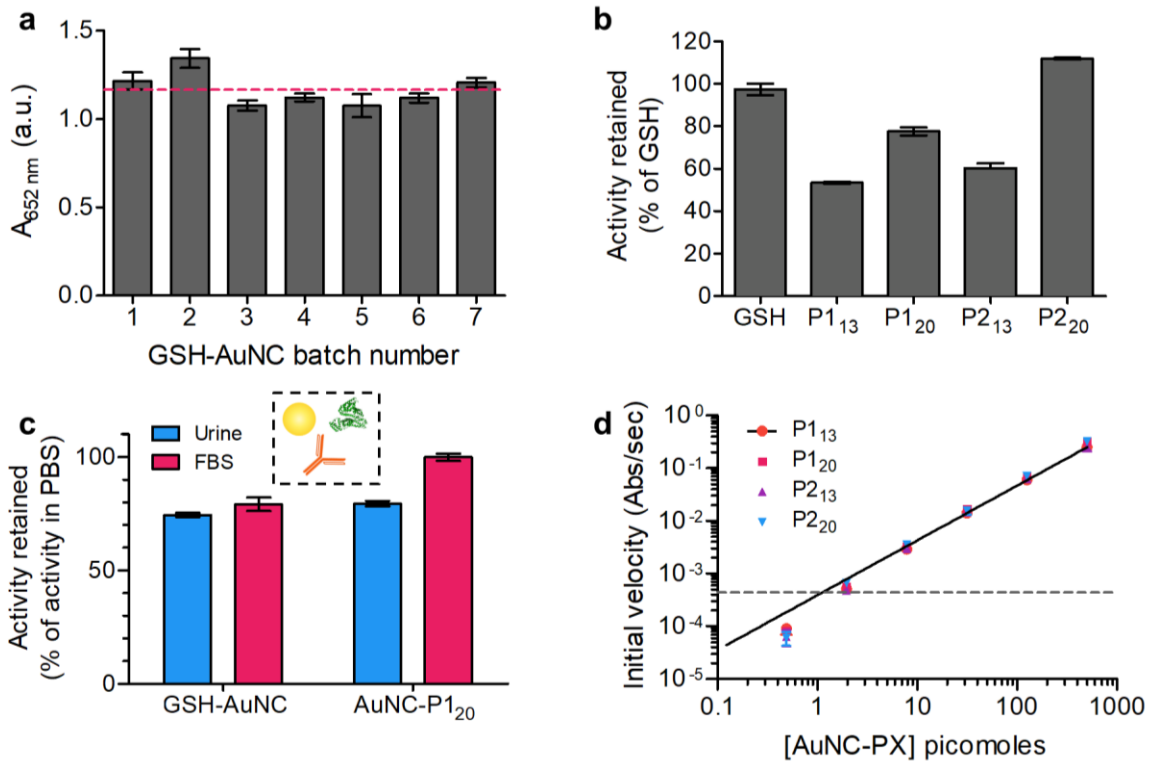


Figure 3.17 Characterization of peptide functionalized AuNCs. (a) AuNC synthesis showed high reproducibility with a coefficient of variation between seven independently synthesized batches of 8.5 %. The red line indicates the average test line intensity across batches. (b) Catalytic activity of AuNCs capped with different cysteine containing protease-cleavable peptide linkers (GSH, $P1_{13}$: GSH 1:5, $P1_{20}$: GSH 1:5, $P2_{13}$: GSH 1:4, $P2_{20}$: GSH 1:4). Activity is measured by the absorbance at 652 nm corresponding to the oxidation of TMB by H_2O_2 and normalized here to the activity of GSH-AuNCs in PBS. (c) Catalytic activity of GSH-AuNCs and representative AuNC-$P1_{20}$ batch incubated in serum and urine environments for 1 h. Activity is normalized to activity of AuNCs in PBS. (d) Limit of detection of reporter probes measured by catalytic activity of AuNCs functionalized with peptides P1 or P2. Catalytic activity is measured by initial rate analysis ($A_{652\ nm}$/s) of TMB oxidation. Solid line indicates activity for AuNCs is linear over 3 orders of magnitude of particle concentration. Dotted line represents limit of detection, which is calculated as 3 times the standard deviation of the blank (urine without AuNCs) (mean ± s.d., n = 3).

Selecting the particle platform to take forward *in vivo* required optimization of protease substrate loading. The biotinylated protease substrate is required to form the AuNC-neutravidin (AuNC-NAv) complex. However, increasing the number of P1 or P2 peptides per AuNC resulted in a decrease in activity, thus requiring a careful balance of synthesis parameters (Figure 3.18a – b). The number of biotin ligands incorporated onto the AuNCs during synthesis was quantified, and a simple paper-based assay was used to test the functional performance of the AuNC formulations. A nitrocellulose membrane bearing a polystreptavidin test line (§2.1.3) was used to test the ability of the AuNCs to effectively bind to avidin, and a subsequent catalytic development step was used to probe the activity of the particles (Figure 3.18d). This test was used to quickly visualize which AuNC formulation performed optimally in terms of forming a complex (binding to avidin) and retention of activity (through the catalytic development at the test line) by simply measuring test line intensity. Indeed, there was an optimal ratio of protease substrate incorporated in the synthesis which led to efficient capping of the gold core with biotinylated protease cleavable ligands while retaining sufficient activity to preserve diagnostic sensitivity: 1:5 ratio for thrombin substrates (P1: GSH) and a 1:4 ratio for MMP substrates (P2: GSH), which was taken forward in synthesis of particles in the following figures.

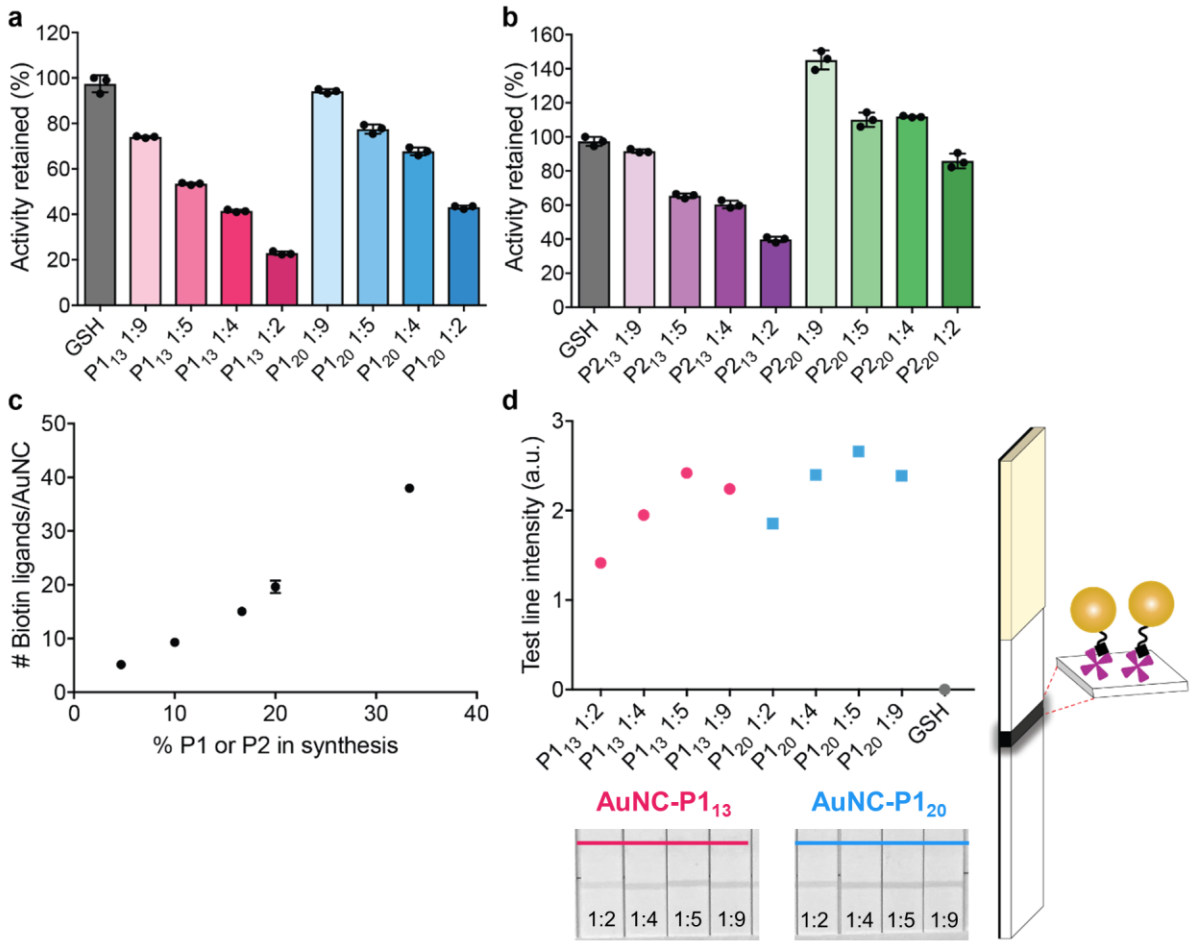


Figure 3.18 (a-b) Catalytic activity of AuNCs synthesized with varying peptide sequences (P1 or P2) and varying ratios of protease-cleavable peptide sequence to glutathione (1:9, 1:5, 1:4, 1:2), where activity is normalized to GSH-AuNCs) (mean ± s.d., *n* = 3). (c) Quantification of biotin ligands per AuNC when ratio of peptide sequence (P1 or P2) to glutathione was varied in the synthesis. (d) Test line intensity, quantified in ImageJ, corresponding to AuNC-P1$_{13}$ or AuNC-P1$_{20}$ bound to polystreptavidin test line. AuNCs bound at the test line catalyze the oxidation of CN/DAB (4-chloro-1-naphthol/3,3′-diaminobenzidine tetrahydrochloride) peroxidase substrate in the presence of hydrogen peroxide producing an insoluble black product. Inset: paper-based assay showing AuNC-P1$_{13}$ or AuNC-P1$_{20}$ bound to test line and visualized by taking advantage of catalytic activity of AuNCs.

The optimal substrate incorporation for efficient synthesis corresponded to *ca*. 15 – 20 biotinylated protease substrates per AuNC after purification (corresponding to 17 % P1 or 20 % P2 used in synthesis, Figure 3.18c). The grafting density of biotinylated peptides on the surface of AuNCs was quantified by measuring the amount of biotinylated ligand not incorporated onto the surface during synthesis. The amount of biotin in the supernatant of AuNC synthesis after purification was measured using 4'-hydroxyazobenzene-2-carboxylic acid (HABA)-avidin reagents, and biotin concentration on the particles was extrapolated using the starting concentration of biotin in synthesis and estimated concentration of AuNCs. This grafting density is an estimate of the biotinylated peptides on the surface, but it does not provide quantification of the number of glutathione ligands on the surface, although it is

expected to scale with the feed ratio. It is hypothesized that there may be variations in ligand incorporation and packing density based on the peptide's radius of gyration, hydrophobicity, and charge, and it will be important to investigate the final grafting density and ratios of PX:GSH for each particle batch to understand how surface composition affects AuNC size, shape, and catalytic activity. This may be better accomplished by decoupling the gold nanoparticle synthesis and surface modification steps. For example, Guldin and coworkers[208] demonstrated fine size control over gold nanoparticle synthesis using oleylamine (OAm) chemistry and subsequent surface modification with precise control over grafting density through thiol-for-OAm ligand exchange. Thiol-for-thiol ligand exchange is challenging to achieve with the current synthesis approach as it would require a large (> 1000) molar excess of biotinylated peptide and long incubation times because of the strong association between the thiolated capping agent and the gold core. However, the decoupled ligand exchange approach would be feasible with a more labile intermediate capping ligand such as oleylamine to facilitate the exchange and achieve a more well controlled and defined grafting density. While biotin quantification was performed here to estimate the number of biotinylated ligands on the AuNC surface, thermogravimetric analysis (TGA) can also be used to quantify total organic content in the ligand shell by measuring the weight loss related to the decomposition of the organic ligands at high temperatures. In future work it would be interesting to decouple AuNC synthesis and modification approaches and quantify the ligand shell using TGA to investigate the relationships between structure, surface composition, and function (*e.g.* catalytic activity).

3.3.6 AuNCs are cleared *via* the kidney and retain their catalytic activity in urine

Previous reports have investigated the renal clearance efficiency of ultra-small glutathione-protected gold nanoclusters by quantifying gold content in urine and other organs using inductively coupled plasma mass spectrometry (ICP-MS).[159,167] Du *et al.* recently highlighted the size precision of the body's response to nanoparticles by examining size-dependent glomerular filtration. In particular, they found that unlike the size dependency observed in glomerular filtration for nanoparticles larger than 2 nm, an inverse size dependency exists for particles in the sub-nanometer regime due to physical entrapment in the endothelial glycocalyx of the glomerulus, similar to the separation principle in gel filtration or size exclusion chromatography (GFC/SEC).[167] Glutathione-capped gold particles in the 1 – 1.7 nm size regime renally cleared at *ca*. 50 % injected dose within 24 h post injection, whereas significantly reduced clearance was observed for clusters smaller or larger than this optimal renal clearance size regime.[167] When not bound to a carrier protein, the protease-responsive AuNCs (*ca*. 1.5 nm) are in the optimal size regime for efficient renal clearance.

In light of their optimal size, it was necessary to determine whether the protease-cleavable AuNCs renally cleared, and whether their catalytic activity was retained after *in vivo* interrogation of healthy mice. The high physiological stability and retention of AuNC catalytic activity after exposure to serum and urine offered a unique opportunity to non-invasively measure AuNC clearance using both intrinsic catalytic activity and gold content with ICP-MS (Figure 3.19). AuNC renal clearance was determined by intravenous (i.v.) injection of AuNCs into the tail vein of healthy mice (200 µL, 10 µM particle concentration), collecting urine 1 h post injection (p.i.), and performing both a catalytic activity assay on the collected urine and ICP-MS analysis on the same urine samples to quantify gold content. To determine renal clearance efficiency, both the catalytic activity and the gold content of AuNCs spiked into urine were used to generate a calibration curve of the injected dose. This was then used to compare activity and gold content of cleared urine. This *in vivo* renal clearance study showed that up to 80 % of the injected dose of functionalized AuNCs left the body *via* this route and retained their catalytic activity in urine (Figure 3.19b). Urine samples were also digested using concentrated acid and ICP-MS was used to corroborate the results of the catalytic activity assay. Analysis of gold content by ICP-MS indicated renal clearance efficiencies up to 80 % on the same urine samples. Encouragingly, the catalytic activity assay and ICP-MS results showed a positive correlation (Pearson correlation coefficient = 0.49). The positive correlation means the results of colorimetric assay could be semi-quantitative if correlated with estimated cleared AuNCs using gold content in ppb from ICP-MS when normalized to gold content in the injected dose.

A Bland-Altman analysis was also performed to compare the two assay methods (Figure 3.19d). The Bland-Altman method plots the difference between the two measurements as a function of the average of the two measurements of each sample.[209] The bias is computed as the value determined by one method minus the value determined by the other method. When the bias or the average of the differences is close to zero it means the methods are producing similar results. Since the bias here is close to zero (2.5), it suggests that the two techniques are comparable and are not systematically producing different results. The analysis also produces the 95 % limits of agreement, which are computed as the mean bias plus or minus 1.96 times the standard deviation of the bias. It will be important in future studies to understand the repeatability of the measurement systems, which will require measuring each urine sample multiple times with each technique (replicates on the same urine sample with each method). The advantage of a dual readout means that catalytic activity assay could be used for a quick (< 30 min) assessment of AuNC presence in urine, and ICP-MS can provide a high sensitivity readout of Au content on a longer time scale (1 – 3 h due to sample digestion and preparation).

As a control, urine from mice injected with PBS was analyzed using the catalytic activity assay to ensure no endogenous peroxidase activity in collected urine.

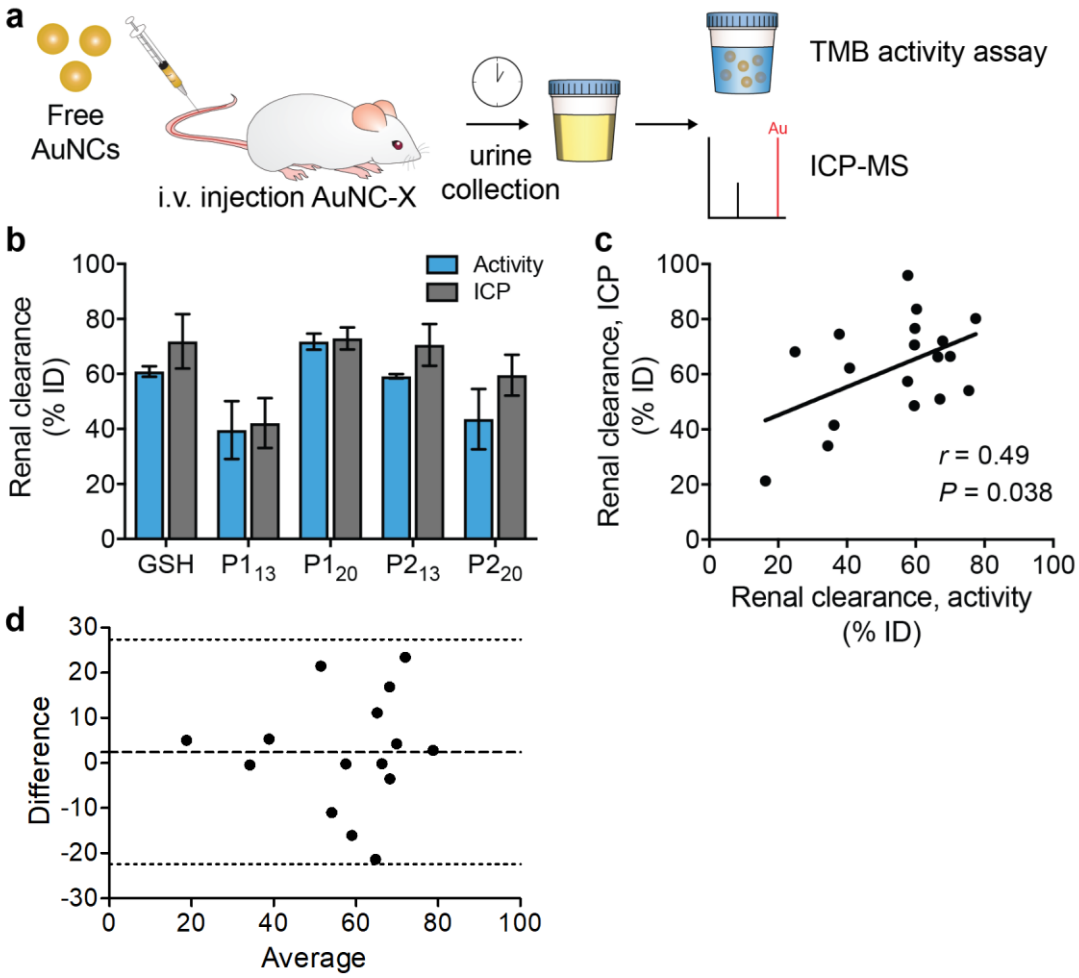


Figure 3.19 Peptide-functionalized AuNCs renally clear and retain their catalytic activity in urine. (a) Schematic of the renal clearance assay. AuNCs were i.v. injected into Swiss Webster mice, and urine was collected 1 h post-injection. Urine was analyzed by both TMB catalytic activity assay and by ICP-MS for gold content. (b) Renal clearance efficiency of GSH-AuNC, AuNC-P1$_{13}$, AuNC-P1$_{20}$, AuNC-P2$_{13}$, AuNC-P2$_{20}$ as measured by colorimetric assay ($A_{652\ nm}$) and by ICP-MS (estimated ppb cleared), normalized to activity and gold content, respectively, of the injected dose ($n \geq 3$ per group). Ava Soleimany performed animal injections and urine collection for *in vivo* experiments. (c) Correlation between estimated renal clearance as measured by colorimetric activity assay and by ICP-MS (Pearson's r = 0.49, *P < 0.05). (d) Bland-Altman analysis comparing the differences and averages of clearance values as measured by ICP-MS and colorimetric assay, with a bias of +2.5 represented by a dotted line and 95 % limits of agreement (-22.3 and +27.3) shown as two thin dotted lines. For any future sample tested, the difference between measurements using these two methods should lie within the limits of agreement approximately 95 % of the time.

3.3.7 Formation and characterization of nanosensor complexes

It next became necessary to confirm whether the peptides coupled to the AuNC and avidin scaffold could still be cleaved by proteases. Biotin functional handles on the protease substrate-modified AuNCs were used to tether it to the neutravidin carrier protein to assemble a complex that was larger than the glomerular filtration cut-off (*ca*. 5.5 nm).[180] The non-clearable nanosensors were designed such that upon interaction with the relevant disease-associated protease, the complex is disassembled, and liberated AuNCs can be subsequently filtered into the urine. AuNC-NAv complexes were successfully assembled from all protease cleavable peptides in Table 3.2. DLS was used to monitor the size of the free AuNCs, neutravidin carrier protein, and assembled AuNC-NAv complex (Figure 3.20), with hydrodynamic sizes 2.3 nm, 7.5 nm, 11.7 nm, respectively. Additionally, complexes were more efficiently formed when protease-substrate functionalized AuNCs were incubated with high concentrations of neutravidin protein (Figure 3.20a), resulting in *ca*. 1 – 2 AuNCs loaded on each neutravidin carrier. Loading efficiency was measured by calculating the difference in catalytic activity of AuNC-NAv before and after ultrafiltration purification to remove unbound AuNCs. Incubation with higher concentrations of avidin increased the efficiency of complex formation by up to 70 % (Figure 3.20a). While theoretically four biotins should be able to simultaneously bind one avidin carrier, it was not possible to load more than two biotinylated AuNCs on an avidin core, even with a large excess of AuNCs (10 molar excess to avidin). This could be in part due to steric hindrance. Each AuNC has *ca*. 20 biotin ligands, so it is also possible that one AuNC could exhibit multivalent binding to the avidin core.

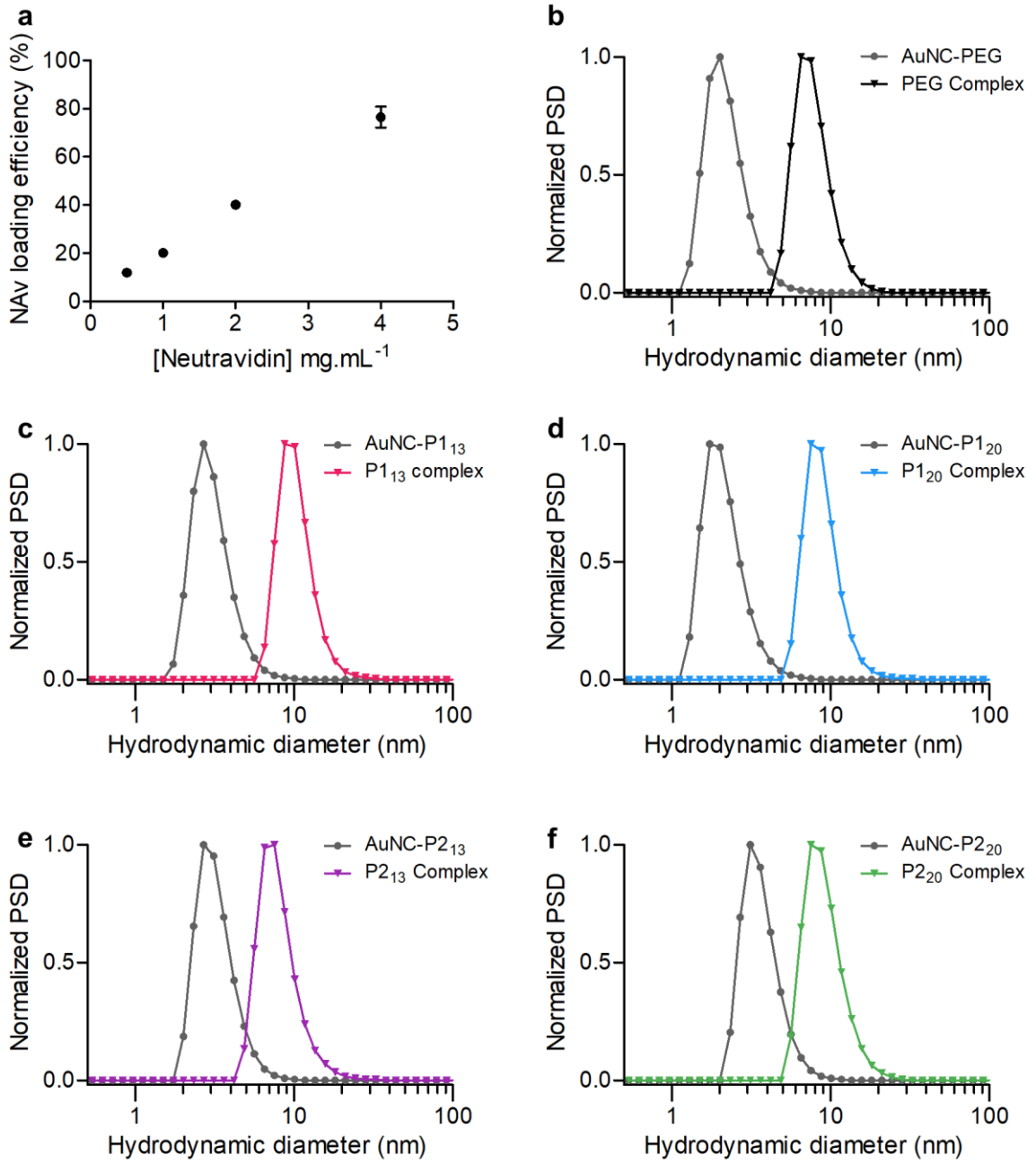


Figure 3.20 (a) Quantification of efficiency of binding of biotinylated AuNCs to neutravidin protein for varying neutravidin concentrations measured by catalytic activity assay, where 4 mg·mL^{-1} represents a 1.2 molar excess of AuNCs to avidin, and 0.5 mg·mL^{-1} represents a 9.6 molar excess of AuNCs to avidin. (b – f) Number particle size distribution (PSD) measured by DLS for AuNC-peptide library and complexes prepared with each particle batch after purification.

The AuNC-NAv complexes were examined using TEM (Figure 3.21). Complexes were desalted and diluted 100-fold before imaging. Using automated image analysis to measure the distance between a particle and its nearest neighbor, it was possible extract a histogram of distances between particles. A common distance of 8.1 ± 2.9 nm suggests that many AuNCs are separated by the length of a neutravidin protein, in which case two AuNCs could

be bound to one core. Although there could be artifacts from drying effects on the TEM grid, this analysis along with DLS and catalytic activity assay confirm that the AuNCs are bound to a protein core to form a larger construct. While it is not conclusive exactly how many AuNCs are bound to each avidin core, the main consideration here was in ensuring that there were no free or unbound AuNCs left after AuNC-NAv purification, which would increase background signal. It would be interesting to further explore how increasing the AuNC loading on the NAv carriers would change enzyme cleavage kinetics. With ≥ 1 – 2 AuNCs bound per avidin core confirmed, it was possible to explore how the complexes are disassembled *in vitro*.

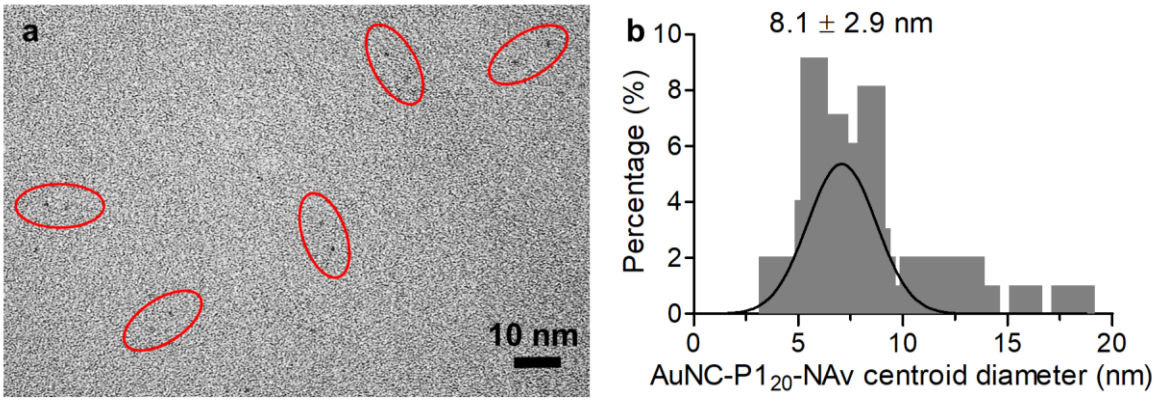


Figure 3.21 (a) TEM of purified AuNC-P1$_{20}$-NAv complexes, where possible AuNC-NAv-AuNC complexes are outlined in red. (b) Histogram of distances between nearest neighbor AuNCs. TEM images analyzed ≥ 10, number of particles analyzed ≥ 200. Dr. Qu Chen assisted with TEM imaging.

3.3.8 Engineered AuNC nanosensor complexes are sensitive to protease activity

Proteolytic cleavage of AuNC complexes was characterized *in vitro* by incubating complexes with recombinant proteases and using gel filtration chromatography (GFC) to separate cleavage products by size (Figure 3.22). Comparisons have been drawn between the glomerular filtration of sub-nanometer AuNCs and separation in size exclusion chromatography, where larger molecules renally clear or elute faster than smaller ones only in the sub-nanometer regime.[167] In GFC, smaller molecules diffuse further into the pores of the beads, moving more slowly through the bed through physical retention. Larger molecules enter the pores less or not at all and thus move through the bed more quickly, filtering through faster. Both molecular weight and three-dimensional shape contribute to the degree of retention. A GFC protocol was developed to separate cleavage products by size. A catalytic activity assay was used to analyze cleavage products and monitor degradation using a simple colorimetric readout. AuNC complexes were incubated with relevant enzymes for 1 – 12 h at 37 °C. After enzyme incubation, samples were loaded onto the column, and fractions were

collected and analyzed using a TMB catalytic activity assay in a microwell plate. AuNC complexes functionalized with the longer thrombin-responsive and MMP-responsive substrates were efficiently disassembled *in vitro* after treatment with the corresponding protease (Figure 3.22c – d). Disassembly of the complexes was monitored by measuring the catalytic activity of column fractions when AuNC-complex, free AuNCs, and AuNC-complex pre-incubated with recombinant protease were eluted through a chromatography column. When catalytic activity is plotted as a function of eluted volume, a clear peak is associated with each cleavage product. The larger AuNC complexes eluted at 5 – 6 mL, while the smaller free AuNCs eluted at 7 – 9 mL. After incubation with the relevant enzyme, AuNC complexes exhibited a peak in absorbance overlapping with the free AuNCs, suggesting cleavage by the enzyme liberated the AuNCs resulting in a smaller cleavage product. Nonspecific cleavage was investigated by incubating AuNC-$P1_{20}$-NAv with MMP9, and AuNC-$P2_{20}$-NAv with thrombin (swapping enzymes with the relevant models). Extremely low background cleavage was observed after incubation with an off-target enzyme (Figure 3.22c – d, dotted line) as evidenced by the peak associated with the AuNC-NAv complex not shifting.

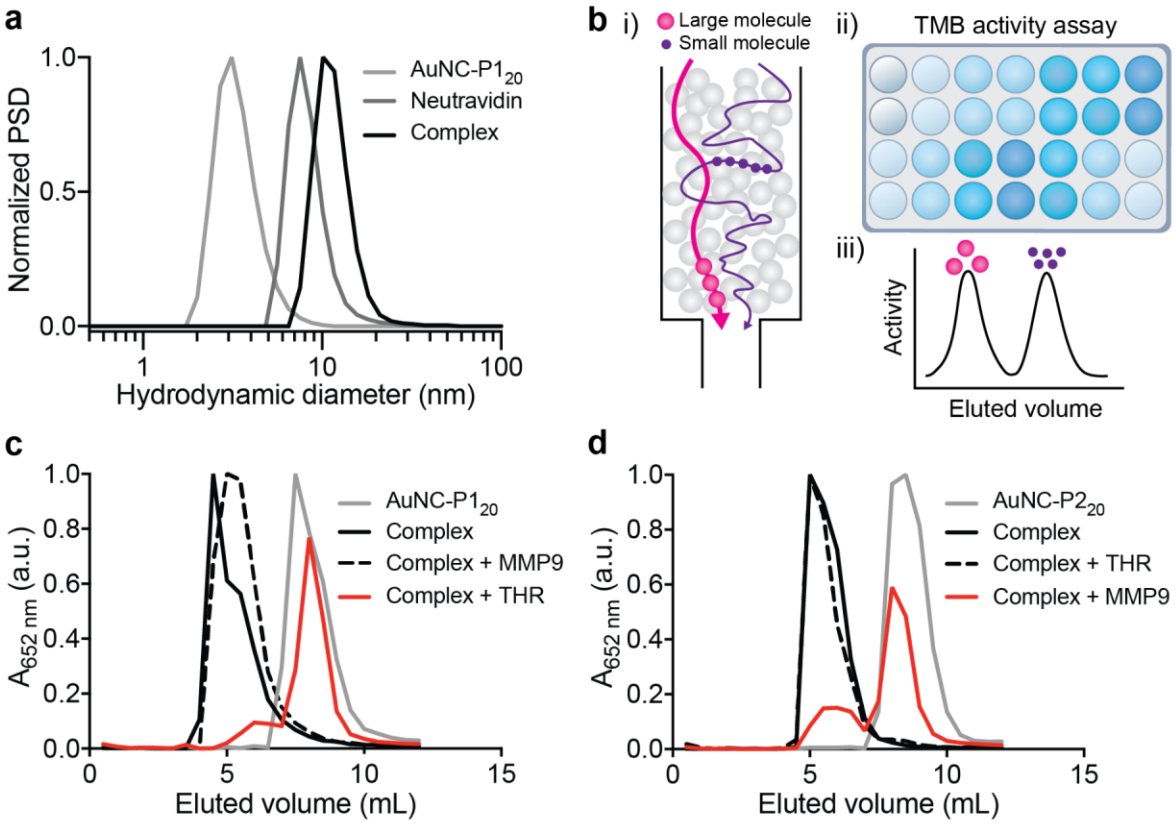


Figure 3.22 AuNC-avidin complexes disassemble *in vitro* in response to protease activity. (a) Number particle size distribution (PSD) measured by DLS of AuNC-P1$_{20}$, neutravidin, and AuNC-P1$_{20}$-NAv complex (Complex). (b) Schematic of *in vitro* assay to monitor size of AuNC-NAv complex in response to recombinant protease activity. (i) gel filtration chromatography is used to separate molecules based on size (free AuNCs are smaller than AuNC-avidin complex). (ii) Catalytic activity assay is performed on collected column fractions. (iii) Activity of column fractions can be plotted against eluted volume and area under curve can be used to determine ratio of free AuNCs to complex. (c) Catalytic activity of gel filtration chromatography (GFC) column fractions associated with AuNC-P1$_{20}$, AuNC-P1$_{20}$-NAv complex (Complex), AuNC-P1$_{20}$-NAv incubated with 75 nM MMP9 with 2000 molar excess P1$_{20}$ peptide substrate for 12 h at 37 °C (Complex + MMP9), and AuNC-P1$_{20}$-NAv complex incubated with 170 nM thrombin with 1000 molar excess P1$_{20}$ peptide for 12 h at 37 °C (Complex + THR). (d) Catalytic activity of GFC column fractions associated with AuNC-P2$_{20}$, AuNC-P2$_{20}$-NAv complex (Complex), AuNC-P2$_{20}$-NAv complex incubated with 170 nM thrombin with 1000 molar excess P2$_{20}$ peptide for 12 h at 37 °C (Complex + THR), and AuNC-P2$_{20}$-NAv incubated with 75 nM MMP9 with 2000 molar excess P2$_{20}$ peptide substrate for 12 h at 37 °C (Complex + MMP9).

For the chosen incubation times and enzyme concentrations, a small peak associated with the original complex was also present, suggesting not all AuNCs were liberated from the complex in the time frame of the experiment. Because the synthesis requires more than one biotinylated protease substrate per AuNC to form the complex, it is possible that not every cleavage event results in liberation of an AuNC. The extent of cleavage of the AuNC complex under different conditions could be quantified by analyzing the area under the curve associated with each cleavage product (Table 3.4). It was hypothesized that varying linker

length will affect cleavage rates for enzyme incubation during the same time frame. This was confirmed by comparing long and short sequences for both MMP and thrombin cleavable complexes. Under the same conditions, complexes formed from shorter sequences exhibited 15 – 20 % cleavage, whereas longer peptide linker exhibited 75 – 90 % cleavage, suggesting the scissile bond was more accessible to the enzyme in this configuration (Figure 3.23a – b).

The specificity of the peptide substrates towards the proteases of interest was explored by incubating the complexes with off-target proteases. While several enzymes in the MMP family share similarities in primary structure and ability to cleave ECM components, the PLG domain is commonly reported as the substrate recognition profile more specifically associated with cleavage by MMP9 over MMP7 and MMP13, and was originally designed based on the consensus of the collagen cleavage site by MMPs.[210–212] Nonspecific protease cleavage was examined by incubating the MMP9-responsive complexes with a fixed concentration of MMP7, MMP13, and MMP9. MMP9 cleaved most robustly, but there was some nonspecific cleavage by MMP13, and very low cleavage by MMP7 (Figure 3.23c – d), which highlights that the nanosensor can only be as specific as the peptide sequences that broadly show cleavage by several enzymes in the MMP family. There was both lower specific and nonspecific cleavage for the shorter linker complex (AuNC-$P2_{13}$-NAv) when incubated with MMPs, suggesting the possibility of tailoring specificity of cleavage site by altering accessibility to the scissile bond through linker length.

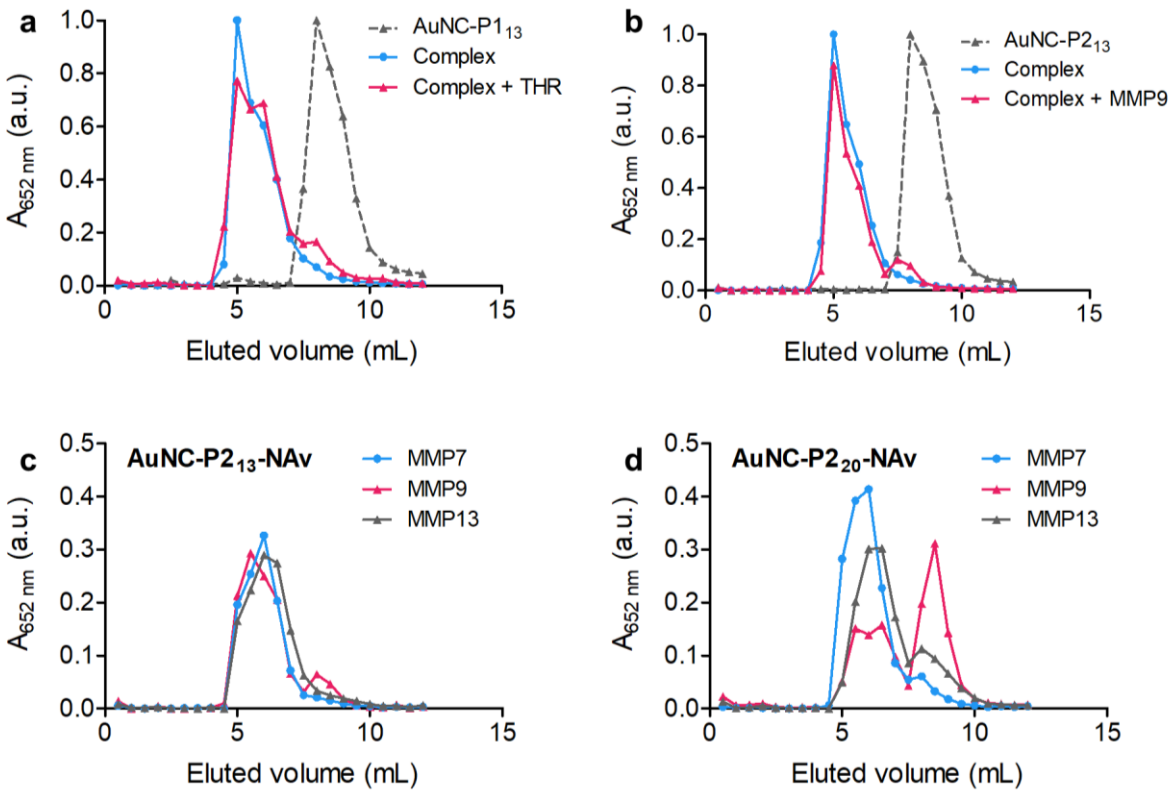


Figure 3.23 Catalytic activity of gel filtration chromatography (GFC) column fractions associated with: (a) AuNC-P1$_{13}$, AuNC-P1$_{13}$-NAv-complex and AuNC-P1$_{13}$-NAv complex incubated with 100 nM thrombin for 12 h at 37 °C. (b) AuNC-P2$_{13}$, AuNC-P2$_{13}$-NAv-complex and AuNC-P2$_{13}$-NAv complex incubated with 100 nM MMP9 for 12 h at 37 °C. (c) 4.5 µM AuNC-P2$_{13}$-NAv complex incubated with 37 nM MMP7, MMP9, and MMP13 for 12 h at 37 °C. (d) AuNC-P2$_{20}$-NAv complex incubated with 37 nM MMP7, MMP9, and MMP13 for 12 h at 37 °C; in all cases incubations represented > 2000 molar excess of peptide to enzyme.

Finally, the effect of biotinylated-protease substrate loading per AuNC on the rate of cleavage over short time frames was investigated. It was hypothesized that by reducing the number of biotin ligands on the AuNC surface, there would be a higher probability of an enzyme cleavage event specifically liberating an AuNC from the complex, rather than cleaving off peptides that are not actively tethering the AuNC to the core. This was indeed the effect that was observed. After incubation with 60 nM thrombin for 1 h, for AuNCs with only 5 biotin ligands per cluster there was 40.3 % more cleavage than for AuNCs presenting 20 biotin ligands per cluster (Figure 3.24). However, forming the AuNC-NAv complex was over twice as efficient when the AuNCs present 20 biotin ligands per AuNC (80 % efficiency in complex formation). As a result, this ratio was maintained for further study. Future work will explore the effects of further altering presentation of ligands and capitalizing on multivalent binding to the protein carrier to introduce logic gates to improve specificity.

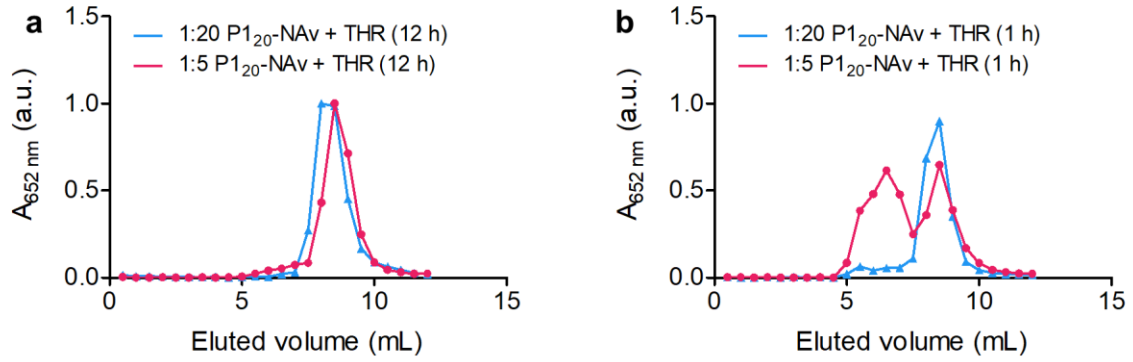


Figure 3.24 Catalytic activity of gel filtration chromatography column fractions associated with: AuNC-NAv complexes prepared with different $P1_{20}$ loadings ($P1_{20}$: GSH 1:5 or 1:20), where 1:5 case has *ca*. 20 biotin ligands per AuNC and 1:20 case has *ca*. 5 biotin ligands per AuNC, for (a) 12 h and (b) 1 h incubation with 60 nM thrombin at 37 °C.

Table 3.4 Quantification of cleavage products from *in vitro* protease cleavage assay

AuNC-NAv complex	% Cleavage (area under curve)	Figure reference
AuNC-$P1_{13}$-NAv + THR (12 h)	21.8 %	Figure 3.23a
AuNC-$P1_{20}$-NAv + THR (12 h)	90.2 %	Figure 3.22
AuNC-$P2_{13}$-NAv + MMP9 (12 h)	15.2 %	Figure 3.23b
AuNC-$P2_{20}$-NAv + MMP9 (12 h)	75.1 %	Figure 3.22
Shorter linker/specificity AuNC-$P2_{13}$-NAv + MMP7/9/13 (12 h)	MMP7: 7.9 % **MMP9: 14.8 %** MMP13: 13.8 %	Figure 3.23c
Longer linker/specificity AuNC-$P2_{20}$-NAv + MMP7/9/13 (12 h)	MMP7: 12.1 % **MMP9: 54.9 %** MMP13: 29.8 %	Figure 3.23d
Enzyme Swap AuNC-$P1_{20}$-NAv + MMP9 AuNC-$P2_{20}$-NAv + THR	 7.1 % 5.5 %	Figure 3.22
Varying peptide loading per AuNC: AuNC-1:20-$P1_{20}$-NAv + THR (1 h) AuNC-1:5-$P1_{20}$-NAv + THR (1 h)	 89.9 % 49.6 %	Figure 3.24b

3.3.9 Kinetics of *in vitro* recombinant protease cleavage

To explore the kinetics of cleavage in more detail using a single-molecule detection method, fluorescence correlation spectroscopy (FCS) was employed.[213–215] FCS is a correlation analysis of temporal fluctuations of fluorescence intensity of fluorescent particles in a small observation volume, giving insight into the diffusion behavior and concentration of detected particles. The method records temporal changes in the fluorescence emission intensity caused by single fluorophores passing through the detection volume (femtoliter scale). The

intensity changes can be quantified in their strength and duration by temporally auto-correlating the intensity signal, leading to the average number of particles and their average diffusion time through the detection volume. The technique is especially useful for monitoring binding or cleavage events by analyzing changes in diffusivity over time. For example, free fluorescently labeled AuNCs exhibit faster diffusion than AuNCs which are complexed to a neutravidin core. Therefore, the diffusivities and corresponding hydrodynamic diameters of free AuNCs or AuNC-NAv complexes can be monitored over time in the presence of enzymes to analyze the kinetics of cleavage.

For FCS analysis, AuNC batches were labeled with Oregon Green fluorescent dye (at the free amino group of GSH) and assembled into complexes with the neutravidin core. FCS was used to analyze disassembly of the fluorescently labeled complex in the presence of an enzyme. In the measurement, labeled particles diffuse through the detection volume, producing a fluctuating fluorescence signal which is subjected to an autocorrelation algorithm yielding a correlation curve (§3.2.9), $G(\tau)$, which shows the mobility of the particles. The diffusion time of the particles, τ_D, can be estimated from the inflection of the decay of the correlation curve. To calculate the percentage of AuNCs cleaved from the AuNC-NAv complex, the stocks of free AuNCs and complexes were first fitted using one component fits ($G_{1comp}(\tau)$), to obtain diffusion time for the pure components. Second, samples incubated with enzymes were fitted with two component fits ($G_{2comp}(\tau)$) with one component fixed to pure cluster diffusion (τ_1) and the other fixed to pure complex diffusion (τ_2) to yield the fraction of free clusters (F_1), which is equivalent to the fraction cleaved.

By inspection, it is clear from the correlation curves that the free dye, free AuNCs, and AuNC-NAv complex diffused at different speeds (Figure 3.25b). After enzyme incubation, the diffusivity of the AuNC-NAv complex shifted toward the one of the free AuNCs over time. The hydrodynamic diameter could be calculated from the diffusivity using Stokes-Einstein equation (Figure 3.25c). From the size analysis, the AuNC-P2_{20}-NAv complex was completely disassembled within 6 h MMP9 incubation. Encouragingly, the size of the complex did not significantly change when incubated with an off-target enzyme, in this case thrombin, indicating that the complex was not nonspecifically disassembled. Additionally, the size of the thrombin cleavable complex, AuNC-P1_{20}-NAv, does not change when incubated with the off-target enzyme MMP9, which is relevant for future *in vivo* control studies (Figure 3.25c, blue).

The main advantage of the FCS measurements over the GFC assays is the ability to capture early time points of enzyme cleavage kinetics. A significant difference in cleavage kinetics was

observed for the AuNC-$P2_{13}$-NAv and AuNC-$P2_{20}$-NAv complexes upon interaction with MMP9 (Figure 3.25d). For the AuNC-$P2_{13}$-NAv complex, the percentage of cleaved AuNCs with time was linear over the first 500 min of MMP9 incubation, whereas the AuNC-$P2_{20}$-NAv was linear over just the first 16 min of enzyme incubation. The linear regions were analyzed by linear regression, and the rates of cleavage were calculated. MMP9 exhibited a rate of 3 % AuNC cleaved per min toward the AuNC-$P2_{20}$-NAv complex, while the rate was only 0.08 % AuNC cleaved per min toward the AuNC-$P2_{13}$-NAv complex. The complex formed of the longer linker was cleaved at a rate *ca*. 40 times faster than the shorter linker. The difference in enzyme kinetics could be attributed to the difference in linker length, and subsequently increased accessibility of the enzyme to the scissile bond. For *in vivo* studies, urine was collected 1 h post injection with the complex. To design a biologically relevant *in vitro* experiment, the amount of cleaved AuNCs was calculated over the first 1 h of enzyme incubation. FCS results show that in the presence of biologically relevant enzyme concentrations (50 nM MMP9), significant cleavage was observed for AuNC-$P2_{20}$-NAv complexes, where 80 % AuNCs were cleaved from the complex within the first hour of incubation with MMP9. In the same time frame, only 20 % AuNCs were cleaved from the AuNC-$P2_{13}$-NAv complex.

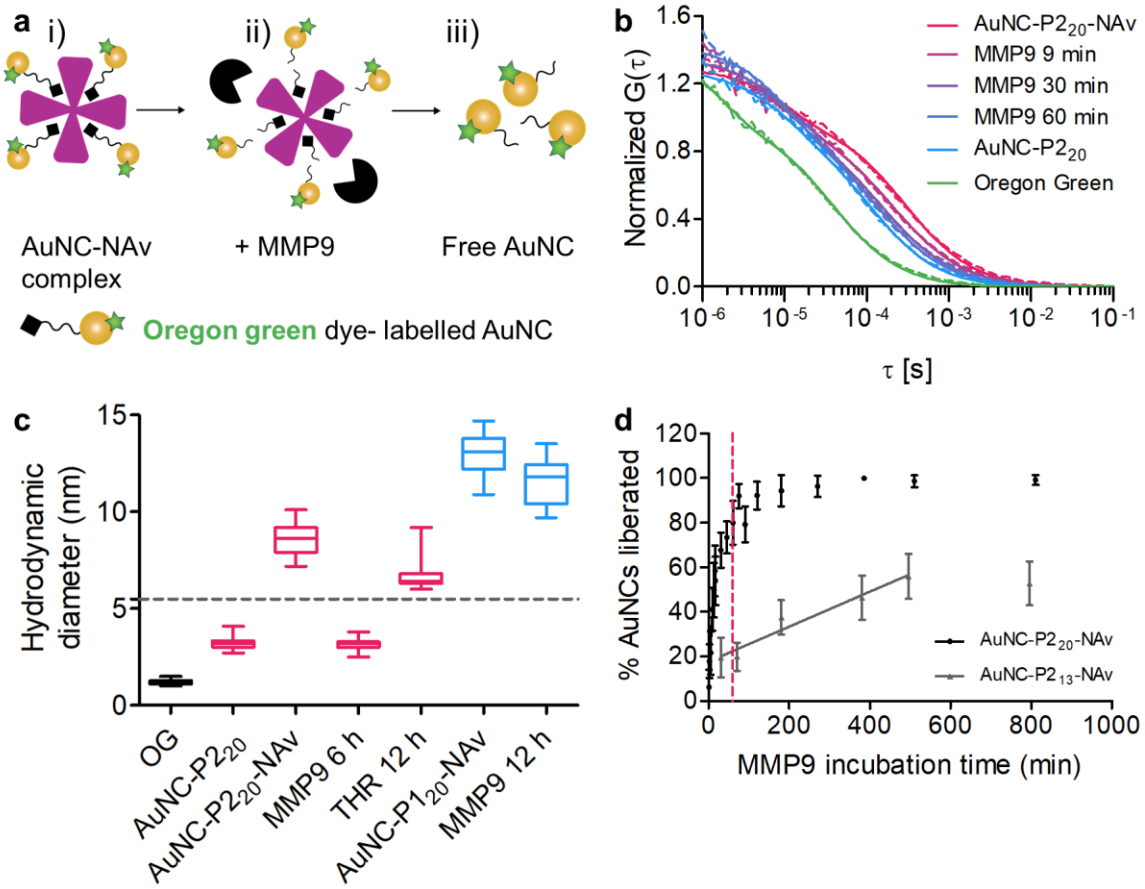


Figure 3.25 (a) Schematic illustration of FCS measurement. First, AuNCs were labeled with fluorescent dye and complexed to neutravidin core. Dye-labeled AuNC-NAv complexes were incubated with relevant enzyme and FCS was used to monitor changes in diffusion time due to enzyme cleavage. (b) Correlation curves from FCS measurements (n = 25) showing AuNC-P2$_{20}$-NAv complex in the presence of MMP9 over time compared to free AuNCs and Oregon green dye. A clear shift to smaller sizes was observed for longer enzyme incubation times (red to blue color change), indicating cleavage of AuNCs. (c) Hydrodynamic diameters extracted from FCS correlation curves showing changes in sizes of complexes after enzyme incubation. Dashed line represents renal filtration size cut-off of *ca*. 5.5 nm.[152] Center line represents median, box limits represent upper and lower quartiles, and whiskers represent minimum and maximum values (n = 25). (d) Plot of fraction of AuNCs liberated from AuNC-NAv complex for MMP9 responsive complexes composed of either short (gray) or long linker (black) incubated with MMP9 up to 16 h. (mean ± s.d., n = 25). Dashed line at 60 min corresponds to time frame of in vivo experiments. Dr. Adrian Najer performed FCS experiments and FCS data analysis.

3.3.10 Biocompatibility of AuNC nanosensors

The biocompatibility of glutathione capped AuNCs has been well reported by others.[164] Zhang *et al*. reports that GSH-AuNCs cause inflammation and kidney function damage after 24 h, but these adverse responses are eliminated after 28 days due to renal excretion.[216] However, Zheng and co-workers have observed no signs of short or long-term systemic toxicity for GSH-AuNCs in mice or non-human primate models.[170] The differences in reported toxicity could be

related to variations in synthesis and purification protocols or in selection of animal models and injected dose. While similarly sized GSH-AuNCs are produced in both cases, the protocol used by Zhang *et al.* employs a sodium borohydride reduction step. Whereas the GSH-AuNC synthesis protocol in this chapter was adopted from Zheng and co-workers who employ a gentler reduction protocol using GSH as both the stabilizer and reducing agent. If not purified fully, the reducing agents could potentially elicit an immune response. This discrepancy in toxicity responses reported in literature highlights the need for standardized sample preparation and purification protocols and quality control measures for materials used in animal studies.

The potential toxicity of the AuNC-NAv complex was further investigated *in vitro* and *in vivo*. First, the biocompatibility of AuNC-$P2_{20}$-NAv was studied with HEK293T *in vitro* cell lines and demonstrated no significant cytotoxicity up to the highest level tested, 15 μM, which is equivalent to the *in vivo* injected dose. Body-weight changes can be an indicator of toxicity in mice. After i.v. administration of complex, there was negligible influence on the body weight of the mice up to 4 weeks, suggesting that protease-cleavable AuNC-NAv complexes did not induce significant systemic liver or kidney toxicity, relative to the PBS control (Figure 3.26). Before moving toward a clinical diagnostic platform, extensive biocompatibility studies will need to be performed, including hematology tests, hepatic and renal function biochemical markers tests, and histology on sections of major organs to investigate any signs of biomaterial-induced inflammation. Given that catalytic activity of AuNCs could be measured directly in cleared urine, it was hypothesized that catalytic activity could be used to produce a colorimetric urinary readout of disease state using the engineered probes.

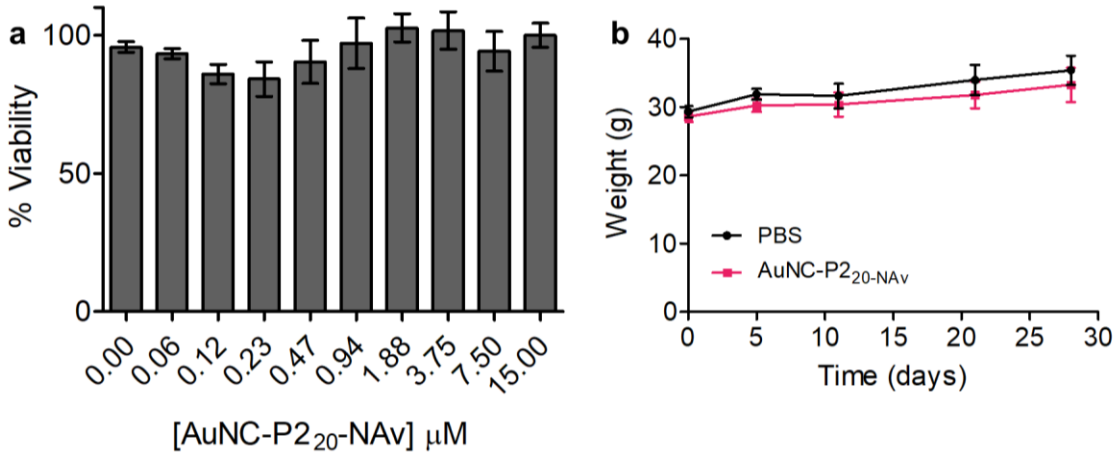


Figure 3.26 (a) *In vitro* cytotoxicity of AuNC-neutravidin nanosensor complex towards HEK293T cells, determined by the MTS assay (mean ± s.d., *n* = 3). AuNC-P2$_{20}$-NAv at the indicated concentrations were incubated with cells for 24 h. (b) Change in body mass of immunocompetent Swiss Webster mice injected with AuNC-P1$_{20}$-NAv (dose = 3000 pmol, 200 μL of 15 μM [AuNC]) compared with PBS control (mean ± s.d., *n* = 4 per group). There was no statistically significant difference in the mass change over a period of 4 weeks between control mice (PBS injection) and mice injected with AuNC-neutravidin complex. Ava Soleimany performed cell viability and *in vivo* weight tracking experiments.

3.3.11 AuNC nanosensors enable colorimetric urinary detection of disease

After confirming successful cleavage by recombinant proteases *in vitro* by GFC and FCS measurements, the protease-responsive AuNC nanosensor platform was applied to *in vivo* disease detection using the colorimetric urinary readout. First, the pharmacokinetics of the neutravidin complex was characterized in terms of blood half-life (Figure 3.27). To analyze blood half-life of the avidin carrier, mice were injected with neutravidin-biotin complexes labeled with a near-infrared dye, blood was collected at time points, and analyzed using an infrared scanner. The blood-half life was calculated to be 10.8 min, which agrees well with published reports of avidin and streptavidin half-lifes.[217,218] It is expected that the blood half-life will increase when AuNCs are tethered to neutravidin, as the overall size of the complex increases by *ca*. 2 nm. For biodistribution studies, nude mice bearing LS174T flank tumors were infused with near-infrared dye-labeled neutravidin-biotin complexes. Mice were sacrificed 1 h p.i., and organ and tumor accumulation were measured using an infrared scanner. The highest concentration of neutravidin complexes was found in the liver, which agrees with previous reports on organ accumulation of avidin and neutravidin.[198,217] Based on the measured blood half-life of the complex and the degree of tumor accumulation 1 h p.i., this was selected as the time point for further urine collection and analysis.

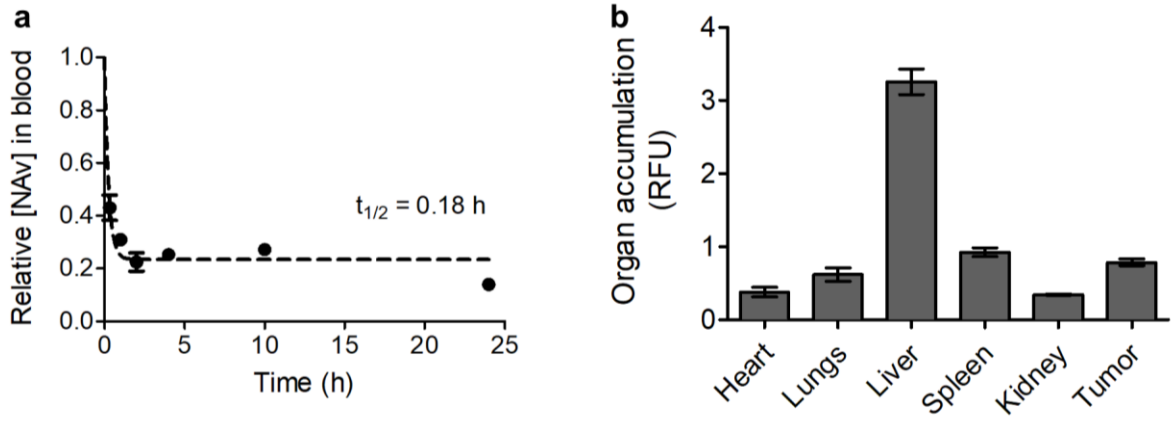


Figure 3.27 Pharmacokinetic characterization of neutravidin protein carrier. (a) Plasma concentration of fluorescently labeled neutravidin protein carrier was fit to a one-phase exponential decay (mean ± s.d., *n* = 4). (b) Organs and tumors were harvested 1 h after intravenous injection of fluorescently labeled neutravidin into LS174T tumor-bearing mice, and the signal intensity in each organ was measured by an Odyssey IR scanner (mean ± s.d., *n* = 4 mice). Fold changes in signal intensity (y-axis) were calculated for each organ between the experimental group (fluorescently labeled neutravidin) versus the PBS-injected control**.** Ava Soleimany performed *in vivo* pharmacokinetics and organ accumulation experiments.

For *in vivo* tumor experiments, mice bearing flank xenografts of the human colorectal cancer cell line LS174T, which secretes MMP9,[41] and healthy control mice were intravenously injected with MMP-responsive AuNC-$P2_{20}$-NAv nanosensors (Figure 3.28). Urine was collected from mice 1 h p.i., and catalytic activity assay was run on 25 µL sample of cleared urine. A clear blue color developed in collected urine samples containing AuNCs due to the oxidation of TMB peroxidase substrate. In the flank tumor model, a mean urinary signal increase of approximately 13-fold was found in tumor-bearing mice relative to healthy mice, as measured by the direct colorimetric readout and initial rate analysis (Abs/min) of cleared AuNC catalytic activity in collected urine (Figure 3.28c). To determine the diagnostic accuracy of the colorimetric assay, the frequency of true positives (sensitivity) and false positives (1 – specificity) was assessed by receiver operating characteristic (ROC) curves. ROC curves characterize the predictive power of a biomarker by returning the area under the curve (AUC) as a metric, with a baseline AUC of 0.5 representing a random biomarker classifier. By ROC analysis, the colorimetric assay was highly accurate and discriminated the presence of colorectal cancer xenografts with an area under the curve (AUC) of 0.95 (P = 0.0023).

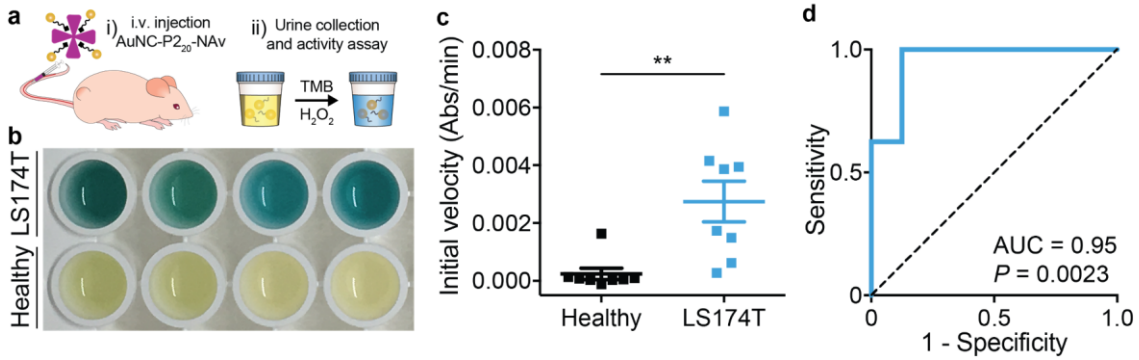


Figure 3.28 AuNC-functionalized protease nanosensors enable direct colorimetric urinary readout of disease state. (a) Mice bearing LS174T flank xenografts and age-matched healthy controls were injected i.v. with AuNC-P2$_{20}$-NAv complex. Urine was collected 1 h post injection, and renal clearance of liberated AuNCs was measured by catalytic activity assay. (b) Photograph of representative examples of colorimetric assay on urine from tumor-bearing (top) and healthy (bottom) mice injected with AuNC-P2$_{20}$-NAv (n = 8 mice per group, 4 shown). (c) Initial velocity of catalytic activity in urine collected from healthy and LS174T tumor bearing mice 1 h after injection with AuNC-P2$_{20}$-NAv complex, as measured by the rate of change of $A_{652\,nm}$ over the first 10 minutes of the assay (**P < 0.01, two-tail Student's t-test). (d) Receiver-operating characteristic (ROC) curve by initial velocity of catalytic activity assay discriminated healthy from diseased mice with an AUC of 0.95 (P = 0.0023 from random classifier). Ava Soleimany performed animal injections and urine collection for *in vivo* experiments.

Having established that the MMP-responsive AuNC nanosensors could discriminate between tumor-bearing and healthy mice, it was necessary to verify that the urinary signal from tumor-bearing mice was proteolytically driven. To ensure that the signal was not coming from endogenous peroxidase activity, tumor-bearing and healthy control mice were injected with PBS, urine was collected 1 h p.i., and catalytic activity assay was performed on a 25 µL sample of cleared urine. No catalytic development was observed in urine from both tumor-bearing and healthy mice, suggesting a lack of any components with endogenous peroxidase activity. To assess whether there was any nonspecific clearance of the nanosensor, tumor-bearing and healthy mice were injected i.v. with non-cleavable AuNC-PEG-NAv complex and urine was collected 1 h p.i. Catalytic activity assay was run on a sample of cleared urine, and no significant difference in catalytic development in tumor-bearing and healthy mice was observed, suggesting no significant differences in nonspecific clearance of the nanosensor between tumor-bearing and healthy mice. This also confirms that glomerular filtration barrier of tumor bearing mice is not compromised.

Finally, to demonstrate the specificity of the MMP-responsive AuNC-P2$_{20}$-NAv nanosensors, AuNC-P1$_{20}$-NAv (thrombin-responsive complexes) were injected into tumor-bearing mice. In contrast to the results following administration of the MMP-responsive complexes which showed high colorimetric signal in urine (Figure 3.28c and Figure 3.29a), the thrombin-responsive complexes did not show any significant colorimetric signal in urine compared to

healthy controls (Figure 3.29b). This demonstrates that in the tumor model, the AuNC-P2_{20}-NAv nanosensors are specifically disassembled through interaction with MMPs at the disease site or through interactions with circulating MMPs. Taken together, these results demonstrate that the AuNC-nanosensor complexes respond to disease-specific proteolytic activity *in vivo* and enable a direct colorimetric readout of disease state, as evidenced by highly accurate discrimination in a flank tumor model of human colorectal cancer.

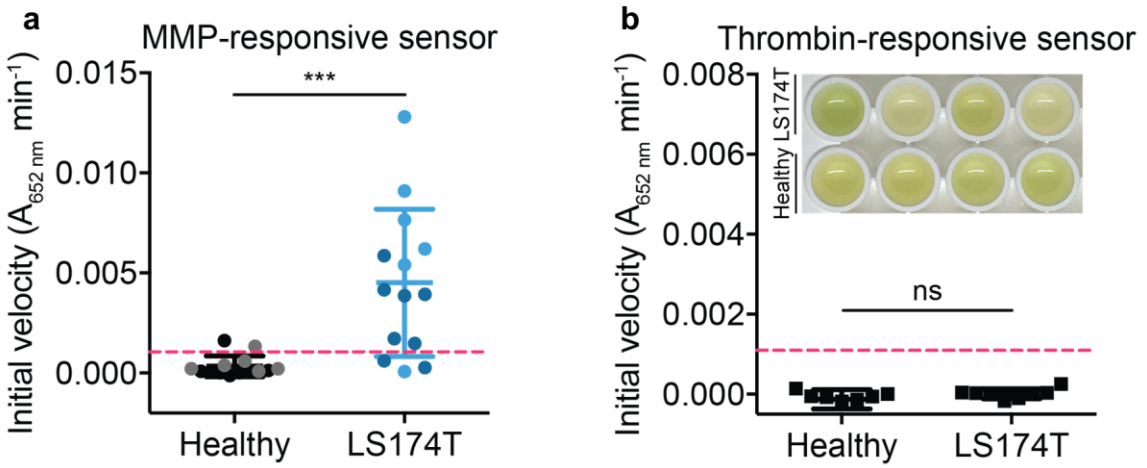


Figure 3.29 (a) Initial velocity of catalytic activity in urine collected from healthy and LS174T tumor bearing mice 1 h after injection with AuNC-P2_{20}-NAv complex (MMP responsive), as measured by the rate of change of $A_{652\ nm}$ over the first 10 minutes of the assay (mean ± s.d., N = 2 independent experiments indicated in shades, n = 6 (gray and light blue) or 8 (black and dark blue) mice per group, Mann-Whitney test, ***P = 0.0002). (b) Initial velocity of catalytic activity in urine collected from healthy and LS174T tumor bearing mice 1 h after injection with AuNC-P1_{20}-NAv complex (thrombin responsive), as measured by the rate of change of $A_{652\ nm}$ over the first 10 minutes of the assay. Inset: photograph of representative examples. No visible colorimetric development was observed in either group, and there was no statistically significant difference between the two groups (mean ± s.d., n = 8 per group, Mann-Whitney test, ns, P = 0.161). Catalytic activity is measured by initial rate analysis ($A_{652\ nm}$ min^{-1}), and dashed line represents limit of detection. Ava Soleimany performed animal injections and urine collection for *in vivo* experiments.

There are several limitations to this sensing platform. While a significant difference in colorimetric signal was observed between tumor-bearing and healthy mice when injected with AuNC-P2_{20}-NAv nanosensors, the absolute concentration of AuNCs cleared was low. The number of AuNCs in cleared urine was estimated against a calibration curve and found to be *ca*. 3 – 5 % of the injected dose, while over 50 % clearance of AuNCs was observed in healthy mice (Figure 3.19). The low clearance of AuNCs in the disease model is not unexpected, considering the concentration of AuNC-P2_{20}-NAv that might eventually accumulate in tumor sites or sense enzyme activity in the tumor microenvironment is quite low compared to the injected dose. Incorporating tumor penetrating peptides onto the AuNC surface during AuNC synthesis or through post-synthesis modifications could significantly increase the

accumulation of the nanosensors at the disease site and further improve the sensitivity. Another limitation of this approach is the variability and heterogeneity of urine. Urine concentration is dependent on many host and environmental factors, such as diet and activity level. In moving the AuNC nanosensors into a diagnostic platform, it would be important to consider the impact of variations in urine volume and hydration state on the final catalytic assay by incorporating a normalization step. A possible normalization strategy could include co-administering a “free reporter” molecule which is readily cleared into the urine independent of disease state and could be used to normalize the level of AuNCs released by protease activity. A similar strategy using the polysaccharide, inulin, as a free reporter was adopted by Kwong *et al.* with promising results.[39]

There are several challenges in imagining scaling the AuNC nanosensor system up to test human urine. Considering the assay is run with a 25 µL volume of urine from mice, to scale up to larger volumes it may be possible to combine the AuNC nanosensors with a paper-based platform like the one described in Chapter 2. If collected urine was first run up a paper strip to concentrate the cleaved AuNC reporters on a single test-line before performing the catalytic readout, the limit of detection could be improved through a concentration effect. In this scenario, AuNCs could be post modified with a specific ligand which could be captured on a paper membrane after clearance. For example, AuNCs could be labeled with biotin or fluorescein isothiocyanate (FITC), and the urine sample would be run up a nitrocellulose membrane bearing a test line containing streptavidin or anti-FITC (or both), which would capture the complementary AuNCs with high affinity. A subsequent catalytic development step could be performed on the test line to generate a colored signal from the concentrated AuNC reporters. If the AuNCs are ligand encoded, they could be selectively and simultaneously captured on a paper membrane which would allow for multiplexing, and the detection of multiple targets in one sample.

3.4 Conclusions and future work

3.4.1 Conclusions

A modular approach has been developed for rapid colorimetric detection of disease state. A library of *ca*. 1.5 nm catalytic gold nanocluster probes modified with protease substrates were synthesized. These were responsive to MMP9 and thrombin, enzymes upregulated in tumor and pulmonary embolism microenvironments, respectively. The peptide-templated AuNCs can be efficiently filtered through the kidneys and excreted into the urine. Additionally, the AuNCs retain activity in physiological environments and can be used as a colorimetric indicator. AuNC probes were assembled into larger complexes, which were then disassembled in response to specific proteases. Finally, MMP-responsive AuNC complexes were deployed *in vivo* in a colorectal cancer mouse model, where AuNCs were successfully detected in urine from tumor-bearing mice with a facile colorimetric readout.

While gold nanoparticles are widely used as biocompatible fluorescence and X-ray contrast imaging agents *in vivo*, here it has been demonstrated that, through rational surface modification, it is possible to engineer nanosensors that exploit gold nanoparticle catalytic activity *in vivo* as a disease indicator. Considering the similarity of rodents and humans in terms of pore sizes of the glomerular filtration membrane,[167] these results will also open new opportunities for developing translatable responsive and catalytic nanomaterial diagnostics for a range of diseases in which proteases can be used as biomarkers.

These results demonstrate that catalytic gold nanoclusters can be exploited for *in vivo* biosensing applications, specifically non-invasive disease detection based on a simple and sensitive colorimetric urinary assay. This chapter outlines a novel system for rapid disease detection that requires minimal equipment and can be read by the naked eye in < 1 h. This approach could be applicable in low-resource settings for rapid detection of a diverse range of disease-associated proteases. Because this is a versatile and modular platform that can be easily translated for detection of other proteases, it should be straightforward to expand to the detection of other relevant diseases that would benefit from PoC detection, including early detection of HIV and malaria.

3.4.2 Mechanism of AuNC catalytic activity

While heterogenous catalysis is a well-established field, there have been few reports on the mechanism of catalytic disproportionation of hydrogen peroxide on thiolate protected gold

nanoclusters. With the aim of developing a deeper understanding of the mechanism of AuNC catalytic activity, quantum mechanical and molecular dynamics simulations of AuNC catalysis are being developed by Dr. Patrick Charchar, Dr. Andrew Christofferson and Prof. Irene Yarovsky at Royal Melbourne Institute of Technology to complement the above experimental work. They have developed a model for AuNCs, specifically $Au_{25}(SG)_{18}$ structure, denotating 25 gold atoms in the core with 18 glutathione ligands bound to surface through Au-S interactions. While the AuNCs prepared in this chapter are not purely one atomic composition, it is anticipated that the interactions of hydrogen peroxide with glutathione protected AuNC surfaces on this size scale should be comparable. Preliminary results show that under certain conditions (pH and salt), there is a dynamic mechanism at play where a glutathione ligand on the AuNC surface can open and close to allow water or peroxide adsorption onto the surface (Figure 3.30). Using water as a proxy for peroxide adsorption, a persistent water molecule occupies the site between a core and staple sulfur over the course of trajectory when the ligands orient to allow for ligand-water H-bonding. Further simulations aim to understand the mechanisms involved in these processes and adsorption energies of key species in the reaction on model surfaces to better inform future experimental work, particularly for exploiting environmental and synthesis parameters (*e.g.* ligand density) to maximize catalytic efficiency.

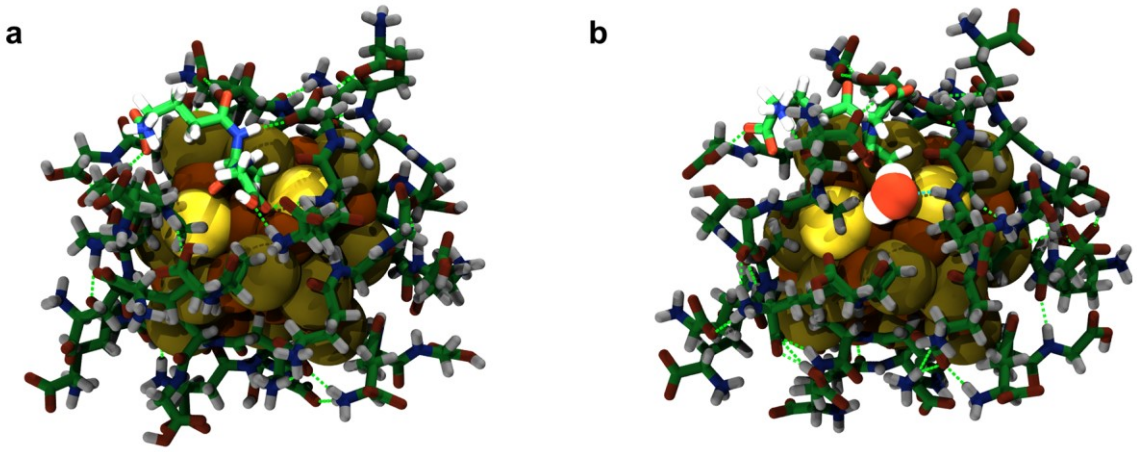


Figure 3.30 Molecular dynamic simulation frames of GSH-AuNCs (no NaCl present) showing a dynamic mechanism where a ligand sterically opens and closes access to a potential H_2O/H_2O_2 adsorption site on the gold cluster. (a) Closed binding site, and (b) the site open to water/peroxide adsorption. The ligand, water molecule and 2 × core sulfur atoms of interest are shown as bright VdW spheres, while other ligand, Au and S atoms are darkly shaded. Ligand–ligand and ligand–water hydrogen bonds shown as green and cyan dotted lines. Simulations were performed by Dr. Patrick Charchar.

3.4.3 Expanding the library of biological templates for nanocluster synthesis

In this chapter, both peptides and proteins were explored as templates for the synthesis of noble metal nanoclusters. However, in nature, biological organisms have evolved to make more exquisite nanostructures like shells and glassy diatoms. Using a bioinspired approach, it is possible to engineer more complex nanostructures. Many biological materials, such as proteins and viruses are rich in cysteine residues and thiolate ligands necessary for sequestering metal ions, offering a large toolkit of templates to generate precisely organized metal nanostructures on a larger scale. To this end, protein-rich membranes of extracellular vesicles (EVs) were investigated as templates for AuNC synthesis (EV-AuNC). First a bicinchoninic assay (BCA) was performed on a batch of EVs isolated from a breast cancer cell line to determine the protein concentration. The EV-AuNC synthesis was modeled on BSA and lysozyme-templated synthesis methods (§3.2.3.1), although the protein to chloroauric acid ratio was optimized for significantly more dilute protein samples. Similarly, the pH had to be adjusted to ~ pH 10 before incubating the sample at 37 °C for 12 h. The resulting EV-AuNC solutions were purified and imaged using cryogenic electron microscopy. Indeed, small gold nanoparticles and clusters could be observed surrounding the membranes of EVs (Figure 3.31c – d).

One of the established EV markers, CD63, a protein typically present on EV membranes will also be investigated for AuNC synthesis to further demonstrate that the AuNCs are being selectively grown within typical EV membrane proteins (Table 3.1). Additionally, focused ion beam scanning electron microscopy (FIB-SEM) was used to characterize the EV-AuNC interaction with cells. After 2 – 4 h EV-AuNC incubation with cells, the cells were fixed, stained and imaged using FIB-SEM. From this technique, gold particles were observed in endosomes and lysosomes. If EV-AuNC synthesis parameters can be optimized to exploit AuNC intrinsic fluorescence, then the EV-AuNC platform may serve as an efficient way to track EV interactions with cells both by fluorescence and electron microscopy. With additional optimization, a simple synthesis protocol may be developed for labelling EVs, where by starting with a known protein concentration in an EV batch, dual-modality EV-AuNC labels can be efficiently produced *in situ*. Further characterization of this system must demonstrate versatility across EVs isolated from several cell lines, and retention of EV markers on the surface (evidence that proteins have not been denatured in the membrane during synthesis). Using the synthesis and characterization methods developed in this chapter, it is possible to expand the library of biological templates used for designing novel functional hybrid organic-inorganic materials that are organized on length scales from nano- to macroscopic by adapting natural biomineralization processes.

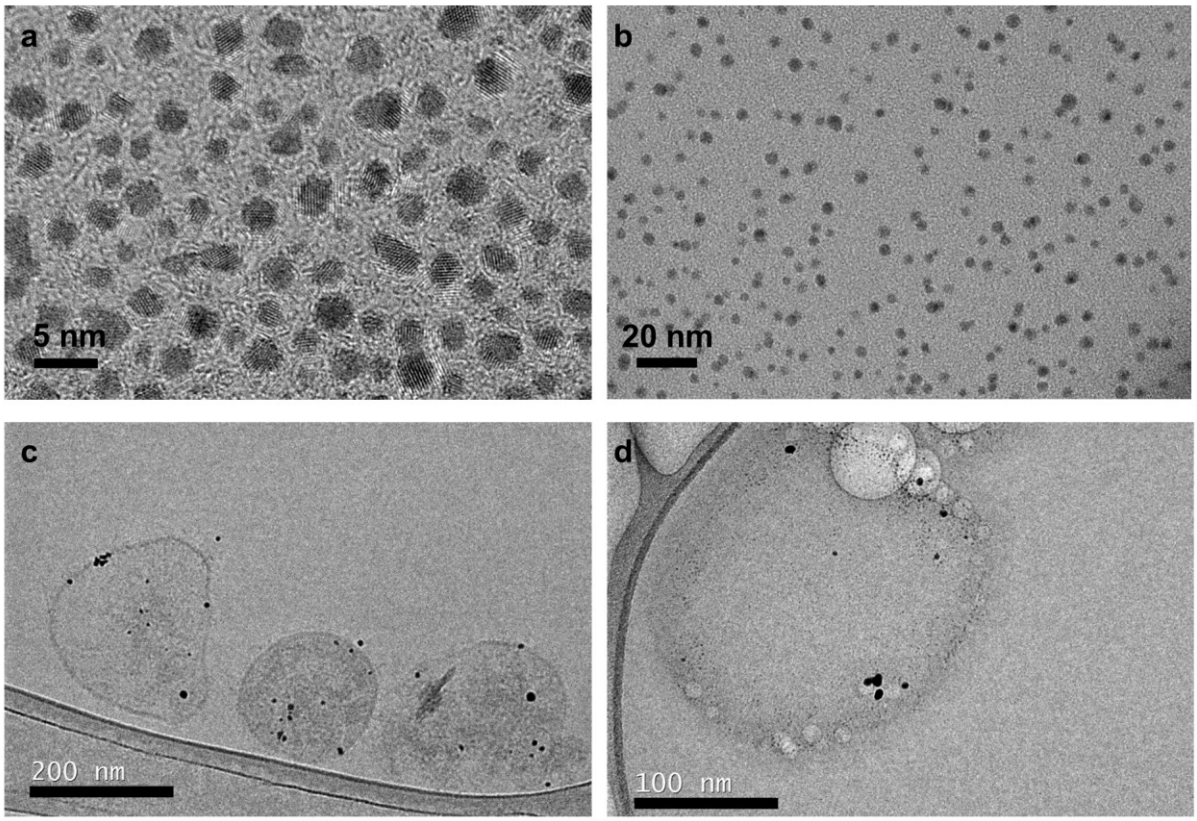


Figure 3.31 Biological templates for AuNC synthesis. (a) peptide glutathione, (b) protein lysozyme, (c-d) extracellular vesicles. High resolution TEM performed with Dr. Qu Chen (a – b). Cryo-TEM performed by Dr. Ulrike Kauscher (c – d).

Chapter 4

Conclusions and Future Work

4. Conclusions and Future Work

4.1 Conclusions

Timely and accurate diagnosis is the first step in managing and treating disease, from HIV to cancer. Sensitive detection of disease state is challenging, even in well-provisioned clinical settings, due to lack of diagnostic sensitivity, diseases that do not present clear symptoms or biomarkers, or diagnostic tests that require more time than is allotted in a typical general practitioner's visit to allow for informed clinical decisions, which may result in loss to follow-up care. These issues are compounded in developing countries where skilled health professionals and clinics may be inaccessible, and resources limited. There is a clear clinical need for rapid diagnostic tests that can provide simple, sensitive, clear and rapid results. This thesis aimed to address this need through the development of nanomaterial amplification platforms incorporated into simple and noninvasive diagnostic systems. This was realized through the development of catalytic nanomaterials that could generate colorimetric products in the presence of hydrogen peroxide and provide an amplified readout that could be read with the naked eye. The goal here was to bridge the sensitivity of established laboratory diagnostics with point-of-care compatible platforms to make life-saving diagnostics globally accessible. This work investigated the synthesis, characterization, and application of catalytic nanomaterials spanning a broad size regime, from small nanoclusters comprising only a handful of atoms, to 300 nm diameter particles. The investigations lay the groundwork for incorporating catalytic nanomaterials into a range of modular diagnostic platforms to enable simple and sensitive diagnostic results that should be accessible in a variety of settings, from a well-equipped doctor's office in London, to a remote clinic in South Africa, or from the comfort and privacy of a patient's home.

4.1.1 *In vitro* sensing

The *in vitro* sensing platform developed here built on a wealth of industrial knowledge and academic literature on optimization of lateral flow assay (LFA) and sandwich immunoassay design.[15,84,85,219] This thesis demonstrated that simple and sensitive protein detection could be achieved by integrating peroxidase-mimicking porous platinum core-shell nanocatalysts (PtNCs) into traditional lateral flow assay platforms. The design and optimization of a nanocatalyst amplification platform for LFA was presented for detection of p24, one of the earliest and most conserved protein biomarkers for HIV. The step change enabling high sensitivity was based on the synthesis of well-defined nanocatalysts for use as highly amplifying labels in LFA. This was achieved through a seed-mediated synthesis method,

where porous platinum shells were grown on gold nanoparticle cores to produce monodisperse PtNCs ranging in size from 50 to 300 nm in diameter. The PtNCs produced using this synthesis method exhibited peroxidase-like activity, which could be exploited to disproportionate hydrogen peroxide, oxidize chromogenic substrates, and generate additional colored signals at the test line of the LFA. This catalytic activity was retained even after exposure to serum conditions, where the internal surface area contribution from the PtNC porous shell was accessible for catalytic reactions even when the surface was passivated with proteins. The ideal size for PtNC labels in the amplified LFA platform was determined to be *ca*. 120 nm diameter PtNCs, and this optimal particle size was taken forward for development of an LFA for early detection of HIV.

An agile and thermally robust antibody fragment, a nanobody with high affinity for p24, was site-selectively modified with biotin and incorporated into the PtNC amplification platform to achieve oriented presentation of recognition elements. The combination of nanobody and nanocatalyst produced an exceptionally stable immunoassay. PtNC LFA components retained activity over long term accelerated aging conditions, compared to conventional antibodies and enzyme labels, which showed signs of denaturation, degradation and loss of activity when exposed to elevated temperatures. The use of biotin-streptavidin for high affinity capture of PtNC conjugates at the test line, and subsequent catalytic amplification step, resulted in unprecedented sensitivity for p24 detection in spiked sera and human plasma pool, achieving a limit of detection of 0.8 $pg \cdot mL^{-1}$ (32 fM). This highly sensitive test is easy to use with a colorimetric output that can read by the naked-eye or by mobile phone camera in less than 20 minutes.

The novelty of the PtNC LFA is that it exhibits a dual dynamic range, where the intrinsic absorbance of the particles can be used in a “low-sensitivity” regime for detection of high concentrations of the target analyte, and catalytic activity of the PtNCs can be exploited to access a “high-sensitivity” regime. For detection of low concentrations of the target, the test line signal intensity can be amplified through immersion of the test strip in the catalytic development solution to take advantage of the PtNC peroxidase-like activity. In the development solution the PtNCs can oxidize chromogenic substrates in the presence of hydrogen peroxide and generate additional colored products at the test line. Using pre- and post- development regimes, a dynamic range spanning over four orders of magnitude can be accessed. This represents a dynamic range that is two orders of magnitude broader than standard solution-based ELISA platforms or 4th generation commercial LFAs, which are limited to either post-catalysis or to the coloration of a particle label, respectively.[15] The PtNC amplified LFA exhibited sensitivity over a clinically relevant range for detection of acute stage

HIV infection. To this end, the clinical utility of the test was demonstrated through the detection of p24 in HIV-positive clinical samples, where p24 was successfully detected pre-seroconversion.

Since the PtNC amplified LFA was built on existing industrially used LFA platforms, and antibody conjugation methods, it is envisioned that this simple amplification method could be readily adopted for detection of other analytes and produced at scale by industrial collaborators. The thesis outlines the development of a pipeline for extension of the PtNC and nanobody detection tools to a variety of diseases that could benefit from ultrasensitive analyte detection.

4.1.2 *In vivo* sensing

Many diseases, including most cancers, have nonspecific blood-based biomarkers, may not present symptoms at early stages when treatment if most effective, and often require invasive biopsies for accurate diagnosis. A promising approach to circumvent challenges with detection of blood-based biomarkers and biopsies, is to develop pro-diagnostic agents that interact with pathological states and provide simple readouts in easily accessible body fluids, such as urine.[43] Dysregulation of protease activity is implicated in many cancers, and can be used as an active biomarker for disease detection.[220] This thesis presented a modular approach for detection of disease state by monitoring protease activity *in vivo,* and linking the measure of protease activity to a simple colorimetric readout in urine. This was accomplished through the development of a nanocatalyst labeled protease nanosensor.

Here, a new one-pot synthesis strategy to produce catalytic gold nanoclusters (AuNC) presenting protease-cleavable peptide substrates was developed. The AuNCs were responsive to MMP9 and thrombin, enzymes upregulated in tumor and pulmonary embolism microenvironments, respectively. Using this synthesis method, a library of *ca*. 1.5 nm diameter catalytic AuNC probes with peroxidase-mimicking activity were produced. The catalytic activity of the AuNCs was retained even in complex serum environments as they could effectively evade nonspecific protein adsorption due to their small size and zwitterionic capping ligand. Because of their size, these catalytic particles were efficiently filtered through the kidneys *in vivo* and excreted into the urine at up to 80 % of the injected dose 1 h post injection. The presence of AuNCs in urine was measured simultaneously using a simple colorimetric assay taking advantage of the peroxidase-like activity of the AuNCs, and by measuring gold content using ICP-MS. Unexpectedly, AuNCs retained significant catalytic activity after *in vivo*

interrogation, and were taken forward for use as probes in the development of a protease nanosensor.

In the protease nanosensor platform, AuNCs were conjugated to an avidin protein scaffold through a biotinylated protease-cleavable peptide linker. The protease-sensitive nanocluster complex was injected intravenously and designed to specifically disassemble when exposed to the activity of relevant dysregulated proteases at the site of disease. After protease cleavage, liberated AuNCs were filtered into the urine. AuNCs were detected in cleared urine by measuring their ability to oxidize a chromogenic peroxidase substrate in the presence of hydrogen peroxide, producing a simple colorimetric readout that could be read with the naked-eye. In this way, complex biological processes *in vivo* could be non-invasively monitored using a simple urinary readout. The length of the linker attaching the AuNCs to the protease nanosensor core was found to play a significant role in dictating the sensitivity of the protease nanosensor. Proteases could more readily access the scissile bond on the longer linkers and were cleaved at a rate *ca*. 40 times faster than the shorter linkers. The clinical utility of this platform was further demonstrated *in vivo*. MMP-responsive AuNC complexes were deployed *in vivo* in a colorectal cancer mouse model, where AuNCs were successfully detected in urine from tumor-bearing mice with a facile colorimetric readout.

Since similar gold nanocluster systems are currently used as biocompatible contrast agents for imaging *in vivo*,[170] it is expected that the results presented in this thesis will also open new opportunities for developing translatable responsive and catalytic nanomaterial diagnostics. The catalytic nanoparticle labeled protease nanosensor outlined here requires minimal equipment and can be read by the naked-eye in less than 1 hour. This approach could be applicable in low-resource settings for rapid detection of disease associated proteases. Because this is a versatile and modular platform that can be easily translated for detection of other proteases, it should be straightforward to expand to the detection of other relevant diseases that would benefit from PoC detection, including early detection of HIV and malaria. Additionally, complexity may be built into the system, by introducing logic gates, where multiple proteases are required to liberate a single AuNC, providing a more multifaceted picture of the pathological milieu. Before clinical translation is possible, extensive cytotoxicity and biocompatibility studies will need to be undertaken to further validate safety and efficacy of this new diagnostic platform.

4.2 Future scope of catalytic nanomaterials for amplified biosensing

Key to the development of both the *in vitro* and *in vivo* biosensing platforms presented in this thesis is the performance of the nanoparticle catalysts. To push these technologies forward will require further understanding of the materials science of the catalysts spanning a large size regime, from sub-nanometer clusters to 300 nm diameter nanoparticles. A deeper understanding of the various parameters affecting nanoparticle catalytic activity, including size, shape, capping ligands, reducing agents used in synthesis, atomic arrangement, and facet presentation will allow for the development of more advanced materials for use as next generation catalytic labels in diagnostic assays. This understanding will aid in the development of nanomaterials with improved catalytic efficiency to achieve maximum benefit of the nanoparticle amplification technology across diverse biosensing platforms. This exploration should include development of nanoparticles with architectures that allow for both outer and inner atoms to participate in catalytic reactions, such as hollow nanostructures and porous architectures.

While both the *in vitro* and *in vivo* sensing platforms presented in this thesis have been demonstrated for detection of specific disease states, a pipeline has been established for employing catalytic nanomaterials for detection of other diseases. Key to translation of these platforms to other disease targets will be the identification of clinically relevant biomarkers and, importantly, high affinity biomolecules (*e.g.* antibodies or aptamers) for detection in the case of LFA, and specific peptide substrates in the case of protease sensing. With the establishment of other detection moieties and biomarkers, it will be possible to develop multiplexed strategies where several biomarkers may be detected in a single sample, providing a more complete picture of disease state.

4.2.1 Rational design of enzyme-mimetic nanomaterials

Catalytic activity of nanomaterials is highly dependent on composition, size, shape, morphology, and surface chemistry. There is a large design space to explore for improving the efficiency of nanomaterial formulations for catalyzing reactions of interest. While biological enzymes may not exhibit as robust thermal and chemical stability as the inorganic mimics, they have evolved over billions of years to perform highly specific reactions in well-defined substrate binding pockets with high efficiency. The biological enzymes should serve as inspiration for the development of high-performance catalytic materials, which should seek to mimic some of the more complex properties of enzymes, including substrate specificity and allosteric regulation.

One example of building complexity into enzyme-mimetic nanomaterials, is the introduction of a substrate binding pocket or active site on the nanomaterial surface, which may serve to recognize the substrate and stabilize the transition state of the catalyzed reaction to accelerate chemical transformations. Zhang *et al.*[221] reported the development of substrate binding pockets on nanoparticles by molecularly imprinting polymers on the surface in the presence of adsorbed substrates as templates. This capping layer with imprinted “binding pockets” led to a 100-fold increase in specificity for the imprinted substrate.

Rotello and coworkers[222] developed a platform of bioorthogonal enzyme-mimetic nanomaterials with more sophisticated enzymatic behaviors. In their system, hydrophobic transition metal catalysts, including ruthenium and palladium, were encapsulated in the monolayer of water-soluble gold nanoparticles. The activity of these nanozymes could be reversibly controlled through binding of a gate-keeper molecule onto the monolayer surface, mimicking the mechanism of allosteric regulation. By tuning the transition metal core and capping layer, it was possible to introduce complexity into the nanozyme system to more closely mimic enzyme function. With added complexity in enzyme-mimetic nanoparticle systems, it is possible to envisage sophisticated cascade reactions which could be performed in harsh conditions by a completely abiotic system.

4.3 Perspective

This thesis investigated *in vitro* and *in vivo* detection of disease through careful engineering of catalytic nanomaterials across diverse size regimes. The technologies presented here provide a route to sensitive, simple, rapid, noninvasive, and semi-quantitative diagnostics, and offer an otherwise unavailable glimpse into disease state that may be exploited in non-hospital settings. It is envisioned that the framework presented here may be exploited for future development of diagnostics that can simply and rapidly detect static biomarkers in blood, or active proteolytic signatures *in vivo*. In this way, nanomaterials may pave the way for democratizing access to sensitive diagnostics.

5. References

1. World Health Organization. Progress Report 2016, Prevent HIV, test and treat all. *World Heal. Organ.* (2016).
2. Kharsany, A. B. M. & Karim, Q. A. HIV Infection and AIDS in Sub-Saharan Africa: Current Status, Challenges and Opportunities. *Open AIDS J.* **10,** 34–48 (2016).
3. WHO Media Centre. Ebola situation assessment. *World Health Organization* (2014). Available at: http://www.who.int/mediacentre/news/ebola/18-november-2014-diagnostics/enf/.
4. Maxmen, A. War zone complicates roll-out of Ebola vaccine. *Nature* **560,** 289–290 (2018).
5. Butler, D. Fast Ebola test limits outbreak. *Nature* **558,** 172 (2018).
6. Semper, A. E. *et al.* Performance of the GeneXpert Ebola Assay for Diagnosis of Ebola Virus Disease in Sierra Leone: A Field Evaluation Study. *PLoS Med.* **13,** 1–15 (2016).
7. Perkins, M. D. & Kessel, M. What Ebola tells us about outbreak diagnostic readiness. *Nat. Biotechnol.* **33,** 464–469 (2015).
8. Selmouni, F. *et al.* Tackling cancer burden in low-income and middle-income countries: Morocco as an exemplar. *Lancet Oncol.* **19,** e93–e101 (2018).
9. Forouzanfar, M. H. *et al.* Global, regional, and national comparative risk assessment of 79 behavioural, environmental and occupational, and metabolic risks or clusters of risks, 1990–2015: a systematic analysis for the Global Burden of Disease Study 2015. *Lancet* **388,** 1659–1724 (2016).
10. Turner, A. P. F. Biosensors: sense and sensibility. *Chem. Soc. Rev.* **42,** 3184 (2013).
11. Rocha-Santos, T. A. P. Sensors and biosensors based on magnetic nanoparticles. *TrAC Trends Anal. Chem.* **62,** 28–36 (2014).
12. Willets, K. A. & Van Duyne, R. P. Localized Surface Plasmon Resonance Spectroscopy and Sensing. *Annu. Rev. Phys. Chem.* **58,** 267–297 (2007).
13. Wang, Y., Hu, R., Lin, G., Roy, I. & Yong, K. T. Functionalized quantum dots for biosensing and bioimaging and concerns on toxicity. *ACS Appl. Mater. Interfaces* **5,** 2786–2799 (2013).
14. Armbruster, D. A. & Pry, T. Limit of Blank , Limit of Detection and Limit of Quantitation. **29,** 49–52 (2008).
15. Wild, D. G. *Immunoassay Handbook - Theory and Applications of Ligand Binding, ELISA and Related Techniques*. (Elsevier, 2013).
16. Turk, B. Targeting proteases: successes, failures and future prospects. *Nat. Rev. Drug Discov.* **5,** 785–799 (2006).
17. Medintz, I. L. *et al.* Proteolytic activity monitored by fluorescence resonance energy

transfer through quantum-dot-peptide conjugates. *Nat. Mater.* **5,** 581–589 (2006).

18. Blum, G. *et al.* Dynamic Imaging of Protease Activity With Fluorescently Quenched Activity-Based Probes. *Nat. Chem. Biol.* **1,** 203–209 (2005).
19. Whitney, M. *et al.* Ratiometric activatable cell-penetrating peptides provide rapid in vivo readout of thrombin activation. *Angew. Chemie - Int. Ed.* **52,** 325–330 (2013).
20. Nguyen, Q. T. & Tsien, R. Y. Fluorescence-guided surgery with live molecular navigation-a new cutting edge. *Nat. Rev. Cancer* **13,** 653–662 (2013).
21. Niemz, A., Ferguson, T. M. & Boyle, D. S. Point-of-care nucleic acid testing for infectious diseases. *Trends Biotechnol.* **29,** 240–250 (2011).
22. Holliger, P. & Hudson, P. J. Engineered antibody fragments and the rise of single domains. *Nat. Biotechnol.* **23,** 1126–1136 (2005).
23. De Meyer, T., Muyldermans, S. & Depicker, A. Nanobody-based products as research and diagnostic tools. *Trends Biotechnol.* **32,** 263–270 (2014).
24. Doshi, R. *et al.* In vitro nanobody discovery for integral membrane protein targets. *Sci. Rep.* **4,** 1–8 (2014).
25. Sharma, S., Byrne, H. & O'Kennedy, R. J. Antibodies and antibody-derived analytical biosensors. *Essays Biochem.* **60,** 9–18 (2016).
26. Gorlani, A. *et al.* Llama Antibody Fragments Have Good Potential for Application as HIV Type 1 Topical Microbicides. *AIDS Res. Hum. Retroviruses* **28,** 198–205 (2012).
27. van Der Linden, R. H. *et al.* Comparison of physical chemical properties of llama VHH antibody fragments and mouse monoclonal antibodies. *Biochim. Biophys. Acta* **1431,** 37–46 (1999).
28. Dolk, E. *et al.* Induced refolding of a temperature denatured llama heavy-chain antibody fragment by its antigen. *Proteins Struct. Funct. Genet.* **59,** 555–564 (2005).
29. Muyldermans, S. Nanobodies: Natural Single-Domain Antibodies. *Annu. Rev. Biochem.* **82,** 775–97 (2013).
30. Saerens, D. *et al.* Engineering camel single-domain antibodies and immobilization chemistry for human prostate-specific antigen sensing. *Anal. Chem.* **77,** 7547–7555 (2005).
31. Holstein, C. A. *et al.* Immobilizing affinity proteins to nitrocellulose : a toolbox for paper-based assay developers. *Anal. Bioanal. Chem.* **408,** 1335–1346 (2016).
32. Gasperino, D., Baughman, T., Hsieh, H. V., Bell, D. & Weigl, B. H. Improving Lateral Flow Assay Performance Using Computational Modeling. *Annu. Rev. Anal. Chem.* **11,** annurev-anchem-061417-125737 (2018).
33. Hsieh, H. V, Dantzler, J. L. & Weigl, B. H. Analytical Tools to Improve Optimization Procedures for Lateral Flow Assays. *Diagnostics* **7,** 29 (2017).
34. Gao, L. *et al.* Intrinsic peroxidase-like activity of ferromagnetic nanoparticles. *Nat.*

Nanotechnol. **2,** 577–83 (2007).

35. Wei, H. & Wang, E. Nanomaterials with enzyme-like characteristics (nanozymes): next-generation artificial enzymes. *Chem. Soc. Rev.* **42,** 6060–93 (2013).
36. Jones, R. J. & Brown, J. Circulating biomarkers in cancer care: What possible use? *Pract. Lab. Med.* **7,** 45–48 (2017).
37. Hori, S. S. & Gambhir, S. S. Mathematical Model Identifies Blood Biomarker-Based Early Cancer Detection Strategies and Limitations. *Sci. Transl. Med.* **3,** 109ra116 (2011).
38. Nomura, D. K., Dix, M. M. & Cravatt, B. F. Activity-based protein profiling for biochemical pathway discovery in cancer. *Nat. Rev. Cancer* **10,** 630–638 (2010).
39. Kwong, G. A. *et al.* Mass-encoded synthetic biomarkers for multiplexed urinary monitoring of disease. *Nat. Biotechnol.* **31,** 63–70 (2013).
40. Kwong, G. A. *et al.* Mathematical framework for activity-based cancer biomarkers. *Proc. Natl. Acad. Sci.* **112,** 12627–12632 (2015).
41. Warren, A. D., Kwong, G. A., Wood, D. K., Lin, K. Y. & Bhatia, S. N. Point-of-care diagnostics for noncommunicable diseases using synthetic urinary biomarkers and paper microfluidics. *Proc. Natl. Acad. Sci. U. S. A.* **111,** 3671–6 (2014).
42. Schuerle, S., Dudani, J. S., Christiansen, M. G., Anikeeva, P. & Bhatia, S. N. Magnetically Actuated Protease Sensors for in Vivo Tumor Profiling. *Nano Lett.* **16,** 6303–6310 (2016).
43. Kwon, E. J., Dudani, J. S. & Bhatia, S. N. Ultrasensitive tumour-penetrating nanosensors of protease activity. *Nat. Biomed. Eng.* **1,** 0054 (2017).
44. D. Howes, P., Rana, S. & M. Stevens, M. Plasmonic nanomaterials for biodiagnostics. *Chem. Soc. Rev.* **43,** 3835–3853 (2014).
45. Howes, P. D., Chandrawati, R. & Stevens, M. M. Colloidal nanoparticles as advanced biological sensors. *Science* **346,** 1247390-1-1247390–10 (2014).
46. Mayer, K. M. & Hafner, J. H. Localized surface plasmon resonance sensors. *Chem. Rev.* **111,** 3828–3857 (2011).
47. Mirkin, C. A., Letsinger, R. L., Mucic, R. C. & Storhoff, J. J. A DNA-based method for rationally assembling nanoparticles into macroscopic materials. *Nature* **382,** 607–9 (1996).
48. Veitch, N. C. Horseradish peroxidase: A modern view of a classic enzyme. *Phytochemistry* **65,** 249–259 (2004).
49. Josephy, D., Eling, T. & Mason, R. The Horseradish Peroxidase-catalyzed Oxidation of 3,5,3',5'- Tetramethylbenzidine. *J. Biol. Chem.* **257,** 3669–3675 (1982).
50. Jiang, B. *et al.* Standardized assays for determining the catalytic activity and kinetics of peroxidase-like nanozymes. *Nat. Protoc.* **13,** 1506–1520 (2018).

51. Lin, Y., Ren, J. & Qu, X. Nano-gold as artificial enzymes: hidden talents. *Adv. Mater.* **26,** 4200–17 (2014).
52. Gao, Z., Xu, M., Lu, M., Chen, G. & Tang, D. Urchin-like (gold core)@(platinum shell) nanohybrids: A highly efficient peroxidase-mimetic system for in Situ amplified colorimetric immunoassay. *Biosens. Bioelectron.* **70,** 194–201 (2015).
53. Xia, X. *et al.* Pd-Ir Core-Shell Nanocubes: A Type of Highly Efficient and Versatile Peroxidase Mimic. *ACS Nano* **9,** 9994–10004 (2015).
54. Ye, H. *et al.* An Enzyme-Free Signal Amplification Technique for Ultrasensitive Colorimetric Assay of Disease Biomarkers. *ACS Nano* **11,** 2052–2059 (2017).do
55. Panchenko, A., Koper, M. T. M., Shubina, T. E., Mitchell, S. J. & Roduner, E. Ab Initio Calculations of Intermediates of Oxygen Reduction on Low-Index Platinum Surfaces. *J. Electrochem. Soc.* **151,** A2016–A2027 (2004).
56. McKee, D. W. Catalytic decomposition of hydrogen peroxide by metals and alloys of the platinum group. *J Catal.* **14,** 355–364 (1969).
57. Liu, Y., Wu, H., Li, M., Yin, J.-J. & Nie, Z. pH dependent catalytic activities of platinum nanoparticles with respect to the decomposition of hydrogen peroxide and scavenging of superoxide and singlet oxygen. *Nanoscale* **6,** 11904–10 (2014).
58. He, W. *et al.* Intrinsic catalytic activity of Au nanoparticles with respect to hydrogen peroxide decomposition and superoxide scavenging. *Biomaterials* **34,** 765–773 (2013).
59. Loynachan, C. N. *et al.* Platinum Nanocatalyst Amplification: Redefining the Gold Standard for Lateral Flow Immunoassays with Ultrabroad Dynamic Range. *ACS Nano* **12,** 279–288 (2018).
60. Farrell, B. O. Lateral Flow Immunoassays Systems: evolution from the current state of the art to the next generation of highly sensitive, quantitative rapid assays. *Immunoass. Handb.* 89–107 (2013).
61. Niemeyer, C. M., Adler, M. & Wacker, R. Detecting antigens by quantitative immuno-PCR. *Nat. Protoc.* **2,** 1918–1930 (2007).
62. Barletta, J. M., Edelman, D. C. & Constantine, N. T. Lowering the detection limits of HIV-1 viral load using real-time immuno-PCR for HIV-1 p24 antigen. *Am. J. Clin. Pathol.* **122,** 20–27 (2004).
63. Mauk, M. *et al.* Miniaturized Devices for Point of Care Molecular Detection of HIV. *Lab Chip* **17,** 382–394 (2017).
64. Nayak, S., Blumenfeld, N. R., Laksanasopin, T. & Sia, S. K. Point-of-Care Diagnostics: Recent Developments in a Connected Age. *Anal. Chem.* **89,** 102–123 (2017).
65. Duan, D. *et al.* Nanozyme-strip for rapid local diagnosis of Ebola. *Biosens. Bioelectron.* **74,** 134–141 (2015).
66. Kim, M. *et al.* Simple and Sensitive Point-of-Care Bioassay System Based on

Hierarchically Structured Enzyme-Mimetic Nanoparticles. *Adv. Healthc. Mater.* **4,** 1311–1316 (2015).

67. Gao, Z. *et al.* Platinum Decorated Gold Nanoparticles with Dual Functionalities for Ultrasensitive Colorimetric In Vitro Diagnostics. *Nano Lett.* **17,** 5572–5579 (2017).
68. Sands, A. Diagnostics for HIV diagnosis. *World Heal. Organ.* (2015).
69. Rosenberg, N. E., Pilcher, C. D., Busch, M. P. & Cohen, M. S. How can we better identify early HIV infections? *Curr. Opin. HIV AIDS* **10,** 61–8 (2015).
70. Fiebig, E. *et al.* Dynamics of HIV viremia and antibody seroconversion in plasma donors: implications for diagnosis and staging of primary HIV infection. *AIDS* **17,** 1871–1879 (2003).
71. Wu, G. & Zaman, M. H. *Low-cost tools for diagnosing and monitoring HIV infection in low-resource settings*. *Bulletin of the World Health Organization* (2012).
72. Branson, B. M. & Stekler, J. D. Detection of acute HIV infection: We can't close the window. *J. Infect. Dis.* **205,** 521–524 (2012).
73. Pilcher, C. D. *et al.* Performance of Rapid Point-of-Care and Laboratory Tests for Acute and Established HIV Infection in San Francisco. *PLoS One* **8,** e80629 (2013).
74. Pandori, M. W. *et al.* Assessment of the ability of a fourth-generation immunoassay for human immunodeficiency virus (HIV) antibody and p24 antigen to detect both acute and recent HIV infections in a high-risk setting. *J. Clin. Microbiol.* **47,** 2639–2642 (2009).
75. Bottone, P. D. & Bartlett, A. H. Diagnosing Acute HIV Infection. *Pediatr. Ann.* **46,** e47–e50 (2017).
76. Rutstein, S. E. *et al.* Clinical and public health implications of acute and early HIV detection and treatment: a scoping review. *J. Int. AIDS Soc.* **20,** 1–13 (2017).
77. Gray, E. R. *et al.* p24 revisited: A landscape review of antigen detection for early HIV diagnosis. *AIDS* **32,** 2089–2102 (2018).
78. van Tienen, C., Rugebregt, S., Scherbeijn, S., Götz, H. & GeurtsvanKessel, C. The performance of the Alere HIV combo point-of-care test on stored serum samples; useful for detection of early HIV-1 infections? *Sex. Transm. Infect.* **94,** 331–333 (2018).
79. Miedouge, M., Grèze, M., Bailly, A. & Izopet, J. Analytical sensitivity of four HIV combined antigen/antibody assays using the p24 WHO standard. *J. Clin. Virol.* **50,** 57–60 (2011).
80. Vallefuoco, L., Mazzarella, C. & Portella, G. Fourth generation assays for HIV testing. *Expert Rev. Mol. Diagn.* **16,** 723–732 (2016).
81. Zhang, S., Garcia-D'Angeli, A., Brennan, J. P. & Huo, Q. Predicting detection limits of enzyme-linked immunosorbent assay (ELISA) and bioanalytical techniques in general. *Analyst* **139,** 439–45 (2014).
82. Nabatiyan, A., Baumann, M. a, Parpia, Z. & Kelso, D. A Lateral Flow-based Ultra-

Sensitive p24 HIV Assay Utilizing Fluorescent Microparticles. *J. Acquir. Immune Defic. Syndr.* **53,** 55–61 (2010).

83. Parpia, Z. a, Elghanian, R., Nabatiyan, A., Hardie, D. R. & Kelso, D. M. p24 Antigen Rapid Test for Diagnosis of Acute Pediatric HIV Infection. *J. Acquir. Immune Defic. Syndr.* **55,** 413–9 (2010).
84. Wong, R. C. & Tse, H. Y. *Lateral Flow Immunoassay*. (Springer, 2009).
85. Millipore. *Rapid Lateral Flow Test Strips: Considerations for product development*. (2008).
86. Huang, X., Aguilar, Z. P., Xu, H., Lai, W. & Xiong, Y. Membrane-based lateral flow immunochromatographic strip with nanoparticles as reporters for detection: A review. *Biosens. Bioelectron.* **75,** 166–180 (2016).
87. Mudanyali, O. *et al.* Integrated rapid-diagnostic-test reader platform on a cellphone. *Lab Chip* **12,** 2678–86 (2012).
88. Wang, D.-B. *et al.* Detection of Bacillus anthracis spores by super-paramagnetic lateral-flow immunoassays based on “Road Closure”. *Biosens. Bioelectron.* **67,** 608–614 (2015).
89. Zhan, L. *et al.* The Role of Nanoparticle Design in Determining Analytical Performance of Lateral Flow Immunoassays. *Nano Lett.* **17,** 7207–7212 (2017).
90. Wang, Y. *et al.* Thermal contrast amplification reader yielding 8-fold analytical improvement for disease detection with lateral flow assays. *Anal. Chem.* **88,** 11774–11782 (2016).
91. Qin, Z. *et al.* Significantly Improved Analytical Sensitivity of Lateral Flow Immunoassays by Using Thermal Contrast. *Angew. Chemie Int. Ed.* **51,** 4358–4361 (2012).
92. Jain, P. K., Lee, K. S., El-Sayed, I. H. & El-Sayed, M. A. Calculated absorption and scattering properties of gold nanoparticles of different size, shape, and composition: Applications in biological imaging and biomedicine. *J. Phys. Chem. B* **110,** 7238–7248 (2006).
93. Hermanson, G. T. *Bioconjugate Techniques*. (Elsevier, 2008).
94. Li, J., Duan, H., Xu, P., Huang, X. & Xiong, Y. Effect of different-sized spherical gold nanoparticles grown layer by layer on the sensitivity of an immunochromatographic assay. *RSC Adv.* **6,** 26178–26185 (2016).
95. Chen, A. & Yang, S. Replacing antibodies with aptamers in lateral flow immunoassay. *Biosens. Bioelectron.* **71,** 230–242 (2015).
96. Jauset-Rubio, M. *et al.* Ultrasensitive, rapid and inexpensive detection of DNA using paper based lateral flow assay. *Sci. Rep.* **6,** 37732 (2016).
97. Greene, M. *et al.* Forming next-generation antibody-nanoparticle conjugates through the oriented installation of non-engineered antibody fragments. *Chem. Sci.* **9,** 79–87

(2018).

98. Richards, D. A., Maruani, A. & Chudasama, V. Antibody fragments as nanoparticle targeting ligands: a step in the right direction. *Chem. Sci.* **8,** 63–77 (2017).
99. Chudasama, V., Maruani, A. & Caddick, S. Recent advances in the construction of antibody–drug conjugates. *Nat. Chem.* **8,** (2016).
100. Grant, B. D., Smith, C. A., Karvonen, K. & Richards-Kortum, R. Highly Sensitive Two-Dimensional Paper Network Incorporating Biotin-Streptavidin for the Detection of Malaria. *Anal. Chem.* **88,** 2553–2557 (2016).
101. Rivas, L., Medina-Sánchez, M., de la Escosura-Muñiz, A. & Merkoçi, A. Improving sensitivity of gold nanoparticle-based lateral flow assays by using wax-printed pillars as delay barriers of microfluidics. *Lab Chip* **14,** 4406–14 (2014).
102. Ye, H. & Xia, X. Enhancing the sensitivity of colorimetric lateral flow assay (CLFA) through signal amplification techniques. *J. Mater. Chem. B* **6,** 7102–7111 (2018).
103. Yang, W. *et al.* A colloidal gold probe-based silver enhancement immunochromatographic assay for the rapid detection of abrin-a. *Biosens. Bioelectron.* **26,** 3710–3713 (2011).
104. Parolo, C., de la Escosura-Muñiz, A. & Merkoçi, A. Enhanced lateral flow immunoassay using gold nanoparticles loaded with enzymes. *Biosens. Bioelectron.* **40,** 412–6 (2013).
105. Dumesic, J. A., Huber, G. W. & Boudart, M. Principles of Heterogenous Catalysis. in *Handbook of Heterogeneous Catalysis* (2008).
106. Narayanan, R. & El-Sayed, M. A. Catalysis with transition metal nanoparticles in colloidal solution: Nanoparticle shape dependence and stability. *J. Phys. Chem. B* **109,** 12663–12676 (2005).
107. Ahmadi, T. S., Wang, Z. L., Green, T. C., Henglein, A. & El-Sayed, M. A. Shape-Controlled Synthesis of Colloidal Platinum Nanoparticles. *Science* **272,** 1924–1925 (1996).
108. Jin, R., Zeng, C., Zhou, M. & Chen, Y. Atomically Precise Colloidal Metal Nanoclusters and Nanoparticles: Fundamentals and Opportunities. *Chem. Rev.* **116,** 10346–10413 (2016).
109. Xia, Y., Gilroy, K. D., Peng, H.-C. & Xia, X. Seed-Mediated Growth of Colloidal Metal Nanocrystals. *Angew. Chemie Int. Ed.* **56,** 60–95 (2017).
110. Guo, S., Wang, L., Dong, S. & Wang, E. A novel urchinlike gold/platinum hybrid nanocatalyst with controlled size. *J. Phys. Chem. C* **112,** 13510–13515 (2008).
111. Lim, B. *et al.* Pd-Pt bimetallic nanodendrites with high activity for oxygen reduction. *Science* **324,** 1302–1305 (2009).
112. Gonzalez, M. *et al.* Interaction of Biotin with Streptavidin. *J. Biol. Chem.* **272,** 11288–11294 (1997).

113. Xia, Y., Xia, X. & Peng, H. C. Shape-Controlled Synthesis of Colloidal Metal Nanocrystals: Thermodynamic versus Kinetic Products. *J. Am. Chem. Soc.* **137,** 7947–7966 (2015).
114. Ye, H., Liu, Y., Chhabra, A., Lilla, E. & Xia, X. Polyvinylpyrrolidone (PVP)-Capped Pt Nanocubes with Superior Peroxidase-Like Activity. *ChemNanoMat* **3,** 33–38 (2017).
115. Gray, E. R. *et al.* Unravelling the Molecular Basis of High Affinity Nanobodies against HIV p24: *In Vitro* Functional, Structural, and *in Silico* Insights. *ACS Infect. Dis.* **3,** 479–491 (2017).
116. Miller, B. S. *et al.* Quantifying Biomolecular Binding Constants using Video Paper Analytical Devices. *Chem. - A Eur. J.* **24,** 9783–9787 (2018).
117. Tobias, R. & Kumaraswamy, S. *Biomolecular Binding Kinetics Assays on the Octet Platform*. *FortéBio-Application Note 14* (2016).
118. Yamada, K., Shibata, H., Suzuki, K. & Citterio, D. Toward practical application of paper-based microfluidics for medical diagnostics: state-of-the-art and challenges. *Lab Chip* **17,** 1206–1249 (2017).
119. ASTM. Standard Guide for Accelerated Aging of Sterile Medical Device Packages. *ASTM F1980-02* (2002).
120. Yang, J. *et al.* The I-TASSER Suite: protein structure and function prediction. *Nat. Methods* **12,** 7–8 (2015).
121. Schindelin, J. *et al.* Fiji: an open-source platform for biological-image analysis. *Nat. Methods* **9,** 676–682 (2012).
122. Lim, B. *et al.* Shape-controlled synthesis of Pd nanocrystals in aqueous solutions. *Adv. Funct. Mater.* **19,** 189–200 (2009).
123. Xia, X. *et al.* Facile synthesis of iridium nanocrystals with well-controlled facets using seed-mediated growth. *J. Am. Chem. Soc.* **136,** 10878–10881 (2014).
124. Turkevich, J; Stevenson, P. C. H. J. A Study of the Nucleation and Growth Processes in the Synthesis of Colloidal Gold. *Discuss. Faraday Soc.* **11,** 55–75 (1951).
125. FRENS, G. Controlled Nucleation for the Regulation of the Particle Size in Monodisperse Gold Suspensions. *Nat. Phys. Sci.* **241,** 20–22 (1973).
126. Xiong, Y. *et al.* Poly (vinyl pyrrolidone): A dual functional reductant and stabilizer for the facile synthesis of noble metal nanoplates in aqueous solutions. *Langmuir* **22,** 8563–8570 (2006).
127. Roy, R. K. *et al.* Deposition of continuous platinum shells on gold nanoparticles by chemical precipitation. *J. Colloid Interface Sci.* **369,** 91–95 (2012).
128. Kondo, T., Morimura, T., Tsujimoto, T., Aikawa, T. & Yuasa, M. Platinum Nanoparticle-embedded Porous Diamond Spherical Particles as an Active and Stable Heterogeneous Catalyst. *Sci. Rep.* **7,** 1–10 (2017).

129. Chudasama, V. *et al.* Bromopyridazinedione-mediated protein and peptide bioconjugation. *Chem. Commun.* **47,** 8781 (2011).
130. Robinson, E. *et al.* Pyridazinediones deliver potent, stable, targeted and efficacious antibody–drug conjugates (ADCs) with a controlled loading of 4 drugs per antibody. *RSC Adv.* **7,** 9073–9077 (2017).
131. Lee, M. T. W. *et al.* Enabling the controlled assembly of antibody conjugates with a loading of two modules without antibody engineering. *Chem. Sci.* **8,** 2056–2060 (2017).
132. Lee, M. T. W., Maruani, A., Baker, J. R., Caddick, S. & Chudasama, V. Next-generation disulfide stapling: reduction and functional re-bridging all in one. *Chem. Sci.* **7,** 799–802 (2016).
133. Saha, K., Agasti, S., Kim, C., Li, X. & Rotello, V. Gold Nanoparticles in Chemical and Biological Sensing. *Chem. Rev.* **112,** 2739–2779 (2012).
134. Charchar, P., Christofferson, A. J., Todorova, N. & Yarovsky, I. Understanding and Designing the Gold-Bio Interface: Insights from Simulations. *Small* **12,** 2395–2418 (2016).
135. Saha, B., Evers, T. H. & Prins, M. W. J. How antibody surface coverage on nanoparticles determines the activity and kinetics of antigen capturing for biosensing. *Anal. Chem.* **86,** 8158–66 (2014).
136. Gorlani, A. *et al.* Llama Antibody Fragments Have Good Potential for Application as HIV Type 1 Topical Microbicides. *AIDS Res. Hum. Retroviruses* **28,** 198–205 (2012).
137. Saerens, D., Conrath, K., Govaert, J. & Muyldermans, S. Disulfide Bond Introduction for General Stabilization of Immunoglobulin Heavy-Chain Variable Domains. *J. Mol. Biol.* **377,** 478–488 (2008).
138. Ramachandran, S., Fu, E., Lutz, B. & Yager, P. Long-term dry storage of an enzyme-based reagent system for ELISA in point-of-care devices. *Analyst* **139,** 1456–62 (2014).
139. Olsson, C., Jansson, H. & Swenson, J. The Role of Trehalose for the Stabilization of Proteins. *J. Phys. Chem. B* **120,** 4723–4731 (2016).
140. Quesada-González, D. & Merkoçi, A. Mobile phone–based biosensing: an emerging "diagnostic and communication" technology. *Biosens. Bioelectron.* **92,** 549–562
141. Philippot, K. & Serp, P. Concepts in Nanocatalysis. in *Nanomaterials in Catalysis: First Edition* 1–54 (Wiley-VCH Verlag GmbH, 2013).
142. Schupbach, J. *et al.* Optimized Virus Disruption Improves Detection of HIV-1 p24 in Particles and Uncovers a p24 Reactivity in Patients with Undetectable HIV-1 RENA Under Long-TERM HAART. *J. Med. Virol.* **78,** 1003–1010 (2006).
143. Ye, H. *et al.* Ru Nanoframes with an fcc Structure and Enhanced Catalytic Properties. *Nano Lett.* **16,** 2812–2817 (2016).
144. World Health Organization. *Global action plan for the prevention and control of*

noncommunicable diseases 2013-2020. (2013).

145. Yepes, D. *et al.* Multiplex profiling of tumor-associated proteolytic activity in serum of colorectal cancer patients. *Proteomics - Clin. Appl.* **8,** 308–316 (2014).
146. Hilderbrand, S. A. & Weissleder, R. Near-infrared fluorescence: application to in vivo molecular imaging. *Curr. Opin. Chem. Biol.* **14,** 71–79 (2010).
147. Whitley, M. J. *et al.* A mouse-human phase 1 co-clinical trial of a protease-activated fluorescent probe for imaging cancer. *Sci. Transl. Med.* **8,** (2016).
148. Choi, J. S. *et al.* Distance-dependent magnetic resonance tuning as a versatile MRI sensing platform for biological targets. *Nat. Mater.* **16,** 537–542 (2017).
149. Savariar, E. N. *et al.* Real-time in Vivo molecular detection of primary tumors and metastases with ratiometric activatable cell-penetrating peptides. *Cancer Res.* **73,** 855–864 (2013).
150. Warren, A. D. *et al.* Disease Detection by Ultrasensitive Quantification of Microdosed Synthetic Urinary Biomarkers. *J. Am. Chem. Soc.* **136,** 13709–13714 (2014).
151. Kwon, E. J., Lo, J. H. & Bhatia, S. N. Smart nanosystems: Bio-inspired technologies that interact with the host environment. *Proc. Natl. Acad. Sci.* **112,** 14460–14466 (2015).
152. Du, B., Yu, M. & Zheng, J. Transport and interactions of nanoparticles in the kidneys. *Nat. Rev. Mater.* **3,** 358–374 (2018).
153. Xie, J. P., Zheng, Y. G. & Ying, J. Y. Protein-Directed Synthesis of Highly Fluorescent Gold Nanoclusters. *J. Am. Chem. Soc.* **131,** 888–889 (2009).
154. Wen, F. *et al.* Horseradish peroxidase functionalized fluorescent gold nanoclusters for hydrogen peroxide sensing. *Anal. Chem.* **83,** 1193–1196 (2011).
155. Liu, C.-L. *et al.* Insulin-Directed Synthesis of Fluorescent Gold Nanoclusters: Preservation of Insulin Bioactivity and Versatility in Cell Imaging. *Angew. Chemie* **123,** 7194–7198 (2011).
156. Chen, T. H. & Tseng, W. L. (Lysozyme type VI)-stabilized Au8 clusters: Synthesis mechanism and application for sensing of glutathione in a single drop of blood. *Small* **8,** 1912–1919 (2012).
157. Luo, Z. *et al.* From aggregation-induced emission of Au(I)-thiolate complexes to ultrabright Au(0)@Au(I)-thiolate core-shell nanoclusters. *J. Am. Chem. Soc.* **134,** 16662–16670 (2012).
158. Jiang, D. E., Tiago, M. L., Luo, W. & Dai, S. The ‘staple’ motif: A key to stability of thiolate-protected gold nanoclusters. *J. Am. Chem. Soc.* **130,** 2777–2779 (2008).
159. Zhang, X.-D. *et al.* Ultrasmall glutathione-protected gold nanoclusters as next generation radiotherapy sensitizers with high tumor uptake and high renal clearance. *Sci. Rep.* **5,** 8669 (2015).

160. Schaaff, T. G., Knight, G., Shafigullin, M. N., Borkman, R. F. & Whetten, R. L. Isolation and Selected Properties of a 10.4 kDa Gold:Glutathione Cluster Compound. *J. Phys. Chem. B* **102,** 10643–10646 (1998).
161. Zhou, C., Long, M., Qin, Y., Sun, X. & Zheng, J. Luminescent Gold Nanoparticles with Efficient Renal Clearance. *Angew. Chemie* **123,** 3226–3230 (2011).
162. Zhou, C. *et al.* Luminescent gold nanoparticles with mixed valence states generated from dissociation of polymeric Au(I) thiolates. *J. Phys. Chem. C* **114,** 7727–7732 (2010).
163. Xu, J. *et al.* In Vivo X-ray Imaging of Transport of Renal Clearable Gold Nanoparticles in the Kidneys. *Angew. Chemie - Int. Ed.* **56,** 13356–13360 (2017).
164. Ning, X. *et al.* Physiological stability and renal clearance of ultrasmall zwitterionic gold nanoparticles: Ligand length matters. *APL Mater.* **5,** (2017).
165. Zheng, J. *et al.* Dose Dependencies and Biocompatibility of Renal Clearable Gold Nanoparticles. *Angew. Chemie Int. Ed.* **57,** 266–271 (2018).
166. Luo, Z., Zheng, K. & Xie, J. Engineering ultrasmall water-soluble gold and silver nanoclusters for biomedical applications. *Chem. Commun.* **50,** 5143–5155 (2014).
167. Du, B. *et al.* Glomerular barrier behaves as an atomically precise bandpass filter in a sub-nanometre regime. *Nat. Nanotechnol.* **12,** 1096–1102 (2017).
168. Tang, S. *et al.* Tailoring Renal Clearance and Tumor Targeting of Ultrasmall Metal Nanoparticles with Particle Density. *Angew. Chemie - Int. Ed.* **55,** 16039–16043 (2016).
169. Yu, M. *et al.* Interactions of Renal-Clearable Gold Nanoparticles with Tumor Microenvironments: Vasculature and Acidity Effects. *Angew. Chemie - Int. Ed.* **56,** 4314–4319 (2017).
170. Xu, J. *et al.* Dose Dependencies and Biocompatibility of Renal Clearable Gold Nanoparticles: From Mice to Non-human Primates. *Angew. Chemie - Int. Ed.* **57,** 266–271 (2018).
171. Liu, J. *et al.* Passive tumor targeting of renal-clearable luminescent gold nanoparticles: Long tumor retention and fast normal tissue clearance. *J. Am. Chem. Soc.* **135,** 4978–4981 (2013).
172. Jin, R. Quantum sized, thiolate-protected gold nanoclusters. *Nanoscale* **2,** 343–362 (2010).
173. Chen, Y. *et al.* Shortwave Infrared in Vivo Imaging with Gold Nanoclusters. *Nano Lett.* **17,** 6330–6334 (2017).
174. Yang, W., Guo, W., Chang, J. & Zhang, B. Protein/peptide-templated biomimetic synthesis of inorganic nanoparticles for biomedical applications. *J. Mater. Chem. B* **5,** 401–417 (2017).
175. Tao, Y., Li, M., Ren, J. & Qu, X. Metal nanoclusters: novel probes for diagnostic and therapeutic applications. *Chem. Soc. Rev.* **44,** 8636–8663 (2015).

176. Tao, Y., Li, M., Kim, B. & Auguste, D. T. Incorporating gold nanoclusters and target-directed liposomes as a synergistic amplified colorimetric sensor for HER2-positive breast cancer cell detection. *Theranostics* **7,** 899–911 (2017).
177. Liu, J., Yu, M., Zhou, C. & Zheng, J. Renal clearable inorganic nanoparticles: A new frontier of bionanotechnology. *Mater. Today* **16,** 477–486 (2013).
178. Longmire, M., Choyke, P. L. & Kobayashi, H. Clearance properties of nano-sized particles and molecules as imagin agents: consideration and caveats. *Nanomedicine (Lond)* **3,** 703–717 (2008).
179. Deen, W., Lazzara, M. & Myers, B. Structural determinants of glomerular permselectivity. *Am J Physiol Ren. Physiol 281* **36,** F579–F596 (2001).
180. Soo Choi, H. *et al.* Renal clearance of quantum dots. *Nat. Biotechnol.* **25,** 1165–1170 (2007).
181. Phillips, E. *et al.* Clinical translation of an ultrasmall inorganic optical-PET imaging nanoparticle probe. *Sci. Transl. Med.* **6,** (2014).
182. Yu, M. & Zheng, J. Clearance Pathways and Tumor Targeting of Imaging Nanoparticles. *ACS Nano* **9,** 6655–6674 (2015).
183. Gu, L., Fang, R. H., Sailor, M. J. & Park, J. H. In vivo clearance and toxicity of monodisperse iron oxide nanocrystals. *ACS Nano* **6,** 4947–4954 (2012).
184. Kumar, R., Roy, I., Ohulchanskky, T. & Vathy, L. In vivo biodistribution and clearance studies using multimodal organically modified silica nanoparticles. *ACS Nano* **4,** 699–708 (2010).
185. Wilhelm, S. *et al.* Analysis of Nanoparicle Delivery to Tumours. *Nat. Rev. Mater.* **1,** 1–138 (2016).
186. Ruoslahti, E., Bhatia, S. N. & Sailor, M. J. Targeting of drugs and nanoparticles to tumors. *J. Cell Biol.* **188,** 759–768 (2010).
187. Davie, E. W. & Kulman, J. D. The structure and function of Thrombin: An overview. *Immunol. Cell Biol.* **74,** A1–A7 (1996).
188. Roy, R., Yang, J. & Moses, M. A. Matrix metalloproteinases as novel biomarkers and potential therapeutic targets in human cancer. *J. Clin. Oncol.* **27,** 5287–5297 (2009).
189. Dudani, J. S., Warren, A. D. & Bhatia, S. N. Harnessing Protease Activity to Improve Cancer Care. *Annu. Rev. Cancer Biol.* **2,** 53–76 (2018).
190. Yu, Y., Luo, Z., Yu, Y., Lee, J. Y. & Xie, J. Observation of cluster size growth in CO-directed synthesis of Au 25(SR) 18 nanoclusters. *ACS Nano* **6,** 7920–7927 (2012).
191. Kapusta, P. Absolute diffusion coefficients: Compilation of reference data for FCS calibration. *PicoQuant GmbH Appl. Note* (2010).
192. Müller, P., Schwille, P. & Weidemann, T. PyCorrFit-generic data evaluation for fluorescence correlation spectroscopy. *Bioinformatics* **30,** 2532–2533 (2014).

193. Larsen, M. T., Kuhlmann, M., Hvam, M. L. & Howard, K. A. Albumin-based drug delivery: harnessing nature to cure disease. *Mol. Cell. Ther.* **4,** 3 (2016).
194. Russell, B. A., Jachimska, B., Komorek, P., Mulheran, P. A. & Chen, Y. Lysozyme encapsulated gold nanoclusters: effects of cluster synthesis on natural protein characteristics. *Phys. Chem. Chem. Phys.* **19,** 7228–7235 (2017).
195. Wei, H. *et al.* Lysozyme-stabilized gold fluorescent cluster: Synthesis and application as Hg2+sensor. *Analyst* **135,** 1406–1410 (2010).
196. Huang, B. X., Kim, H. Y. & Dass, C. Probing three-dimensional structure of bovine serum albumin by chemical cross-linking and mass spectrometry. *J. Am. Soc. Mass Spectrom.* **15,** 1237–1247 (2004).
197. Elci, S. G. *et al.* Surface Charge Controls the Suborgan Biodistributions of Gold Nanoparticles. *ACS Nano* **10,** 5536–5542 (2016).
198. Jain, A., Barve, A., Zhao, Z., Jin, W. & Cheng, K. Comparison of Avidin, Neutravidin, and Streptavidin as Nanocarriers for Efficient siRNA Delivery. *Mol. Pharm.* **14,** 1517–1527 (2017).
199. Yu, M. *et al.* Noninvasive Staging of Kidney Dysfunction Enabled by Renal-Clearable Luminescent Gold Nanoparticles. *Angew. Chemie - Int. Ed.* **55,** 2787–2791 (2016).
200. Chen, L. Y., Wang, C. W., Yuan, Z. & Chang, H. T. Fluorescent gold nanoclusters: Recent advances in sensing and imaging. *Anal. Chem.* **87,** 216–229 (2015).
201. Negishi, Y., Nobusada, K. & Tsukuda, T. Glutathione-protected gold clusters revisited: Bridging the gap between gold(I)-thiolate complexes and thiolate-protected gold nanocrystals. *J. Am. Chem. Soc.* **127,** 5261–5270 (2005).
202. Schmidt, K. *et al.* Dynamics of renal electrolyte excretion in growing mice. *Nephron - Physiol.* **124,** 7–13 (2014).
203. Rennke, H. G., Patel, Y. & Venkatachalam, M. A. Glomerular filtration of proteins: Clearance of anionic, neutral, and cationic horseradish peroxidase in the rat. *Kidney Int.* **13,** 278–288 (1978).
204. Straus, W. Renal reabsorption and excretion of horseradish peroxidase. *Kidney Int.* **16,** 404–408 (1979).
205. Steinman, R. M. & Cohn, Z. A. The interaction of soluble horseradish peroxidase with mouse peritoneal macrophages in vitro. *J. Cell Biol.* **55,** 186–204 (1972).
206. Gajhede, M., Schuller, D. J., Henriksen, A., Smith, A. T. & Poulos, T. L. Crystal structure of horseradish peroxidase C at 2.15 Å resolution. *Nat. Struct. Biol.* **4,** 1032–1038 (1997).
207. Manning, M. C., Chou, D. K., Murphy, B. M., Payne, R. W. & Katayama, D. S. Stability of protein pharmaceuticals: An update. *Pharm. Res.* **27,** 544–575 (2010).
208. Yang, Y., Serrano, L. A. & Guldin, S. A Versatile AuNP Synthetic Platform for Decoupled

Control of Size and Surface Composition. *Langmuir* **34,** 6820–6826 (2018).

209. Martin Bland, J. & Altman, D. G. Statistical Methods for Assessing Agreement Between Two Methods of Clinical Measurement. *Lancet* **327,** 307–310 (1986).
210. Eckhard, U. *et al.* Active site specificity profiling of the matrix metalloproteinase family: Proteomic identification of 4300 cleavage sites by nine MMPs explored with structural and synthetic peptide cleavage analyses. *Matrix Biol.* **49,** 37–60 (2016).
211. Kridel, S. J. *et al.* Substrate Hydrolysis by Matrix Metalloproteinase-9. *J. Biol. Chem.* **276,** 20572–20578 (2001).
212. Fields, G. B. Using Fluorogenic Peptide Substrates to Assay Matrix Metalloproteinases. *Methods Mol. Biol.* **151,** 495–518 (2001).
213. Magde, D., Elson, E. & Webb, W. W. Thermodynamic fluctuations in a reacting system measurement by fluorescence correlation spectroscopy. *Phys. Rev. Lett.* **29,** 705–708 (1972).
214. Rigler, R., Mets, Ü. ., Widengren, J. & Kask, P. Fluorescence correlation spectroscopy with high count rate and low background: analysis of translational diffusion. *Eur. Biophys. J.* **22,** 169–175 (1993).
215. Rigler, P. & Meier, W. Encapsulation of fluorescent molecules by functionalized polymeric nanocontainers: Investigation by confocal fluorescence imaging and fluorescence correlation spectroscopy. *J. Am. Chem. Soc.* **128,** 367–373 (2006).
216. Zhang, X. D. *et al.* In vivo renal clearance, biodistribution, toxicity of gold nanoclusters. *Biomaterials* **33,** 4628–4638 (2012).
217. Rosebrough, S. F. & Hartley, D. F. Biochemical modification of streptavidin and avidin: in vitro and in vivo analysis. *J. Nucl. Med. Off. Publ. Soc. Nucl. Med.* **37,** 1380–1384 (1996).
218. Chinol, M. *et al.* Biochemical modifications of avidin improve pharmacokinetics and biodistribution, and reduce immunogenicity. *Br. J. Cancer* **78,** 189–197 (1998).
219. Gasperino, D., Baughman, T., Hsieh, H. V., Bell, D. & Weigl, B. H. Improving Lateral Flow Assay Performance Using Computational Modeling. *Annu. Rev. Anal. Chem.* **11,** 219–244 (2018).
220. Ong, I. L. H. & Yang, K.-L. Recent developments in protease activity assays and sensors. *Analyst* **142,** 1867–1881 (2017).
221. Zhang, Z., Zhang, X., Liu, B. & Liu, J. Molecular Imprinting on Inorganic Nanozymes for Hundred-fold Enzyme Specificity. *J. Am. Chem. Soc.* **139,** 5412−5419 (2017).
222. Tonga, G. Y. *et al.* Supramolecular regulation of bioorthogonal catalysis in cells using nanoparticle-embedded transition metal catalysts. *Nat. Chem.* **7,** 597–603 (2015).